Understanding the Molecular Mechanism of Ion and Amino Acid Transport in Neurons

Agnese Baroniņa

Linacre College

A thesis submitted to the Medical Sciences Division for the degree of Doctor of Philosophy in the University of Oxford

Michaelmas Term, 2020



Structural Genomics Consortium

Nuffield Department of Medicine

University of Oxford

UNDERSTANDING THE MOLECULAR MECHANISM OF ION AND AMINO ACID TRANSPORT IN NEURONS

ABSTRACT

In this thesis I aimed to understand how two membrane proteins, a solute carrier transporter and an ion channel, function in neuronal membranes. I used structural and biophysical methods to identify the molecular elements involved in the substrate selectivity and transport regulation.

EAAT3, a member of SLC1 family, is a glutamate transporter. It is expressed ubiquitously in brain but is thought to play distinct roles in different areas of the brain. EAAT3 malfunction is linked to several neurological diseases and disorders, making it a therapeutic target. Due to its complex regulation, EAAT3 activity could be modulated at various levels. The lack of EAAT3-specific inhibitors has hindered our understanding of EAAT3 involvement in cellular processes with the efforts so far focusing on ligand-based approaches. To study the basis of substrate selectivity in the SLC1 family, I solved two structures of EAAT3 at 3.3 Å resolution with bound inhibitors using the cryo-EM method. I report two novel inhibitor binding modes, expanding the current knowledge of the substrate binding site and how small molecules inhibitors interact with this site within the SLC1 family. To determine the kinetic parameters of ligand binding *in vitro*, I established a proteoliposome reconstitution system for detergent-purified EAAT3 and showed that the protein is functional and transports substrates with affinities consistent with results from cell-based studies reported in the literature.

TREK-2 is a member of the K2P potassium channel family, expressed in the CNS and implicated in neuropathic pain. The polymodal regulation of TREK-2 is not well understood, despite available 3D structures in two conformations. Here I describe functional binders (nanobodies) which I used to investigate the mechanism underlying TREK-2 regulation. I used X-ray crystallography to determine the structures of TREK-2 with bound activatory and inactivatory nanobodies at 2.4 Å and 3.5 Å resolution, respectively. Both nanobodies bind to the channel from the extracellular side but interact with different domains to elicit the opposite effects on the channel conductivity. These structures provide us with new insights into TREK-2 channel regulation.

AUTHORSHIP DECLARATION

This thesis and the work presented here was completed at the University of Oxford (Nuffield Department of Medicine) between January 2017 and December 2020, under the supervision of Prof Liz Carpenter, Prof Stephen Tucker and Dr Seungil Han (Pfizer, USA). The SURFE^{2}R experiments of EAAT3 were carried out by Antje Pommereau (Sanofi, Germany), as it was not possible for AB to visit their labs during the COVID-19 pandemic. The EAAT3 cryo-EM data sets that were used to solve the structures were collected by Dr Xiaodi Yu (Pfizer, USA). Electrophysiology studies on TREK-2 were carried out by Alexander Cloake (Dept. of Physics, University of Oxford). The TREK-2 dataset with Nanobody 67 bound was collected by Dr Ashley Pike. All contributions made by others have been clearly stated in the text. This work has not been submitted in full or partial fulfilment of any other degree.

Agnese Baroniņa

December 2020

ACKNOWLEDGEMENTS

First and foremost, I would like to express my sincere gratitude to my supervisor, Prof Liz Carpenter, for the opportunity to work on projects I found most engrossing and for her guidance and support throughout this thesis. Her enthusiasm for the field and support for new ideas whilst guiding me as a scientist was essential for me to develop as one. I would also like to thank Dr Seungil Han, my industrial supervisor, who showed his generosity while hosting me during my placement at Pfizer. I have greatly benefited from his helpful discussions. This was invaluable experience and I learned so much about life and work at pharmaceutical industry. I am greatly thankful to Prof Stephen Tucker for the helpful discussions about TREK-2 project.

My special thanks go to all the people who allowed me to adopt them as my mentors. I would like to thank IMP1 group members – Dr Laiyin Nie, Dr Ashley Pike and Dr Chitra Shintre – who shared their wisdom and kept their patience with me. Together, they have taught me everything I know in structural biology and biophysics and made my DPhil an unforgettable experience.

I would like to thank the present and past members of the IMP1 group and the whole SGC team, for the help and support throughout my DPhil. I would like to thank the members of IMP1 who were always ready to help and share their experience, including Dr Yin Dong, Dr Andrew Quigley, Dr Didi He, Tomas Pascoa, Amy Chu and Adam Evans. In particular, I would like to thank all of the SGC Biotech team for their support with cloning and cell work, and all the people in cryo-EM bubble, for sharing their knowledge and advice.

My special thanks go to all the people who helped me with my experiments in Pfizer and Sanofi.

I would like to thank the many friends I have made in the SGC and across the university, who made the life in Oxford so enjoyable. I would like to thank my lunch group, Dr Jong Wong, Dr Zhuoyao Chen, Elizabeth Brown and Ailefeila Aihemaiti and my orienteering group, Dr Aini Vuorinen and Dr Johanna Michl. Special thanks go to Chady, who has been invaluable support and has helped me through the finishing of thesis.

I would also like to acknowledge The Biotechnology and Biological Sciences Research Council (BBSRC) iCASE Studentship for their financial support over the last four years.

I would like to thank INSTRUCT, part of the European Strategy Forum on Research Infrastructures (ESFRI) and the Hercules Foundation Flanders for their support to the Nanobody discovery.

Visbeidzot, vislielāki paldies manai ģimenei – mammai, tētim, Ievai, Zanei un Matīsam, kuri mani vienmēr ir atbalstījuši un iedrošinājuši, un kuru kompānija man pietrūka visvairāk.

LIST OF ABBREVIATIONS

±HIP-B – (±)-3-Hydroxy-4,5,6,6a-tetrahydro-3aH-pyrrolo[3,4-d]isoxazole-6-carboxylic acid

2D - two-dimensional

3D - three-dimensional

ABC - ATP-binding cassette

AP2 - adaptor (or assembly) protein-2

ASCT - alanine, serine, cysteine transporter

ATP - adenosine triphosphate

AU - asymmetric unit

B - temperature factor

ß-OG - octyl β-D-glucopyranoside

CC - cross-correlation

$CC_{1/2}$ - correlation coefficient between random half-datasets

CCF - cross-correlation function

CDR1/2/3 - complementarity determining regions 1-3

CHO - Chinese hamster ovary

CHS - cholesteryl hemisuccinate tris salt

CMC - critical micelle concentration

CMD - carboxylated methyl dextran

CNS - central nervous system

cryo-EM - cryogenic transmitting electron microscopy (cryo-EM)

CTF - contrast transfer function

CV - column volumes

DA - dicarboxylic aminoaciduria

DB - desalting buffer

DDD - direct detection devices

DDM - n-Dodecyl-β-D-Maltopyranoside

DL-TBOA - DL-threo-β-benzyloxyaspartic acid

DMSO - dimethyl sulfoxide

DTT - dithiothreitol

EAAT - excitatory amino acid transporter

EB - elution buffer

EC1/2 - extracellular helices 1-2 in K2Ps

EC_{50} - half maximal effective concentration

EDTA - ethylenediaminetetraacetic acid

EM - electron microscopy

ER - endoplasmic reticulum

EXB - extraction buffer

FL - full-length

FSC - Fourier shell correlation

FT - Fourier transform

GABA - γ-aminobutyric acid

GHK - Goldman-Hodgkin-Katz

GltPh - EAAT homologue from Pyrococcus horikoshii

GltTk - EAAT homologue from Thermococcus kodakarensis

GPCRs - g-protein coupled receptors

GSH - glutathione

GTRAP3-18 - glutamate transporter EAAC1-associated protein

GWAS - genome-wide association study

HEK - human embryonic kidney cells

HP1/2 - helical hairpins

HPLC - high performance liquid chromatography

I-V - current-voltage

IC_{50} - half maximal inhibitory concentration

Ig - immunoglobulin

IMAC - immobilized metal affinity chromatography

IPTG - Isopropyl β- d-1-thiogalactopyranoside

K2P - two-pore domain potassium channel

K_D - equilibrium dissociation constant

K_I - inhibition constant

K_M - substrate affinity constant

L-PDC - L-trans-Pyrrolidine-2,4-dicarboxylic acid

L-TBOA - L-threo-β-Benzyloxyaspartic acid

LCP - lipidic cubic phase

LMNG - lauryl maltose neopentyl glycol

LPR - lipid to protein

LTP - long-term potentiation

M1/2/3/4 - transmembrane helices 1-4 in K2Ps

MAG - monoacylglycerol

MDCK - Madin–Daney canine kidney cell line

ML - maximum-likelihood

MPD - 2-Methyl-2,4-pentanediol

MR - molecular replacement

mRNA - messenger RNA

MTF - modulation transfer function

MWCO - molecular-weight cut-off

nanoDSF - nano differential scanning fluorimetry

NCS - non-crystallographic symmetry

NRF2 - nuclear factor erythroid 2-related factor 2

OCD - obsessive-compulsive disorder

OGNG - octyl glucose neopentyl glycol

P1/2 - pore forming loops 1-2 in K2Ps

PBS - phosphate buffered saline

PDB - Protein Data Bank

PDGF - platelet-derived growth factor

PDZK1 - PDZ-domain-containing protein 1

PE - phosphatidylethanolamine

PEG - polyethylene glycol

PH1/2 - pore helices 1-2 in K2Ps

pI - isoelectric point

PI - phosphatidylinositol

PI3K - phosphoinositide 3-kinase

PKC - protein kinase C

PNS - peripheral nervous system

Po - open probability

POPC - 1-Palmitoyl-2-oleoyl- PC

POPE - 1-Palmitoyl-2-oleoyl- PE

PSF - point spread function

R_{max} - analyte binding capacity (SPR)

RTN2B - reticulon-2B

RU - response units

SEC - size exclusion chromatography

SF - selectivity filter

Sf9 - Spodoptera frugiperda

SGD - stochastic gradient descent

SLC - solute carrier

SNAP-23 - synaptosomal-associated protein 23

SNPs - single-nucleotide polymorphisms

SNR - signal-to-noise ratio

SorCS2 - sortilin related VPS10 domain containing receptor 2

SPA - single particle analysis

SPR - surface plasmon resonance

SSM - Solid-supported membrane

STX1 - syntaxin-1A

TALK - two-pore domain alkaline activated K+ channels

TASK - two-pore domain, acid-sensitive K+ channel

TB - terrific broth

TEV - tobacco etch virus

TFB-TBOA - (3S)-3-[[3-[[4-(Trifluoromethyl)benzoyl]amino]phenyl]methoxy]-L-aspartic acid

THIK - two-pore domain halothane inhibited K+ channels

T_M - melting temperature

TMH - transmembrane helices

TRAAK - two-pore domain related arachidonic acid activated K+ channel

TREK - TWIK-related K+ channels

TRESK - TWIK-related spinal cord potassium channel

TWIK - tandem of P-domains in a weak inward rectifying K+ channel

UCPH-101 - 2-Amino-5,6,7,8-tetrahydro-4-(4-methoxyphenyl)-7-(naphthalen-1-yl)-5-oxo-4H-chromene-3-carbonitrile

VD - vapour diffusion

VGIC - voltage-gated ion channel

V_H - variable domains of heavy chain

V_L - variable domains of light chain

V_{max} - maximum rate of uptake

WB - wash buffer

WT- wild type

CONTENTS

ABSTRACT 3

AUTHORSHIP DECLARATION 4

ACKNOWLEDGEMENTS 5

LIST OF ABBREVIATIONS 6

1 INTRODUCTION 14

1.1 Introduction to membrane proteins involved in membrane permeability 14
1.1.1 Solute carrier (SLC) transporters 14
1.1.1.1 SLC Transport modes 15
1.1.1.2 SLC Transport mechanisms 16
1.1.2 Ion channels 17
1.1.2.1 Selectivity and gating of ion channels 18

1.2 SLC1 family transporters 18
1.2.1 Molecular properties of EAAT3 19
1.2.2 EAAT3 Expression and regulation patterns 24
1.2.2.1 Indirect regulation of EAAT3 activity by small molecules via signalling pathways 27
1.2.3 Physiological functions 27
1.2.3.1 Glutamate clearance in the CNS 28
1.2.3.2 Synaptic modulation 29
1.2.3.3 GABA synthesis 29
1.2.3.4 Cysteine uptake 30
1.2.3.5 Glutamate/ Aspartate absorption 30
1.2.4 Regulation of EAAT3 by small molecules 30
1.2.5 EAAT3 in disease 32
1.2.5.1 The CNS pathologies 32
1.2.5.1.1 Epilepsy 32
1.2.5.1.2 Schizophrenia 33
1.2.5.1.3 Obsessive-compulsive disorder (OCD) 33
1.2.5.2 Renal pathology 34
1.2.5.2.1 Dicarboxylic aminoaciduria (DA) 34

1.3 Summary and aims of the EAAT3 project 34

1.4 Two-pore domain potassium channels (K2Ps) 35
1.4.1 Expression and Function of K2Ps 37
1.4.2 The architecture of potassium channels 38
1.4.3 Structural studies of TREK-2 40
1.4.4 Biophysical and pharmacological characteristics of TREK-2 44
1.4.5 Nanobodies as functional modulators to study TREK-2 function 45

1.5 Summary and aims of the TREK-2 work 47

2 METHODS AND MATERIALS 49

2.1 Biochemical methods 49
2.1.1 Protein production and purification 49

2.1.1.1 Baculovirus generation and membrane protein expression 49
2.1.1.2 Nanobody expression 50
2.1.1.3 Membrane protein purification 50
2.1.1.4 Membrane preparation for SURFE^{2}R studies 52
2.1.1.5 Nanobody purification 52
2.1.2 Protein reconstitution systems 53
2.1.2.1 Proteoliposomes 53

2.2 Biophysical methods 53
2.2.1 Characterisation of TREK-2 Nanobodies using Surface plasmon resonance (SPR) 54
2.2.2 EAAT3 Activity assays 55
2.2.2.1 Radiolabelled ligand uptake assay 55
2.2.2.2 SURFE^{2}R assay 55
2.2.3 nanoDSF 56

2.3 Structural biology 56
2.3.1 EAAT3 Structure determination by Cryo-EM 56
2.3.1.1 Sample preparation 56
2.3.1.2 Grid screening and data collection 57
2.3.1.3 Data processing 57
2.3.1.4 Model building, refinement and validation 60
2.3.2 Structure determination of TREK-2 Nanobody complexes using X-Ray crystallography 61
2.3.2.1 Crystallisation of TREK-2 nanobody complexes 61
2.3.2.2 Crystal screening and data collection 62
2.3.2.3 X-ray crystallography data processing 63
2.3.2.4 Model building, refinement and validation 64
2.3.2.5 Structure presentation and analysis 64

3 CHARACTERISATION OF EAAT3 FUNCTION *IN VITRO* 65

3.1 Introduction 65
3.1.1 The pharmacology of EAATs 65
3.1.2 In vitro assays for functional characterisation of solute transporters 66
3.1.2.1 Kinetic uptake assay 68
3.1.2.2 Dose-response assay 69

3.2 Solid-supported membrane (SSM) based electrophysiology 70
3.2.1 EAAT3 functional characterisation using the SURFE^{2}R technology 72
3.2.1.1 Optimization of EAAT3 reconstitution in proteoliposomes for functional studies 72
3.2.1.2 Optimization of the liposome lipid composition 73
3.2.1.3 Optimization of EAAT3 reconstitution in liposomes 75
3.2.1.4 Characterisation of EAAT3 substrate transport using the SURFE^{2}R system 80
3.2.1.5 Pharmacological characterisation of EAAT3 using the SURFE^{2}R system 84

3.3 Optimisation of radiolabelled substrate uptake assay for EAAT3 functional characterisation 86
3.3.1 Radioligand uptake assay 86
3.3.2 Preliminary results of EAAT3 pharmacological characterisation using radioligand uptake assay 86

3.4 Comparison of the two methods used to characterise EAAT3 transport activity 90

3.5 Summary of the functional characterisation of EAAT3 91

4 EAAT3 STRUCTURES REVEAL NOVEL BINDING MODES FOR TWO INHIBITORS 92

4.1 Introduction 92

4.2 Sample optimisation for structural studies of EAAT3 with bound inhibitors 92

4.2.1 Selection of ligands for structural studies ... 92
4.2.2 Cryo-EM grid optimisation ... 96

4.3 Structure determination of EAAT3 with bound inhibitors ... 97
4.3.1 Data processing and model building for EAAT3-ligand structures ... 97
4.3.2 The characteristic fold of the SLC1 family ... 102
4.3.3 Structural interpretation of disease associated mutations in EAATs ... 110
4.3.4 Post-translational modifications in EAAT3 ... 113
4.3.5 Ion coordination in EAAT3 ... 113
4.3.6 EAAT3 lipid interactions ... 115
4.3.7 The binding sites for the inhibitors TFB-TBOA and ±HIP-B in EAAT3 ... 118
4.3.7.1 The TFB-TBOA inhibitor binding site ... 118
4.3.7.2 The ±HIP-B inhibitor binding site ... 121
4.3.8 Comparison of Inhibitor binding modes ... 124

4.4 Summary of the structural studies of EAAT3 ... 126

5 STRUCTURAL CHARACTERISATION OF FUNCTIONAL TREK-2 NANOBODIES ... 128

5.1 Introduction ... 128
5.1.1 Structural studies of TREK-2 ... 128
5.1.1.1 Channel gating in the TREK subfamily ... 128
5.1.1.2 TREK-2 structures reveal two conformations of the channel ... 130
5.1.1.3 Crystallisation chaperones for membrane proteins ... 131

5.2 Biophysical characterisation of TREK-2 binders ... 132

5.3 Structure determination for complexes of TREK-2 with functional nanobodies ... 135
5.3.1 Crystallisation, data collection and structure solution ... 135
5.3.2 Structure of a complex of TREK-2 with the activating nanobody Nb67 ... 139
5.3.2.1 Crystal packing in the TREK-2:Nb67 complex ... 139
5.3.2.2 Overall structural features in the TREK-2:Nb67 complex ... 141
5.3.2.3 How Nb67 activates the TREK-2 channel ... 147
5.3.3 The structure of TREK-2 in complex with the inactivating nanobody Nb61 ... 154
5.3.3.1 Crystal packing in the TREK-2:Nb61 complex ... 154
5.3.3.2 Overall structural features the TREK-2:Nb61 complex ... 155
5.3.3.3 How nanobody inactivates the TREK-2 channel ... 158
5.3.3.4 Complementarity of structural and biophysical studies ... 159

5.4 Summary of the structural characterisation of functional TREK-2 binders ... 160

6 DISCUSSION ... 161

7 APPENDIX ... 169

7.1 THEORETICAL BASIS OF BIOPHYSICAL AND STRUCTURAL METHODS ... 169
7.1.1 Surface plasmon resonance (SPR) ... 169
7.1.2 Cryo-EM ... 172
7.1.2.1 Theory and basic principles of Cryo-EM ... 172
7.1.2.1.1 Sample preparation ... 172
7.1.2.1.2 Achievable resolution with electron microscopes ... 174
7.1.2.1.3 Imaging using Electron microscopes ... 176
7.1.2.1.4 Image formation ... 178
7.1.2.2 Single particle analysis ... 181
7.1.2.2.1 Pre-processing of images ... 181
7.1.2.2.2 CTF Estimation ... 181
7.1.2.2.3 CTF Correction ... 182
7.1.2.2.4 Particle picking ... 182

7.1.2.2.5 Image normalisation and particle sorting 183
7.1.2.2.6 2D classification 184
7.1.2.2.7 From 2D to 3D reconstruction 185
7.1.2.2.8 Initial model 186
7.1.2.2.9 3D Refinement 187
7.1.2.2.10 Validation 188
7.1.3 X-ray crystallography 188
7.1.3.1 Theory of protein X-ray crystallography 188
7.1.3.2 Data pre-processing in X-ray crystallography 191
7.1.3.3 Data post-processing in X-ray crystallography 193
7.1.3.4 Phasing – Molecular replacement 193
7.1.3.5 Membrane Protein crystallisation techniques 194
7.1.3.5.1 Vapour diffusion 194
7.1.3.5.2 Lipidic cubic phase 195

7.2 Sequence alignment of human and bacterial SLC1 transporters 195

BIBLIOGRAPHY 198

CHAPTER 1

1 INTRODUCTION

1.1 INTRODUCTION TO MEMBRANE PROTEINS INVOLVED IN MEMBRANE PERMEABILITY

The cell membrane is a semipermeable barrier to ion and polar molecule movement due to its hydrophobic interior. It allows cells to form and maintain an electrochemical gradient required for normal function. To form and take advantage of this gradient, cells rely on specialised transmembrane proteins. The movement of selected ions and molecules across the plasma membrane or the membranes of intracellular organelles involve members of three classes of proteins: pumps, carriers and channels (Alberts 2002). The electrochemical gradient is established by pumps that use a free energy source (such as adenosine triphosphate (ATP)-hydrolysis or light) to perform the thermodynamically unfavourable movement of ions against the concentration gradient. While the majority of pumps only transport ions, a class of ATP-dependent pumps, the ATP-binding cassette (ABC) transporter superfamily, also transport small molecules. This is called *primary active* transport as it uses energy, and the pumps establish the ion gradient that is used by the *secondary active* transporters – solute carriers – to mediate transport of another solute without further energy consumption. Channels also rely on a pre-existing ion gradient to perform *passive* transport by forming a regulatable pore that allows a rapid downhill movement of selected ions. Cells have specific requirements regarding the ionic composition and substrate availability, so each cell type expresses a distinct set of membrane proteins (Berg, Tymoczko et al. 2012).

1.1.1 SOLUTE CARRIER (SLC) TRANSPORTERS

Solute carriers (SLCs) comprise the second largest superfamily of membrane proteins in humans (preceded by G-protein coupled receptors) (Alexander, Kelly et al. 2019) but unlike other superfamilies, SLCs are highly diverse structurally, with a variety of folds identified to date (Colas, Ung et al. 2016). Classification based on the human genome nomenclature have identified 67 transporter families where members share at least 20% sequence identity (Povey, Lovering et al. 2001,

Hediger, Romero et al. 2004, Alexander, Kelly et al. 2019). Grouping of SLCs based on biological function and sequence similarity has also been implemented (Saier 2000). Secondary active transporters are found in both prokaryotes and eukaryotes, and, in many cases, extensive studies on prokaryotic homologues have provided archetypes for several SLC families (Berg, Tymoczko et al. 2012).

1.1.1.1 SLC TRANSPORT MODES

Many SLCs transport various water-soluble substrates across the membrane, including ions, molecules and drugs, by coupling the movement of one solute down its electrochemical gradient to an unfavourable movement of another against its concentration gradient. The rate of this process is limited by the number of molecules the transporter can carry and by the conformational changes it must undergo. Based on the energy coupling mechanism, SLCs are classified as antiporters (exchangers) or symporters (Figure 1.1) (Berg, Tymoczko et al. 2012). A simpler type of SLC – uniporters – facilitate the movement of their substrate down a concentration or electrochemical gradient. Uniporters have two classes – carriers and channels, divided based on the transport rates, with channels transporting molecules much quicker than carriers. This is related to the membrane-spanning pore accessibility in the open and conductive (specific ions can pass through the pore) state. While the open channel transmembrane pore is accessible from both sides simultaneously, the carrier binding site is not, with the carrier flipping between two conformations (Wolfersberger 1994). For many members of the SLC superfamily, the transport mechanism is still unknown, some possess other functions, such as enzymatic or ion channel activities (Alexander, Kelly et al. 2019), while SLC3 family members act as chaperones to form functional heterodimers with a selection of members of SLC7 family (Colas, Ung et al. 2016).

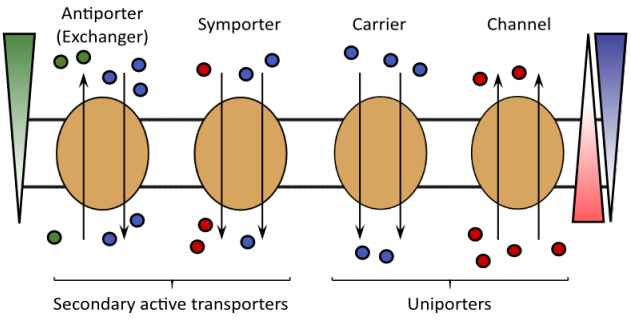


Figure 1.1: Mechanism of antiporters, symporters, and uniporters. Secondary transporters use the

electrochemical gradient to transport substrates across the lipid bilayer. Antiporters transport two substrates in opposite directions, with one moving down its chemical gradient. Symporters transport one substrate down a gradient, coupled to the transport of another substrate up a concentration gradient, with both molecules moving in the same direction. Uniporters transport a single species down their concentration gradients and are divided into carriers and channels, with channels transporting molecules much quicker than carriers. Three different substrates are depicted as coloured ovals with the concentration gradients for each indicated by the triangles on each side, with darker shading indicating more concentrated area. Adapted from (Alberts 2002).

1.1.1.2 SLC TRANSPORT MECHANISMS

SLC transporters use an alternating access mechanism, where substrate binding site is exposed to either side of the membrane in an alternating fashion, to move substrates across the plasma membrane. During the transport cycle, the transporter adopts successive conformational states which exposes the binding site to either side of the membrane (termed inward- or outward-facing conformations) or completely shields it from solvent exposure (termed an occluded conformation). The transport mechanism is defined by the domain movements as well as substrate interactions with the transporter.

There are three known mechanisms of alternating access for SLC transporters (Figure 1.2): rocker-switch, gated pore and elevator mechanisms (Colas, Ung et al. 2016). The rocker-switch type is used by SLCs with two homologous helix bundle domains with a central binding site. Both domains move synchronously to adopt an inward- or outward-facing state. In the gated pore mechanism, the binding site accessibility is regulated by two gates, one at each side of the membrane. Both gates work in a coordinated manner so that the binding site is never exposed to both sides of the membrane simultaneously. Transporters using the elevator mechanism consist of a transport domain with the substrate binding site and a scaffold domain, which forms contacts between protomers. The elevator domain moves perpendicular to the membrane plane to expose the binding side to the extracellular and intracellular sides, while the scaffold domain remains static (Colas, Ung et al. 2016).

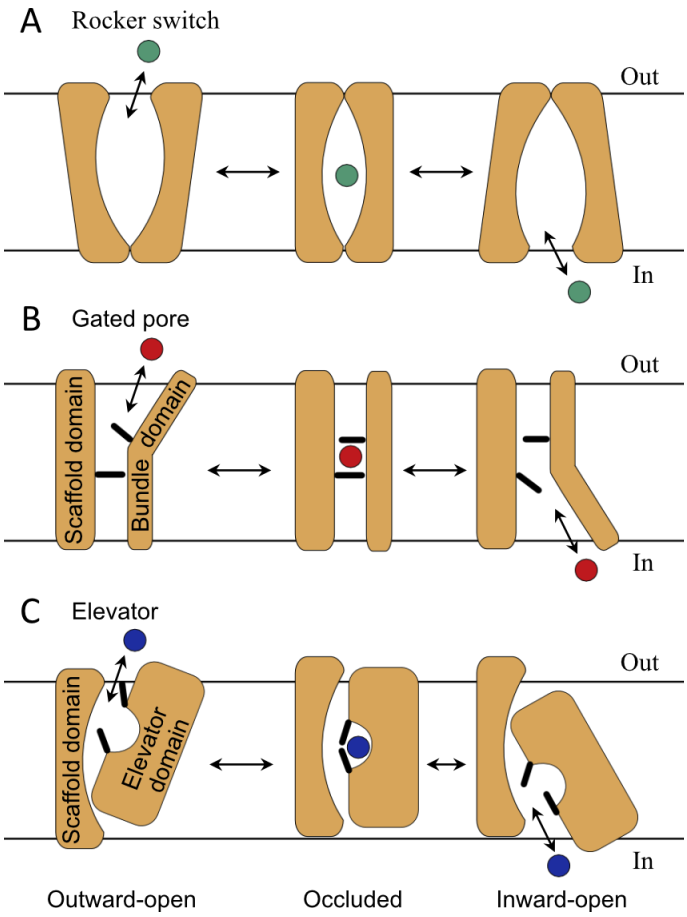


Figure 1.2: Types of alternating-access mechanism in secondary active transporters. A schematic representation of three states (outward-open, occluded, inward-open) associated with the transport cycle. **A** Rocker switch. The transporter opens to the either side of the membrane while simultaneously sealing the pathway across the membrane on the other side. The substrate (green) binds to the exposed binding site and induces conformational changes, resulting in its release on the other side of the membrane. **B** Gated pore. The transporter consists of a static scaffold domain and a moving bundle domain that undergoes conformational changes to bind and release the substrate. The substrate (red) binding site accessibility is regulated by two gates. **C** Elevator. Similar to a gated pore, the transporter consists of a static scaffold domain involved in oligomerisation, and a elevator domain, that undergoes rigid body movement across the membrane plane, exposing the binding site to either side of the membrane. The binding site accessibility is regulated by two gates. Adapted from (Colas, Ung et al. 2016).

1.1.2 ION CHANNELS

Ion channels are membrane proteins that are essential for many physiological functions involving controlled passive transport of inorganic ions (Figure 1.1). There are more than 300 types of ion channels that have many different roles, including signalling in electrically excitable cells (neurons and muscles) and regulation of cell volume and homeostasis (Gadsby 2009). K^+ selective channels are

one of the most common channel types, found in all mammalian cell types and in all organisms including bacteria. Of these, K^+ leak channels are of particular importance since the cell uses K^+ ions to maintain the osmotic balance and the resting membrane potential by balancing the K^+ electrochemical gradient across the plasma membrane (Renigunta, Schlichthorl et al. 2015).

1.1.2.1 SELECTIVITY AND GATING OF ION CHANNELS

Unlike aqueous pores, ion channels impose ion selectivity through close contacts with the permeating ions. The narrowest part of the channel, called the selectivity filter, is lined with residues that interact with the ions they transport, while excluding other types of ions. The selectivity is based on the size and charge of the ions, which possess a hydration shell made up of interacting water molecules. For ions to cross the membrane, they must lose the water molecules before passing through the selectivity filter (Gadsby 2009).

Yet, while SLC transporters can achieve transport rates of several thousand molecules per second, ion channels can achieve rates that are 1000-fold higher, by allowing ions to move down the concentration gradient at the speed close to that of free diffusion. This requires a precise gating mechanism so the channels can respond to the rapid chemical and physical changes in the environment (Berg, Tymoczko et al. 2012). There are three types of activation mechanisms that broadly categorize all ion channels. Type one includes ligand-gated channels, that are activated by the binding of small molecules or proteins causing channel opening or closing. The second type, pH-gated channels, senses changes in the cellular acidity. Finally, the third type of channels is a much broader group that respond to physical stimuli and includes voltage-, mechanical,- and temperature-gated channels (Goldschen-Ohm and Chanda 2017).

1.2 SLC1 FAMILY TRANSPORTERS

Members of the solute carrier 1 (SLC1) family are secondary active, Na^+-dependent transporters that use the alternating access mechanism to mediate the transport of anionic (both L- and D-aspartate, but only L-glutamate (Gazzola, Dall'Asta et al. 1981)) and/or neutral amino acids across the plasma membrane. The family consists of five excitatory amino acid transporters (EAATs) and two neutral amino acid transporters (Alanine, Serine, Cysteine Transporters; ASCTs) (Figure 1.3). Initially, the protein names were assigned without systematic nomenclature, resulting in multiple names for the

same protein (for example, GLAST/ GLT1/ EAAC1 are alternative names for EAAT1/ EAAT2/ EAAT3, respectively). The EAAT nomenclature corresponds to the order in which the genes were cloned (Danbolt 2001). The SLC nomenclature refers to the gene, the EAAT/ASCT nomenclature refers to the protein name.

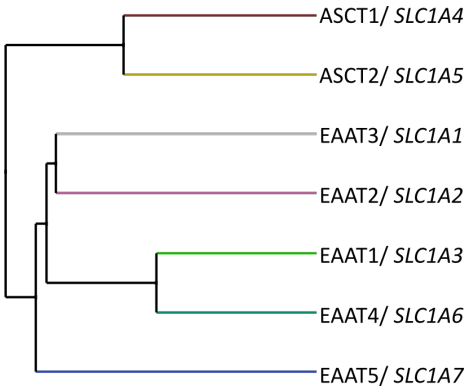


Figure 1.3: Dendrogram of the human SLC1 family. Protein sequences of the human SLC1 family were aligned using COBALT (Papadopoulos and Agarwala 2007). Distances, calculated using the BLOSUM62 matrix, were plotted as a dendrogram. Both protein and gene name (in italic) are indicated.

The EAATs are expressed and selectively localised in brain and peripheral tissues. Of these, EAAT1 is mainly found in the glial cells (predominantly cerebellum) and EAAT2 is found in the glial cells everywhere in brain. EAAT3 and EAAT4 have neuronal localisation, with EAAT3 expressed in forebrain and EAAT4 expressed predominantly in cerebellar Purkinje cells. EAAT5 is only expressed in retina cells in the eye (Danbolt 2001). The two ASCTs (encoded by the SLC1A4 and SLC1A5 genes) were identified based on sequence homology to the EAATs (Danbolt 2001). They are obligate homo- and heteroexchangers (same transporter substrate is transported across the membrane or uptake of one transporter substrate cause the release of another one, respectively) of small neutral amino acids that co-transport a single Na^+ ion with the substrate amino acid. Both have widespread tissue expression (Kanai and Hediger 2003).

1.2.1 MOLECULAR PROPERTIES OF EAAT3

EAAT3 (the product of the *SLC1A1* gene), the focus of this thesis, was originally cloned from a rabbit (Kanai and Hediger 1992) and is the most efficient among the EAATs, with a turnover rate in the millisecond range (Grewer, Watzke et al. 2000). Through cell-based functional studies on the human

homologues EAAT1-3, the molecular mechanism and coupling stoichiometry was determined (Grewer, Gameiro et al. 2014). All EAATs exhibit complex transport stoichiometry, where three Na^+ ions are co-transported with the substrate and a proton, followed by a counter-transport of one K^+ ion (Zerangue and Kavanaugh 1996). Additionally, SLC1 family transporters show chloride conductance that is kinetically, but not stoichiometrically coupled to substrate transport, making them dual function transport proteins (Figure 1.4) (Kanai and Hediger 2003, Grewer and Rauen 2005, Rose, Ziemens et al. 2018). In fact, EAAT4 and EAAT5 are suggested to function as chloride channels, since they are not efficient in glutamate transport (Danbolt 2001, Gameiro, Braams et al. 2011). This electrogenic transport mechanism ensures that substrate transport only reverses under extreme conditions (Rose, Ziemens et al. 2018).

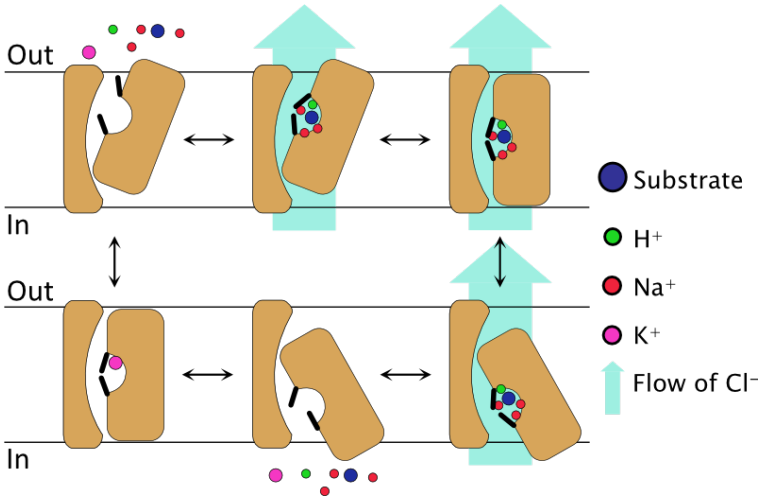


Figure 1.4: The EAAT transport cycle. All EAATs share the same transport cycle. Three sodium ions (red circles), a proton (green circle) and a substrate amino acid (blue circle) bind to an outward-facing transporter. This initiates conformational changes required for substrate translocation. The elevator domain with bound substrate and ions translocates across the membrane, and disassociation of a sodium ion triggers release of the substrate on the cytoplasmic side. Subsequently a potassium ion (pink circle) binds to the empty transporter and the transporter returns to the outward facing state. The EAATs also show chloride channel activity, that is kinetically but not stoichiometrically coupled to the substrate binding and translocation steps. The chloride ions move to counterbalance the influx of a net positive charge, shown as teal arrows. The transporters can run in reverse, indicated by the double headed arrows. Adapted from (Malik and Willnow 2019).

Under pathophysiological conditions, EAAT3 is more likely to run in reverse due to the high glutamate concentration in neurons (~10 mM) and thus contribute to glutamate excitotoxicity (Rossi, Oshima et al. 2000, Grewer, Gameiro et al. 2008). This is particularly significant in the brain, since ischemic

conditions lead to ATP depletion and subsequent disruption of ion gradients mostly established by Na^+/K^+ ATPase. The following increase in extracellular [K^+] leads to membrane depolarisation, which promotes the reversal of the EAAT transport cycle and release of glutamate. This acts as a positive feedback for further membrane depolarisation, leading to toxic levels of glutamate concentration (~100 μM) in the extracellular space (Nicholls and Attwell 1990).

EAAT3 has a membrane topology shared by all the members of SLC1 family consisting of 8 transmembrane helices (TMH) (Figure 1.5).

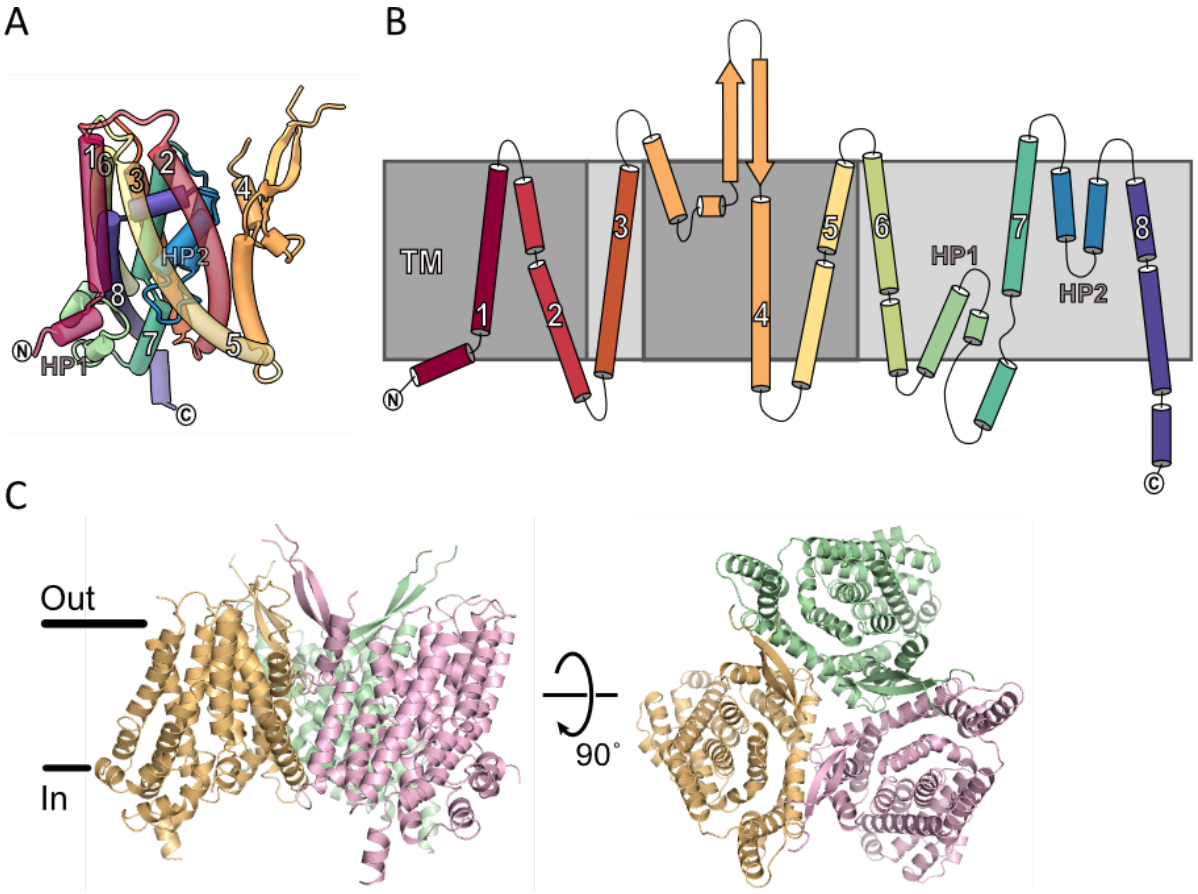


Figure 1.5: Overall fold and organisation of EAAT3. The schematic representation of an EAAT3 monomer – overall fold (**A**), 2D representation (**B**) and the trimeric assembly (**C**). The same colour scheme is used in panels A and B. TMH 1-2 and 4-5 form the scaffold domain (dark grey shading) while TMHs 3, 6-8 arrange in a bundle that moves across the membrane – elevator domain (light grey shading). The binding site accessibility is regulated by two helical hairpins – HP1-2. The 2D representation is based on EAAT1 structure and adapted from (Canul-Tec, Assal et al. 2017). Monomers (in light green, light pink and light yellow) assemble in a trimer, as seen from the plane of the membrane (panel C, left) and extracellular side (panel C, right).

The crystal structures of the bacterial orthologue from *Pyrococcus horikoshii* (GltPh) (Yernool, Boudker et al. 2004) showed for the first time the overall architecture of the transporter. Further structure-function studies of GltPh and another orthologue from *Thermococcus kodakarensis* (GltTk) (Jensen, Guskov et al. 2013) established that these transporters assemble in homotrimers, with each monomer comprising two domains. The N-terminal part forms a crescent-shaped scaffold domain, with the C-terminus forming the barrel-shaped functional transport domain, where two re-entrant helical hairpins at each side of the membrane regulate the access of the substrate binging site (HP1 and HP2 in Figure 1.5 B) (Yernool, Boudker et al. 2004). The protomers interact only through the rigid scaffold domains, while the transport domains accommodate the substrate and ion binding sites (Boudker, Ryan et al. 2007, Groeneveld and Slotboom 2007, Reyes, Ginter et al. 2009). Three different states of the transport domain relative to the scaffold domain have been captured so far: outward-facing (Yernool, Boudker et al. 2004), intermediate (Verdon and Boudker 2012) and inward-facing (Reyes, Ginter et al. 2009), with the monomers shown to be functioning independently (Grewer, Balani et al. 2005). The rigid-body movement of the transport domain resembles that of an elevator, moving substrate and ions across the membrane plane.

The overall SLC1 architecture was shown to be conserved in the human homologues with human SLC1s possessing an extracellular loop between sections of TMH4 not present in bacterial structures. The three-dimensional (3D) structure of thermostabilized human EAAT1, which includes 75% of the residues from wild-type EAAT1, was solved using X-ray crystallography at 3.3 Å (Canul-Tec, Assal et al. 2017), while ASCT2 structure was solved by cryogenic transmission electron microscopy (cryo-EM) at 3.8/ 3.5 Å ((Garaeva, Oostergetel et al. 2018, Yu, Plotnikova et al. 2019). Both EAAT1 and ASCT2 form homotrimers, where each protomer consists of a transport and a scaffold domain. The human transporters were captured in different conformational states (see Table 1.1) with all the transport domains adopting either outward- (EAAT1, ASCT2) or inward-facing (ASCT2) conformations.

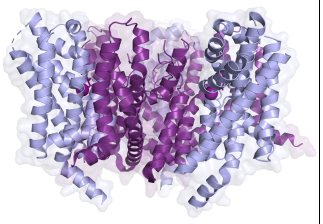
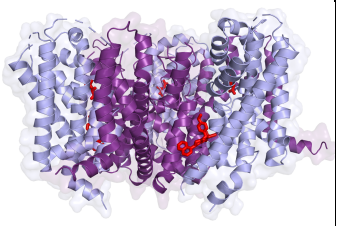
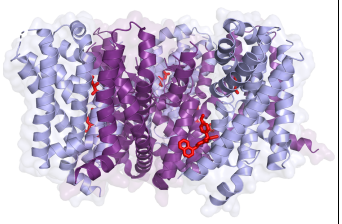
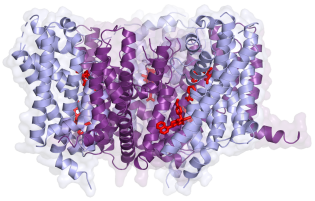
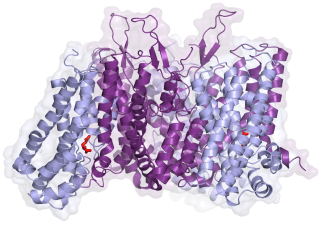
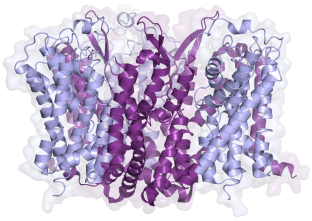
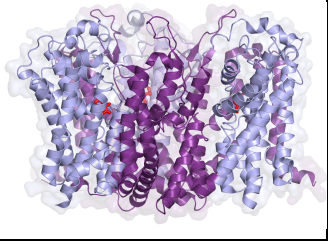
Transporter	PDB ID	Resolution	Ligands	Conforma-tion	3D representation
$EAAT1_{cryst\text{-}II}$	5LLU[1]	3.32 Å	L-Asp	Outward	
$EAAT1_{cryst}$	5LLM[1]	3.25 Å	L-Asp; UCPH101	Outward	
$EAAT1_{cryst\text{-}II}$	5LM4[1]	3.10 Å	L-Asp; UCPH101	Outward	
$EAAT1_{cryst}$	5MJU[1]	3.71 Å	TFB-TBOA; UCPH101	Outward	
ASCT2	6GCT[2]	3.85 Å	L-Gln	Inward	
ASCT2	6MP6[3]	3.54 Å	apo	Outward	
ASCT2	6MPB[3]	3.84 Å	L-Gln	Outward	

Table 1.1: Published and released structures of human SLC1 family members. In the 3D models, the scaffold domain is coloured in purple and the elevator domain in blue and the different conformations

are represented by the orientation of the elevator domain relative to the scaffold domain. The ligands are coloured in red and shown in stick representation. The conformation refers to the binding site availability relative to the membrane, with outward-facing (outward) being exposed to the extracellular side and inward-facing (inward) being exposed to the cytoplasm. UCPH-101: 2-Amino-5,6,7,8-tetrahydro-4-(4-methoxyphenyl)-7-(naphthalen-1-yl)-5-oxo-4H-chromene-3-carbonitrile, L-Asp: aspartate; L-Gln: glutamine; TFB-TBOA: (3S)-3-[[3-[[4-(Trifluoromethyl)benzoyl]amino]phenyl]methoxy]-L-aspartic acid. [1] (Canul-Tec, Assal et al. 2017), [2] (Garaeva, Oostergetel et al. 2018), [3] (Yu, Plotnikova et al. 2019).

1.2.2 EAAT3 EXPRESSION AND REGULATION PATTERNS

EAAT3 is a high affinity glutamate transporter with tissue selective expression. It is highly expressed in neurons in the central nervous system (CNS), where in contributes to the uptake of glutamate and cysteine (Danbolt 2001). It is found in the soma and dendrites of glutamatergic (involved in glutamate signalling) and γ-aminobutyric acid (GABA)ergic neurons, and most of the neurons in the forebrain (Holmseth, Dehnes et al. 2012). The GABAergic and glutamatergic neurons establish inhibitory and excitatory synapses, respectively (Turko, Groberman et al. 2019). It is also found in the retina, where glutamate mediates the relay of visual information to the brain (Brandstatter, Koulen et al. 1998, Kugler and Beyer 2003), and the epithelial cells of the kidney and intestine, where it mediates the uptake of dicarboxylic amino acids (Danbolt 2001, Bailey, Ryan et al. 2011). Recently, EAAT3 was shown to be expressed in the peripheral nervous system (PNS), in Schwann cells, where it has localisation patterns similar to those observed in neuronal cells. Glutamate has been shown to be a signalling mediator between an active axon and its surrounding Schwann cells (Perego, Di Cairano et al. 2012).

Most SLC1s are found predominantly in the plasma membranes of cells. In the apical layer of epithelial cells, EAAT3 has cell membrane localisation (Shayakul, Kanai et al. 1997), while in the CNS, it behaves anomalously. EAAT3 is predominantly found in intracellular vesicles in the cytoplasm with only 20 - 30% found in the plasma membrane (Figure 1.6). There is a constant turnover of the protein since the half-life of EAAT3 in the plasma membrane is just 5-7 min (Fournier, Gonzalez et al. 2004). The trafficking of proteins between intracellular compartments and the plasma membrane is energetically expensive and it has been proposed to be important for a rapid regulation of the steady-state levels of membrane-located proteins (Gonzalez, Susarla et al. 2007).

Evidence that EAAT3 has cell-type specific modulation comes from the studies of protein kinase C (PKC) mediated regulation of the transporter. For studies of EAAT3 regulation in the CNS, C6 glioma cells (an immortalised cell line of CNS origin that endogenously expresses only EAAT3 and no other EAATs) are commonly used (Palos, Ramachandran et al. 1996). Activation of PKC increases cell surface localised EAAT3 in C6 glioma cells (and thus the uptake activity) due to redistribution of EAAT3 from the intracellular stores rather than *de novo* synthesis (Dowd and Robinson 1996, Trotti, Peng et al. 2001). However, when EAAT3 is expressed in the Madin–Daney canine kidney (MDCK) cell line, its activity was inhibited by PKC via internalisation of the membrane localised EAAT3 (Trotti, Peng et al. 2001).

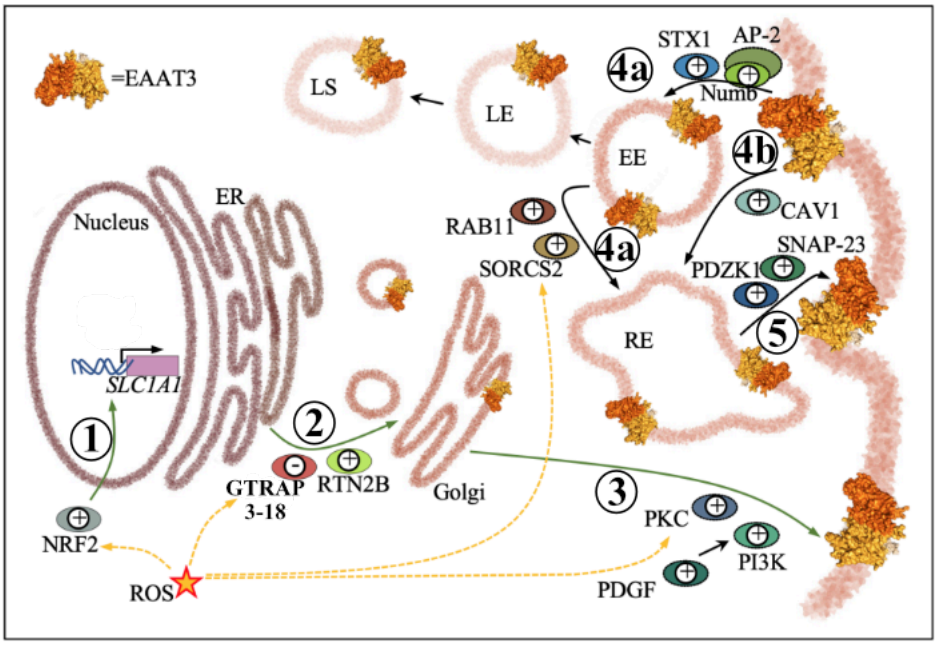


Figure 1.6: Regulation of EAAT3 expression. EAAT3 expression levels and activity are regulated at multiple stages: the transcription level (1), endoplasmic reticulum (ER) exit (2), plasma membrane targeting (3/ 5) and recycling (4). There are two independent pathways for endocytosis (4a, b). Nuclear factor erythroid 2-related factor 2 (NRF2); reticulon-2B (RTN2B); glutamate transporter EAAC1-associated protein (GTRAP3-18); protein kinase C (PKC); phosphoinositide 3-kinase (PI3K); platelet-derived growth factor (PDGF) Numb - clathrin adaptor; adaptor protein-2 (AP-2); syntaxin-1A (STX1); Rab11 - small GTPase; sortilin related VPS10 domain containing receptor 2 (SorCS2); synaptosomal-associated protein 23 (SNAP-23); PDZ-domain-containing protein 1 (PDZK1); caveolin-1 (CAV1); early endosomes (EE); recycling endosome (RE); late endosomes (LE); lysosomes (LS); reactive oxygen species (ROS). Adapted from (Malik and Willnow 2019).

In the CNS, EAAT3 expression levels and activity are regulated at multiple stages (Figure 1.6). Under oxidative stress conditions, nuclear factor erythroid 2-related factor 2 (Nrf2), a transcription factor in

antioxidant responsive element (ARE) pathway, was shown to increase EAAT3 transcription levels, resulting in an increase in EAAT3 expression levels (Escartin, Won et al. 2011). Newly synthesized EAAT3 travels through the endoplasmic reticulum (ER) and Golgi where its exit from the ER is positively regulated by reticulon-2B (RTN2B) (Liu, Vidensky et al. 2008). Glutamate transporter EAAC1-associated protein (GTRAP3-18) negatively regulates EAAT3 activity and trafficking to the plasma membrane. However, this is only observed under increased GTRAP3-18 expression (Liu, Vidensky et al. 2008). When GTRAP3-18 binds to EAAT3, it reduces EAAT3 affinity for glutamate and cysteine, effectively inhibiting uptake (Lin, Orlov et al. 2001, Watabe, Aoyama et al. 2008). The plasma membrane targeting is stimulated by PKC and phosphoinositide 3-kinase (PI3K), with platelet-derived growth factor (PDGF) receptor modulating EAAT3 trafficking through PI3K stimulation (Davis, Straff et al. 1998, Sims, Straff et al. 2000, Trotti, Peng et al. 2001, Fournier, Gonzalez et al. 2004).

The quick turnover rate of plasma membrane expressed EAAT3 requires a recycling route, which is achieved through both clathrin-dependent and independent endocytosis (Gonzalez, Susarla et al. 2007). The C-terminus of EAAT3 contains an internalization signal (YVNGGF motif), recognized by Numb, a clathrin adaptor protein, which associates with the adaptor (or assembly) protein-2 (AP2) complex that controls EAAT3 endocytosis (D'Amico, Soragna et al. 2010, Su, Wei et al. 2016). SNARE protein Syntaxin-1A (STX1) binds EAAT3 and mediates clathrin- and dynamin-dependent internalization that direct EAAT3 to early endosomes for sorting (Yu, Shen et al. 2006). Clathrin-independent pathways are less well characterised but are linked to plasma membrane domains enriched in cholesterol, sphingolipids and caveolin (Gonzalez, Susarla et al. 2007). Caveolin-1 binding to EAAT3 facilitates recycling of the transporter between the plasma membrane and the intracellular compartments (Gonzalez, Krizman-Genda et al. 2007). Depletion of cholesterol levels in C6 glioma cells and neurons increased EAAT3 cell surface expression levels (Gonzalez, Susarla et al. 2007, Lortet, Canolle et al. 2008). Small GTPase Rab11 and a specialized sorting receptor sortilin related VPS10 domain containing receptor 2 (SorCS2) are crucial for sorting EAAT3 to recycling endosomes, from where it can be returned to the plasma membrane via interactions with a SNARE protein synaptosomal-associated protein 23 (SNAP-23) and a scaffold protein PDZ-domain-containing protein 1 (PDZK1) (Fournier and Robinson 2006, Gonzalez, Susarla et al. 2007, D'Amico, Soragna et al. 2010, Malik,

Szydlowska et al. 2019). Failure in either Rab11 or SorCS2 activity re-directs EAAT3 to late endosomes for degradation in lysosomes. The importance of EAAT3 in the oxidative stress response is emphasized by the multiple points of stimulation of EAAT3 plasma membrane targeting by reactive oxygen species (Figure 1.6).

1.2.2.1 INDIRECT REGULATION OF EAAT3 ACTIVITY BY SMALL MOLECULES VIA SIGNALLING PATHWAYS

The identification of the different pathways involved in the regulation of EAAT3 expression and activity has led to the identification of many compounds that indirectly modulate EAAT3 activity. This can be achieved through changes in EAAT3 cell surface expression (nicotine, reduced surface expression through PKC and PI3K pathways (Yoon, Lim et al. 2014), isoflurane, increased cell surface expression through PKC-α pathway (Huang, Feng et al. 2006), and riluzole, increased cell surface expression through PKC and PI3K pathways (Dall'Igna, Bobermin et al. 2013)). Alternatively, compounds can modulate EAAT3 substrate affinity (carbamazepine, one of the most frequently prescribed drugs for the treatment of epilepsy, increases EAAT3 activity via PI3K pathways at clinically relevant concentrations) (Lee, Huang et al. 2005). The tissue-specific expression and localisation of EAAT3, as well as modulation through different pathways, portray a highly regulated mechanism that should be accounted for in functional studies.

1.2.3 PHYSIOLOGICAL FUNCTIONS

Glutamate, aspartate and cysteine transport by EAAT3 is important for multiple cellular processes. In brain, glutamate is the main excitatory neurotransmitter and is involved in the normal brain development and function, including memory, learning and cognition. Since excessive activation of the glutamate receptors is toxic to cells and to maintain the glutamatergic system, it is crucial to keep extracellular glutamate levels low (Danbolt 2001). Glutamate taken up by cells may be then used for metabolic purposes (protein synthesis, energy metabolism, etc.) or reused as a neurotransmitter (Danbolt 2001). In neurons, the majority of cysteine uptake is through EAAT3, where it is used for glutathione synthesis (Shanker, Allen et al. 2001). EAAT3 is the only one of the EAATs found in the kidney and intestine and it plays a major role in aspartate and glutamate reuptake from food (Hu,

Ottestad-Hansen et al. 2018). The diversity of EAAT3 substrates reflect on the various roles it plays in different tissues.

1.2.3.1 GLUTAMATE CLEARANCE IN THE CNS

In the CNS, EAAT3 is located in neurons. It is expressed in both glutamatergic and non- glutamatergic neurons. When EAAT3 is located in the plasma membrane, it has been mapped to dendritic and somatic compartments, with the exception of GABAergic neurons where it is found in presynaptic terminals (Rothstein, Martin et al. 1994). As EAAT3 is not generally found in the vicinity of the synapses, it is thought that it is not crucial for the glutamatergic signalling termination. Instead, this function is thought to be mainly carried out by glial-expressed EAAT1 and EAAT2 proteins (Figure 1.7) (Rothstein, Dykes-Hoberg et al. 1996). Glial cells surround the synaptic clefts, positioning the EAATs for rapid glutamate uptake from the synapse. Thus, it has been proposed that in general EAAT3 plays a minor role in glutamate clearing after signalling events. However, it may be important in specific areas such as the hippocampus where EAAT3 accounts for 40% of glutamate transport, and where there are no glial cells close to the synapses (Rothstein, Dykes-Hoberg et al. 1996). EAAT3 might have a role in clearing up glutamate spill-overs if the glutamate concentrations reach high levels in the extracellular space (Bianchi, Bardelli et al. 2014) or act as a buffer, binding glutamate and then releasing, without transporting it into the cell, to limit its release from the active synapses and to limit extrasynaptic receptor activation (Scimemi, Tian et al. 2009).

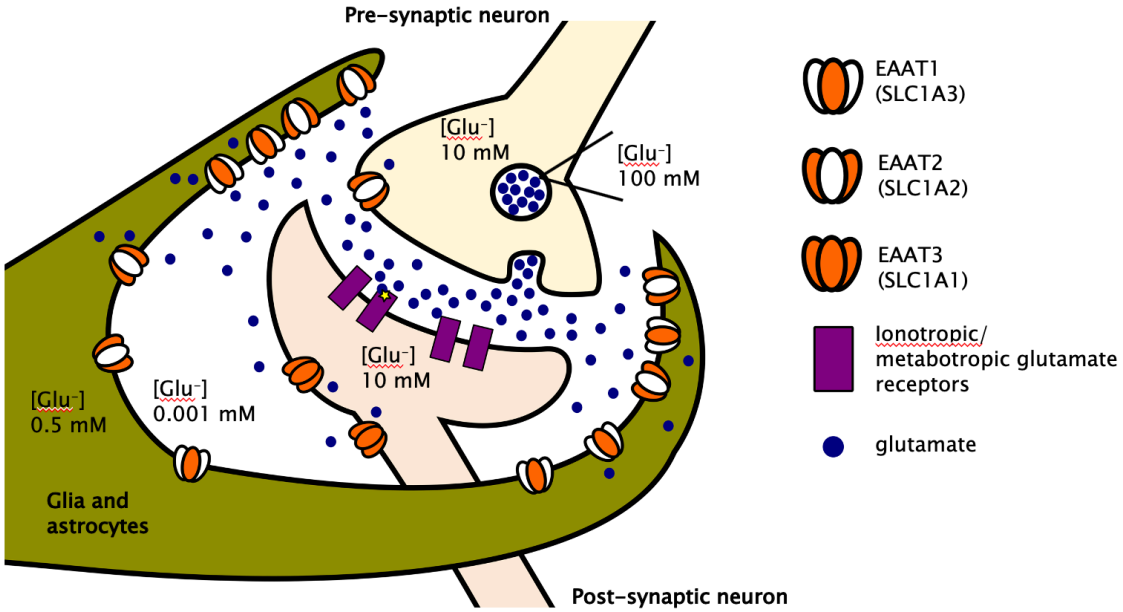


Figure 1.7: Termination of glutamatergic signalling in the CNS by EAATs. Depolarisation of the presynaptic neuron triggers the exocytosis of glutamate vesicles, releasing the neurotransmitter in the synaptic cleft where it can diffuse and bind to the ionotropic/ metabotropic glutamate receptors expressed on the post-synaptic neuron. Glutamate is cleared from the synapse by re-uptake by EAATs that terminate neurotransmission. Adapted from (Vandenberg and Ryan 2013).

1.2.3.2 SYNAPTIC MODULATION

Although EAAT3 is not thought to play a major role in glutamate clearing from the synaptic clefts, it could have an important function in synaptic modulation. Glutamatergic pathways are crucial for memory, learning and long-term potentiation (LTP) – a process that both strengthens the synapse and increases signalling efficacy between two neurons. LTP depends on glutamate receptors in the hippocampal region of the brain, which play an important role in synaptic transmission (Andin, Hallbeck et al. 2007). Due to its expression in glutamatergic neurons in the hippocampus, it has been suggested that EAAT3 could be involved in the glutamate uptake from these synapses (Bergles, Diamond et al. 1999). More recently, it has been shown that in the hippocampus, EAAT3 messenger RNA (mRNA) expression is changed upon environmental enrichment (stimulation of the brain by its physical and social surroundings) (Andin, Hallbeck et al. 2007), and that LTP is associated with increased EAAT3 trafficking to the cell surface (Levenson, Weeber et al. 2002), shown to be required for the early phase LTP but not for the late phase LTP (Pita-Almenar, Collado et al. 2006). This has led to speculation that the effect of volatile anaesthetics and compounds have on the regulation of EAAT3 cell surface expression and activity may come from the pharmacological modulation of these pathways (Bianchi, Bardelli et al. 2014).

1.2.3.3 GABA SYNTHESIS

EAAT3 localisation to presynaptic GABAergic neurons could play a role in the uptake of glutamate for y-aminobutyric acid synthesis (Rothstein, Martin et al. 1994). The high expression of EAAT3 in the GABAergic neurons together with the decreased *in vivo* GABA synthesis after the antisense knockdown of EAAT3 (Sepkuty, Cohen et al. 2002) and the observation that inhibition of EAAT3 reduced vesicular GABA content (Mathews and Diamond 2003) further supports it. Increased glutamate levels were shown to increase glutamate uptake and GABA synthesis, which increases

synaptic plasticity and suggest that EAATs strengthen the inhibitory synapses (Mathews and Diamond 2003).

1.2.3.4 CYSTEINE UPTAKE

Of all the EAATs, only EAAT3 is able to transport L-Cysteine at physiological concentrations at a rate comparable to that of glutamate (Zerangue and Kavanaugh 1996). It provides the major route for L-Cysteine uptake in neurons (Shanker, Allen et al. 2001). Glutathione (GSH) is a tripeptide (containing glycine, L-cysteine and L-glutamate) and is a major antioxidant in most cells. GSH synthesis is limited by substrate availability, and in particular, by the availability of L-cysteine (Griffith 1999). Oxidative stress and glutathione deficiency has been implicated in the pathogenesis of multiple neurodegenerative diseases (Schulz, Lindenau et al. 2000). Knock-out EAAT3 mouse models showed that aged animals had reduced glutathione levels in the hippocampal region and developed brain atrophy and behavioural changes (Aoyama, Suh et al. 2006).

1.2.3.5 GLUTAMATE/ ASPARTATE ABSORPTION

Amino acids have many important roles in the body, such as neurotransmitters, substrates for energy metabolism, and many others. However, amino acids are not stored within the body, so it is important to limit their loss in the urine. This is achieved in kidney, where amino acids are efficiently recovered from the primary filtrate (Makrides, Camargo et al. 2014). EAAT3 is the only member of the EAATs expressed in kidneys. It is responsible for the reabsorption of dicarboxylic amino acids (glutamate and aspartate) in the kidney since knock-out mice develop dicarboxylic aminoaciduria (DA), characterised by excessive excretion of glutamate and aspartate (Peghini, Janzen et al. 1997).

1.2.4 REGULATION OF EAAT3 BY SMALL MOLECULES

Early pharmacological studies of EAATs were performed in tissue preparations from parts of the CNS using radiolabelled ligand uptake assays. The initial compounds were designed around the structure of the transported amino acids with minor substitutions. These experiments identified the general properties of inhibitors that would compete with glutamate uptake. They include requirement for unmodified acid groups (with an exception for a number of aspartate derivatives), tolerated substitutions of the carbon in the acid group (sulfinic or sulfonic acid but not phosphate derivatives)

and the tolerated length (2-4 carbon atoms from the α-carboxyl group) (Bridges and Esslinger 2005). When the EAAT subtypes were identified and cloned, pharmacological characterisation of EAATs (mostly EAAT1-3) was carried out using mainly heterologous expression systems. The electrogenic nature of the transport meant substrate and compound kinetics could be measured using electrophysiological techniques. Most of the competitive inhibitors are transportable, and induce a measurable transport current, while some are non-transportable, associated with a lack of transport current (Wadiche, Amara et al. 1995). This could be easily determined using electrophysiological techniques and led to identification of a variety of EAAT inhibitors (Bridges and Esslinger 2005). Non-transportable inhibitors are crucial for functional studies, as EAATs can function in a heteroexchange mode, non-transportable blockers are crucial for functional studies (Shimamoto 2008). The summary of compounds sorted by their common chemical structures are shown in Figure 1.8.

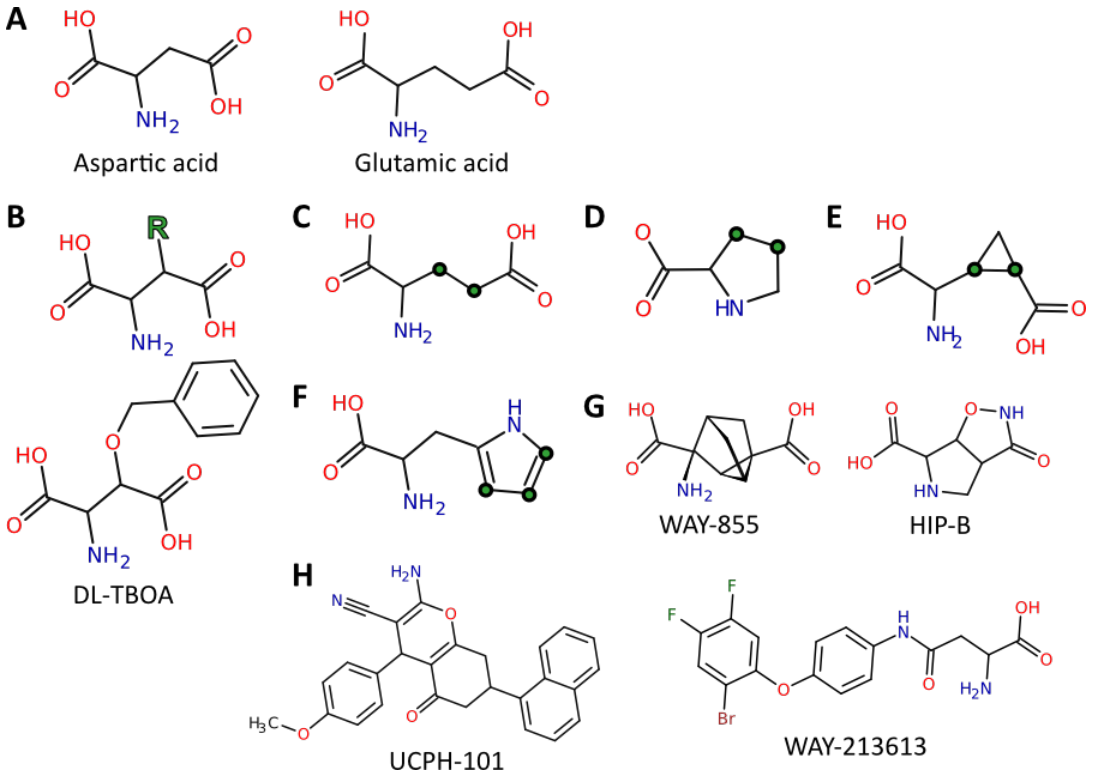


Figure 1.8: Types of EAAT-specific inhibitors. **A** EAAT substrates. **B** β-Hydroxy-substituted aspartates. Positions where substitution groups are added is indicated by R. The most commonly used compound, DL-TBOA is shown. **C** Methyl-substituted glutamates. Methyl groups are added at one or both positions marked by green circles. **D** Pyrrolidine dicarboxylates. Substitutions are added at one or both positions marked by a green circle. **E** 2-(Carboxycyclopropyl)glycines. Stereoisomers are formed around chiral centres identified by green circles. **F** Substituted azoles. Substitutions are added at one or both positions marked by green circle. **G** Compounds with conformationally restricted positions of amino and carboxylate groups. **H** Subtype-specific inhibitors (left: EAAT1 selective, right:

EAAT2 selective). DL-TBOA DL-threo-β-benzyloxyaspartic acid; WAY-855 3-amino-tricyclo[2.2.1.02.6]heptane-1,3-dicarboxylate; HIP-B (±)-3-Hydroxy-4,5,6,6a-tetrahydro-3aH-pyrrolo[3,4-d]isoxazole-6-carboxylic acid; UCPH-101 2-Amino-5,6,7,8-tetrahydro-4-(4-methoxyphenyl)-7-(naphthalen-1-yl)-5-oxo-4H-chromene-3-carbonitrile; WAY-213613 (2S)-2-Amino-3-([4-(2-bromo-4,5-difluorophenoxy)phenyl]carbamoyl)propanoic acid. Adapted from (Bridges and Esslinger 2005).

To date, the most commonly used inhibitors are non-selective β-Hydroxy-substituted aspartate analogues, in particular DL-threo-β-benzyloxyaspartic acid (DL-TBOA) and its analogues (Shimamoto, Lebrun et al. 1998, Shimamoto, Sakai et al. 2004). The majority of EAAT-specific compounds are substrate analogues, exhibiting low EAAT subtype selectivity. Pharmacological studies of EAATs have identified subtype-specific inhibitors for EAAT1 and EAAT2 (UCPH-101 and WAY-213613, respectively (Dunlop, McIlvain et al. 2005, Huynh, Abrahamsen et al. 2012)) but there are no commercially available inhibitors that are EAAT3 selective. Structural information of each subtype together with high-throughput screening assays would facilitate structurally novel EAAT ligand design and characterisation.

1.2.5 EAAT3 IN DISEASE

1.2.5.1 THE CNS PATHOLOGIES

Altered plasma membrane localisation of EAAT3 has been reported for multiple neurological conditions, including epilepsy, schizophrenia and obsessive-compulsive disorder, while malfunction has been linked to obsessive-compulsive disorder (OCD) and are causative of DA (Bianchi, Bardelli et al. 2014).

1.2.5.1.1 EPILEPSY

Epilepsy is a chronic neurological disorder which involves recurrent seizures caused by neuronal dysfunction involving aberrant neuronal firing (Stafstrom 2006). Diverse phenotypes of the disease are thought to arise from disruptions in GABA-ergic and glutamatergic systems (Sheldon and Robinson 2007). Although EAAT3 knockout mice did not develop seizures, treatment with antisense oligonucleotides in the hippocampus of adult rats caused mild neurotoxicity and resulted in an epilepsy phenotype (Rothstein, Dykes-Hoberg et al. 1996). A follow-up study identified the phenotype as a

result of reduced GABA synthesis and the consequent reduction in an inhibitory amino acid neurotransmitter system activity in the hippocampus (Sepkuty, Cohen et al. 2002). A common antiepileptic drug, carbamazepine, is known to inhibit sodium channels, but has been shown to have other targets in the nervous system. It was shown to increase EAAT3 activity, which would increase GABAergic neurotransmission that could counteract the over-activation of glutamatergic systems (Lee, Huang et al. 2005).

1.2.5.1.2 SCHIZOPHRENIA

EAAT3 has been implicated in schizophrenia, a psychiatric disorder associated with altered glutamatergic, GABAergic and dopaminergic systems (Afshari, Yao et al. 2017). Decreased striatal EAAT3 mRNA levels were detected in brain slices from schizophrenic patients. However, it was noted that the medications taken by the subjects might have affected striatal EAAT3 expression levels, so the significance of this data is unclear (McCullumsmith and Meador-Woodruff 2002). Nevertheless, a genome-wide association study (GWAS) for the treatment response to antipsychotics in patients with schizophrenia revealed that three novel single-nucleotide polymorphisms (SNPs) in *SLC1A1* were associated with altered response to general antipsychotic treatment (Yu, Yan et al. 2018). A study in a five-generation family with psychotic disorders identified a heterozygous deletion which removed the upstream elements and the region encoding the N-terminus of the EAAT3 from the *SLC1A1* gene, resulting in one of the chromosomes expressing non-functional EAAT3 (Myles-Worsley, Tiobech et al. 2013). Follow up studies showed that the protein can be expressed but has reduced plasma membrane localisation, leading to a lack of activity (Afshari, Myles-Worsley et al. 2015). Expression of truncated EAAT3 in cell lines caused changes in gene expression related to GABA and glutamate signalling. These were also observed in patients with the EAAT3 hemi-deletion, emphasizing the strong biological relationship between different signalling systems and the pathophysiology of schizophrenia (Afshari, Yao et al. 2017). Hemi-deletion (a hemizygous deletion) is a deletion of a gene on one of the chromosomes in a diploid organism (Gambin, Akdemir et al. 2017). Still, the exact role of EAAT3 in schizophrenia is not yet fully understood.

1.2.5.1.3 OBSESSIVE-COMPULSIVE DISORDER (OCD)

OCD is a neuropsychiatric condition which involves two behavioural issues: obsessions, such as obtrusive thoughts, and compulsions, such as repetitive behaviours (Delgado-Acevedo, Estay et al. 2019). Two GWAS of OCD have been carried out, but none of the genetic variants achieved significance (Browne, Gair et al. 2014). However, in linkage and case-control studies *SLC1A1* was identified as the strongest candidate gene (Delgado-Acevedo, Estay et al. 2019). On the other hand, animal models lacking EAAT3 do not exhibit OCD relevant behaviour (Peghini, Janzen et al. 1997, Aoyama, Suh et al. 2006). Mice models with inducible EAAT3 overexpression in forebrain show increased repetitive behaviours. This was attributed to changes in synaptic activity (Delgado-Acevedo, Estay et al. 2019). This agrees with the previous observations that increased glutamatergic signalling may underlie the symptoms of OCD (Sheldon and Robinson 2007).

1.2.5.2 RENAL PATHOLOGY

1.2.5.2.1 DICARBOXYLIC AMINOACIDURIA (DA)

DA manifests as amino acid (glutamate and aspartate) excretion after failed reabsorption in the kidneys. DA is an autosomal recessive disorder caused by homozygous loss-of-function mutations (I395del and R445W) in *SLC1A1*. Both mutations severely affected EAAT3 cell surface expression and nearly (R445W) or fully (I395del) abolished transport activity. Studies of patients with DA who had these mutations in their *SLC1A1* genes established EAAT3 as the main glutamate and aspartate transporter in the kidney (Bailey, Ryan et al. 2011).

1.3 SUMMARY AND AIMS OF THE EAAT3 PROJECT

In summary, although EAAT3 was initially labelled as a minor player in glutamate clearance from synapses in brain, it has now emerged as a key multifunctional target involved in the oxidative stress response and modulation of both glutamatergic and GABAergic pathways. EAAT3 upregulation in neurons upon oxidative stress and the extensive studies to understand the mechanisms behind it has made it a promising target for preventing oxidative damage to neurons. Oxidative stress has been attributed as a hallmark to multiple neurodegenerative disorders (Liu, Zhou et al. 2017), epilepsy (Pearson-Smith and Patel 2017) and ischemic stroke (Allen and Bayraktutan 2009). The reversal of

transport of EAAT3 under ischemia contributes to glutamate toxicity, and a specific inhibitor not affecting the glial EAATs would allow blocking this process (Kanai and Hediger 2003).

In this thesis, I describe the structure, function and small molecule binding studies of EAAT3 to further our understanding of how EAAT3 activity could be regulated. I describe the establishment of proteoliposome reconstitution protocol for EAAT3 in collaboration with Antje Pommereau at Sanofi for use in functional studies in Chapter 3. Using the SURFE^{2}R system, the kinetic properties of various EAAT3 substrates are determined and set the foundation for small molecule screening capabilities. Two inhibitors are characterised as proof-of-concept measurements. I report sample optimisation for cryo-EM studies that lead to the first structures of human EAAT3 in Chapter 4. Finally, I describe the two structures of EAAT3-inhibitor complexes and discuss the novel binding modes of the two inhibitors, which provide new insights in the binding site differences within SLC1A family.

1.4 TWO-PORE DOMAIN POTASSIUM CHANNELS (K2PS)

In addition to my work on the EAAT3 transporter, I studied a family of neuronal ion channels, K2Ps, which are members of the voltage-gated ion channel (VGIC) superfamily and are involved in regulation of neuronal excitability and maintenance of the membrane potential. The resting membrane potential is established by the concerted function of Na-K ATPase and K2Ps (Figure 1.9).

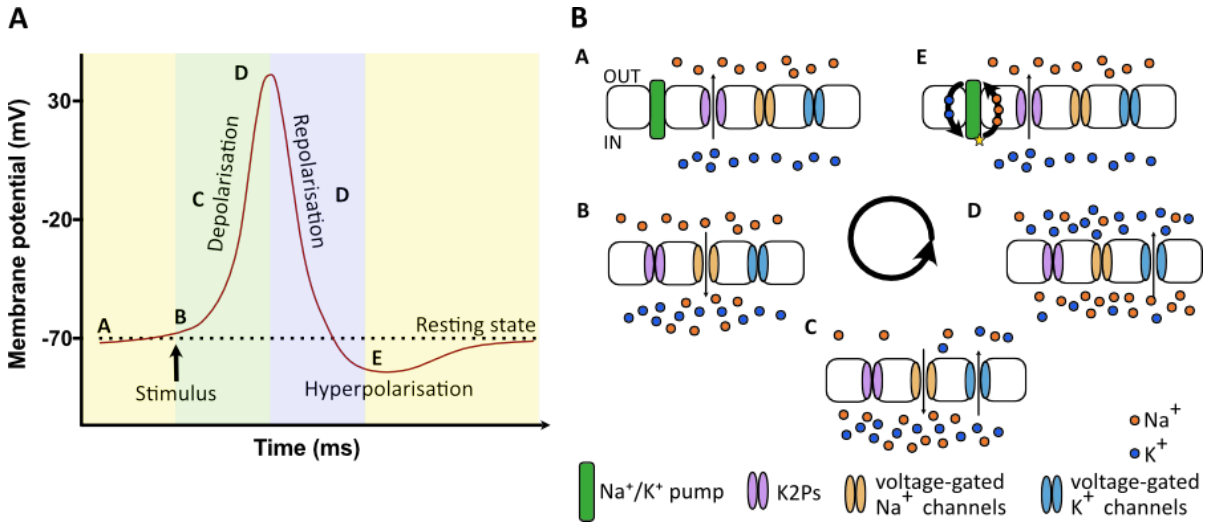


Figure 1.9: Action potential generation in excitable cells. **A** In response to stimuli, the cell undergoes concerted opening of voltage-gated Na^+ and K^+ channels causing depolarisation and repolarisation, respectively. The opening and closing of Na^+ channels happen during the time period shaded in light green, K^+ channels open and close during the time period shaded in light purple. The membrane is returned to resting membrane potential state (shaded in light yellow) by the action of Na^+/K^+ pumps

and K^+ leak channels where it remains until next stimulus. **B** Diagram showing the flow of ions during the action potential. The occurrence of steps A-E are labelled in panel A. The opening of the channels is indicated by arrows and the active transport by Na^+/K^+ pump (movement of three Na^+ outside the cell and two K^+ in) is indicated by black arrows in bold. The energy requirement for this step is indicated by yellow star. Adapted from (Berg, Tymoczko et al. 2012).

The Na-K ATPase pump uses energy from ATP hydrolysis to import two K^+ ions and export three Na^+ ions for each ATP hydrolysed. This establishes a high potassium concentration inside the cell. Conversely, K2Ps allow K^+ ions to flow ("leak") down their gradient until electrochemical equilibrium is reached (Alberts 2002). Since both K^+ and Na^+ ions are positive, this process creates a net negative charge inside the cell – the resting membrane potential (Hodgkin and Huxley 1952). All cells have a resting membrane potential but only excitable cells, such as neurons and muscle cells, use it to generate action potentials. Action potentials are the fundamental electrical impulses neurons use to transfer stimuli from one part of a neuron to another along axons (Alberts 2002). K2Ps are expressed in neurons, where they regulate excitability, sensory transduction and neuroprotection (Lotshaw 2007, Enyedi and Czirjak 2010). Under physiological conditions K2Ps are responsible for hyperpolarising the cell membrane, which prevents action potential generation. Disruption of K2P function leads to increased excitability (Tsantoulas and McMahon 2014). Only the first identified K2P, tandem of P-domains in a weak inward rectifying K+ channel (TWIK) 1, is voltage independent which means it can provide K^+ ion conductance over a wide range of membrane potentials (Lesage, Guillemare et al. 1996). Other K2Ps display time and voltage dependency, with increased channel conductance upon membrane depolarisation (Schewe, Nematian-Ardestani et al. 2016). K2Ps are gated by remarkably diverse stimuli, including chemical, thermal, and mechanical modalities and are represented throughout the plant and animal kingdoms (Feliciangeli, Chatelain et al. 2015, Renigunta, Schlichthorl et al. 2015). The molecular and structural mechanisms that allow K2Ps to respond to such diverse stimuli have been extensively studied (Feliciangeli, Chatelain et al. 2015). Structurally, K2Ps have two pore forming domains and assemble as homo- or heterodimers. Due to their specific expression patterns and low sequence identity even between the same family members, K2Ps have become attractive targets for pain modulation (Tsantoulas and McMahon 2014). Consequently, K2Ps represent important clinical

targets for the treatment of cardiovascular disease and several neurological disorders, including pain and depression (Honore 2007, Acosta, Djouhri et al. 2014, Pereira, Busserolles et al. 2014).

1.4.1 EXPRESSION AND FUNCTION OF K2PS

K2Ps are divided in six subfamilies (TWIK, TWIK-related K^+ channels (TREK), two-pore domain, acid-sensitive K^+ channels (TASK), two-pore domain alkaline activated K^+ channels (TALK), two-pore domain halothane inhibited K^+ channels (THIK) and TWIK-related spinal cord potassium channel (TRESK)) based on the sequence and functional similarities (Bayliss D.A. 2019). The variation in sequence identity between different subfamilies is surprisingly high, comparable to the similarity between different families of K^+ channels (e.g., 28% sequence identity between TWIK-1 and TREK-1 (Fink, Duprat et al. 1996)). The focus of the second part of my thesis was TREK-2 channel, a member of TREK subfamily.

Functionally active splice variants contribute to the diversity of subfamilies (Renigunta, Schlichthorl et al. 2015). This is particularly notable in TREK subfamily, where the protein-coding gene contains seven exons. The sequence diversity is mainly restricted to the N-terminus, arising from alternative splicing of exon1, as splice variants in other exons lead to non-functional protein expression (Renigunta, Schlichthorl et al. 2015). Three different isoforms have been characterised for TREK-2, with one longer and two shorter forms. The long isoform (TREK-2a) was shown to have lower conductance than the shorter isoforms (TREK-2b,c) but all the isoforms have identical response to the different regulatory mechanisms (since these are thought to be modulating the channel via interactions at the C-terminus) (Enyedi and Czirjak 2010). The isoforms show tissue-specific mRNA expression patterns, with TREK-2a showing weak expression in brain, TREK-2b being expressed in kidney and pancreas, while TREK-2c is mainly expressed in brain (Gu, Schlichthorl et al. 2002).

K^+ currents that develop independently of changes in membrane potential are known as “leak” or background conductances (Zilberberg, Ilan et al. 2001). K2Ps are well known for their role in generating the background current that stabilises the negative resting membrane potential, preventing depolarisation and associated excitability (Enyedi and Czirjak 2010). Historically, K2Ps have been described as constitutively open K^+-selective pores, whose current-voltage (I-V) relationship can be described by the Goldman-Hodgkin-Katz (GHK) equation (Chen, Zuo et al. 2014). The GHK equation

assumes that the ions are driven across the plasma membrane by a constant electrical field and that the ions do not interact with each other but cross the membrane instantaneously. It also requires that the conductance depends on the ion concentration with higher conductance when the ions move down their concentration gradient (Renigunta, Schlichthorl et al. 2015). An ideal background channel, according to the GHK equation, is voltage independent with the open probability (Po) the same at all membrane potential values, with increasing ionic conductance with increased membrane depolarisation (Lotshaw 2007, Enyedi and Czirjak 2010). Together, this would result in a channel with strong tendency to let K^+ flow out of the cell (outward rectification) under physiological conditions. This is not the case for the majority of K2Ps since the Po is voltage and time dependent. K2Ps are not permanently open, on the contrary, increasing depolarisation increases the Po (Renigunta, Schlichthorl et al. 2015). Both inwardly and outwardly rectifying (allowing K^+ flow into the cell and out, respectively) behaviours have been described for different K2P isoforms even under symmetric K^+ distribution across the plasma membrane (Lotshaw 2007). Some of the K2Ps have been labelled "silent" since no currents have been measured in heterologous expression systems for these subunits. Recent studies suggest this is due to specific requirements for activity that are yet unknown (Feliciangeli, Chatelain et al. 2015).

The TREK subfamily members, TREK-1, TREK-2, and two-pore domain related arachidonic acid activated K^+ channel (TRAAK), are background K^+ channels exhibiting a low, weakly voltage-dependent Po that is strongly modulated by both chemical and physical stimuli. TREK-2 channels show highly variable, voltage-dependent Po and openings are short lived and occur in bursts (Lotshaw 2007).

1.4.2 THE ARCHITECTURE OF POTASSIUM CHANNELS

Members of the K2P channel family share structural features common to K^+ channels. The majority of K^+ channels have a signature sequence (TXXTXGYG, where X is a hydrophobic residue) forming the selectivity filter (SF) but the K^+ affinity is subtype-dependent, suggesting that the surrounding environment affects ion binding within the pore (Ogielska and Aldrich 1999). In TREK-2, the selectivity filter is made from the sequences TIGYG (SF1) and TVGFG (SF2) (Dong, Pike et al. 2015). The architectural features specific to the K^+ channel SF include main chain carbonyl groups, which create a column of four K^+ binding sites. The dimensions of these sites are suitable for

dehydrated K^+ ion binding where the surrounding carbonyl oxygens mimic the water molecules around hydrated K^+ ions (Zhou, Morais-Cabral et al. 2001). Most K2P channels show voltage-dependent gating without having a specific voltage-sensing domain. Highly conserved threonines within the SF motif (**T**I/VGY/FG) in both P1 and P2 loops were identified as crucial for voltage sensing (Schewe, Nematian-Ardestani et al. 2016). These threonines (T172 and T281 in TREK-2) are the only side chains to interact with the K^+ ions directly while the other side chains in the SF form contacts with residues in the respective pore helices. For a K^+ ion to cross the membrane, it must overcome the electrostatic repulsion caused by the dielectric lipid bilayer environment. The architecture of K^+ channels uses both a helix dipole effect and polarised residues within the SF to overcome these electrostatic effects (Figure 1.10). The pore helices (PH1-PH4 in canonical K^+ channels and PH1-PH2 in K2Ps) are oriented with the main chain carboxyls pointing towards the centre of the aqueous pore vestibule, formed by the transmembrane helices M2 and M4, so that their dipole moments would favour cations just before the SF due to accumulated negative electrostatic potential (Doyle, Morais Cabral et al. 1998).

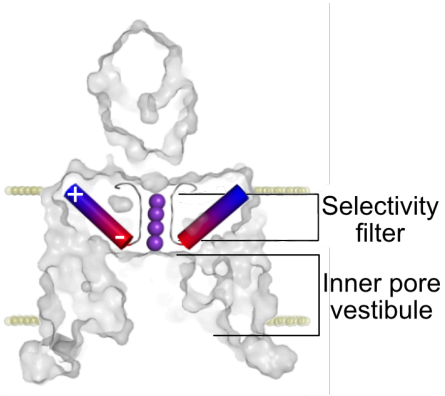


Figure 1.10: K2P channels have structural features shared by all K^+ channels. The selectivity filter coordinates four K^+ ions while dipole moments of pore helices (PH) stabilise the cations due to negative electrostatic potential formed in the central pore vestibule. Cartoon representation of two PHs and SFs shown for TREK-2 (PDB: 4BW5). Colouring of PH represent the N-terminus (blue) and C-terminus (red).

K^+ channels are characterised by three channel inactivation mechanisms. For the majority of K^+ channels, gating involves an opening of the bundle-crossing (gate) formed by the C-terminal helices lining the pore vestibule, which, when closed, closes the inner pore vestibule from the intracellular side. In the so-called C-type inactivation mechanism, the inactivation of the channel occurs due to molecular rearrangements within the narrow SF. C-type gating has been shown to be slow as the

structural rearrangements required for inactivation can only happen once the external ion binding site is empty (Baukrowitz and Yellen 1995, Pau, Zhou et al. 2017). The binding of K^+ ions to the external site is voltage dependent, with a lower ion occupancy (and faster inactivation of the channel) at more positive voltages (Baukrowitz and Yellen 1996). A third mechanism for control of gating - N-type inactivation - is attributed typically to the N-terminal peptide blocking the channel pore opening on the cytoplasmic side. N-type inactivation requires the formation of the bundle-crossing (Yellen 2002). As has been shown for TREK-1, in most K2P channels, C-type gating mechanism alone is sufficient to explain K2P channel regulation (Piechotta, Rapedius et al. 2011).

1.4.3 STRUCTURAL STUDIES OF TREK-2

The structures of six members of the K2P family have been solved to date, TWIK1 (Miller and Long 2012), TRAAK (Brohawn, del Marmol et al. 2012, Brohawn, Campbell et al. 2013), TREK-2 (Dong, Pike et al. 2015), TREK-1 (Lolicato, Arrigoni et al. 2017), TASK-1 (Rodstrom, Kiper et al. 2020) and TASK-2 (Li, Rietmeijer et al. 2020). The structures of TREK-1 (unpublished), TREK-2 (Dong, Pike et al. 2015) and TASK-1 (Rodstrom, Kiper et al. 2020) were solved in our group. Human TREK-2 channel was solved in two conformations (Figure 1.12), and in complex with a state-dependent inhibitor, norfluoxetine.

The shared topology of K2Ps is shown in Figure 1.11. A cytosolic N-terminal domain is followed by 4 TMHs, interspersed by an extracellular cap domain, and a long C-terminal domain. Structurally, all K2Ps form dimers. Each subunit consists of two outer helices (M1 and M3), two inner helices (M2 and M4), two extracellular helices (EC1 and EC2) and two pore forming domains (P1 and P2), which contain the re-entrant pore helices (PH1 and PH2) and the loops connecting them to the M1-4 helices (Figure 1.11). The name of the family reflects the specific topology of the K2Ps. Each monomer contains two pore forming domains, in contrast to most other K^+ channel families which are tetrameric and have only one pore forming region per chain. Hence in the K2Ps a dimer is a functional unit, forming the characteristic K^+ selectivity filter consisting of four pore forming domains with pseudotetrameric symmetry (Enyedi and Czirjak 2010).

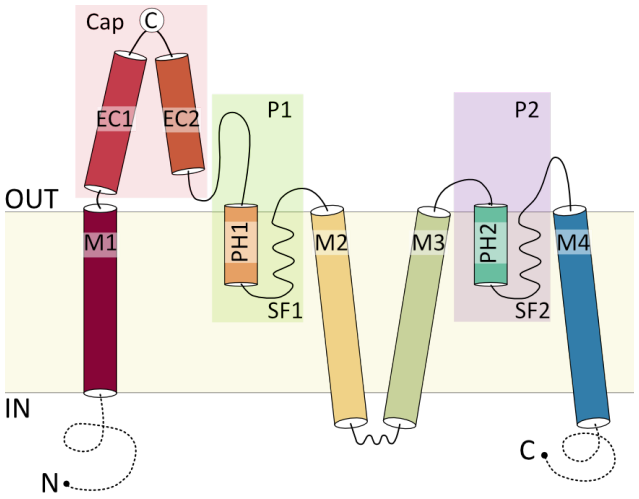


Figure 1.11. Schematic representation of the structural organisation of a K2P subunit. Four transmembrane helices (M1-M4) are interspersed by the cap domain, formed by two extracellular helices (EC1-2), and two pore domains (P1 and P2). Each pore domain consists of a pore helix (PH) and the selectivity filter forming region (SF1-2, squiggly line). The majority of K2Ps have a conserved cysteine (C) in between the EC1 and EC2 that forms a disulphide bridge in assembled K2P dimers.

A structurally unique domain, named the cap domain is formed by EC1 and EC2 between M1 and P1 domains (Brohawn, del Marmol et al. 2012). A highly conserved cysteine is found in most K2Ps, with the exceptions of the TASK channels, located at the top of the cap domain and is involved in the interchain disulphide bond formation, resulting in covalently bound homodimers (Lesage and Lazdunski 2000). The role of the extracellular cap domain is still unclear, particularly since the TASK channels lack this disulphide but still form the same cap architecture as seen in all other K2P structures (Goldstein, Rinne et al. 2016, Rodstrom, Kiper et al. 2020). Mutagenesis studies suggest that residues around the pore exit play a role in the channel gating and that these mechanisms are independent of the intracellular gating signals (Renigunta, Schlichthorl et al. 2015). The SF is the narrowest part of the channel that allows selective conductance of K^+ ions and in K2Ps is thought to be able to adopt nonconducting states through small structural changes (Brennecke and de Groot 2018). Apart from the two members of TASK subfamily (TASK-1 and TASK-2), the rest of the K2Ps are thought to be solely gated at the SF (Li, Rietmeijer et al. 2020, Rodstrom, Kiper et al. 2020).

The structure of TREK-2 was solved in two conformations, termed “up” and “down” (Figure 1.12). In the “up” conformation (PDB: 4BW5) M2 and M4 flank the central cavity and open up the central, hydrophobic cavity to the cytoplasm. The selectivity filter in “up” conformation forms four K^+

coordination sites, typical of other K^+ channels. Thus the "up" state represents an open and unobstructed ion conduction pathway through the channel.

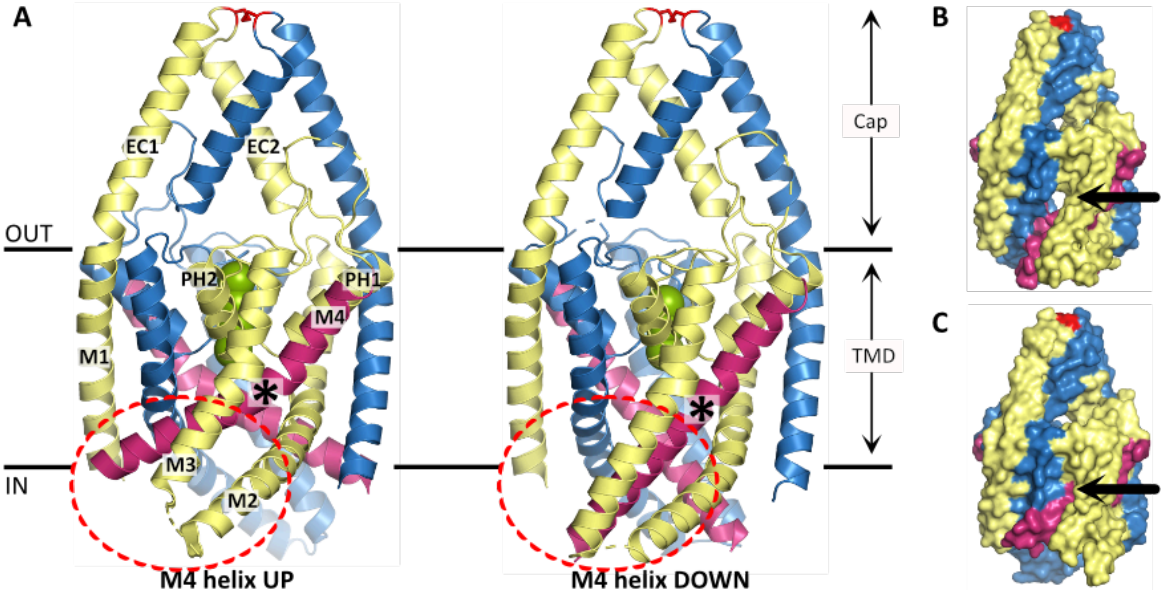


Figure 1.12: The two conformations of the TREK-2 channel. **A** TREK-2 can adopt "up" (4BW5) or "down" (4XDJ) conformations depending on the conformation adopted by M4. The two TREK monomers are show in yellow and blue cartoon representation with the M4 in both monomers coloured in magenta. The disulphide bond is shown in stick representation. The movement of M2.3 and M4 helices between the two conformations is indicated by a red, dashed circle. The conserved glycine position in M4 helix is indicated by a black asterisk. **B** Surface representation of TREK-2 in DOWN conformation with the side fenestration open (indicated by and arrow). **C** Surface representation of TREK-2 in UP conformation with the side fenestration closed (indicated by and arrow).

In the "down" conformation (PDB: 4XDJ), there is a local movement of the M2, M3 and M4 compared to the "up" state, which is associated with the transfer of the regulatory signals to the filter gate. Reorientation of a number of side chains between the helices were found to be functionally important, as mutagenesis revealed reduced stretch activation (Dong, Pike et al. 2015). The biggest movement is observed for the M4, which is rotated around the conserved glycine that forms a hinge point in the helix (Figure 1.12 A). This movement straightens the helix, allowing it to extend further into the cytoplasm but not sealing the intracellular vestibule off from the cytoplasm. Due to the M4 movement, side fenestrations are formed between M2 and M3, connecting the intracellular vestibule to the lipid bilayer (Figure 1.12 B-C). Extra density is observed in the top part of the intracellular vestibule just below the selectivity filter, assumed to be either lipid acyl chains or polyethylene glycol molecules from the crystallisation condition (Dong, Pike et al. 2015). These conformational changes explain the

stretch activation of TREK-2 channels as opening and closing of the side fenestrations due to channel adopting wider or flatter conformations. With open fenestrations, the ion conductance could be obstructed.

The binding site for the inhibitor norfluoxetine is within these fenestrations and therefore is only present in the "down" conformation (Dong, Pike et al. 2015). As norfluoxetine is known to inhibit TREK-2 (albeit at non-physiological concentrations), this suggested that the up state is the more active conformation and the down state is the less active state (Dong, Pike et al. 2015). Functional and pharmacological evidence further support this model (McClenaghan, Schewe et al. 2016). Molecular dynamics simulations suggest that the selectivity filter senses the electrochemical gradient and adjusts the ion occupancy with inactive channel still being permeable to K^+ ions at very low rate (Schewe, Nematian-Ardestani et al. 2016).

Using the TREK-2 structures in molecular dynamics simulations, it was proposed that the down state represents a less conductive channel (Brennecke and de Groot 2018). The simulations also provided evidence that the SF gate is stabilised by the pore helices while the gating mechanism is achieved through carbonyl flips within the SF-forming backbone (Brennecke and de Groot 2018). However, the conformation of the M4 helix alone is not the only determinant of the channel activity, since in TREK-1 the M4 helix was observed to adopt an "up" conformation while the channel was not in conductive state (Lolicato, Natale et al. 2020). To explain the observations from the TREK structures and functional studies, a polymodal gating model was proposed where structurally different open states are adopted by the channel (McClenaghan, Schewe et al. 2016). This model explains the previously conflicting models regarding the channel activity in "up" and "down" states and how TREK channels can respond to the diverse regulatory stimuli.

The structures of TREK-2 in two conformational states provided us with insights on how the intracellular stimuli could be transmitted to the channel pore through the movement of the transmembrane helices. This also support recent evidence that mechanosensitive K2Ps sense force directly through interactions with lipids (Dong, Pike et al. 2015). However, many questions are still unanswered, including the mechanisms that relay regulatory stimuli to the pore, and how drugs

modulate this process. Additionally, since the crystallised TREK-2 construct lacks N- and C-terminal regions, the roles of these domains in the regulation of the channel remain unclear.

1.4.4 BIOPHYSICAL AND PHARMACOLOGICAL CHARACTERISTICS OF TREK-2

TREK-2 channel opening hyperpolarises neurons, reducing neuronal firing, while opening of non-selective mechanosensitive channels will depolarise the cell causing neuronal excitability. Such opposing actions allow cells to regulate the response to mechanical stress (Brohawn 2015). Many stimuli have been identified that activate TREK-2, observed as increased Po of the channel. Such diverse regulation of TREK-2 activity indirectly suggests that the Po is maintained at low levels under basal conditions (Woo, Jeon et al. 2019). To date, stimuli that regulate TREK-2 activity include activation by stretch (Lesage, Terrenoire et al. 2000), heat (Kang, Choe et al. 2005), membrane voltage (Lesage, Terrenoire et al. 2000), acidic cytosolic pH (Woo, Jun et al. 2018), polyunsaturated fatty acids and lysolipids, inactivation by phosphorylation and interaction with regulatory proteins (Lesage, Terrenoire et al. 2000). A cytosolic C-terminal sensor region starting immediately after the M4 has been identified to sense these stimuli and relay to the channel pore (Honore, Maingret et al. 2002). From the mechanosensitive model, it has been proposed that this sensor region affects the state of the channel via interactions with the inner membrane lipid leaflet, with activating signals promoting such interactions and inactivating signals disrupting them (Brohawn 2015). Truncations that remove residues from this sensor region reduce TREK-2 mechanosensitivity, while C-terminus truncations after this region had no effect (Enyedi and Czirjak 2010).

Potentially more intriguing is the activation of TREK-2 and other members of the subfamily by clinically used volatile anaesthetics (Patel, Honore et al. 1999), antidepressants, neuroleptics, and sedatives (Brohawn 2015). Direct interactions between TREK family members and anaesthetics would mean such interactions are conserved across all mammalian species, which is rather unlikely, but the underlying mechanisms are still unclear.

TREK-2 channel activity is not exclusively mediated by the C-terminal domain. Extracellular acidification is thought to activate TREK-2 via H151 protonation (Renigunta, Schlichthorl et al. 2015). Small molecule binding to an allosteric site within the cap domain has been reported to inhibit all TREK subfamily members (Luo, Chen et al. 2017).

1.4.5 NANOBODIES AS FUNCTIONAL MODULATORS TO STUDY TREK-2 FUNCTION

Antibodies or Immunoglobulins (Ig) are soluble glycoproteins that play an essential role in recognition of antigens by the immune system. IgG is the most common class of antibodies found in vertebrates. The tetrameric structure of antibodies is highly conserved and consists of two heavy chains and two light chains, held together by disulphide bonds. Both chains are further divided in variable and constant domains (Figure 1.13) (Jovcevska and Muyldermans 2020).

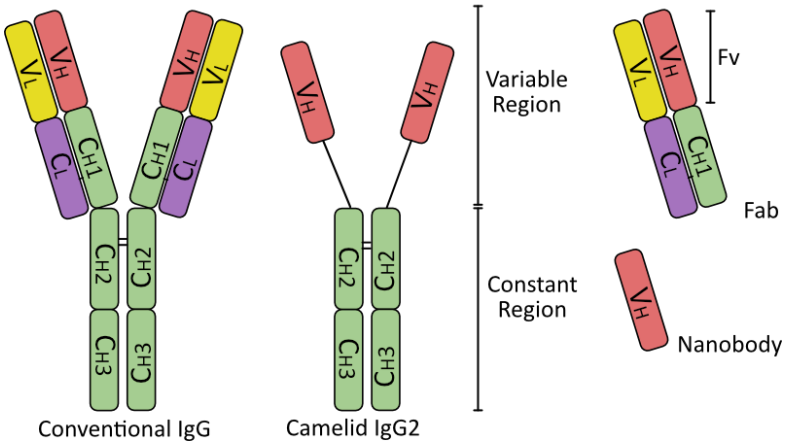


Figure 1.13: Schematic representation of the architectural differences between conventional and camelid antibodies. Camelids produce both conventional antibodies (IgG) and unique heavy chain (IgG2) antibodies that bear the same Y shape, held together by disulphide bonds (shown as two black lines), but consist of just two heavy chains with antigen binding domains in the variable region. The two heavy chains in conventional IgG consist of variable (V_H) and constant ($C_H1,2,3$) domains while the two light chains consist of variable (V_L) and constant (C_L) domains. IgG2 antibodies consist of only the heavy chains. Fabs (antigen binding fragments) contain a variable fragment (Fv) and are derived from conventional antibodies, while nanobodies consist of a single variable domain and are obtained from camelid IgG2. Adapted from (Muyldermans 2013).

Antigen recognition is limited to the variable region loops within the variable domains of heavy (V_H) and light (V_L) chains. The specificity and affinity of antibody interactions have been used in clinical practice to treat various types of cancer by using the antibody as a delivery vehicle for a therapeutic drug. However, the relatively large size (~150 kDa) and fragility of antibodies present complications with the administration of the treatment.

The discovery of functional heavy-chain-only antibodies in the serum of camelids (camels, llamas and alpacas) provided us with new tools. These antibodies lack light chains and the single variable domain with the antigen recognition region is called a nanobody (Nb; Figure 1.13). The nanobody can be

removed from its heavy chain scaffold, maintaining full functionality of the binder (Jovcevska and Muyldermans 2020).

The overall architecture of nanobodies is the same as the V_H domains of canonical antibodies (Figure 1.14). The scaffold is formed by 9 ß-strands arranged in 2 ß-sheets, held together by a disulphide bond between two conserved cysteines. The three hypervariable antigen-binding loops form a continuous surface, complementary to the recognised epitope (complementarity determining regions—CDR1/2/3). While the sequence of CDRs is highly variable, the length variation is limited, except for the CDR3 loop (Muyldermans 2013).

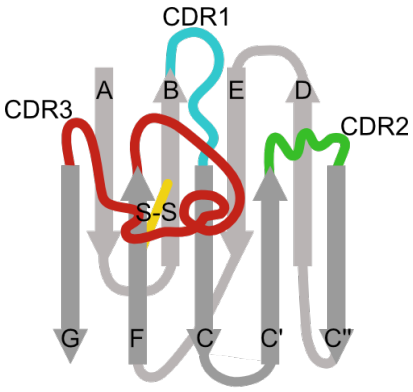


Figure 1.14: Schematic representation of a nanobody. The two ß-sheets are held together by a conserved disulphide bond, forming a prolate shape. The complementarity determining regions 1-3 (CDR1-3) are all facing in one direction. C′ and C″ denote ß-strands that are found in the variable domains but not in the constant domains of IgGs. The scaffold domain is coloured in grey, CDRs1-3 are shown in blue, green and red, respectively. Disulphide bond is shown in yellow. Adapted from (Muyldermans 2013).

In most cases, CDR3 confers the specificity of the nanobody while CDR1 and CDR2 increase the binding affinity. The unique structure of nanobodies allows them to bind epitopes not accessible to conventional antibodies either due to the size of the CDR loops (longer loops can access deeper binding sites) or due to their size (nanobodies are ~12-15kDa allowing them to explore a more diverse set of epitopes). Functional folded nanobodies can be produced in prokaryotic expression systems, unlike conventional antibodies, making them more affordable for research (Jovcevska and Muyldermans 2020).

In terms of structure and mechanism, nanobodies have been used successfully as crystallisation chaperones in a wide array of membrane proteins, where they stabilise disordered loops or particular

conformations to allow better crystal packing. This could help to increase the resolution in structural studies or trap the channel in novel states (Beghein and Gettemans 2017). This has been successfully used to study the G protein-coupled receptors (GPCRs), where the nanobodies were used to lock the receptors in functional states (for example, GPCRs in active state: ß$_2$AR (PDB: 4LDE), M2R (PDB: 4MQS); GPCR in inactive state: ß$_2$AR (PDB: 5JQH)) or to stabilise the signalling complexes (for example, GPCR–G protein–β-arrestin megacomplex (PDB: 6NI2)) (Manglik, Kobilka et al. 2017). Thus, nanobodies that are able to impose functional modulation of the channel would allow us to explore the structural mechanisms that regulate TREK-2 activity, both extracellularly and intracellularly.

To date, there is one nanobody-based therapeutic drug (Caplacizumab), approved for treating rare blood clotting disorder, and there are many more in clinical trials (Jovcevska and Muyldermans 2020). Caplacizumab is a bivalent (two identical, linked nanobodies developed to increase the half-life *in vivo*) nanobody. Patients with thrombotic thrombocytopenic purpura disorder have inactive enzyme that fails to cleave a blood glycoprotein (von Willebrand factor, vWf), which leads to vWf aggregate formation and thrombosis. The Caplacizumab binds to vWf and inhibits the aggregate formation. It can be administered both subcutaneously and intravenously, and is a promising alternative for the current available treatment – a daily plasma exchange in combination with immunosuppressive therapy (Jovcevska and Muyldermans 2020). As well as their potential use as therapeutics, nanobodies may be able to provide important insights into K2P localisation, structure and mechanism.

So far, there are no commercial monoclonal antibodies raised against a folded TREK-2, so a nanobody which is selective towards the channel could be used to better understand the localisation of these channels in tissues. This may in turn reveal more specific roles of these channels in different tissues and shed more light on the (patho-)physiological mechanisms.

1.5 SUMMARY AND AIMS OF THE TREK-2 WORK

TREK-2 is a polymodally regulated potassium channel expressed in the CNS and peripheral tissues where it is involved in maintaining the resting membrane potential. The structures of TREK-2 in two distinct conformations, assigned as conducting and inactive states, were previously solved in our group

(Dong, Pike et al. 2015). These structures revealed how TREK-2 is activated by mechanical force within the membrane, while the mechanisms that relay other regulatory stimuli to the pore are still not well understood. To elucidate the gating mechanism of TREK-2, small binders, such as nanobodies, can be used as tools to trap alternative functional states of the protein. This would allow us to investigate TREK-2 channel activity through physiological or structural studies. These tools and the understanding of channel function they afford will have value in biomedical imaging and as therapeutics for pain and neurological disorders.

In the second part of my thesis, I describe the structural and biophysical studies of TREK-2 in the presence of functional nanobodies, performed to gain new insights in the K2P regulation. I discuss the determination of binding affinities for three TREK-2 nanobodies using surface plasmon resonance (SPR). Two nanobodies, identified by Alexander Cloake as having opposite functional effects on TREK-2, were used for crystallographic studies to determine the 3D structures of TREK-2-nanobody complexes. I report the sample optimisation requirements that resulted in crystals of diffraction quality. The solved structures reveal the dissimilar nanobody binding sites on the extracellular side of TREK-2. Finally, I describe the structural rearrangements arising from the nanobody binding and how this provides new insights in the extracellular modulation of TREK-2 channels.

CHAPTER 2

2 METHODS AND MATERIALS

2.1 BIOCHEMICAL METHODS

2.1.1 PROTEIN PRODUCTION AND PURIFICATION

2.1.1.1 BACULOVIRUS GENERATION AND MEMBRANE PROTEIN EXPRESSION

SLC1A1 gene is from Mammalian Gene Collection. EAAT3 was expressed using a construct with a C-terminal truncation (residues 1-480, WT: 1-524) containing a C-terminal tobacco etch virus (TEV) protease cleavage site followed by a His10 tag and a FLAG tag and was cloned into pFB-CT10HF-LIC expression vector. The construct used included a rare variant (L92V) and also a point mutation introduced during the cloning (S42R), both of which were not in conserved positions. Both substitutions (S42R and L92V) are found in human EAAT5.

KCNK10 gene is from Mammalian Gene Collection. For TREK-2 and nanobody co-crystallisation studies, construct 11 (c011; G67- E340, full-length: 543 amino acids) and construct 38 (c038; K75-E340) were used, where c038 has point mutations (N149Q, N152Q, N153Q) in positions listed in Uniprot as glycosylation sites. All constructs contain C-terminal TEV protease cleavage site followed by a His10 tag and FLAG tag and were cloned into pFB-CT10HF-LIC vector.

For biophysical characterisation, construct 22 (c022; G67- E340) was used. The construct contains C-terminal TEV protease cleavage site followed by a His10 tag and FLAG tag and was cloned into pFB-Mam-CT10HF-LIC vector.

EAAT3 and TREK-2 (except for c022) were overexpressed in Spodoptera frugiperda (*Sf9*) cells in Sf-900™ II Serum Free Medium (Gibco/Thermo-Fisher), infected with a recombinant baculovirus. Bacmids were produced by transformation of DH10Bac cells. Cells were transfected with bacmid DNA using JetPrime® transfection reagent (Polyplus-transfection). The recombinant baculoviral stock was amplified twice (passage (P) 1 and 2) before infecting mid-log phase *Sf9* cells for large-scale expression. 5 ml of P2 virus was used to infect 1 L of *Sf9* cells at $2x10^6$ cells ml^{-1}. After the infection,

cells were incubated for ~72h at 27°C in 3 L shaker flasks (105 rpm) or 2 L roller bottles (180 rpm) before harvesting.

TREK-2 c022 was overexpressed in human embryonic kidney (HEK)293F cells in FreeStyle293 Expression medium (Thermo Fisher Scientific), infected with recombinant baculovirus as described above. The cells were infected with 3% virus amplified three times before infecting mid-log phase ($2x10^6$ cells ml^{-1}) HEK293F cells. 5 mM sodium butyrate (Sigma-Aldrich) was added with the virus and cells were incubated for ~48h at 37°C in roller bottles at 180 rpm and 8% CO_2.

Cells were harvested at 900×g for 10 min, the cell pellets were resuspended in phosphate buffered saline (PBS) and pelleted at 900×g for 20 min before flash-freezing in liquid nitrogen and storing at -80°C.

2.1.1.2 NANOBODY EXPRESSION

Nanobodies raised against TREK-2 (immunisation sample prepared by Dr. Jackie Ang) were provided by Jan Steyaert, Els Pardon (VUB, Brussels, Belgium), cloned in a phage display vector pMESy4 with a C-terminal His6-tag.

Nanobodies were expressed following a previously published protocol (Beghein and Gettemans 2017), with minor modifications. Fresh transformation was performed for each purification. Purified plasmid was transformed into *E.coli* WK6 cells. Starter cultures were inoculated with 4-5 colonies in 15 ml of LB medium supplemented with 100 µg/ml ampicillin, 2% (w/v) glucose and 2 mM $MgCl_2$. Starter cultures were grown at 37˚C until cloudy, then inoculated into 500 ml terrific broth (TB) medium supplemented with 100 µg/ml ampicillin, 0.1% (w/v) glucose and 2 mM $MgCl_2$ in a 2 L baffled flask with 5 ml of the starter culture. Flasks were shaken at 37˚C, 180 rpm until OD_{600} reached 1.5-2. Nanobody expression was induced with the addition of freshly prepared 1 mM (final concentration) Isopropyl β- d-1-thiogalactopyranoside (IPTG) and grew at 28˚C overnight, with shaking at 180 rpm. Harvested the bacteria by centrifugation for 10 min, 3063×g, 4˚C. The pellets were flash frozen in liquid nitrogen before storing at -80˚C.

2.1.1.3 MEMBRANE PROTEIN PURIFICATION

All purification steps were performed at 4°C. For EAAT3 purifications, cell pellets were resuspended in 50 ml Extraction buffer (EXB: 50 mM HEPES-NaOH, pH 7.5, 200 mM NaCl, 5% (w/v) glycerol, 5 mM imidazole) per litre of insect cell culture, supplemented with a Roche cOmplete, Ethylenediaminetetraacetic acid (EDTA)-free protease inhibitor cocktail (Sigma) tablet. Cells were lysed by 2 passes through EmulsiFlex-C3 homogeniser (Avestin), 10000 - 15000 psi. 1% Lauryl maltose neopentyl glycol (LMNG; Anatrace)/ 0.1% cholesteryl hemisuccinate tris salt (CHS; Sigma-Aldrich) was added to the cell lysate and the membranes were solubilised for 1-2 h, with gentle agitation. The lysates were centrifuged at 35 000×g for 45 min to remove the insoluble protein and cell debris. For immobilized metal affinity chromatography (IMAC) step, supernatant was incubated with Co^{2+} Talon (Clontech) resin for 1-2 h with gentle agitation to capture the His-tagged target. 1 ml 50% Talon resin was used per L of cell culture.

Resin was collected on Econo-column (BioRad) and washed with 20 column volumes (CV) Wash buffer (WB, EXB supplemented with 15 mM imidazole, 0.003% LMNG/CHS) to remove non-specifically bound proteins. The target protein was eluted with Elution buffer (EB, EXB supplemented with 245 mM imidazole, 0.003% LMNG/CHS) and the fractions with the highest protein concentration, as determined on NanoDrop 2000 (ThermoFisher), were combined and desalted on P10 columns (GE Healthcare) pre-equilibrated with Desalting buffer (DB, EXB without imidazole added, 0.003% LMNG/CHS). 1:10 (w:w) TEV protease was added and the sample was left overnight, with gentle agitation. The following day, a reverse IMAC step was performed for 1 h, with gentle agitation to remove the cleaved His-tag and TEV protease. The resin was collected on a Poly-Prep column (BioRad) and the flow through containing the target protein was collected. The sample was concentrated in a 6 ml concentrator with molecular-weight cut-off (MWCO) of 100 kDa (Vivaspin, GE Healthcare) until the volume was less than 600 µl and then spun for 20 min, at 21000×g before loading on Superose 6 Increase (GE Healthcare) column using a Äkta Purifier system (GE Healthcare) pre-equilibrated with size exclusion chromatography (SEC) buffer (20 mM HEPES, pH 7.5, 200 mM NaCl, 0.002% LMNG/CHS). The protein concentration in peak fractions was determined on NanoDrop 2000, and the fractions with the highest protein concentration were combined and concentrated in a 2 ml 100 kDa MWCO concentrator (Vivaspin, GE Healthcare) to the desired final

protein concentration. The protein could be kept at 4ºC for 1 day, and for long term storage the protein was aliquoted, frozen in liquid nitrogen and kept at -80ºC.

For TREK-2 purifications, the protocol remained the same with the following modifications: KCl was used instead of NaCl in all buffers, octyl glucose neopentyl glycol (OGNG, Anatrace) was used instead of LMNG at 0.17% in WB, EB and DB and at 0.12% in SEC buffer, and the protein was concentrated using concentrator with MWCO of 30 kDa (Vivaspin, GE Healthcare).

2.1.1.4 MEMBRANE PREPARATION FOR SURFE^{2}R STUDIES

A membrane preparation of HEK293 or *Sf9* cells expressing EAAT3 was used on the SURFE^{2}R 96SE. All steps were performed at 4°C. The cell pellets were resuspended in 40 ml cell resuspension buffer (50 mM HEPES-NaOH, pH 7.5, 1 mM EDTA, 0.6 M sorbitol) per L of cell culture. The cells were lysed by sonication (cycle of 5s on/ 10 s off for 10 min). The cells were kept on ice during the sonication. The lysed cells were centrifuged for 15 min (10 000×g, 4˚C) to remove the cell debris. The supernatant was transferred to ultracentrifuge tubes and centrifuged at 100 000×g for 1h to pellet the membranes. Next, the supernatant was discarded and the pellets resuspended in membrane resuspension buffer (50 mM HEPES-NaOH, pH 7.5, 0.3 M sucrose, 0.1 mM $CaCl_2$). The protein concentration was determined using DC protein assay kit (BioRad). The membrane preparation was aliquoted, frozen in liquid nitrogen and kept at -80ºC.

2.1.1.5 NANOBODY PURIFICATION

Nanobodies were purified following a previously published protocol (Beghein and Gettemans 2017), with the following changes: cell pellets of 1 litre of bacterial culture were resuspended in 100 ml TES buffer (0.2 M Tris pH 8.0, 0.5 mM EDTA, 0.5 M sucrose). 5 mM $MgCl_2$ solution was used instead of TES/4 buffer and the periplasmic extract was incubated with Co^{2+} Talon (Clontech) resin for 2-3h with gentle agitation. The resin was washed with 20 CV Buffer 1 (50 mM NaH_2PO_4 / Na_2HPO_4, pH 7.0, 1 M NaCl) followed by 20 CV Buffer 2 (50 mM NaH_2PO_4 / Na_2HPO_4, pH 6.0, 1 M NaCl). The protein was eluted with Elution buffer 2 (50 mM HEPES, pH 7.5, 300 mM KCl, 300 mM imidazole, pH 8.0). Protein concentration was determined using NanoDrop 2000, and the fractions with the highest protein concentration were combined and desalted on PD10 columns, pre-equilibrated with SEC buffer 2 (20 mM HEPES, pH 7.5, 200 mM KCl). The protein was concentrated in 20 ml 5 kDa MWCO concentrator

(Vivaspin, GE Healthcare) to the desired protein concentration. The protein was aliquoted, frozen in liquid nitrogen and kept at -80ºC.

2.1.2 PROTEIN RECONSTITUTION SYSTEMS

2.1.2.1 PROTEOLIPOSOMES

Purified protein was reconstituted in *E.coli* polar lipid extract (Avanti) liposomes. Liposomes were prepared from lipid stocks in chloroform and evaporated under vacuum in rotary evaporator. The lipid film was re-hydrated in the hydration buffer (25 mM HEPES-KOH, pH 7.5, 100 mM KCl, 2 mM dithiothreitol (DTT)) to the final concentration of 10 mg/ml and left shaking for 90 min, 600 rpm, 37°C. The suspension was extruded 15 times through 400 nm mesh pore size membrane using the LiposoFast liposome extruder (Avestin) to prepare uniform liposomes. The liposomes were aliquoted, flash frozen in liquid nitrogen and stored at -80°C.

Proteoliposomes were prepared in lipid to protein (LPR) ratio of 50:1. 750µL thawed liposome suspension (7.5mg lipid) was mixed with 0.15mg protein on ice. Octyl β-D-glucopyranoside (ß-OG, Anatrace, 1% wt/v) and 225mg Bio-Beads SM-2 (Bio-Rad, 0.3g/ml) were added to the lipid-protein mix. The Bio-Beads were prepared by first washing in 50 CV methanol, followed by extensive washing in water (10 times 50 CV washes). The suspension was left on a rotary wheel overnight, 4°C. Next, the supernatant was exchanged to fresh Bio-Beads (225mg) and left rotating for 1h, 4°C. The supernatant was ultracentrifuged for 1h, 100 000×g, 4°C. The pellets were resuspended in 0.75 mL reconstitution buffer (75 mM HEPES-KOH, pH 7.5, 300 mM KCl, 5mM $MgCl_2$, 1 mM DTT) and extruded 15 times through 400 nm mesh pore size membrane. The proteoliposome solution was aliquoted in 50µL aliquots (at 10 mg/ml lipid concentration), flash frozen in liquid nitrogen and stored at -80°C.

Control liposomes were prepared in parallel by substituting the protein sample with an equal volume of purification buffer.

2.2 BIOPHYSICAL METHODS

2.2.1 CHARACTERISATION OF TREK-2 NANOBODIES USING SURFACE PLASMON RESONANCE (SPR)

All proteins were purified as described before. Three biological replicates of four Nanobodies were tested in a consecutive manner (1.1-1.2-1.3-2.1-2.2-… etc.). Ideally, the experiment is performed so that each biological replicate is run at various times (e.g., as first/ in the middle/ as last) to check that there are no binding artefacts caused by protein degradation.

Three different constructs of TREK-2 were immobilised on Series S Sensor Chip CM5 (Cytiva) using Biacore S200 (Cytiva). Constructs were selected based on their posttranslational modifications (N-linked glycosylations) to see if different expression systems affect nanobody affinity (Table 2.1). Running buffer was the same as SEC buffer from protein purification (20 mM HEPES-KOH, pH 7.5, 200 mM KCl, 0.12% OGNG/CHS).

Construct	Residues	Expression system	Comments
c011	G67-E340	Sf9 (insect cells)	Intact glycosylation
c022	G67-E340	HEK293 (mammalian cells)	Intact glycosylation
c038	K75-E340 (N149Q/N152Q /N153Q)	Sf9 (insect cells)	Crystallisation construct used to determine the structural models with bound nanobodies; no glycosylation

Table 2.1: Summary of TREK-2 constructs used for SPR analysis.

Initial tests were performed with 20 µg/ml protein concentration. The pH scouting identified pH 4.5 as the best for immobilisation. Binding was done by aiming for immobilisation level of 500 RU.

The proteins were immobilised in on Series S Sensor Chip CM5 (Cytiva) as outlined:

Channel 1: empty (reference surface)

Channel 2: TREK-2 c038 (20 µg/ml)

Channel 3: TREK-2 c022 (10 µg/ml)

Channel 4: TREK-2 c011 (10 µg/ml)

Channel 1 surface was prepared the same way as the rest of the channels without added protein. The 20 µg/ml protein concentration was too high for the immobilisation of c022 and c011, so was diluted two-fold. Nanobody two-fold dilution series (80-10240 nM) were prepared in 96-well microplate. For each cycle used custom method of 90 s contact time (nanobody association step), 450 s dissociation time (nanobody removal step) at 30 µL/ min flow rate.

Raw data was evaluated and fitted to a steady-state 1:1 binding model using the Biacore S200 software in order to determine the binding affinity, expressed as equilibrium dissociation constants (K_D), calculated from the ratio of the dissociation rate to the association rate. The results were plotted using Prism 8 GraphPad software.

2.2.2 EAAT3 ACTIVITY ASSAYS

2.2.2.1 RADIOLABELLED LIGAND UPTAKE ASSAY

Activity of the purified protein was assessed using radioligand uptake assay. The detergent- solubilised EAAT3 was reconstituted in proteoliposomes and the transport activity measured by establishing the required ion/ substrate gradients. Proteoliposomes were extruded 15 times through 400 nm mesh pore size membrane before use and left for at least 30 min to equilibrate to room temperature (RT).

The assay was performed at RT. For the time-course experiment, the assay was started by diluting 10 mg/ml proteoliposome sample six times in Start buffer (20 mM HEPES-NaOH, pH7.5, 140 mM NaCl, 1 µM valinomycin, 10 µM Glutamic acid, 1 µM ^{3}H-Glutamic acid). At the defined time points, 30 µL sample was removed and diluted in 2 ml Stop buffer (20 mM HEPES-KOH, pH 7.5, 140 mM choline chloride). The sample was vacuum filtered over 0.22 µm pore size filters (Millipore), washed with 4 ml Stop buffer and transferred to a vial. 3.5 ml scintillation fluid (Ultima Gold, Perkin Elmer) was added per vial and left to incubate for 2h.

For the end-point assay with inhibitors, the inhibitors were added to the Start buffer and the samples were incubated for the indicated time frame before stopping the reaction by dilution in Stop buffer.

The total radioactivity was counted using MicroBeta2 counter (Perkin Elmer) in 4 ml vials (Perkin Elmer). The results were analysed and plotted using Prism 8 GraphPad software.

2.2.2.2 SURFE^{2}R ASSAY

All the SURFE^{2}R experiments were performed by Antje Pommereau at Sanofi (Frankfurt, Germany) using SURFE²R 96SE instrument (Nanion Technologies). The proteoliposomes and control liposomes were prepared by Agnese Baronina, the experiments were designed by Agnese Baronina. and Antje Pommereau, and the measurements were performed by Antje Pommereau. The experiments were performed using double solution exchange, using resting buffer (140mM KCl; 30mM HEPES; 2mM

$MgCl_2$; pH7.4 with KOH), base buffer (140mM NaCl; 30mM HEPES; 2mM $MgCl_2$; pH 7.4 with NaOH) and activating buffer (base buffer + amino acids/ inhibitors added). Amino acid/ inhibitor stock solutions (1 mM) were prepared fresh in base buffer and pH adjusted to 7.4 using NaOH. All the measurements were performed with the following program:

1. 3x negative control measurements (resting buffer → base buffer → base buffer → resting buffer)
2. 2x measurements (resting buffer → base buffer → activating buffer → resting buffer)
3. 2x wash (resting buffer)

2.2.3 NANODSF

Nano differential scanning fluorimetry (nanoDSF) was used to monitor the thermal stability of proteins in the presence or absence of ligands using intrinsic fluorescence signals from tryptophan or tyrosine residues. This label free system allows to determine the melting temperature (T_M) of the proteins, defined as the temperature at which 50% of the protein is unfolded, by plotting the recorded fluorescence signal against the increasing temperature gradient.

Here, Prometheus (nanoTemper) system was used. Protein samples were centrifuged for 20 min, 21 000×g before adding ligands and the final protein concentration adjusted to 0.5 mg/ml. The samples were left at RT for 15 min before centrifuging for 5 min, 21000×g. The samples were loaded in capillaries (nanoTemper) and thermal shift monitored by running 1°C/min, 20°-90°C program.

2.3 STRUCTURAL BIOLOGY

2.3.1 EAAT3 STRUCTURE DETERMINATION BY CRYO-EM

2.3.1.1 SAMPLE PREPARATION

Freshly purified protein was ultracentrifuged for 30 min, 100 000×g. The sample was diluted to the required final concentration with SEC buffer and the ligands added (±**HIP-B dataset:** 2mg/ml final protein concentration with 2 mM ±HIP-B added (10 mM stock, dissolved in SEC buffer with no detergent added); **TFB-TBOA dataset:** 2 mg/ml final protein concentration with 1 mM TFB-TBOA added (50 mM stock dissolved in dimethyl sulfoxide (DMSO). 0.01% n-Dodecyl-β-D-Maltopyranoside (DDM) (in SEC buffer with no detergent added, final concentration) was added to

the samples just before loading on the grid. Immediately before use grids were glow discharged in air for 30 s. 3 µL sample was applied on a Quantifoil grid (Quantifoil R1.2/1.3 holey carbon, 300 mesh gold grid) and prepared using a Vitrobot Mark IV (FEI, Thermo Fisher Scientific; 4-4.5 s blot time, -15 blot force, 5˚C, 100% humidity).

2.3.1.2 GRID SCREENING AND DATA COLLECTION

Grid optimisation and preliminary data collection were performed on a Talos Arctica operating at 200kV equipped with a Falcon3 detector (Thermo Fisher) at the Central Oxford Structural Microscopy and Imaging Centre (COSMIC) Oxford University.

The high-resolution datasets were collected on a Titan Krios (Thermo Fisher) TEM operating at 300 keV equipped with a direct electron detector (K2 Summit; Gatan) at Pfizer (Groton, USA). Data collection was carried out using SerialEM (Mastronarde 2005) software in super-resolution mode at a calibrated pixel size of 0.543 Å and a defocus range of -1.6 to -2.4 µm. The movies were recorded with a 10 s exposure (40 (±HIP-B dataset) and 48 (TFB-TBOA dataset) total frames) corresponding to a total dose of 42 (±HIP-B dataset) and 40 (TFB-TBOA dataset) electrons per $Å^2$.

2.3.1.3 DATA PROCESSING

Super-resolution movies were binned twofold, motion-corrected and dose-weighted using MotionCor2 (the resulting pixel size of 1.086 Å was used for the rest of the processing) (Zheng, Palovcak et al. 2017). The CTF estimation was carried out using CTFFIND-4.1 (Rohou and Grigorieff 2015). Micrographs with bad CTF estimation were discarded and the remaining movies were processed using RELION 2.1 (Kimanius, Forsberg et al. 2016) and RELION 3.0 (Zivanov, Nakane et al. 2018). Reference free particle picking was done using Gautomatch (URL: http://www.mrc-lmb.cam.ac.uk/kzhang/) to generate 2D references used for autopicking. Extracted particles with a box size of 200 pixels were twofold binned for 2D classification in RELION 2.1 and 2-4 rounds of classification were done in an iterative manner to remove bad particles. A low-resolution reference model was generated *ab initio* from a subset of particles and used for the first round of 3D classification without symmetry imposed. Multiple rounds of 3D classification were performed with no symmetry imposed before selecting particles from the 3D class with the highest resolution details. These particles were then autorefined and masked. Further particle classification was done without particle alignment

during autorefinement over multiple classes. Finally, particles from the 3D class with the highest resolution details were subjected to another round of 3D classification with no symmetry imposed and autorefinement jobs with C3 symmetry imposed. Per-particle CTF-refinement and Bayesian polishing was done in RELION 3.0. This required movies to be motion-corrected in RELION 3.0 framework and particles contributing to the highest resolution 3D reconstruction from processing in RELION 2.1 re-extracted. CTF-refinement with beam tilt estimation, followed by Bayesian polishing was repeated in an iterative manner until no further improvement in resolution was achieved. The final polished map was used for the postprocessing. The modulation transfer function (MTF) was deconvoluted from the map. Global resolution (FSC) for masked map (soft mask applied to exclude the disordered micelle region and for "solvent flattening") and unmasked map was estimated with the 0.143 cut-off criterion (Rosenthal and Henderson 2003). B-factor for map sharpening was estimated from the Guinier plot. Local resolution estimation was calculated in Relion. The summary of processing for the ±HIP-B and TFB-TBOA datasets is shown in Figure 2.1 and Figure 2.2, respectively.

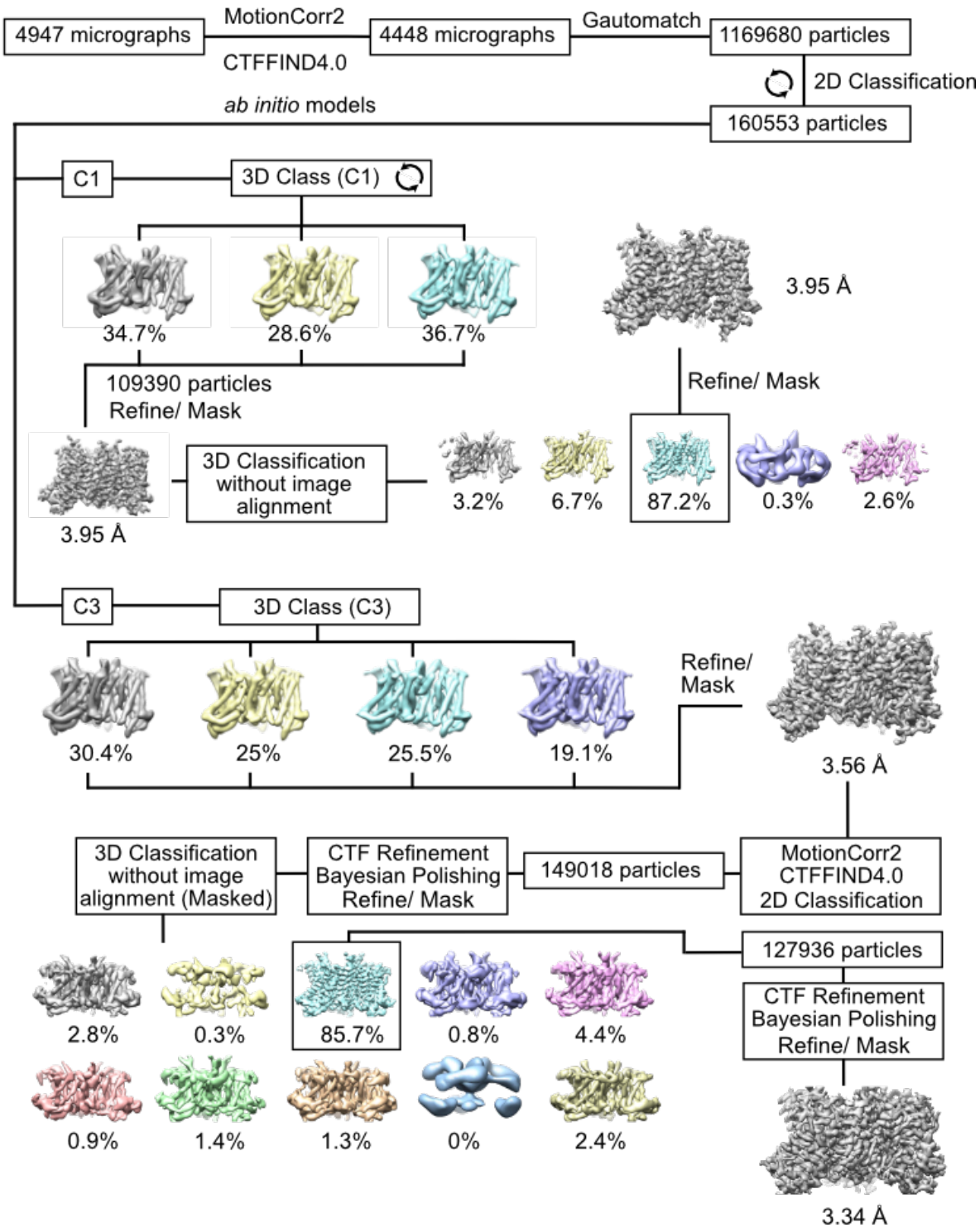


Figure 2.1: Workflow of the processing steps for ±HIP-B dataset.

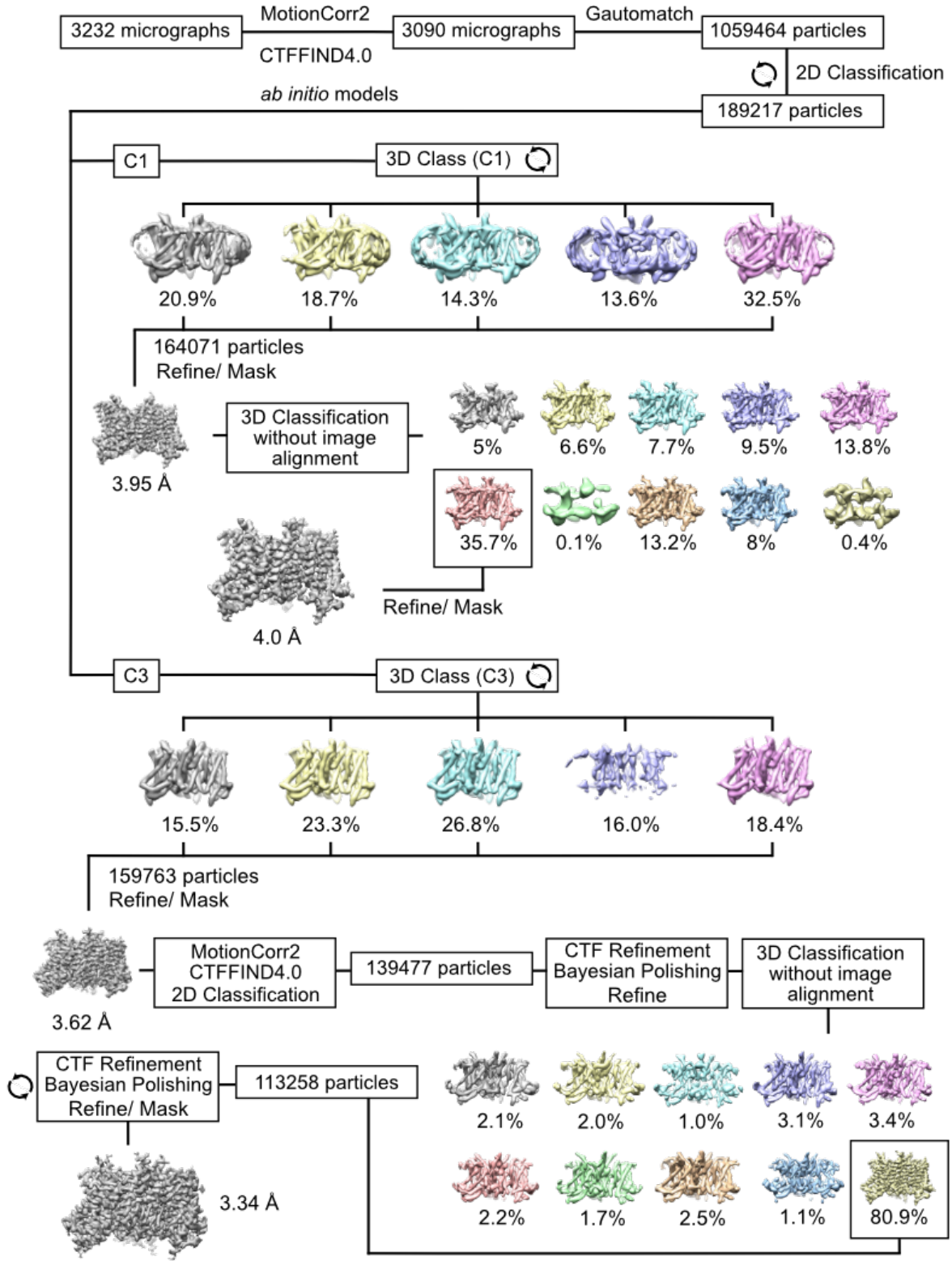


Figure 2.2: Workflow of the processing steps for TFB-TBOA dataset.

2.3.1.4 MODEL BUILDING, REFINEMENT AND VALIDATION

The homology-based model was created using SWISS-MODEL (Waterhouse, Bertoni et al. 2018) with ASCT2 (PDB: 6GCT) as a model. The generated model was docked into the EM density map using Chimera (Pettersen, Goddard et al. 2004), and the model building was done in Coot (Emsley, Lohkamp

et al. 2010). The model was refined against the postprocessed, sharpened map in PHENIX (Liebschner, Afonine et al. 2019) using real space refinement with non-crystallographic symmetry (NCS) constraints and secondary structure, rotamer, C-beta deviations restraints applied. Ramachandran restraints were applied to the ±HIP-B but not to TFB-TBOA dataset. The coordinates were updated in Coot and resubmitted for refinement in PHENIX in an iterative manner until no further improvements were observed. For ±HIP-B molecule positioning, I modelled +HIP-B position and further exploration of -HIP-B binding modes was carried out by Dr. Ashley Pike. The final model comprises one pose for + and one for '-' with equal half occupancy. Model validation was done by calculating a FSC (FSC_{sum}) between the model and the final masked map. To estimate potential overfitting, random shifts (up to 0.5 Å) were introduced in the model using phenix.pdbtools, and the "shaken" model was refined against the first half map (postprocessed and *B*-factor sharpened in an identical manner to the full map). The FSC (FSC_{work}) was calculated between the shaken model and the first half map. The FSC (FSC_{free}) was calculated between the "shaken" model and the second half-map, not previously used in the refinement. The model quality was validated using MolProbity (Williams, Headd et al. 2018) within PHENIX and the FSC curves generated using Mtriage (Afonine, Klaholz et al. 2018) validation tool. The ligand dictionary for ±HIP-B was created using Grade Web Server (O. S. Smart 2011).

2.3.2 STRUCTURE DETERMINATION OF TREK-2 NANOBODY COMPLEXES USING X-RAY CRYSTALLOGRAPHY

2.3.2.1 CRYSTALLISATION OF TREK-2 NANOBODY COMPLEXES

Thawed TREK-2 constructs were centrifuged for 20 min, 21000×g before mixing with nanobodies (1:2 TREK-2 dimer to nanobody molar ratio) and left on ice for 15 min before centrifuging for 20 min at 21 000×g prior to crystallization plate set up. **TREK-2-Nb61 complex**: Crystals were grown using the LCP method in Scripps-style glass LCP plates (Marienfeld, Germany) at 20°C. TREK-2 c038 at 10 mg/ml final concentration was mixed with Nb61 (1:2 molar ratio). LCP was formed by incorporating the protein solution into MAG7.9 at 3:2 (lipid: protein) ratio using a system of two 100 µL gastight Hamilton glass syringes connected with a coupler. The protein solution and lipid were loaded in the separate syringes, which were then connected with a coupler, taking care not to introduce air. The mixing was always started from the protein side. The sample was mixed by pushing through the coupler

back and forward until the initially opaque mixture became translucent (a sign that cubic phase was formed). The freshly prepared LCP was used immediately. Plates were set up using Mosquito (TTP Labtech) crystallisation robot. 50 nl mesophase was dispensed per well and covered with 800 nl of crystallisation solution. The plate was kept at humidified chamber (~60% humidity) during the plate set up. Crystals grew in 0.1M sodium acetate pH 4.5, 0.3M KCl, 23% (v/v) polyethylene glycol (PEG)400 over a period of two weeks. Crystals were harvested at room temperature, under a stream of humid air, to slow down the evaporation of the precipitant solution. The phase of the lipid mesophase depends on the water:lipid ratio and any changes in this ratio cause the lipid mesophase to undergo a phase change. This process can be seen under cross-polarised light and the crystals are destroyed due to changes is the ratios between the components of the crystallisation solution (e.g., increase in concentration of salt, polymers). The crystals were mounted using dual thickness MicroMounts (MiTeGen) loops and vitrified in liquid nitrogen directly from the drop.

TREK-2-Nb67 complex: TREK-2 c038 at 10 mg/ml final concentration was mixed with Nb67 (1:2 molar ratio). Crystals were grown using vapour diffusion method in sitting drops. Three drops of 150 nL total volume (2:1, 1:1 and 1:2 protein: reservoir solution ratio, v:v) were dispensed in 3-position 96-well plates (SwissCi) at 4°C. Commercially available sparse matrix crystallisation screens, covering conditions identified from previous successful membrane protein crystallisation trials, were used for the initial screening. These included MemGold, MemGold2 and MemStart™ + MemSys™ HT-96 (Molecular Dimensions). Crystals that were used for the final dataset collection grew in 0.1M Tris pH8.0, 65% (v/v) 2-methyl-2,4-pentanediol (MPD)(MemGold2 – condition H8). Crystallisation optimisation around this condition was performed, by testing if change of pH, added KCl, or additives (non-volatile and volatile organics, salts, polymers) would improve the diffraction. While crystals that diffracted <3Å could be obtained, the resolution could not be further improved. The crystals were mounted at 4˚C using Mounted CryoLoops (Hampton Research). Since the crystals grew in 65% (v/v) MPD, additional cryoprotection was not used and the mounted crystals were vitrified in liquid nitrogen directly from the drop.

2.3.2.2 CRYSTAL SCREENING AND DATA COLLECTION

Crystal screening and data collection were performed on the I24 microfocus beamline at Diamond Light Source at 100K using a Pilatus3 6M detector. Crystals were screened at 0.9116 Å wavelength and three 0.5 s exposures with oscillation angle of 0.5˚ were taken separated by 45˚ rotation. For VD crystals, beam size used varied between 9x6 and 20x20µm, depending on crystal size. Transmission energy was used in a range of 5-100%, depending on the crystal diffraction quality. For LCP crystals, grid scans were used with 20x20 µm beam size and 10x10 µm box size to locate the crystals within the loop. Transmission energy was used in a range of 20-100%, with exposure time reduced to 0.2 s. For both datasets that were used to solve the structures, single crystals were used for the data collection. Data collection strategies were developed using iMOSFLM (Powell, Battye et al. 2017) based on the three screening images. Diffraction images were autoindexed and a strategy to collect data with maximal completeness was used. The transmission energy and exposure time used were estimated from the screening images. Typically, crystals were rotated in 0.2˚ increments and exposed for 0.2 s with the beam attenuated to 2%.

2.3.2.3 X-RAY CRYSTALLOGRAPHY DATA PROCESSING

Data was processed with XDS program package (Kabsch 2010) to index, integrate and scale the data. The data was merged and anisotropy of the diffraction analysed using STARANISO (Tickle 2018). In STARANISO, anisotropic diffraction limits can be defined in reciprocal space, meaning the data in directions with good diffraction does not have to be spherically averaged to the resolution of the direction with the worst diffraction. The resolution cut-off was selected based on the spherical completeness in the outer shell (>30%). The number of molecules in each asymmetric unit was estimated using Matthew's coefficient program (Matthews 1968) based on the unit cell dimensions and the molecular weight of the TREK-2 monomer with one bound nanobody. Molecular replacement was done using PHASER (McCoy, Grosse-Kunstleve et al. 2007). TREK-2 in "up" or "down" conformations (4BW5 and 4XDJ, respectively) and nanobodies from 5UKB (for Nb67) and 5IMK (for Nb61) were used as search models. For the search model, both TREK-2 dimer and 1-3 nanobodies were used together. To aid the search, the flexible loops in TREK-2 were removed using CCP4 program CHAINSAW (Stein 2008). The solutions were inspected manually in Coot v0.8.9 (Emsley, Lohkamp et al. 2010).

2.3.2.4 MODEL BUILDING, REFINEMENT AND VALIDATION

All models were built using Coot v0.8.9 (Emsley, Lohkamp et al. 2010) using σA-weighted 2mFo-DFc and mFo-DFc maps from BUSTER (Bricogne G. and Roversi P 2019). The phase estimation of maps was improved by density modification using Parrot (Cowtan 2010). Initial models for TREK-2 structures were prepared in Coot by removing flexible loop regions. Chainsaw (Stein 2008) program within the CCP4 suite was used to trim the sidechains with no conservation in Nb61 or Nb67 to alanines. Models were iteratively refined using BUSTER using automated NCS restraints and individual B-factors (Smart, Womack et al. 2012). To improve the model, translation, rotation, and screw-rotation (TLS) refinement was included for the final rounds of refinement using a single TLS body per protein chain. After each refinement cycle the coordinates were manually adjusted in Coot before submission for another round of refinement until all Fo-Fc (difference) map density was accounted for and R_{work}/R_{free} factors had converged. Model validation was performed using global (all-atom contacts) and local (covalent-geometry and torsion-angle) analysis using MolProbity (Williams, Headd et al. 2018).

2.3.2.5 STRUCTURE PRESENTATION AND ANALYSIS

Figures were prepared in PyMOL (Schrödinger, LLC) and Chimera (Pettersen, Goddard et al. 2004) or ChimeraX (Pettersen, Goddard et al. 2020). FFT was used to convert maps to CCP4-format for electron density map visualisation in PyMOL (Read and Schierbeek 1988). PDBePISA was used to determine the interfaces between molecules or protein domains (Krissinel and Henrick 2007). For EAAT3 figures, TFB-TBOA model was used unless otherwise stated. For TREK-2 figures, TREK-2 in apo form (PDB:4BW5) was used unless stated otherwise.

CHAPTER 3

3 CHARACTERISATION OF EAAT3 FUNCTION *IN VITRO*

3.1 INTRODUCTION

In the CNS, glutamatergic neurotransmission is involved in memory and learning. L-glutamate signalling is crucial for neuronal interactions, yet high extracellular glutamate concentration is toxic to cells and must be tightly regulated. The steep glutamate gradient across the cell membrane is established by Na^+-dependent high-affinity glutamate transporters, EAATs. These transporters are expressed throughout the brain and they use secondary active transport to maintain extracellular glutamate concentration in synapses at ~1 μM (Shimamoto 2008). Extensive functional and pharmacological characterisation of EAAT3 has been performed in a series of heterologous expression systems (such as *Xenopus* oocytes, COS-1/7 or HEK cells (Arriza, Fairman et al. 1994, Shimamoto, Shigeri et al. 2000, Jensen and Brauner-Osborne 2004)). However, difficulties remain in obtaining purified protein reconstituted into membranes for functional studies and this has hindered the *in vitro* studies required for subtype-specific ligand design and characterisation. In this chapter, the development of a reconstitution protocol for obtaining active EAAT3 in proteoliposomes is described. The reconstituted EAAT3 was then used to study the transport kinetics of EAAT3 using direct and indirect measurement methods. In addition, the assays were used to characterise the two inhibitors that were used in subsequent structural studies.

3.1.1 THE PHARMACOLOGY OF EAATS

The pharmacology of EAATs is well studied *in vivo* with a range of inhibitors synthesized. All EAATs exhibit complex transport stoichiometry, where three Na^+ ions, a proton and the substrate are exchanged for one K^+ ion (Zerangue and Kavanaugh 1996). Members of the SLC1 family also exhibit Cl^- ion conductance in parallel with amino acid transport. Overall, the transport is electrogenic, with net positive charge moved into the cells associated with observable inward current (Shimamoto 2008). The majority of the compounds identified from studies *in vivo* are substrate analogues that act as competitive inhibitors and can be transported by several of the EAATs, producing ion currents in the

same manner as substrates. Since EAATs can function in a heteroexchange mode, non-transportable blockers are crucial for functional studies (Shimamoto 2008). Although substrate analogues have been developed with sub-μM affinity, they generally show poor selectivity towards the EAAT subtypes. This makes it difficult to attribute the observed effects of a compound *in vivo* to a particular EAAT. The most frequently used inhibitor, DL-TBOA and its analogues, is an L-aspartate analogue and a competitive inhibitor (Shimamoto, Lebrun et al. 1998, Shimamoto, Sakai et al. 2004). Structural studies of members of the *SLC1* family and the prokaryotic homologues have revealed binding modes for both L-aspartate and its analogues, where the aspartate-moiety mimics the substrate binding mode. Glutamate binding is less well characterised. To date, there are no structures with glutamate bound since the bacterial homologues, most commonly used for the structural studies, only weakly bind glutamate (Boudker, Ryan et al. 2007). ±HIP-B is a glutamate analogue that inhibits substrate transport in EAAT1-3. For EAAT3, of the two enantiomers, (+)-HIP-B shows ~10 times higher potency than (-)-HIP-B (Colleoni, Jensen et al. 2008). In the absence of a structural model, docking studies using the scaffold of the bacterial homologue GltPh proposed ±HIP-B binding within the binding site (Pinto, Conti et al. 2008). Yet, work with enantiopure (+)-HIP-B and EAAT3 indicated that the inhibitor can bind to both apo and glutamate-bound forms of the transporter (Callender, Gameiro et al. 2012). While subtype-specific allosteric inhibitors have been identified for EAAT1 and EAAT2 (UCPH101 and WAY-213613, respectively (Dunlop, McIlvain et al. 2005, Huynh, Abrahamsen et al. 2012)), there are no commercially available inhibitors that are EAAT3 selective. The purification of functional human EAATs is also not trivial, further hindering structure-based ligand synthesis and screening abilities. Further structural studies of EAATs with inhibitors bound are needed to elucidate the basis of substrate selectivity observed within the subtypes of SLC1 family.

3.1.2 IN VITRO ASSAYS FOR FUNCTIONAL CHARACTERISATION OF SOLUTE TRANSPORTERS

The functional characterisation of secondary active transporters can be performed by direct or indirect measurement methods. In case of EAAT3, which co-transports a substrate and ions, the substrate transport can be measured by quantifying the transported substrate in an uptake assay (direct measurement) or by performing electrophysiological measurements to measure charge movement,

which is stoichiometrically coupled to the substrate transport (indirect measurement). Here, I characterised proteoliposome-reconstituted EAAT3 activity using radiolabelled substrate uptake assay. I had planned to use SSM – based electrophysiology to measure the activity of EAAT3 using the SURFE^{2}R system available in our collaborator Thomas Licher's lab in Sanofi (Germany). I performed extensive sample optimisation, where I shipped the prepared proteoliposomes to Sanofi for Antje Pommereau (A.P.) to test them for activity on the SURFE^{2}R system. We had planned a series of experiments at Sanofi in which I would have run the experiments in their labs myself. Unfortunately, the Covid-19 lockdown occurred just at the time when I would have gone to Germany to complete these experiments, so it was not possible for me to do the work myself. I was however fully involved in the optimization of samples, and I visited the Sanofi labs once to learn about the use of the equipment and the experimental set up and procedure. Here, I use the data that was collected by A.P. using proteoliposomes that I had produced. I received the raw data from A.P.; however, all the analysis presented here was done by myself. The radiolabelled substrate uptake assay and the solid support methods complemented each other, and provide the kinetic parameters required to characterise the transport of substrates and the mode of action of the inhibitors.

The transport of substrates by solute carriers can be described using the same approach as for enzymes, treating transporters as though they carry out topological reactions (translocation of substrate across the membrane). The mathematical model of the enzyme reaction can be represented schematically as:

$$E + S \leftrightarrow ES \rightarrow E + P$$

where E is enzyme, S is substrate, P is product, the double arrow before ES (enzyme-substrate complex) indicate that this is a reversible step, and the single arrow after ES indicate the formation of the product (irreversible) (Chen, Niepel et al. 2010). The kinetics of many enzymes can be described using the Michaelis-Menten equation:

$$v = V_{max} / \left(1 + \frac{K_M}{[S]}\right)$$

where v is the rate of the reaction, V_{max} is the maximum rate of the reaction, K_M is the Michaelis constant and S is the substrate concentration. Michaelis-Menten kinetics is obeyed by most transporters

with non-cooperative binding, since they have a single substrate binding site that during the transport cycle is occupied by a single substrate molecule (Diallinas 2014). The Michaelis-Menten equation is used to determine substrate affinity, inhibition or dissociation constants (K_M, K_I, K_D, respectively) and transport capacities or rates (V or V_{max}). The Michaelis-Menten equation is fitted to the experimental results using nonlinear least-squares fitting in a data analysis algorithm of choice. The K_M value in this case is the binding affinity of the substrate which is determined from the initial, linear relationship between substrate and transporter for all the substrate concentrations measured, where the limiting factor of the reaction is the substrate availability (Aggarwal and Mortensen 2017).

3.1.2.1 KINETIC UPTAKE ASSAY

Commonly used assay to characterise interactions between ligands and transporters is a kinetic uptake assay. **Kinetic uptake assays** involve incubation of the transporter (either expressed in cells or reconstituted in proteoliposomes) with varying concentrations of substrate to determine the K_M and V_{max} values (Figure 3.1).

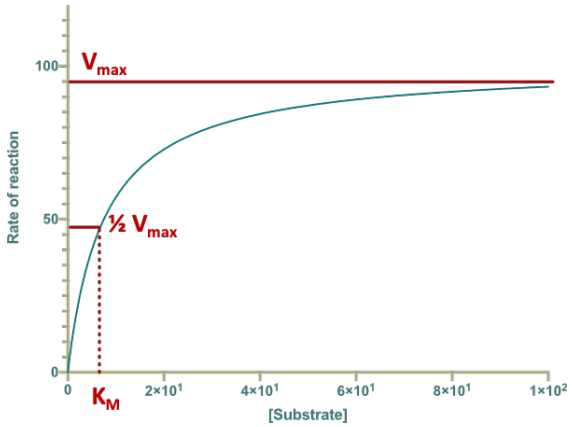


Figure 3.1: The graphical representation of the relationship between substrate concentration and the enzymatic rate of reaction that obeys Michaelis-Menten kinetics. Michaelis constant (K_M) is defined as the substrate concentration at which the enzyme functions at half its maximal rate (1/2 V_{max}). The rate of reaction when the enzyme is saturated with the substrate is V_{max}.

The substrate uptake is terminated after specified time period by a rapid removal of the ligand. A control experiment is performed in parallel to identify the amount of non-specific substrate uptake, which is then subtracted from the total measured substrate uptake in the presence of the transporter.

3.1.2.2 DOSE-RESPONSE ASSAY

The **dose-response assay** is used to determine the ability of a ligand to inhibit the uptake of the substrate. The compound is prepared in serial dilutions covering a range of concentrations and applied to the sample in the presence of a fixed substrate concentration to determine the inhibitory effect. The measured response is plotted against the inhibitor concentrations and can be normalised to compare separate measurements. The potency of the ligand is quantified by determining how much of ligand is needed to inhibit the measured process by 50%, referred to as the half maximal inhibitory concentration (IC_{50}). If the response involves activation instead of inhibition, then the half maximal effective concentration (EC_{50}) is reported. The dose-response assay can also be used to determine if the ligand interacts with the same binding site as the substrate and the type of inhibition (competitive, non-competitive or allosteric) as shown in Figure 3.2. The IC_{50} is dependent on substrate concentration and can be used to calculate the inhibition constant of the ligand (K_i) if the binding is competitive, using equation:

$$K_i = {IC_{50}}\Big/\left(1 + {[S]}\Big/{K_M}\right)$$

where [S] is the substrate concentration, IC_{50} is the potency of the inhibitor and K_M is the Michaelis constant (Aggarwal and Mortensen 2017).

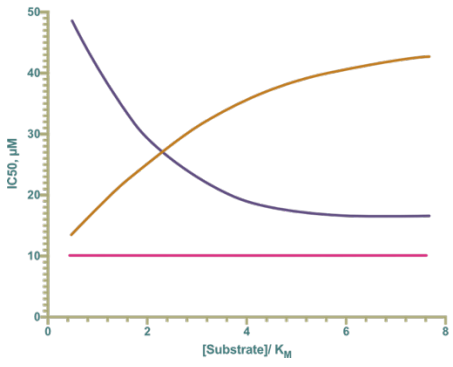


Figure 3.2: Ligand binding modality as a dependence of IC_{50} values on substrate concentration. The three types of inhibition (competitive – gold; non-competitive – magenta and uncompetitive – blue line) are best identified at multiple substrate concentrations both above and below the K_M. Figure adapted from (Strelow, Dewe et al. 2004).

3.2 SOLID-SUPPORTED MEMBRANE (SSM) BASED ELECTROPHYSIOLOGY

Classical electrophysiology methods (such as patch-clamp) are used to measure electrical currents associated with the flow of ions across the membranes of cells. It is one of the most common electrophysiological techniques used to study ion channel functions (Rubaiy 2017). However, it is not well suited for studying low turnover transporters as the signal-to-noise ratio from single-cell measurements is low. SSM-based electrophysiology is an alternative technique that allows functional characterisation of membrane proteins for reactions where a displacement of charge occurs. This involves transport of charged species across the membrane, or changes in the exposure of charged residues on the protein surface in response to substrate binding. The measurements can be performed using crude membrane-vesicles or proteoliposome reconstituted protein. The vesicles are adsorbed onto the sensor and the electrogenic transport activity is recorded during rapid application of substrate-containing solution, as shown in Figure 3.3.

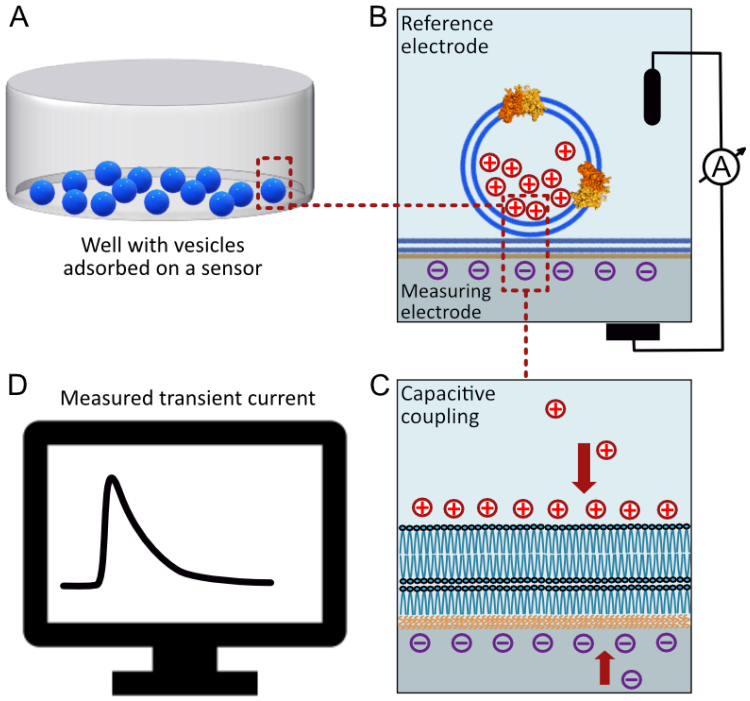


Figure 3.3: Graphical representation of SSM measurements. **A** A sample of choice (ranging from membrane vesicles to proteoliposomes) is adsorbed to a lipid-monolayer coated sensor (SSM) in a well. As many vesicles are adsorbed to the same sensor, during a measurement, signals from many proteins at the same time are recorded, leading to high signal to noise ratio. **B** The adsorbed vesicles form a capacitively coupled membrane system with the lipid-coated sensor. **C** During measurement, the charge movement into the protein containing vesicle arising from active transport by the protein

can be then detected by the capacitive coupling. **D** The transient currents can be observed that represent the stationary transport activity of the protein. Adapted from (Bazzone, Barthmes et al. 2017).

Proteoliposomes prepared with low LPR and adsorbed on the sensor result in high total protein density leading to signal amplification and increased sensitivity of the measurements. The robustness of the system allows multiple repeated measurements without loss of sensitivity, preferred for determination of kinetic parameters for substrate transport and compound screening (such as EC_{50}/IC_{50}, K_M, K_D) (Bazzone, Barthmes et al. 2017). The commercialised instrument available from Nanion Technologies, called SURFace Electrogenic Event Reader ($SURFE^2R$), is fully automated and available in 96-well plate format, allowing for high-throughput screening. As proof of principle, the $SURFE^2R$ assay has been previously used for characterisation of the mouse EAAT3 (EAAC1) using membrane vesicles from Chinese hamster ovary (CHO) cells heterologously expressing mEAAT3 (Krause, Watzke et al. 2009).

The typical workflow involves sensor plate preparation with adsorbed proteoliposomes, followed by measurements using a double-solution exchange protocol, as EAAT3 requires an established Na^+ gradient across the membrane (Figure 3.4). Three buffers are used consecutively: “resting buffer” (potassium-containing, sodium-free) is replaced with “non-activating buffer” (sodium-containing, substrate-free) to establish the Na^+ gradient. The exchange to “activating buffer” (sodium- and substrate-containing) activates the transporter and the induced currents are measured. The exchange to “resting buffer” results in EAAT3 running in reverse and returns the system to the initial state.

The amplitude of the peak currents recorded on SSM are proportional to the currents generated by the transporter and is used to determine the kinetic properties of the transporter. The recorded current represents substrate binding and initiation of the transport cycle, prior to membrane potential build-up that would affect the kinetic properties. Due to the variability of the vesicle adsorption onto the sensors, the measured amplitudes can only be directly compared when obtained from the same sensor. Measurements of the peak currents with substrate concentration jumps allow calculation of K_M values, and different inhibitor concentrations in the presence of a fixed concentration of a substrate give IC_{50} values (Bazzone, Barthmes et al. 2017). In both cases, the integrated area under the peak is normalised and averaged, then plotted against the substrate/inhibitor concentration, followed by fitting with an appropriate model function. As the measurements were performed in 96-well format, measurements

from different sensors were normalised before averaging by fitting the highest current amplitude as 100%.

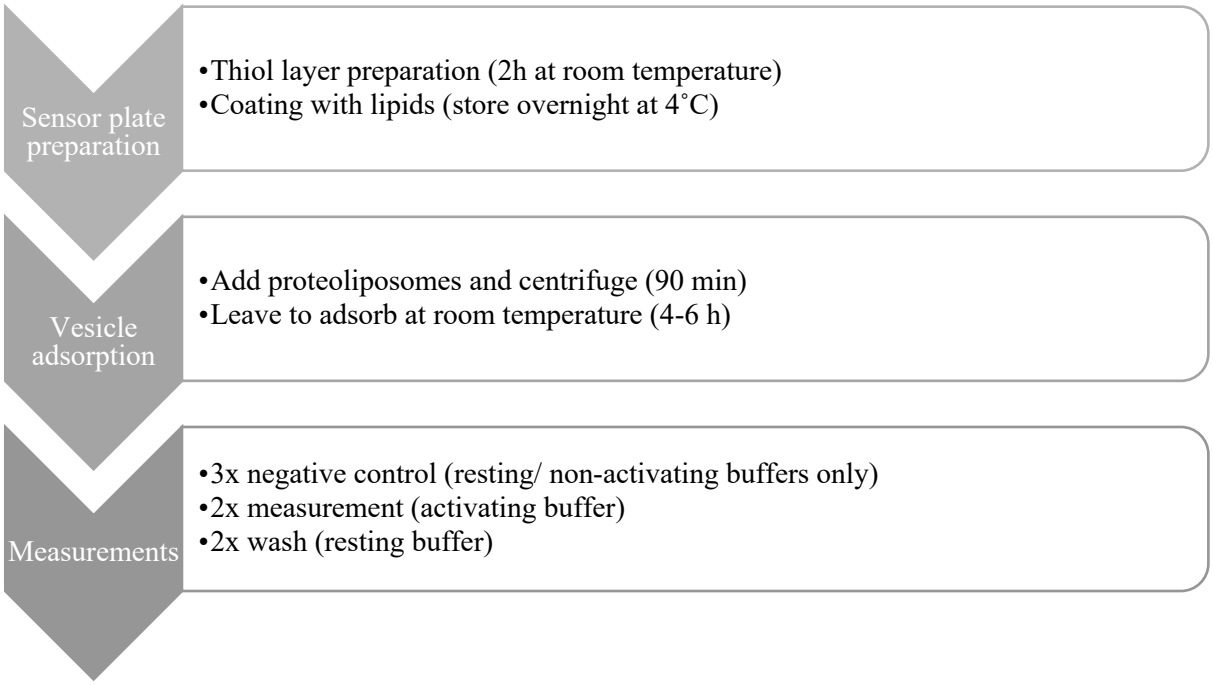


Figure 3.4: Workflow for experiments on the SURFE^{2}R system. The sensors in a 96-well plate format are first thiolated before adding a lipid solution to prepare a solid-supported membrane. Next, membrane or proteoliposome suspension is added and the plate centrifuged for at least 30 min to aid vesicle sedimentation. To improve the adsorption process, the plate is left at room temperature for a couple of hours. Once the proteoliposomes have adsorbed, the double solution exchange protocol is used for the measurements. This involves sequential exchange between resting, non-activating, activating and non-activating buffers. For each measurement, a protocol of three negative controls, two measurements and two wash cycles are used. Negative controls consisted of the same steps as measurements but instead of activating buffer, non-activating buffer is used.

Functional characterisation of transporters that perform electrogenic transport can be done using SSM-based electrophysiology. This method is well suited for proteins with low turnover rates as the signal is increased by recording multiple proteins at once. The substrate translocation across the protein-embedded lipid bilayer is detected by the capacitive coupling between the vesicle and lipid bilayer on the sensor. The recorded peak currents are then used to characterise the kinetic properties of the protein.

3.2.1 EAAT3 FUNCTIONAL CHARACTERISATION USING THE SURFE^{2}R TECHNOLOGY

3.2.1.1 OPTIMIZATION OF EAAT3 RECONSTITUTION IN PROTEOLIPOSOMES FOR FUNCTIONAL STUDIES

The general protocol for membrane protein reconstitution into liposomes is shown in Figure 3.5. In practice, many parameters have to be optimised before functional protein suitable for transporter activity studies is obtained.

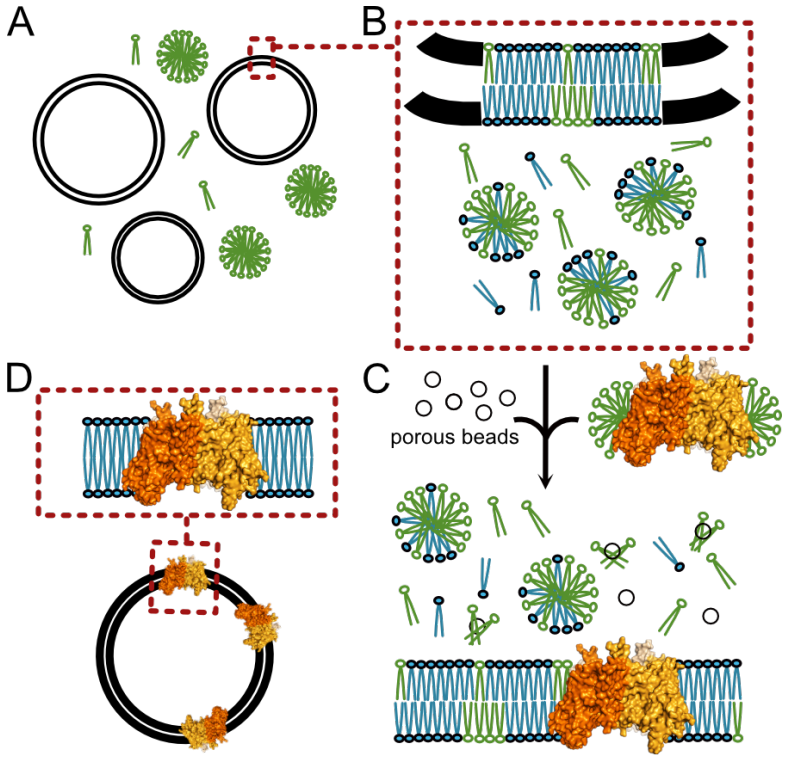


Figure 3.5: The workflow of membrane protein reconstitution in liposomes. **A** Unilamellar liposomes are incubated with detergent (shown in green) to disrupt the lipid bilayer. Detergent is used above critical micelle concentration (CMC) so that the majority of the detergent molecules are assembled in micelles that can solubilise the bilayer. **B** Above the CMC, detergent molecules either insert into the lipid bilayer (individual lipid molecules shown in blue) and destabilising it or extract lipid molecules and form lipid-detergent micelles. **C** Detergent solubilised membrane proteins (represented by EAAT3 trimer with each monomer coloured in a shade of orange) are added to the detergent-lipid suspension and detergent removal is started by adding porous beads that bind free detergent molecules, reducing the detergent concentration in solution to below its CMC. **D** During the detergent removal, lipids spontaneously arrange in the bilayer with membrane protein incorporated. Vesicles of various sizes are formed and are ready for downstream applications.

3.2.1.2 OPTIMIZATION OF THE LIPOSOME LIPID COMPOSITION

First, the choice of lipids used for the liposome preparation is important. Whilst the majority of lipids spontaneously form a preferred lipid bilayer structure when exposed to aqueous solution, some lipids are known to favour different phase arrangements (e.g., phosphatidylethanolamine (PE) arranges in hexagonal phase) (Sharom and Eckford 2003). The chemical characteristics of lipids have to be

considered (e.g., charge of the head group, length and unsaturation of the fatty acyl chains) as many human proteins are known to require the presence of specific lipids and/or cholesterol for activity (Sharom and Eckford 2003). Finally, identifying a suitable reconstitution protocol for incorporation of the target protein into the lipid bilayer is crucial to obtain functional activity. Each protein behaves differently, and suitable conditions must be identified empirically. The detergent used for lipid solubilisation should not disrupt the folded state of the protein, and the rate of detergent removal must be tuned to find the optimal conditions. At this stage, the protein can insert in the proteoliposome in two ways: with its extracellular side facing outwards or inwards. Finally, the ionic composition of the reconstitution system is important to retain the functionality of the protein (Sharom and Eckford 2003). As an initial experiment, membrane preparations overexpressing the protein of interest can be used to evaluate the protein activity. However, membrane preparations contain a range of proteins that might affect the experiment, such as endogenous expression of homologous proteins, or proteins that transport the same substrate, leading to complicated analysis of the results. Thus, it is desirable to work with proteoliposome reconstituted proteins. Initially, membrane preparations of EAAT3 expressed in mammalian or insect cells were tested for activity using the SURFE^{2}R system. Mammalian membrane vesicles with overexpressed EAAT3 produced robust signals in response to application of the substrate (1 mM glutamate), while membrane vesicles prepared with EAAT3 overexpressed in insect cells showed very low signal, not suitable for kinetic measurements (Figure 3.6). Admittedly, there was an extra point mutation in the insect-cell expressed EAAT3 construct compared to the mammalian EAAT3 construct, however, its position within a flexible extracellular loop at a not conserved position suggested it might not affect the function of the protein. In both cases, control membranes prepared from uninfected cells showed no signal in response to substrate application.

One of the possible explanations for the observed differences in the activity of EAAT3 could be owing to the differences in the lipid composition of the mammalian and insect cell membranes. The main differences in the lipid composition in insect cell lines versus cultured mammalian cells include higher content of PE and phosphatidylinositol (PI) and the lack of glyco- and sphingolipids (Marheineke, Grunewald et al. 1998). The most noticeable difference is in the cholesterol content, with mammalian cells having about 10 times higher cholesterol to phospholipid ratios compared to insect cells (Gimpl, Klein et al. 1995).

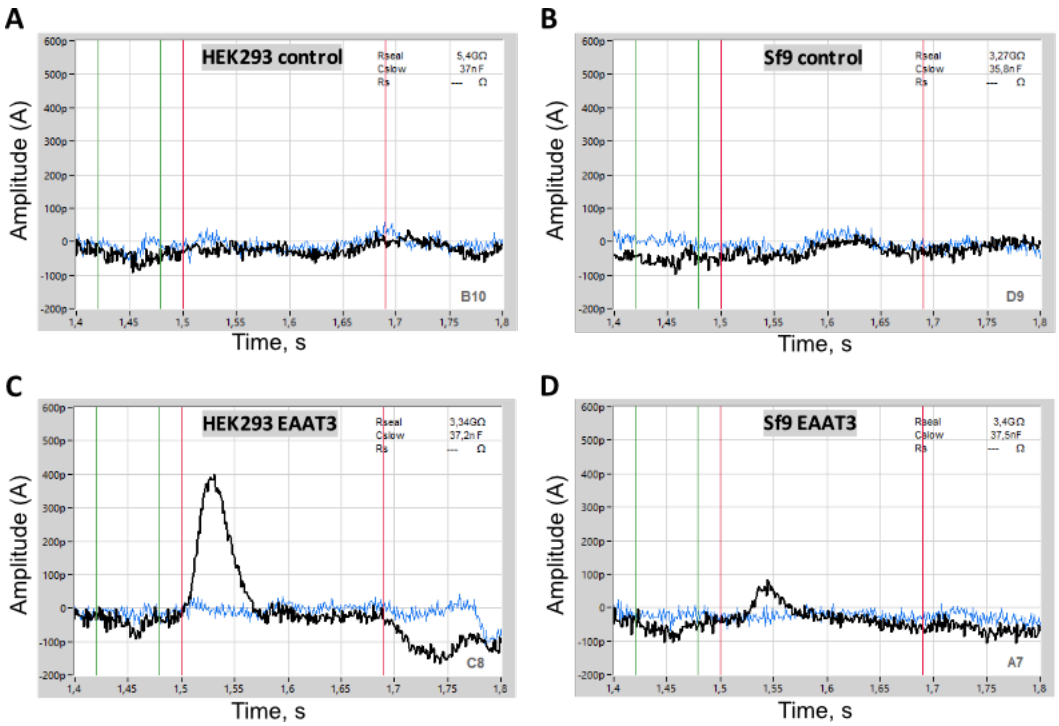


Figure 3.6: SURFE^{2}R measurements for membrane preparations of EAAT3 overexpressed in mammalian or insect cell systems. Raw data traces for control (**A, B**) membranes and EAAT3 overexpressing membranes (**C, D**). Blue traces show responses to non-activating solution, black lines show responses to activating solution (non-activating solution with 1 mM glutamate), the two red lines indicate where the signal in response to substrate application is expected. Screenshots provided by A.P. (Sanofi).

Based on these observations, I tested different lipid mixes to identify conditions that would maintain the functionality of EAAT3. I tested the mix of two synthetic lipids 1-Palmitoyl-2-oleoyl- PC (POPC) : 1-Palmitoyl-2-oleoyl- PE (POPE), 3:1 (w:w), the 2 most common lipids in mammalian plasma membranes (van Meer and de Kroon 2011). The ratio is based on the soybean phospholipid mixture (asolectin) composition, which is commonly used for the reconstitution of membrane proteins, taking into account that PE should make up less than 70% (by weight) for proper bilayer formation (Sharom and Eckford 2003). The use of synthetic lipids mimics the natural phospholipids while providing the highest purity and reproducibility (Sharom and Eckford 2003).

3.2.1.3 Optimization of EAAT3 reconstitution in liposomes

The proteoliposome reconstitution method may affect the protein activity, as the protein has to insert into the membrane during this process. The most commonly used technique involves detergent removal from a solution with detergent solubilised protein in the presence of lipids (Figure 3.5). The removal

of the detergent causes the lipids to assemble in bilayer assemblies (Figure 3.5 C). The removal step can be done quickly or incrementally, with some proteins tolerating only one to retain activity (e.g., only fast detergent removal yields active reconstituted protein). Detergent removal can be done in multiple ways: using absorbent, porous beads (biobeads) that bind detergents with high capacity, by rapid dilution or dialysis (Sharom and Eckford 2003). In all cases the detergent concentration must be below its critical micelle concentration (CMC). At concentrations below the CMC, detergent molecules exist as monomers in a solution, but when the CMC is reached, they assemble into micelles. Detergents can only solubilise lipids at concentrations higher than their CMC. Different types of detergent have very different CMC values ranging from µM to mM, with mM ones being easier to remove (Sharom and Eckford 2003). The characteristics of detergents I used during proteoliposome reconstitution optimisation process are listed in Table 3.1.

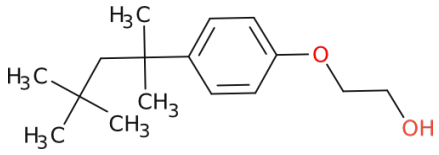
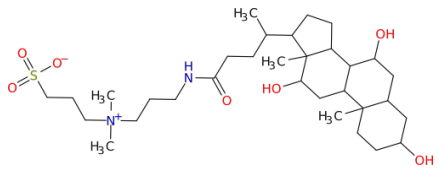
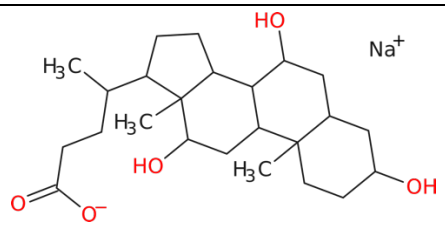
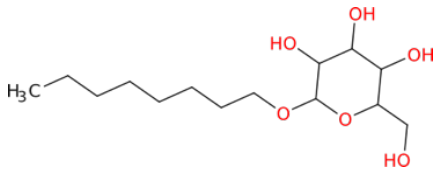
Detergent	2D representation	CMC (mM)	Charge
Triton-X100		0.2	Nonionic
CHAPS		8-10	Zwitterionic
Sodium Cholate		9-15	Anionic
ß-Octyl Glucoside		23-25	Nonionic

Table 3.1. The properties of the detergents used for proteoliposome reconstitution. CMC - critical micelle concentration.

For the reconstitution process, preformed liposomes are destabilised by detergent addition to make the bilayer "leaky" and aid the protein incorporation. Three stages of liposome solubilisation can be

identified by following the optical density at 540 nm (OD_{540}) while titrating the detergent of choice (Figure 3.7).

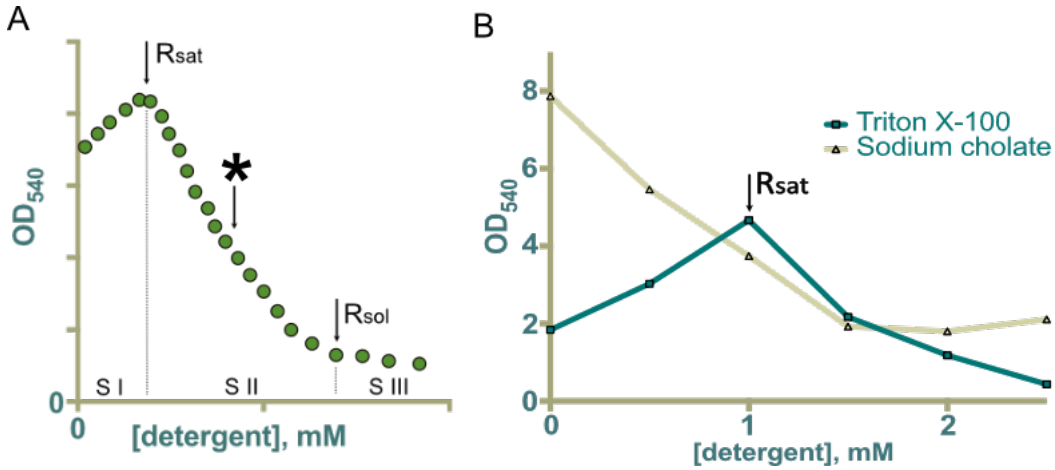


Figure 3.7: Titrations of preformed liposomes with detergent. **A** Theory of the detergent solubilisation of preformed liposomes. The initial stage (S I) or liposome swelling continues until the liposomes are saturated with the detergent (R_{sat}). The second stage (S II) represents detergent solubilisation of the liposomes. The protein incorporation in liposomes is the most efficient at the point indicated by an asterisk. The final stage (S III) is reached, when the lowest reading of OD_{540} is observed (R_{sol}). Adapted from (Knol 1999, Geertsma, Nik Mahmood et al. 2008). **B** POPC:POPE liposome titrations in the presence of different detergents. Preformed liposomes (POPC:POPE, 3:1 wt:wt) at 4 mg/ml were titrated with Triton X-100 or Sodium cholate and the OD_{540} values recorded. Defined R_{sat} point was only obtained with Triton X-100 titrated liposomes. The different starting points are most likely the result of an initial sample dilution (pipetting error).

During the initial stage, the detergent molecules insert in the bilayer of the liposomes, causing swelling and increased turbidity as indicated by the increase in OD_{540} value. Once the liposomes are saturated with the detergent (R_{sat}), the next stage starts, where detergent solubilisation of the liposomes occur. The protein incorporation in liposomes is the most efficient just after R_{sat} value. Final stage is reached, when the lowest reading of OD_{540} is observed (R_{sol}) and the liposomes are assumed to be fully solubilised and present as a mixture of detergent/lipid micelles of various compositions (Knol 1999, Geertsma, Nik Mahmood et al. 2008).

Detergents have different effects on the liposome structure and at different concentrations result in a formation of a variety of bilayer structures, which incorporate proteins in different manners. It has been reported that Triton X-100 mediates unidirectional protein incorporation due to the maintenance of intact liposome structures even at high detergent concentrations, while DDM disrupts lipid vesicles

into bilayer sheets, which in turn promoted random protein incorporation (Knol 1999). Since EAAT3 can function reversibly, unidirectional protein incorporation is preferred as the substrate affinity for the binding sites on either side of the membrane are markedly different, resulting in different transport kinetics (Zhang, Tao et al. 2007). The initial POPC:POPE liposomes were titrated with multiple detergents (sodium cholate, Triton X-100, OGNG/CHS) to identify conditions suitable for reconstitution. Only in the presence of Triton X-100, a distinct maximum (R_{sat}) was observed (Figure 3.7 B), while sodium cholate and OGNG/CHS had no distinct peak. Therefore, a protocol reported for reconstitution of ABC transporters was followed, and 2 mM Triton X-100 was used for preformed liposome solubilisation as determined for the lipid mix used here (Geertsma, Nik Mahmood et al. 2008).

Since the signal observed on the SURFE^{2}R system is related to the amount of active protein present, different LPRs were tested (10:1 and 50:1) but no activity was observed. Based on the observation that EAAT3 expressed in mammalian cells was functional while little activity was seen for the insect-cell expressed protein, I hypothesised that cholesterol might be required for the protein activity. Next, I tested cholesterol dependency by adding 5% or 10% cholesterol to the POPC: POPE lipid mix and also used EAAT3 purified from mammalian cells to see if it retained activity. In addition, I tested different LPRs (up to 5:1) as EAATs are known to have relatively slow turnover rates (EAAT3 is the fastest within the SLC1A family with turnover in the millisecond range (Malik and Willnow 2019)). Tests on SURFE^{2}R system performed by A.P. showed that these alterations did not result in detectable EAAT3 activity.

Based on these results, I hypothesised that EAAT3 required a particular lipid environment to retain its activity, since it had been shown previously EAAT3 activity is increased in the presence of cholesterol (Shouffani and Kanner 1990). I tested natural lipid mixes reported previously in the literature used for reconstitution of EAAT3 or the human homologue ASCT2 (Kavanaugh, Bendahan et al. 1997, Pingitore, Pochini et al. 2013, Garaeva, Oostergetel et al. 2018, Yu, Plotnikova et al. 2019). Similarly, different detergents (CHAPS, sodium cholate) used for liposome solubilisation were tested, since the exposure to denaturing detergents could be the cause of inactivation of the protein during reconstitution. Some transient currents were observed on the SURFE^{2}R with proteoliposomes made following previous EAAT3 reconstitution protocol with minor adaptions (Kavanaugh, Bendahan et al.

1997). However similar currents were observed with control empty liposomes, indicating that the vesicles were leaky to ions and passive diffusion of ions across the lipid bilayer of liposomes lead to the observed signals. The summary of the tested conditions is shown in Table 3.2.

Sample	Lipid composition	LPR (w/w)	Signal on SURFE^{2}R
EAAT3-c102	POPC:POPE 3:1	50:1	No
EAAT3-c102	POPC:POPE 3:1	10:1	No
EAAT3-c004	POPC:POPE:Cholestrol 3:1:10%	10:1	No
EAAT3-c004	POPC:POPE:Cholestrol 3:1:5%	10:1	No
EAAT3-c102	POPC:POPE:Cholestrol 3:1:10%	10:1	No
EAAT3-c102	POPC:POPE:Cholestrol 3:1:5%	10:1	No
EAAT3-c102	Asolectin:BrainLipidExtract:Cholesterol 24:4:5%	50:1	Yes
EAAT3-c004	Asolectin:BrainLipidExtract:Cholesterol 24:4:5%	50:1	Yes
EAAT3-c004	Asolectin:BrainLipidPolar:Cholesterol 24:4:5%	50:1	Yes
EAAT3-c004	EggPC:BrainLipidPolar:Cholesterol	50:1	Yes
EAAT3-c102	Asolectin:BrainLipidPolar:Cholesterol 24:4:5%	12:1	Yes
EAAT3-c004	Asolectin:BrainLipidPolar:Cholesterol 24:4:5%	12:1	Yes
empty	Asolectin:BrainLipidPolar:Cholesterol 24:4:5%	-	Yes

Table 3.2: Summary of EAAT3 proteoliposome optimisation. EAAT3-c102 – EAAT3 overexpressed in *Sf9* cells (purple shade), EAAT3-c004 – EAAT3 overexpressed in HEK293 cells (green shade). LPR – lipid to protein ratio.

The protocol that resulted in reconstitution of active EAAT3 was the one adapted from a method provided by our collaborators at Sanofi. Antje Pommereau (A.P.) at Sanofi identified *E. coli* total lipid extract as a good host lipid for EAAT3, in combination with ß-OG as the solubilisation detergent. The initial measurements were not very reproducible, so I decided to replace the *E. coli* total lipid extract with *E. coli* polar lipid extract, which, in contrast to the total lipid extract, is a defined lipid mix with no impurities. With *E. coli* polar lipid extract, we obtained transient currents in response to substrate

application, these currents were not easy to reproduce, and the amplitude was not as high as seen with membrane vesicles. A.P. determined that only when the proteoliposomes were extruded through 100 nm mesh membrane, as opposed to 400 nm in the final step, then the proteoliposomes gave reproducible results of a sufficient amplitude. This result could be explained by a larger number of small vesicles being able to adsorb on the same sensor area compared to the larger, 400 nm ones, resulting in a better SNR.

In summary, functional EAAT3 was reconstituted in proteoliposomes and the activity was confirmed using the SURFE^{2}R system. This work was a collaboration between the author of this thesis and A.P. at Sanofi. We found that optimisation of all the steps in the proteoliposome reconstitution protocol was necessary before reproducible signals corresponding to charge movement across the membrane was observed. These results indicated that our EAAT3 samples were active, giving a signal arising from ion co-transport with substrate.

3.2.1.4 CHARACTERISATION OF EAAT3 SUBSTRATE TRANSPORT USING THE SURFE^{2}R SYSTEM

Once the EAAT3 reconstitution protocol was established, the substrate affinity could be determined. The measurements were performed by A.P. at Sanofi, since I was unable to perform the measurements myself due to Covid-19 pandemic. However, the experiments were designed by me and A.P. First, the protein and sodium dependencies were determined to identify optimal conditions for the subsequent measurements (Figure 3.8 A, B). To start with, the amount of protein per well that gives the highest response was identified, as the signal amplitude is dependent on the sensor coverage. If the coverage is too dense, the solution exchange is not as efficient, resulting in lower observed signal amplitude. Different amounts of protein per well were tested in the presence of 1 mM glutamate and we found that 100 ng of protein per well give the highest signal (Figure 3.8 A). Similarly, a range of sodium concentrations were tested in the presence of 100 ng/ well protein and 1 mM glutamate where 140 mM Na^+ gave the highest signal amplitude (Figure 3.8 B). Since this is the physiological concentration of sodium ions, higher concentrations were not tested.

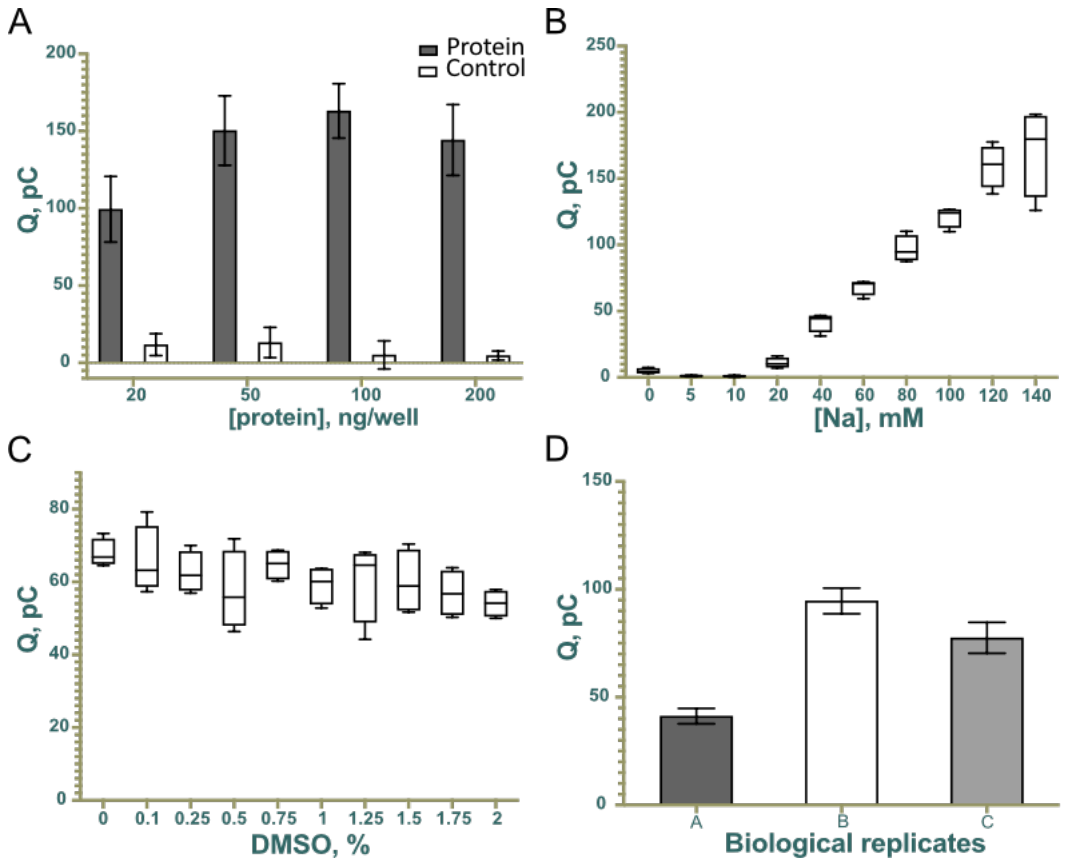


Figure 3.8: Optimisation of SURFE^{2}R set up and measurement quality control. **A** Protein dependency. Error bars represent mean ±SD, n=8 **B** Sodium dependency. Error bars represent mean ±SD, n=4 **C** DMSO dependency. Error bars represent mean ±SD, n=4 **D** Repeated measurement stability test. Error bars represent mean ±SD, n=7 Q – the charge proportional to the membrane voltage. Data was kindly provided by A.P. (Sanofi). Data was plotted in Prism 8 GraphPad software.

After identifying the optimal conditions for the measurements, the specific affinities for all the substrates (L/D-aspartate, L-glutamate and L-cysteine) were measured using a concentration range of the substrates between 1.6 and 400 µM (L/D-aspartate) and between 1.6 and 1000 µM for (L/D-glutamate). L-cysteine gave only artefact signals, so it was not possible to measure the K_M for L-cysteine on the SURFE^{2}R. Difficulties working with cysteine have been observed previously (A.P., unpublished results) and it has been suggested that since the sensors are prepared with a thiol layer underneath a lipid layer, it could result in a cross-reaction between the thiol group in L-cysteine and the sensor. As controls, D-glutamate, L-/D-serine were tested and none produced any signals (Figure 3.9).

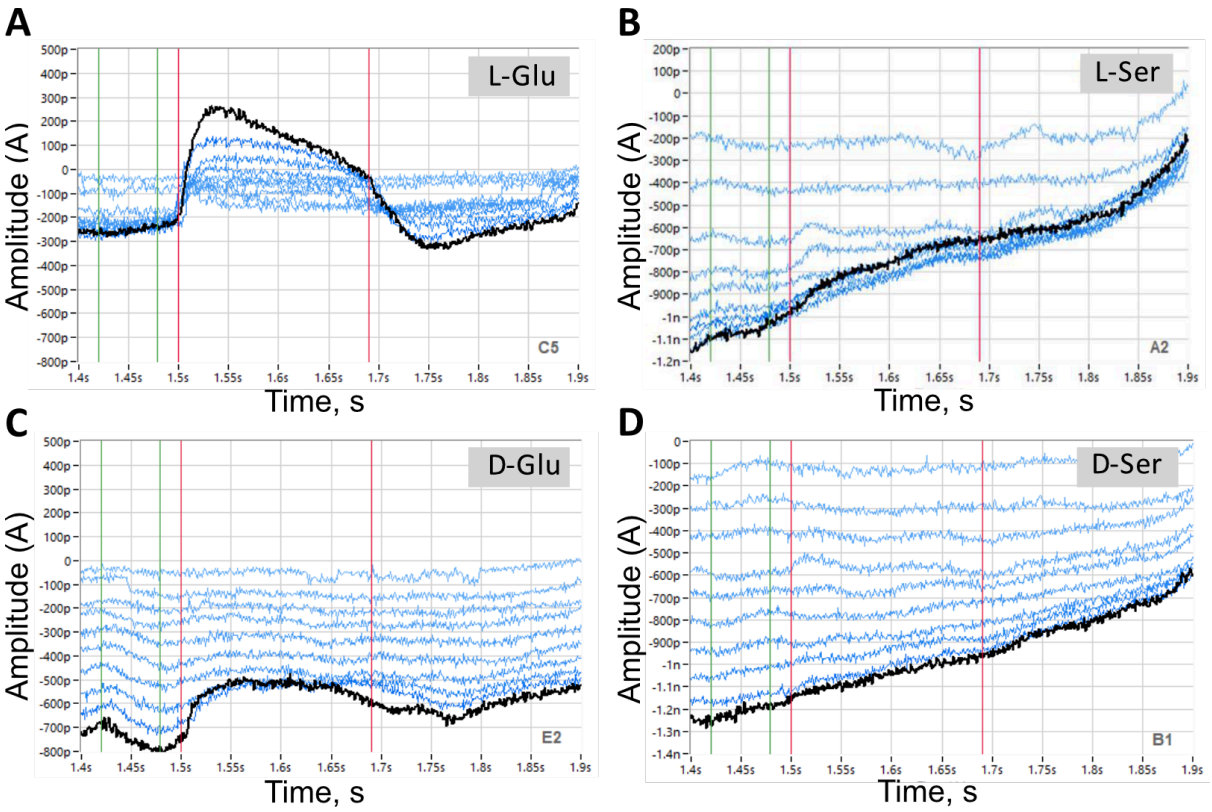


Figure 3.9: Substrate selectivity of EAAT3 reconstituted in proteoliposomes. Raw data traces of the substrate (**A**) and control amino acids (**B-D**) measured on the SURFE^{2}R. Traces of amino acids at increasing concentrations (1 µM – 1 mM) are shown as blue lines, with the highest concentration shown in black. Amino acids that are transported by EAAT3 produce concentration-dependent signals, while non-transported amino acids do not produce measurable signals. L-Glu – L-glutamate, L-Ser – L-serine, D-Glu – D-glutamate, D-Ser – D-serine. Screenshots provided by A.P. (Sanofi).

The kinetics of the EAAT3 substrate transport is shown in Figure 3.10. Data was normalised before averaging to the highest substrate concentration and the rest of the measurements expressed as a ratio. The averaged data points were analysed by nonlinear regression and fitted to the Michaelis-Menten equation. L-aspartate showed the highest affinity (7.2 µM), followed by D-aspartate and L-glutamate (9.8 µM and 23.5 µM, respectively). This can be seen as a shift to the right of the curves in Figure 3.10. It has been reported that D-glutamate is not transported by EAAT3 and had no detectable affinity (Arriza, Fairman et al. 1994). We therefore used it as a negative control for the substrate isomer selectivity and, as expected, it gave no measurable signal. Unlike the other substrates, L-aspartate was saturated at 400 µM substrate concentrations, so it was possible to calculate a more accurate K_M. For the other substrates, the calculated affinity is an approximation, as the binding should be saturated at 10x K_M value. The lack of saturation indicates that the transport did not follow standard Michaelis–

Menten kinetics, most likely due to the presence of transporters in both inward and outward-facing orientations. Since substrate transport can occur in both directions, as long as Na^+/K^+ gradients exist and substrate is applied from the high [Na^+] side (Watzke, Rauen et al. 2000), it is likely that both forward and reverse transport events were being measured simultaneously. It has been reported that the cytoplasmic substrate binding site has lower affinity for the substrate compared to the extracellular binding site (for glutamate applied to the extracellular surface at pH 7.4 the K_M was 5.9 ± 1.3 µM, whereas for glutamate applied to the intracellular surface, the K_M was 280 ± 30 µM (Watzke, Rauen et al. 2000)). This would result in a mixed readout for a system where the protein can be in either orientation. V_{max} values cannot be determined from this assay as the exact amount of active protein per well is not known.

These results agree to within at least a factor of 5 with the previous reports for EAAT3 and its mouse homologue, EAAC1, as measured using membrane vesicles of unpurified protein on the SURFE^{2}R (Table 3.3).

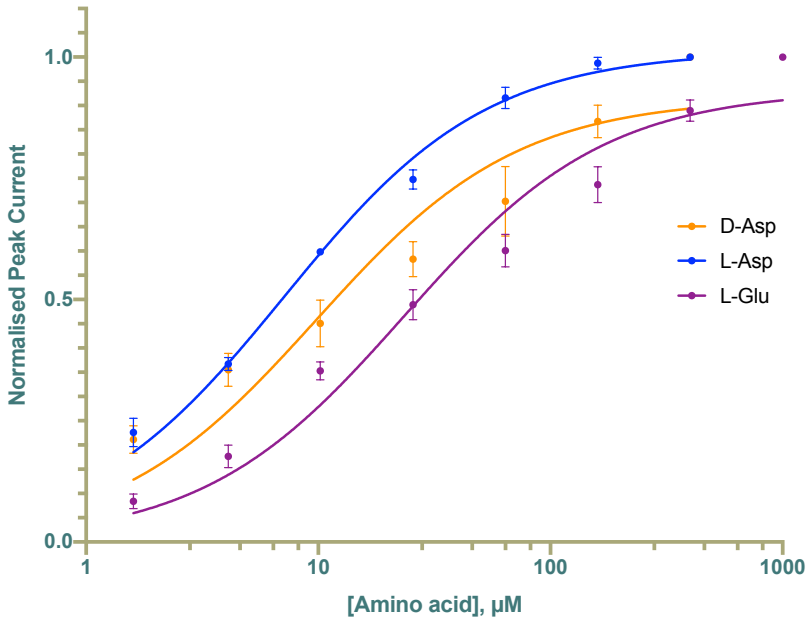


Figure 3.10. EAAT3 substrate affinity determination using the SURFE^{2}R. Plots of the normalised current at a range of substrate concentrations are shown. All experiments were done with 3 biological replicates in 5-8 technical repeats. All error bars represent mean ± SD. Data was normalised and Michaelis-Menten equation fitted using non-linear regression analysis in Prism 8 GraphPad software. Data was collected by A.P. (Sanofi).

Substrate	EAAT3	mEAAC1 (CHO)	EAAT3 (COS-7)	EAAT3 (HEK293)
L-Glutamate	23.5±3.0 μM	24 μM	62 ± 8 μM	42 ± 13 μM
L-Aspartate	7.2±0.4 μM	5 μM	ND	ND
D-Glutamate	> 500 μM	N/D	ND	ND
D-Aspartate	9.8±1.6 μM	N/D	47 ± 9 μM	14 ± 5 μM

Table 3.3: Measured EAAT3 substrate affinities. The affinities for L/D-aspartate and L/D-glutamate for EAAT3 reconstituted in proteoliposomes were measured using SURFE^{2}R system (data collected by A.P. (Sanofi)). The results are comparable to values obtained for a murine homologue (mEAAC1) membrane preparations from CHO cells (Krause, Watzke et al. 2009), transiently-expressed in COS-7 cells (Arriza, Fairman et al. 1994), and HEK293 stable-cell line (Jensen and Brauner-Osborne 2004).

3.2.1.5 PHARMACOLOGICAL CHARACTERISATION OF EAAT3 USING THE SURFE^{2}R SYSTEM

Next, the IC_{50} values of two inhibitors (TFB-TBOA and ±HIP-B) used for the structural studies were determined. As TFB-TBOA is prepared in DMSO, the effect of DMSO on EAAT3 activity was tested and concentrations of up to 2% were shown to be well tolerated (Figure 3.8 C). For the inhibitor measurements, multiple activations per well were tested to check the stability of the signal, as this is important for the measurements with multiple compounds and the signal amplitude was not lost over multiple activations (Figure 3.8 D). Inhibition of EAAT3 by the available compounds was assessed using a similar assay to the one described for the substrate kinetics, with a fixed glutamate concentration (30 or 300 μM, selected based on the previously determined K_M for glutamate at 1x and 10x K_M) and varying inhibitor concentrations (between 0.19 to 100 μM) to determine their potency and specificity. Data was normalised and the averaged data points analysed by nonlinear regression and fitted to the dose-response equation to determine IC_{50} values (Figure 3.11).

IC_{50} is a substrate concentration-dependent value, and inhibitor modality can be determined from the dependence of IC_{50} values on substrate concentration (Figure 3.2). In this work we only determined the effects at two substrate concentrations, so the results are preliminary. The available data is consistent with, ±HIP-B being a competitive inhibitor, with IC_{50} = 5.7±1.1 μM in the presence of 30 μM L-glutamate, while IC_{50} could not be determined in the presence of 300 μM L-glutamate. TFB-TBOA, a supposedly competitive inhibitor, had IC_{50} = 0.9±0.2 μM at 30 μM L-glutamate and an IC_{50} = 0.5±0.1 at 300 μM L-glutamate, suggesting non-competitive inhibition. Overall, the IC_{50} values for

TFB-TBOA and ±HIP-B in the presence of 30 µM glutamate would tend to suggest that TFB-TBOA is a more potent EAAT3 glutamate transport inhibitor than ±HIP-B.

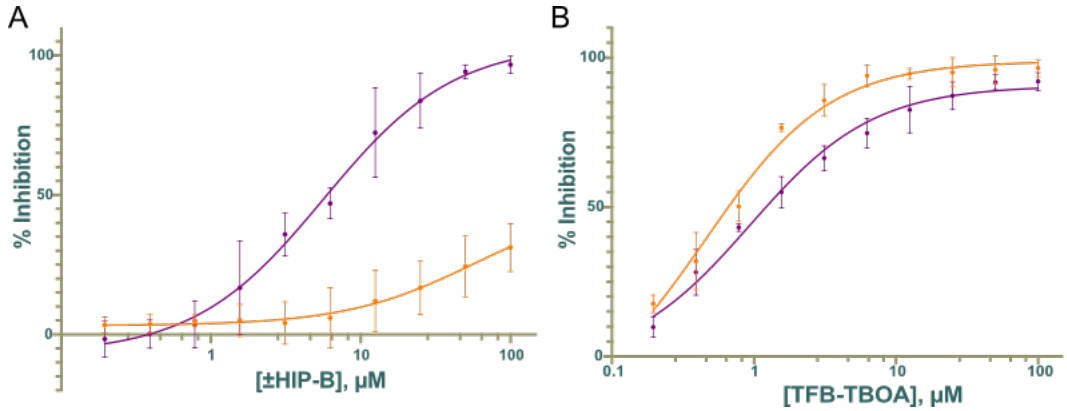


Figure 3.11. Dose-response curves for EAAT3 inhibitors measured using the SURFE^{2}R system. Glutamate transport inhibition was measured in the presence of 30 µM glutamate (magenta line) or 300 µM glutamate (orange line) **A** Glutamate transport inhibition by ±HIP-B and **B** by TFB-TBOA. Data points represent mean ±SD for three biological replicates in 5-8 technical repeats. IC_{50} values were calculated by fitting the normalised data to an equation Y=100/(1+X/IC50) in Prism 8 GraphPad software. Data was collected by A.P. (Sanofi).

While the measured IC_{50} values for the inhibitors correlate with the previously reported values measured for EAAT3 overexpressed in heterologous systems in the presence of low glutamate concentrations (Table 3.4), the mode of interaction observed here is the opposite of previously reported. Both inhibitors are substrate analogues and would be expected to behave as competitive inhibitors. Yet, ±HIP-B was previously reported not to exhibit purely competitive inhibition (Callender, Gameiro et al. 2012). The observed non-competitive mode of interaction for TFB-TBOA might suggests it is a tight binder, since only initial binding events are measured on the SURFE^{2}R. TFB-TBOA has been reported to exhibit tight binding in previous studies (Shimamoto, Sakai et al. 2004).

	EAAT3[a]		**EAAC1[b]**		**EAAC1[c]**		**EAAT3[d]**	
	IC_{50} (µM)	[Glu] µM	IC_{50} (µM)	[Glu] µM	IC_{50} (µM)	[Glu] µM	IC_{50} (µM)	[Glu] µM
±HIP-B	5.7	30	8.7	20	7.5	15		-
	NA	300	9.2	100	13.2	100		-
TFB-TBOA	0.9	30	-	-	-	-	0.03	1*
	0.5	300	-	-	-	-	0.3	1**

Table 3.4: Measured IC_{50} values for EAAT3 inhibitors ±HIP-B and TFB-TBOA. a – $SURFE^2R$ measurements from this work, b – transiently transfected HEK 293T cells expressing EAAT3 (Callender, Gameiro et al. 2012), c – murine homologue (mEAAC1) membrane preparations from CHO cells (Krause, Watzke et al. 2009); d – EAAT3 stably expressed in MDCK cell line (*) or transiently transfected in COS-1 cell line (**)(Shimamoto, Sakai et al. 2004).

3.3 OPTIMISATION OF RADIOLABELLED SUBSTRATE UPTAKE ASSAY FOR EAAT3 FUNCTIONAL CHARACTERISATION

3.3.1 RADIOLIGAND UPTAKE ASSAY

Direct measurements of transported substrate are commonly used to characterise the kinetics of transporters. In cases where the substrate can be labelled with an isotope, radiolabelled ligand uptake assays provide a highly sensitive method with a direct readout for the amount of substrate translocated. Radiolabelled substrate uptake assay involves incubation of the transporter (either expressed in cells or reconstituted in proteoliposomes) with varying concentrations of radiolabelled ("hot") substrate. The radiolabelled substrate uptake is terminated after specified time period by a rapid removal of the radiolabelled ligand. This is usually achieved by filtration or centrifugation to separate the cells/proteoliposomes with incorporated radiolabelled substrate from the free radiolabelled substrate. The total radioactivity, which includes both specific and non-specifically bound substrate, can then be determined using liquid scintillation counting. For the uptake assays, non-specific substrate uptake must be taken into account due to the non-specific ligand binding to the liposomes and/or filter membrane. A control experiment with liposomes is performed in parallel to identify the amount of non-specific binding of substrate to liposomes, which is then subtracted from the raw data of the total substrate detected in the presence of the transporter. The results are presented as a relationship between the rate of reaction and the substrate concentration, defined by the Michaelis-Menten equation.

3.3.2 PRELIMINARY RESULTS OF EAAT3 PHARMACOLOGICAL CHARACTERISATION USING RADIOLIGAND UPTAKE ASSAY

After identification of a proteoliposome reconstitution protocol that produced functionally active EAAT3, I performed radiolabelled ligand uptake assays for the glutamate and dose-response assay for TFB-TBOA and ±HIP-B.

I optimised the assay set up and verified it by performing a time course experiment at a single glutamate concentration. For this, I did five time points (at 2, 5, 8, 15 and 40 min) with control liposomes tested in parallel. The glutamate concentration used in initial assays was based on the standard curve produced for the ^{3}H-glutamate (Figure 3.12). Assuming only 5% incorporation of the "hot" ligand during the substrate uptake assay, the measured counts per minute (CPM), detected by the scintillation counter, would be ~ 40,000. The final concentration used was 11 µM (10 µM glutamate + 1 µM ^{3}H-glutamate).

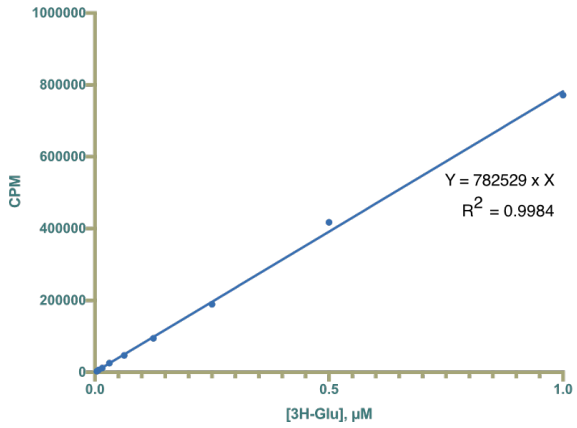


Figure 3.12: The standard curve for ^{3}H-L-Glutamate.

The ratio between "hot" and "cold" (not radiolabelled) ligand was chosen based on literature, where ratios up to 1:40 were used for proteoliposome-reconstituted EAAT1 assays (Canul-Tec, Assal et al. 2017). The assay was performed as described in Materials and Methods. The data was analysed as described previously (Aggarwal and Mortensen 2017), and plotted as pmol/min/µg protein against increasing concentrations of L-glutamate. The data analysis was performed in GraphPad Prism by fitting the data to a Michaelis-Menten equation using nonlinear regression analysis to determine K_M and V_{max}. Briefly, the raw data (in counts per minute, CPM) for the control liposomes (non-specific uptake) was averaged and then subtracted from the total counts measured for the proteoliposome samples to obtain the specific counts. The counter efficiency was determined by measuring known amount of the radioligand (2 µL) with known disintegrations per minute (DPM) value for the isotope (^{3}H; 4 440 000 dpm per 2 µL) and following the formula:

$$counter\ efficiency\ (\%) = \frac{CPM}{DPM}\ X\ 100$$

This was identified as ~39%. To obtain the values in DPM, the specific counts were divided by the counter efficiency. Next, the DPM was converted to Curies (Ci) (1μCi = 2.2 × 10^6 DPM) To convert from Ci to millimoles, the values were divided by the specific activity of the radioligand. To account for the "hot" ligand dilution, the specific activity value was divided by the dilution factor used. Finally, the values per minute were calculated by dividing by the time point used (5 min). As 1 μg protein was used per assay, no further calculations were required.

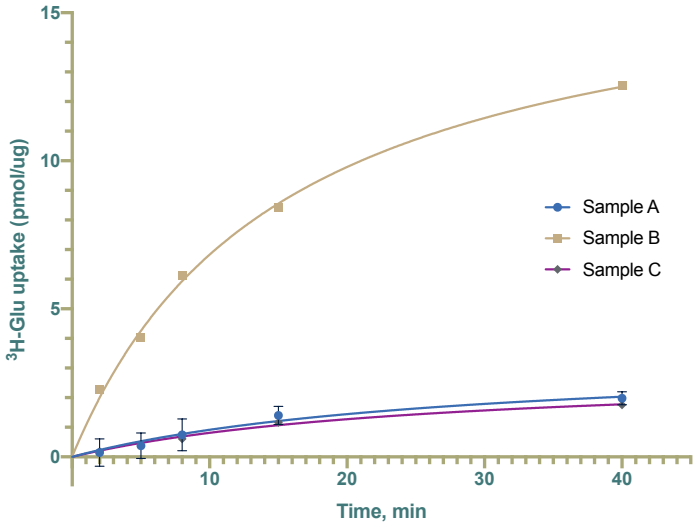


Figure 3.13: Time course uptake assay at a single ^{3}H-Glu concentration. 3 biological replicates were tested (A-C), with 3 technical repeats performed for Sample A (B, C is a single technical repeat). For Sample A, the mean of three biological replicates is plotted with SD as error bars. Background signal subtracted, fitted Michaelis-Menten equation using nonlinear regression analysis in Prism 8 GraphPad software.

As shown in Figure 3.13, there was considerable variability in protein activity with different proteoliposome preparations. The differences between total glutamate uptake after 40 min varied by up to 6 times. The reasons behind such variability could be that there were variations in EAAT3 activity between different preparations, or that lower fraction of the protein in the liposomes was active. Nevertheless, these results proved that the protein was active and I attempted to characterise the transport kinetics. For this, ^{3}H-Glu uptake must be measured in the presence of increasing glutamate concentrations. Those were chosen as 3, 10, 30, 60, 150 and 300 μM (final concentration including both "hot" and "cold" glutamate), assuming the K_M is ~ 30 μM, to cover the 0.1 – 10x K_M range. From the initial time course experiments, it was decided to terminate the uptake after 5 min as this should provide high enough readings to distinguish signal from noise while the uptake reaction is still in the

linear range. Due to the limitations imposed by the low concentration of the radiolabelled glutamate stock (21 µM), I decided to use two dilution factors (10 and 30), as previous results suggested dilutions as high as 1:40 for "hot":"cold" ligand ratio did not affect the measurable transport for EAAT1 (Canul-Tec, Assal et al. 2017). Therefore, for glutamate concentrations of 3, 10 and 30 µM, a dilution factor of 10 was used for "hot" ligand, while a dilution factor of 30 were used for the 60, 150 and 300 µM glutamate concentrations.

While measurements at lower total glutamate concentration (up to 30 µM) were stable for total radioactivity, the readings for higher glutamate concentrations (≥60 µM) became erratic. The counts for control liposomes were inconsistent for technical repeats, with variations in the readings of up to 10-fold. The cause of such behaviour could not be identified and remained unsolved. While similar behaviour was observed with proteoliposomes in the presence of higher glutamate concentrations, the consistent readings in the presence of low glutamate concentrations between different proteoliposome batches ruled out inconsistencies in buffer preparation as the cause of such behaviour. The observed readings could have been caused by the scintillation counter malfunctioning. However, after engineer visit and the detector normalisation, it was clear that the scintillation counter was not the source of the inconsistencies. Different liquid scintillation fluids were tested to see if the problem was caused by inefficient dissolution of the sample, which would affect the sample uptake capacity of the fluid and result in inaccurate readings. However, the issue persisted with different liquid scintillation fluids tested.

To verify the activity observed in the presence of glutamate was due to EAAT3 activity, I tested the effect of TFB-TBOA and ±HIP-B. Ideally, substrate concentration at its K_M value is used but as the assay was not consistent at higher L-glutamate concentrations, I used the initial conditions at lower glutamate concentration. Different inhibitor concentrations were titrated in the presence of 11 µM glutamate (1 µM "hot" and 10 µM "cold") and the reaction was terminated after 40 min as this is when the uptake reaction is saturated. For ±HIP-B, concentrations in the range of 1 to 100 µM were used, while for TFB-TBOA, the range of 0.1 to 10 µM were used, based on the IC_{50} values obtained from the SURFE^{2}R. The results of a single measurement from two biological replicates are shown in Figure 3.14. In both cases, addition of the lowest concentration of inhibitor caused a slight increase in glutamate transport when compared to the uptake of glutamate without any inhibitor added. The IC_{50}

value of 6.5 ± 3.8 µM for ±HIP-B was consistent with the IC_{50} values reported in the presence of low glutamate concentrations (Table 3.4). Unfortunately, for TFB-TBOA the lack of a plateau at the lowest inhibitor concentrations prevented calculation of an accurate IC_{50} value. More repeats of the experiment, covering a broader range of inhibitor concentrations would be required to determine the IC_{50} values more accurately. Unfortunately, I was prevented from completing these experiments by the Covid-19 lockdown.

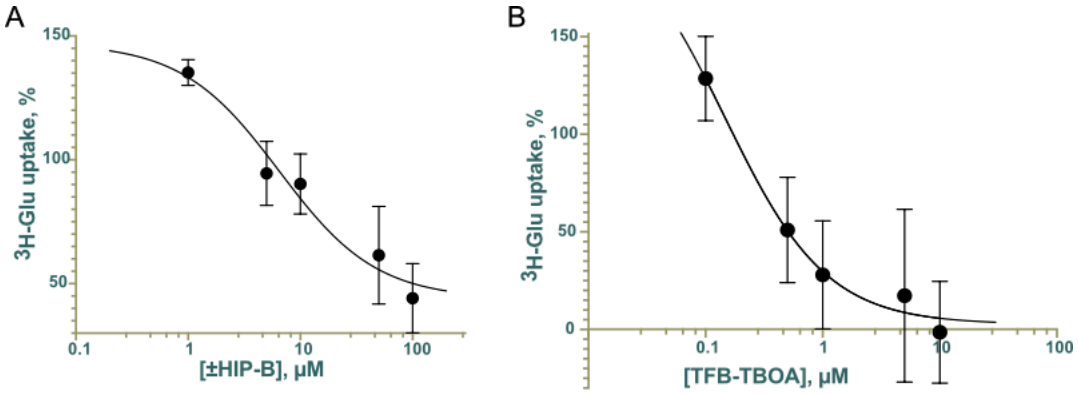


Figure 3.14: Dose-response curves for EAAT3 inhibitors measured using ^{3}H-glutamate uptake assay. Glutamate transport inhibition was measured in the presence of 11 µM glutamate **A** ^{3}H-glutamate transport inhibition by ±HIP-B and **B** by TFB-TBOA. Data points represent mean ±SD for two biological replicates in 1 technical repeat. IC_{50} values were calculated by fitting the normalised data to equation Y=100/(1+X/IC50) in Prism 8 GraphPad software.

3.4 COMPARISON OF THE TWO METHODS USED TO CHARACTERISE EAAT3 TRANSPORT ACTIVITY

The transport kinetics of EAAT3 substrates and inhibitors are presented here, determined from *in vitro* assays. The measured substrate affinities are in the low micromolar range and are comparable to results reported from studies in cells, suggesting the EAAT3 construct used here had retained its full transport activity. The use of reconstituted protein in proteoliposomes has advantages in screening for potential inhibitors, since only the protein of interest is present. Two types of kinetic measurements – direct and indirect – are described, that complement each other. While indirect, SSM-based electrophysiology measurements provide us with information on substrate affinity, inhibitor potency and the pharmacological properties of inhibitors (whether the inhibitors are transported or not, based on the presence or absence of transport currents, respectively), they have limitations. The information on the transport rates cannot be determined from the SURFE^{2}R measurements, as the amount of active protein

in each well is not easy to assess. EAAT3 is the only member in the family that can transport cysteine, and it was disappointing that the kinetic studies of cysteine cannot be performed on the SURFE^{2}R system. This is most likely due to cross-reactivity with the agents used to prepare the wells for sample adsorption.

As an alternative to the indirect electrophysiology measurements, direct functional assays such as radioligand uptake assay, could be performed to answer these questions. This technique would have the advantage that substrate transport is measured directly and the total concentration (although not the active fraction) of protein is each sample is a known. While I did not succeed in establishing the assay, promising initial conditions for further optimisation are presented.

3.5 SUMMARY OF THE FUNCTIONAL CHARACTERISATION OF EAAT3

I have presented the transport kinetics of EAAT3 investigated using direct and indirect measurement methods and characterised the binding of two inhibitors. Extensive optimisation was necessary to obtain active EAAT3 reconstituted in proteoliposomes. I investigated several factors that could have affected the activity of EAAT3 in the proteoliposomes. EAAT3 in different lipid environments showed clear differences in transport activity. When reconstituted in synthetic lipids, there was no transport activity observed, which was not rescued by the addition of cholesterol, previously reported to increase the transport activity of EAAT3 (Butchbach, Tian et al. 2004). An *E. coli* Polar lipid extract mixture was identified as a good host lipid composition that retained EAAT3 activity. This allowed functional characterisation of EAAT3 i*n vitro* using the SSM technology and a radiolabelled ligand uptake assay. SSM was used to determine the kinetic parameters of EAAT3 substrates as well as potency and specificity of two inhibitors (±HIP-B and TFB-TBOA). All the measured values are in agreement with previous reports of the activity of EAAT3 in cell membranes and membrane preparations. A radiolabelled ligand uptake assay was shown to work in principle, and preliminary data provided an estimate of the IC_{50} value for ±HIP-B which was similar to that obtained with the SURFE^{2}R assay, suggesting that this method is effective. However, further optimisation would be required to obtain reproducible measurements necessary to accurately determine the kinetic parameters and inhibition behaviour of the two inhibitors studied. This was not possible in the last year of my DPhil, due to the Covid-19 lockdown.

CHAPTER 4

4 EAAT3 STRUCTURES REVEAL NOVEL BINDING MODES FOR TWO INHIBITORS

4.1 INTRODUCTION

Despite extensive functional studies of mammalian glutamate transporters, there are only a few subtype selective inhibitors identified to date. This is mostly due to the cross-reactivity, as human EAATs share ~50% amino acid sequence identity, with higher similarity in the highly conserved substrate binding sites. While there are differences in substrate selectivity (e.g.., EAAT3 is the only EAAT that can transport cysteine), so far inhibitors that are substrate analogues have shown little selectivity towards glutamate transporter subtypes. Structure determination would provide us with information about the environment of the binding site as well as potential allosteric sites, which would allow targeted, subtype-specific ligand design.

In this chapter, I describe the determination of the structure of EAAT3 in complex with two inhibitors at 3.3 Å resolution, using cryo-EM. The structures reveal novel binding modes for the inhibitors and provide structural insights to their potency.

4.2 SAMPLE OPTIMISATION FOR STRUCTURAL STUDIES OF EAAT3 WITH BOUND INHIBITORS

4.2.1 SELECTION OF LIGANDS FOR STRUCTURAL STUDIES

EAATs show stereoselectivity for the transported substrates – only L-glutamate but both L- and D-forms of aspartate are transported. The affinity for all is similar, in low micromolar range, depending on the system and method used to determine the K_M (Danbolt 2001). While there are subtype-selective inhibitors for both EAAT1 and EAAT2 (more than 400-fold and 45-fold selectivity compared to EAAT3, respectively (Dunlop, McIlvain et al. 2005, Jensen, Erichsen et al. 2009)), up until recently there were none for EAAT3. A promising report of Imidazo[1,2- a]pyridine-3-amines showing ~35-fold selectivity for EAAT3 over EAAT1,2, and 4 was published where structure–activity relationship (SAR) study was verified in cell based assay (Wu, Bjorn-Yoshimoto et al. 2019). Overall, while some

of the reported compounds are more effective at inhibiting EAAT3, they do generally also inhibit other family members. The summary of IC_{50} values for the most potent commercially available EAAT3 inhibitors are shown in Table 4.1.

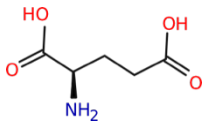
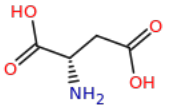
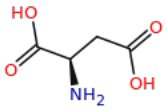
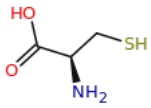
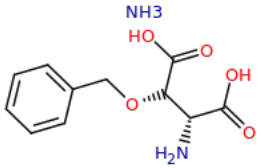
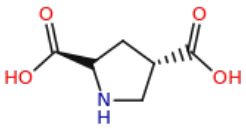
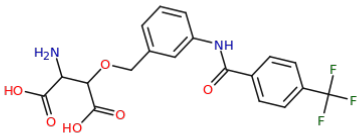
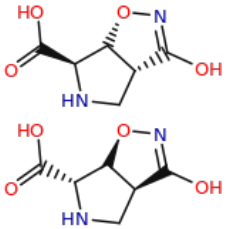
EAAT3 substrate	Chemical Structure	K_M (µM)	Reference
L-Glutamic acid		23.5	as described in Chapter 3
D-Aspartic acid		9.8	as described in Chapter 3
L-Aspartic acid		7.2	as described in Chapter 3
L-Cysteine		190	(Zerangue and Kavanaugh 1996)
EAAT3 inhibitor	**Chemical Structure**	**IC_{50} (µM)**	**Reference**
L-TBOA (ammonia salt)		7.0	(Shimamoto, Shigeri et al. 2000)
L-*trans*-2,4-PDC		1.5	(Koch, Kavanaugh et al. 1999)
TFB-TBOA		0.3	(Shimamoto, Sakai et al. 2004)
(±)-HIP-B	 -HIP-B +HIP-B	16.9	(Conti, Dallanoce et al. 1999)

Table 4.1: Overview of the chemical structures of EAAT3 substrates and substrate analogue inhibitors. L-TBOA - L-threo-β-Benzyloxyaspartic acid; L-PDC – L-trans-Pyrrolidine-2,4-dicarboxylic acid;

TFB-TBOA – (3S)-3-[[3-[[4-(Trifluoromethyl)benzoyl]amino]phenyl]methoxy]-L-aspartic acid; ±HIP-B – (±)-3-Hydroxy-4,5,6,6a-tetrahydro-3aH-pyrrolo[3,4-d]isoxazole-6-carboxylic acid.

In theory, to achieve the highest resolution possible for the protein-ligand complex, a homogeneous sample is preferred, where only one conformation of the protein is present. This allows for simpler calculations during cryo-EM structure determination as, in an ideal case, all the particles can contribute to the final reconstruction. In the case of oligomers, such as EAAT3, a conformationally homogeneous sample would allow symmetry to be imposed during data processing, which enforces strong signal while limiting noise and increases the effective particle number (have n-times more information for each subunit, were n – number of monomers). Heterogeneous samples require more extensive computation to correctly identify and reconstruct all the states but may reveal more about the mode of action of the protein. Such analysis requires a larger number of total particles, since essentially multiple models are solved from a single dataset. If there are insufficient number of particles for each conformation, the resolution is likely to be compromised.

Homogeneous sample can be achieved by use of ligands. To identify the ligands for structural studies of EAAT3, I used the increase in the melting temperature (T_M) as an indication of the ligand binding that resulted in protein with stabilised conformation. Changes in the T_M of EAAT3 in the presence of substrates or commercially available inhibitors were screened using nanoDSF. Since the K_M value for the ligands is reported to be in low μM range, in order to saturate the protein, the ligands were added at a minimum concentration of 10x K_M. To compare the results, the screening was performed at 2 mM for all the ligands (Figure 4.1).

L-aspartate stabilised detergent solubilised EAAT3 the most effectively among all the substrates tested, increasing the melting temperature by ~5˚C compared to the apo protein. Among the inhibitors, TFB-TBOA showed the highest EAAT3 stabilisation, increasing the T_M by almost 15˚C. Other inhibitors showed more modest effects, with a general trend of inhibitors with a lower IC_{50} value imposing greater thermostabilisation.

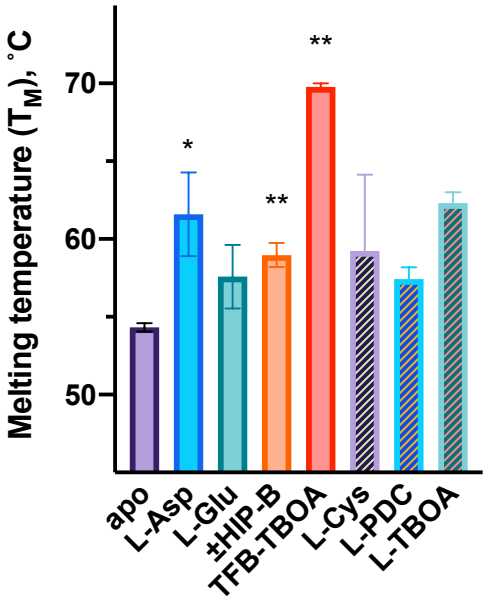


Figure 4.1: Thermostabilisation of EAAT3 by substrates and inhibitors. Measurements for three biological replicates (average from 3 technical repeats) are shown in solid colour; for two biological replicates (average from 3 technical repeats) are shown with a pattern. Error bars denote ±SD. ∗ indicates significance, t test $p < 0.01$, ∗∗ indicates significance, t test $p < 0.001$. Apo – EAAT3, L-Aspartate– L-aspartic acid, L-Glutamate – L-glutamic acid, L-Cys – L-cysteine, ±HIP-B – (±)-3-Hydroxy-4,5,6,6a-tetrahydro-3aH-pyrrolo[3,4-d]isoxazole-6-carboxylic acid, TFB-TBOA – (3S)-3-[[3-[[4-(Trifluoromethyl)benzoyl]amino]phenyl]methoxy]-L-aspartic acid, L-PDC – L-trans-Pyrrolidine-2,4-dicarboxylic acid, L-TBOA - L-threo-β-Benzyloxyaspartic acid. Data were analysed and plotted using Prism 8 GraphPad software.

Based on these results, TFB-TBOA (a competitive inhibitor (Tsukada, Iino et al. 2005)) and ±HIP-B (a non-competitive inhibitor (Colleoni, Jensen et al. 2008)) were selected for structural studies. TFB-TBOA is an L-aspartate analogue while ±HIP-B is a constrained glutamate analogue and, based on their structural characteristics, both are expected to bind to the substrate binding site. The basis of conformationally constrained substrate analogue synthesis is to create a "locked" conformation of the ligand with potentially higher affinity for the binding site, as well as to increase the selectivity over other proteins with similar substrates (Bridges and Esslinger 2005). However, observations from functional studies suggests ±HIP-B acts as a non-competitive inhibitor (Callender, Gameiro et al. 2012). This was not reproduced *in vitro* studies as described in Section 3.2.1.5, where ±HIP-B behaved in a non-competitive manner. The selection of these two inhibitors should reveal more about the stereochemically different substrate binding modes and how different inhibition modalities (competitive vs non-competitive) block substrate transport.

4.2.2 CRYO-EM GRID OPTIMISATION

The initial stage of the project involved extensive cryo-EM grid preparation optimisation. There are a number of parameters that can be changed to improve the sample quality when working with the Vitrobot (Thermo Fisher) sample preparation system, summarised in Table 4.2.

<table>
<tr><th colspan="2">Reconstitution system</th><th colspan="2">Sample optimisation</th><th colspan="2">Grid optimisation</th></tr>
<tr><td rowspan="3">Peptide-based</td><td>Nanodiscs</td><td rowspan="3">Buffer additives</td><td>detergents</td><td rowspan="3">Grid parameters</td><td>material</td></tr>
<tr><td>Saposins</td><td>cryoprotectants</td><td>mesh size</td></tr>
<tr><td>Peptidiscs</td><td>salts</td><td>hole size</td></tr>
<tr><td rowspan="2">Polymer-based</td><td>Amphipols</td><td rowspan="2">Protein additives</td><td>ligands</td><td rowspan="2">Grid surface modifications</td><td>Graphene/ graphene oxide</td></tr>
<tr><td>SMALPs</td><td>binders</td><td>coating with lipids/ tags</td></tr>
<tr><td rowspan="3">Detergent</td><td>ionic (cationic or anionic)</td><td rowspan="3">Buffer composition</td><td rowspan="3">optimisation for low background from buffer components</td><td rowspan="3">Grid preparation</td><td>Glow discharge/ plasma cleaning</td></tr>
<tr><td>nonionic</td><td>Detergent blocking</td></tr>
<tr><td>zwitterionic</td><td>Blotting parameters</td></tr>
</table>

Table 4.2: Optimisation parameters in Cryo-EM grid preparation. Optimisation steps can be split in three groups – reconstitution system optimisation, sample optimisation and grid preparation optimisation, with further parameter optimisation as listed.

Overall, the optimisation of grid preparation involves identification of protein reconstitution systems that maintain the folded protein structure (e.g., detergents, amphipols (Popot, Berry et al. 2003), SMALPs (Knowles, Finka et al. 2009), nanodiscs (Bayburt and Sligar 2003), saposins (Frauenfeld, Loving et al. 2016), peptidiscs (Carlson, Young et al. 2018), minimisation of sample buffer components that contribute to the background noise and reduce contrast (e.g., free detergent micelles, glycerol, sugars, salts, additives, ligands), identification of a suitable grid support type (types of materials, hole and mesh sizes) and optimal grid surface preparation (glow discharge, plasma cleaning, detergent block (Cheung, Kajimura et al. 2013), graphene/ graphene oxide, other surface modifications– lipids, tag attachments, etc.), as well as the actual grid preparation itself (blotting time/ force, humidity, temperature, sample concentration, etc.). To obtain the grids that were used for the final dataset collection, I had to test and optimise the majority of the parameters listed.

The issues I had to address in particular included poor blotting reproducibility, sample aggregation and uneven ice coverage. For full dataset collections, Quantifoil grids were used as these are more robust, so they can endure the manipulations associated with the clipping process required for automated grid

screening. Many different parameters were optimised before the conditions that yielded reproducible grids were identified (*apo* protein concentration at 1.8-2 mg/ml, 0.01% DDM (final concentration, used as detergent additive) added just before applying sample on a grid, blotting time 4-4.5 seconds, blotting force -15, 100% humidity and 5˚C chamber temperature). The particles showed orientational bias that correlated with the ice thickness, where, for example, in thick ice, particles preferentially adopted orientations where the longest dimension (along the membrane plane) were observed to align perpendicular to the ice layer (Figure 4.2).

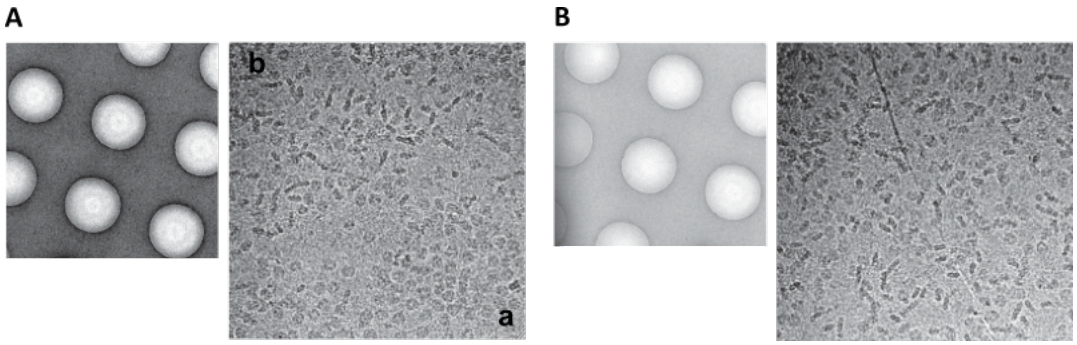


Figure 4.2: EAAT3 particles showed preferred orientation correlating to ice thickness. **A** For thin ice in the middle of the hole (left), mainly top views were observed (right, a) while in thicker ice closer to the hole edge, side views dominated (right, b). **B** With even ice in holes (left), side views were over-represented (right). Top view - particle oriented with membrane plane parallel to viewer; side - particle oriented with membrane plane perpendicular to viewer.

For the final dataset collections, ligands were added, and the sample incubated on ice for at least 30 min prior to making grids. The stock of TFB-TBOA (50 mM) was prepared in 100% DMSO and used at a final concentration of 1mM. As described previously in Section 3.2.1.4, a final DMSO concentration of 2mM did not affect the activity of EAAT3 when measured using the SURFE^{2}R system. ±HIP-B is supplied as a racemic mixture of enantiomers, and the eudismic ratio (the difference in pharmacologic activity between the two enantiomers) was determined to be 10, with +HIP-B shown to bind EAAT3 with higher affinity (Pinto, Conti et al. 2008). ±HIP-B stock (10 mM) was prepared in GFB buffer with no detergent added, and higher final concentration (2 mM) used to account for the enantiomers. The grid preparation parameters were not changed.

4.3 STRUCTURE DETERMINATION OF EAAT3 WITH BOUND INHIBITORS

4.3.1 DATA PROCESSING AND MODEL BUILDING FOR EAAT3-LIGAND STRUCTURES

Details of cryo-EM grid preparation, data acquisition and structure determination for EAAT3 in the presence of two inhibitors are described in the Section 2.3.2. The global resolution of the final EM maps for both inhibitor complexes was determined to be 3.3 Å according to the FSC 0.143 criterion (Rosenthal and Henderson 2003). Data collection parameters and model statistics are summarised in Table 4.3 and final model validation statistics show in Figure 4.3.

	EAAT3 – TFB-TBOA (EMD-10094, PDB: 6S3Q)	EAAT3 – ±HIP-B (EMD- 12566, PDB: 7NSG)
Data collection		
Magnification	22500	22500
Voltage (kV)	300	300
Electron dose (e−/Å2)	40	42
Defocus range (μm)	−1.6 to −2.4	−1.6 to −2.4
Pixel size (Å)	0.543	0.543
Reconstruction		
Particles (no.)	113258	127936
Symmetry	C3	C3
Final resolution (Å) masked / unmasked	3.7 / 3.3	3.6 / 3.3
Map-sharpening *B* factor ($Å^2$)	-111.4	-135.7
Model composition		
Nonhydrogen atoms	10290	10356
Protein residues	1290 (430 per protomer)	1290 (430 per protomer)
Ligands	3	3
Lipids	6	6
Refinement		
Starting model used (PDB code)	6GCT	6S3Q
Resolution (Å)	3.3	3.3
R.m.s. deviations		
Bond lengths (Å)	0.011	0.008

Bond angles (°)	1.004	0.893
Validation		
MolProbity score	1.36	1.25
Clashscore	2.55	2.81
Poor rotamers (%)	0.57	0.00
Ramachandran plot		
Favored (%)	95.44	96.93
Allowed (%)	4.32	3.07
Outliers (%)	0.24	0.00

Table 4.3: Cryo-EM data collection, refinement and validation statistics.

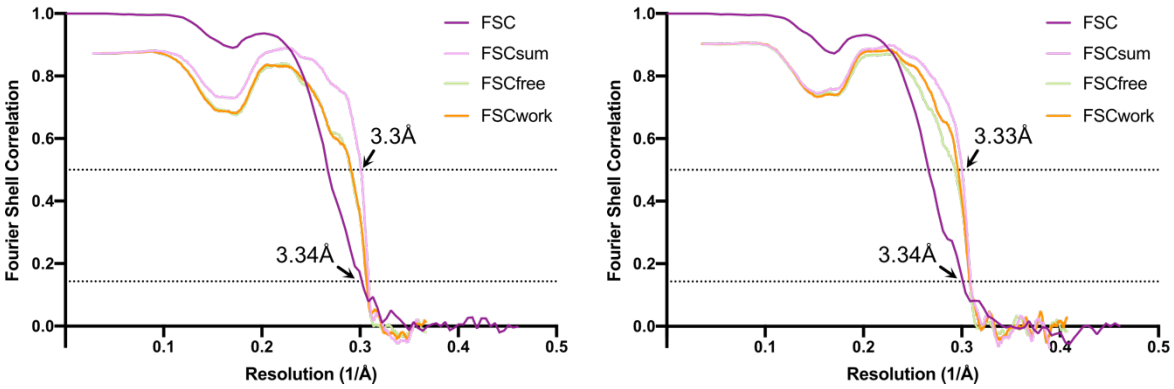


Figure 4.3: Model validation for ±HIP-B (left) and TFB-TBOA (right) datasets. Fourier shell correlation (FSC) plot of the final refined masked map calculated using relion_postprocess (purple). The resolution at which the curve drops below the 0.143 threshold is indicated. Cross-validation FSC curves: the refined model compared to the full masked dataset (FSC_{sum}) shown in pink, the "shaken" refined model compared to the masked half-map 1, postprocessed in the same way as full map (FSC_{work}) shown in orange, and the "shaken" refined model compared to the masked half-map 2, not previously used in the refinement (FSC_{free}) shown in green. The dashed lines are indicating the FSC 0.143 and 0.5.

From the 2D classifications it is useful that the trimeric assembly of the protein can be distinguished and the extracellular loops, proposed to be glycosylated, protrude from the micelle, assisting particle alignment (Figure 4.4).



Figure 4.4: Representative 2D classes from the TFB-TBOA dataset. The trimeric assembly can be seen for the class circled in purple; the extracellular loops with potential glycosylation sites appear as fuzzy protrusions from micelles (indicated by orange arrow) and are circled in orange. 2D classification was carried out in RELION (Zivanov, Nakane et al. 2018).

The EM maps had good density for the majority of the protein sequence (Figure 4.5). The cryo-EM structure of human ASCT2 (PDB: 6GCT) was used to generate a homology model using SWISS-MODEL Homology Modelling tool (Waterhouse, Bertoni et al. 2018). Guided by the maps, a model of EAAT3 could be built. All of the structure was visible, apart from the extreme N- and C- termini, the loop between TMH 3 and 4 (residues 123-135), and the extracellular loop extending from TMH 4 (residues 172-195), where the putative glycosylation sites are located. Overall, 430 residues in total (spanning residues 10-476 out of 480) could be modelled for TFB-TBOA dataset, where 417 had side chains modelled and 13 had alanine assignment only. For ±HIP-B dataset, same 430 residues were modelled in total; 421 with side chains modelled and 9 residues with alanine assignment only. The densities for the peripheral elevator domains were of lower resolutions (~3.7 Å) compared to the central scaffold domain (~3.1 Å) suggesting local flexibility (Figure 4.6).

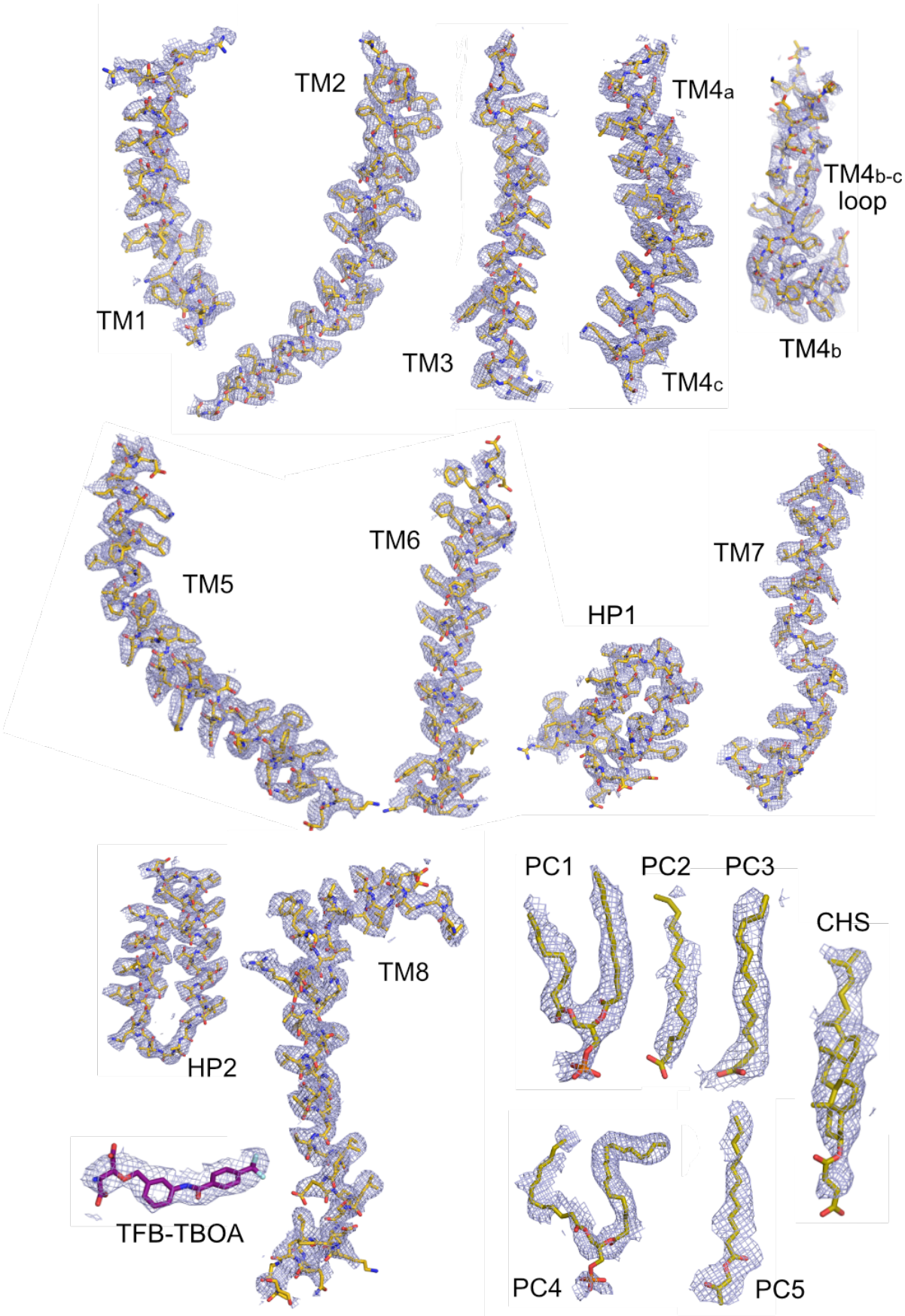


Figure 4.5: Cryo-EM density for TFB-TBOA bound EAAT3 structure. Sections of cryo-EM density of the EAAT3 map shown for the respective refined models. Models are shown in stick representation

for the secondary structure elements (TM1-8, HP1-2) and the modelled ligands (TFB-TBOA, CHS, PC1-5). Densities are plotted at 3σ.

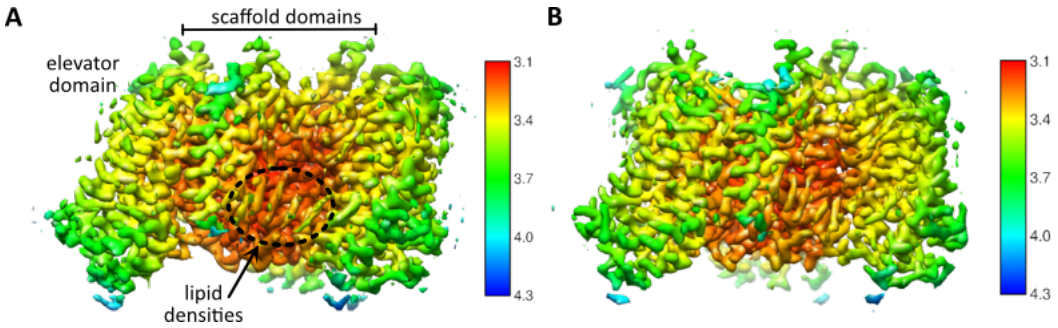


Figure 4.6: Cryo-EM maps coloured by local resolution **A** ±HIP-B and **B** TFB-TBOA final refined masked maps. The final masked reconstruction map local resolution estimation was carried out in RELION (Zivanov, Nakane et al. 2018). Figures made in Chimera (Pettersen, Goddard et al. 2004).

In both EAAT3-inhibitor complexes, all the subunits were in the inward-facing conformation. There was no noticeable conformational heterogeneity in both data sets, with 3D reconstructions with no symmetry applied looking very similar to maps with C3 symmetry applied. Additional density was seen in the proposed substrate binding site and could be assigned to the two inhibitors added - TFB-TBOA and ±HIP-B. In addition to the polypeptide chain, six lipid tails were built in the densities seen lining the membrane-exposed scaffold domain surface. Similarly, a single CHS molecule could be seen interacting with the elevator domain of each monomer.

4.3.2 THE CHARACTERISTIC FOLD OF THE SLC1 FAMILY

The first structure revealing the fold shared by all members of the SLC1 family was of the bacterial homologue from GltPh (Yernool, Boudker et al. 2004). The trimeric assembly of monomers with the central scaffold domains and peripheral elevator domains was subsequently found in bacterial homologue from GltTk (Jensen, Guskov et al. 2013) and all the reported structures of human SLC1 family members (Canul-Tec, Assal et al. 2017, Garaeva, Oostergetel et al. 2018).

The structure of the human EAAT3 has the characteristic trimer conformation (Figure 4.7). The subunits have been proposed to function independently (Grewer, Balani et al. 2005).

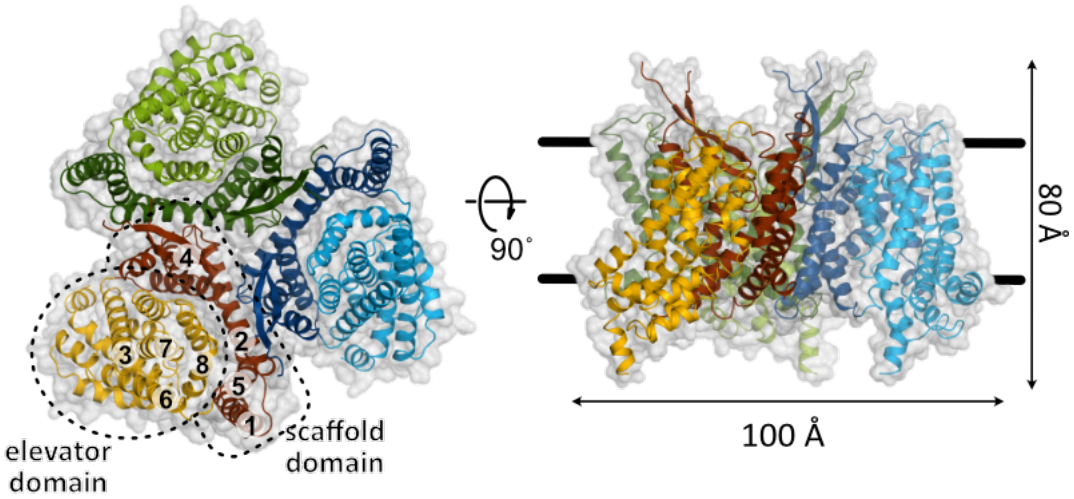


Figure 4.7: Overall fold of EAAT3. The trimer organisation is shown from extracellular (left) and membrane (right) views. The three monomers (coloured yellow, green and blue) oligomerise through static scaffold domains (darker shade) with peripheral flexible elevator domains (lighter shade). The positions of the TMH1-8 are indicated. The dimensions of the trimer are ~100 Å diameter and ~80 Å height. The extent of the membrane is indicated by two black lines.

The N-terminal part of EAAT3 is arranged in a crescent-shaped scaffold domain, formed by TMH 1,2,4 and 5, which form a static central core and provide all the molecular contacts in the oligomeric complex. The overall interface area between each monomer is ~ 1400 $Å^2$ and specific interactions between monomers are formed exclusively between the extracellular part of TMH2 and residues from the TMH4 of a neighbouring monomer (Figure 4.8 A). Three intermolecular salt bridges are formed between R147 (TMH4) and E57 (TMH2), and E152 (TMH4) and K64 (TMH2), as well as a number of hydrogen bonds (E199 – T46, R166 – Y51, D140 – Y51, R147 – R61 and F150 – R61). The rest of the interface is formed by hydrophobic interactions (Figure 4.8 B).

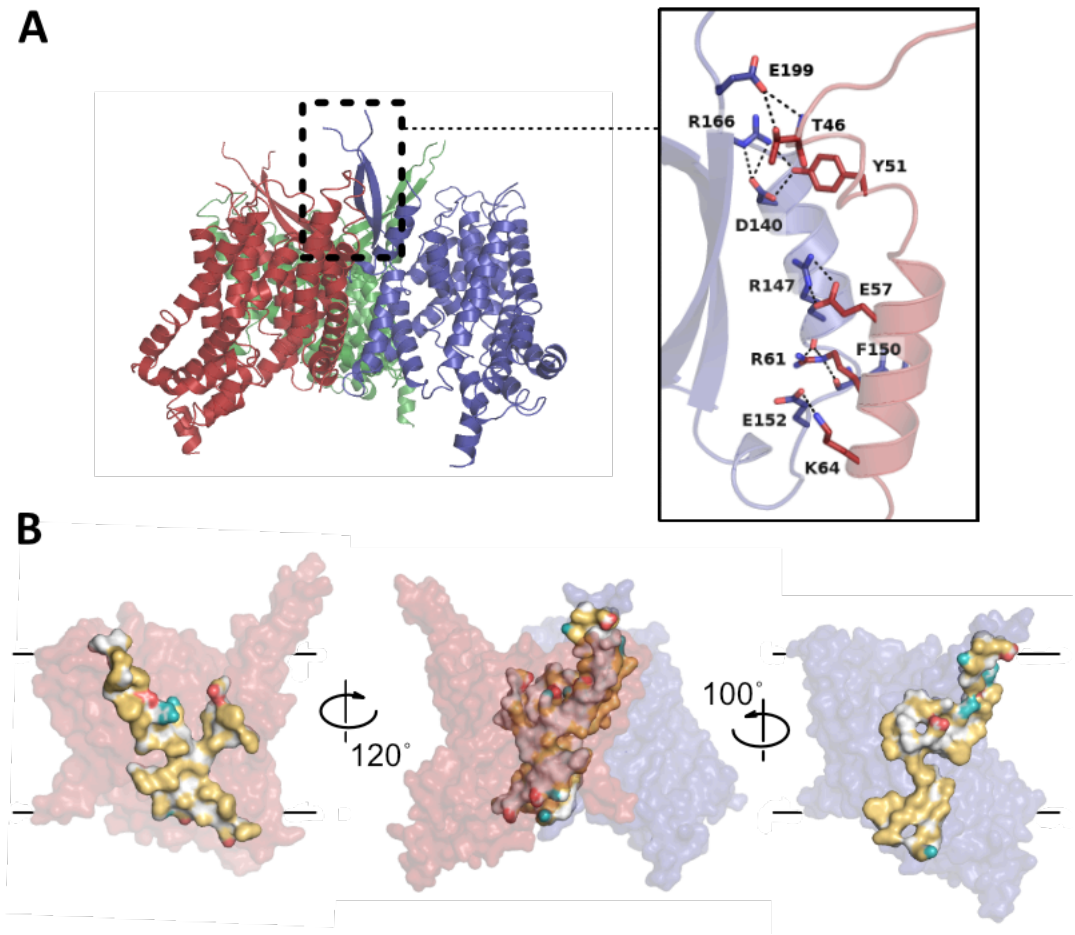


Figure 4.8: The interface between monomers in EAAT3 is formed exclusively by the scaffold TMH2, TMH5 and the TMH4 of neighbour monomer. **A** Electrostatic interactions between two monomers between TMH4 (blue) and TMH2 (red). **B** The hydrophobic interface area buried between monomers (shown in red and blue). The hydrophobic interactions are formed between TMH2 and TMH5 from one monomer (red) and TMH4 from other (blue). For clarity, the third monomer is not shown. The residue side chains are coloured to highlight hydrophobicity and charge using YRB code, where only side chain atoms are coloured (Hagemans, van Belzen et al. 2015). Carbon atoms that can form hydrophobic contacts are coloured in yellow, nitrogen atoms in blue and oxygen atoms in red.

Although the transmembrane domains show remarkable conservation from prokaryotes to eukaryotes, eukaryotic EAATs have a unique feature, a long, flexible loop inserted between the TMH4b and TMH4c, where b and c indicate the sequential transmembrane segments of the TMH4 that are connected by loops (Appendix Figure 7.16). In EAAT3, the region closest to the core of the molecule forms a ß-hairpin. Tip of loop (residues 172-195) is poorly defined and could not be resolved. This loop extends on the extracellular side from a hydrophilic bowl-shaped surface (Figure 4.10 A), forming contacts between monomers and within protomers. The length of this loop varies between the human

homologues, yet all contain predicted N-glycosylation sites (Figure 4.9). This suggests these loops play important roles in the post-translational processing and the structural integrity in SLC1 family.

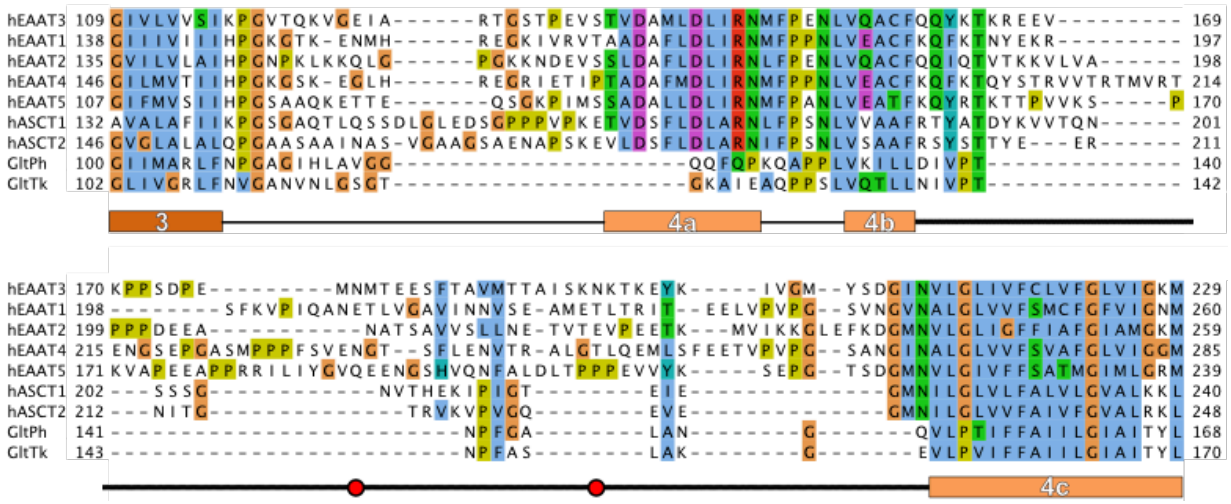


Figure 4.9: Eukaryotic SLC1 family members have an extra loop between TMH 4b and 4c with extensive posttranslational processing. Amino acid sequences of EAAT1-5, ASCT1-2 and bacterial homologues GltPh and GltTk are compared for the region between TMH 3-4c. The boundaries of TMH3 and TMH4a,b and part of TMH4c (rectangles) and the putative glycosylation sites of EAAT3 are shown (red circles). The loop of interest is shown as a thick line. Residues are coloured based on Clustal X colour scheme (Larkin, Blackshields et al. 2007), the alignments were made using COBALT (Papadopoulos and Agarwala 2007).

When assembled as a trimer, the scaffold domains of monomers enclose a large, hydrophobic cavity in the centre of the trimer that measures 18 Å in diameter and 14 Å in height (Figure 4.10 B). Non-protein density is seen in this cavity in all the solved EAAT3 structures, but due to poor resolution in this region, I could not interpret this density. The cavity is completely sealed off from both intracellular and extracellular sides. Similar densities were seen in the ASCT2 structures (Garaeva, Oostergetel et al. 2018, Yu, Plotnikova et al. 2019) and the EAAT1 crystal structure (Canul-Tec, Assal et al. 2017). The C158 (conserved in EAAT1-4) residue sidechain from each monomer appears to be interacting with the unknown polymer, with the rest of the density wrapped in the cavity (Figure 4.10 C, D).

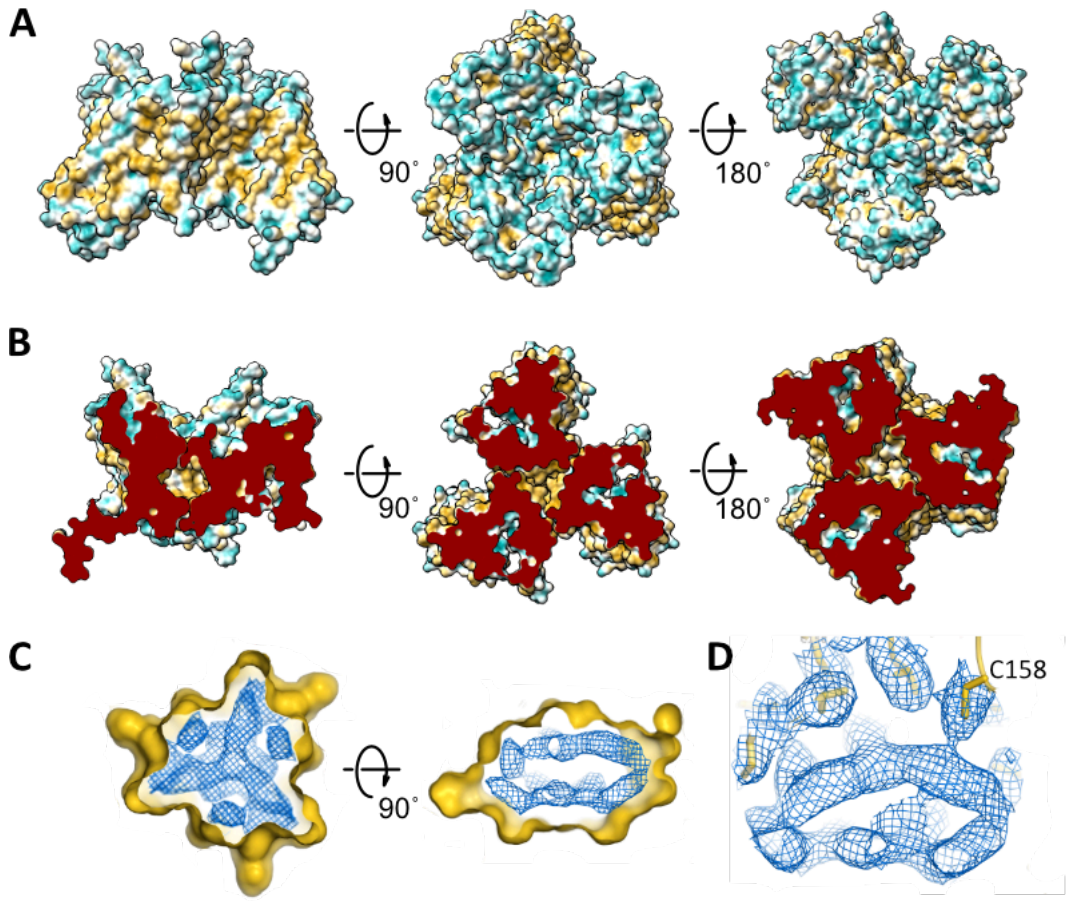


Figure 4.10: EAAT3 has a buried central cavity. **A** Hydrophobicity of the surface of EAAT3 shown from the plane of the membrane (left), extracellular (middle) and cytoplasmic (right) sides. **B** Central slices reveal a buried hydrophobic cavity in the centre of the protein. Slices through the central cavity, viewed from the plane of the membrane, (left), the extracellular (middle) and cytoplasmic (right) faces of EAAT3. **C** The non-protein density occupying the central cavity as seen from the extracellular face (left) and from the plane of the membrane (right). The map contour level is at 4σ. **D** Cys158 is positioned to potentially interact with the polymer. Map contour level at 3σ. The surface is represented by molecular lipophilicity potential, with dark cyan being the most hydrophilic and goldenrod being the most lipophilic surface (with white being in between) calculated in ChimeraX (Pettersen, Goddard et al. 2020).

The C-terminal region of EAAT3 is arranged in an elevator domain (TMH3, 6-8) with short cytoplasmic extensions between the helices. Apart from a long flexible loop (21 amino acid residues) connecting TMH3 and TMH4, which connects the elevator domain to the scaffold, the connections between TMH2-3 and TMH5-6 are generally short (3 and 8 amino acid residues, respectively), suggesting that the TMH3 helix moves the most during the transport cycle (Appendix Figure 7.16). Each elevator domain consists of two outer helices (TMH3 and 6) and two central ones - TMH7-8. The two characteristic helical hairpins (HP1 and HP2) located between TMH6-7 and TMH7-8,

respectively, reinsert from either side of the membrane and regulate the binding site accessibility, as well as substrate coordination during the transport cycle. They form the interface between the scaffold and elevator domains and are referred to as gates (Figure 4.11 A). Originally, the transport mechanism was proposed to be a two-gate model, where both gates open and close during substrate binding and release. However, this view was challenged after the structures of ASCT2 were determined and a gating mechanism with a single gate was proposed with HP1 remaining static during the transport cycle (Garaeva, Guskov et al. 2019).

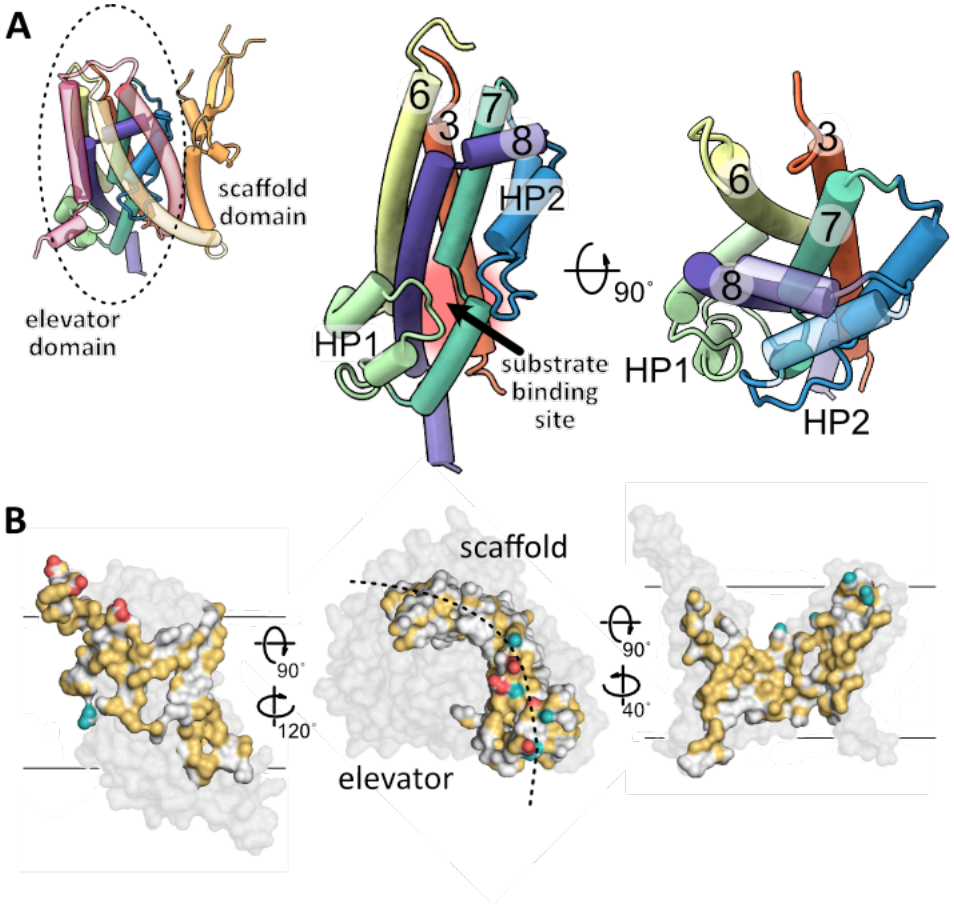


Figure 4.11: The C-terminal region of EAAT3 forms the elevator domain. **A** Cartoon representation of the transport domain as seen from the plane of the membrane (middle) and extracellular side (right). The elevator domain location within EAAT3 monomer is indicated by a dashed oval (left). The domain is formed by two outer (TMH3 and TMH6) and two inner (TMH7-8) helices. Two re-entrant hairpin loops between TMH6-7 and TMH7-8 (HP1 and HP2, respectively), form the so-called gates that regulate binding site accessibility. The binding site region is shown in red shading (middle). **B** The interface between the elevator and scaffold domains is formed by mainly hydrophobic residues. The interface as seen from the top of the monomer (middle) with side views of the interface of the elevator (left) and scaffold (right) domains. The residue side chains are coloured to highlight hydrophobicity and charge using YRB code, where only side chain atoms are coloured (Hagemans, van Belzen et al. 2015). Carbon atoms that can form hydrophobic contacts are coloured in yellow, nitrogen atoms in

blue and oxygen atoms in red. While there are some charged residues visible (red and blue spheres), none of them form contacts with each other.

In both structures solved in this thesis, EAAT3 adopts an inward-facing conformation. This results in the substrate binding site, located in the inner leaflet part of the membrane, being accessible from the cytoplasm.

The elevator domains have a peripheral location, and they are known to move perpendicular to the lipid bilayer plane as seen in a homologue structure (Canul-Tec, Assal et al. 2017). The substrate transport across the membrane requires the cotransport of three Na^+ ions as the driving force. The elevator domain has only a few interactions with the corresponding scaffold domain, the movement happens mostly along a hydrophobic concave surface formed by the scaffold domain (Figure 4.11 B). In our EAAT3 structures the buried surface area between the scaffold and elevator domains is ~1900 $Å^2$, which is the largest between the *SLC1* family members observed so far (compared to ~1300 $Å^2$ /~1300 $Å^2$ and ~1700 $Å^2$ in ASCT2 outward-/ inward-facing structures and in EAAT1, respectively), indicating that the elevator domain remains closer to the scaffold domain in EAAT3.

So far, the structures available for *SLC1* family are of EAAT1 and ASCT2. During the writing of this thesis, a publication describing the human EAAT3 structures in presence of L-Aspartate and in *apo* form was deposited in bioRxiv (Qiu 2020), however, the coordinates of the models were not made available, so I could not use them for comparison here. EAAT1 was only captured in an outward-facing conformation (Canul-Tec, Assal et al. 2017) while ASCT2 has been trapped in both, outward- and inward- facing states (Figure 4.12 A) (Garaeva, Oostergetel et al. 2018, Yu, Plotnikova et al. 2019). Structural comparison of EAAT3 with the EAAT1 and ASCT2 reveal a remarkable conservation in the general structural organisation. The most noticeable differences are in the loop between TM4b-c, with EAAT3 having the longest amongst the three (Appendix Figure 7.16). In ASCT2, this loop is reported to form a retroviral docking site (Tailor, Nouri et al. 1999). The EAAT1 structure had this part of the protein mutated to resemble that of ASCT2, the shortest in the family, as extensive construct engineering was necessary in order to obtain crystals, so there is no information available on the structure of this loop in EAAT1.

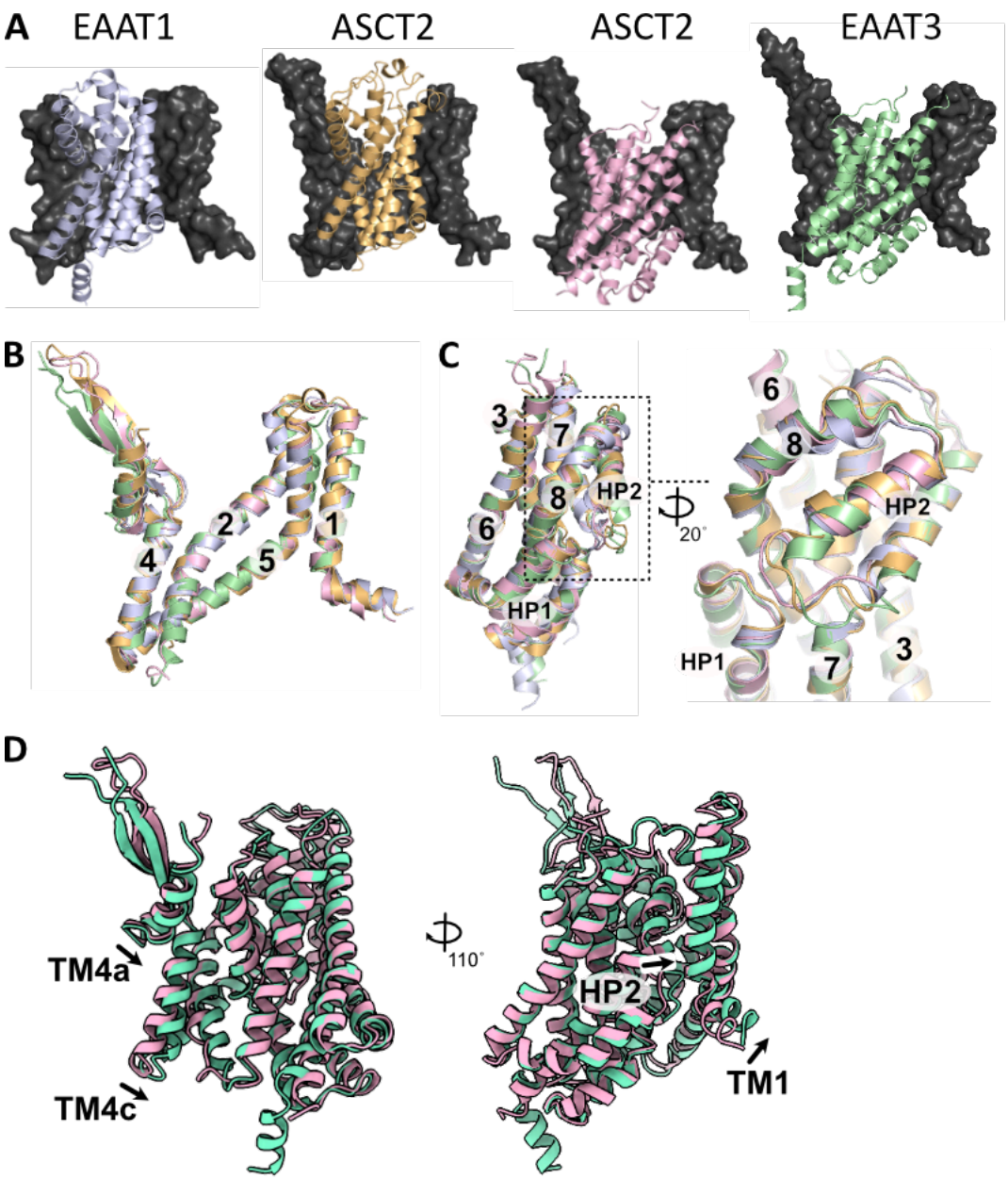


Figure 4.12: Comparison of the EAAT3 structure with the structures of other members of the SLC1 family **A** Solved structures of human SLC1 family members to date. Outward-facing: EAAT1 (PDB:5LLU), ASCT2 (PDB: 6MP6) and inward-facing structures: ASCT2 (6GCT), EAAT3 (6S3Q). The scaffold domain is shown as a black molecular surface while the elevator domains are shown in cartoon representation. A single monomer is shown for clarity. **B** Alignment of the scaffold domains of EAAT1, both ASCT2, and EAAT3 models (coloured and positioned as in **A**). The positions of TMH 1, 2, 4 and 5 are indicated. **C** Alignment of elevator domains of EAAT1, both ASCT2, and EAAT3 models with a zoomed in window for HP2 loop region (coloured as in **A**). The positions of TMH 3, 6, 7 and 8 are indicated. In both outward- and inward-facing conformations (shown in panel **A**) the elevator domain maintains the same structure. **D** Global alignment of EAAT3 and ASCT2 (inward-facing) models. The view on the right is positioned as in **A**. The main structural differences are indicated with black arrows and include shifts in the positions of the scaffold-forming TMH1 and 4, and the tip of the HP2 loop.

The scaffold domains can be superimposed with Cα root-mean-square deviation (RMSD) values of 1.7 Å over 970 Cα atoms, 1.4 Å (928 Cα atoms) and 1.3 Å (945 Cα atoms) for EAAT3 scaffold compared to EAAT1, ASCT2 (outward-facing conformation) and ASCT2 (inward-facing conformation), respectively (Figure 4.12 B). The flexible loop between TMH4b-c adopts multiple conformations in these structures. Similarly, the EAAT3 elevator domain can be superimposed with Cα RMSD values of 0.7 Å (1158 Cα atoms), 0.9 Å (1163 Cα atoms) and 0.9 Å (1194 Cα atoms) for EAAT1, ASCT2 (outward-facing conformation) and ASCT2 (inward-facing conformation), respectively (Figure 4.12 C). This demonstrates that the elevator domains primarily undergo rigid-body movements, since both inward- and outward-facing states are practically identical. The biggest variation is seen in the flexible HP2 loop region, as both closed and open conformations are compared. Overall, the EAAT3 and ASCT2 (inward-facing conformation) monomer structures have a Cα RMSD of 1.4 Å (Figure 4.12 D). The differences are most pronounced in scaffold domain (shift in TM1 (Cα RMSD of 2.5 Å over 32 Cα atoms) and TM4 (Cα RMSD of 1.7 Å over 10 Cα atoms in TM4a, Cα RMSD of 2.0 Å over 17 Cα atoms in TM4c)) as well as HP2 loop region, arising from HP2 loop closing over the substrate binding site in ASCT2 model (Cα RMSD of 3.0 Å over 29 Cα atoms) (Figure 4.12 D).

4.3.3 STRUCTURAL INTERPRETATION OF DISEASE ASSOCIATED MUTATIONS IN EAATS

Disease-associated mutations identified in EAAT transporters have been studied *in vitro* and *in vivo* in order to understand the underlying causes of disease. The EAAT3 model presented here provides the means for structural interpretation of the mutations that can be mapped to this structure (Figure 4.13).

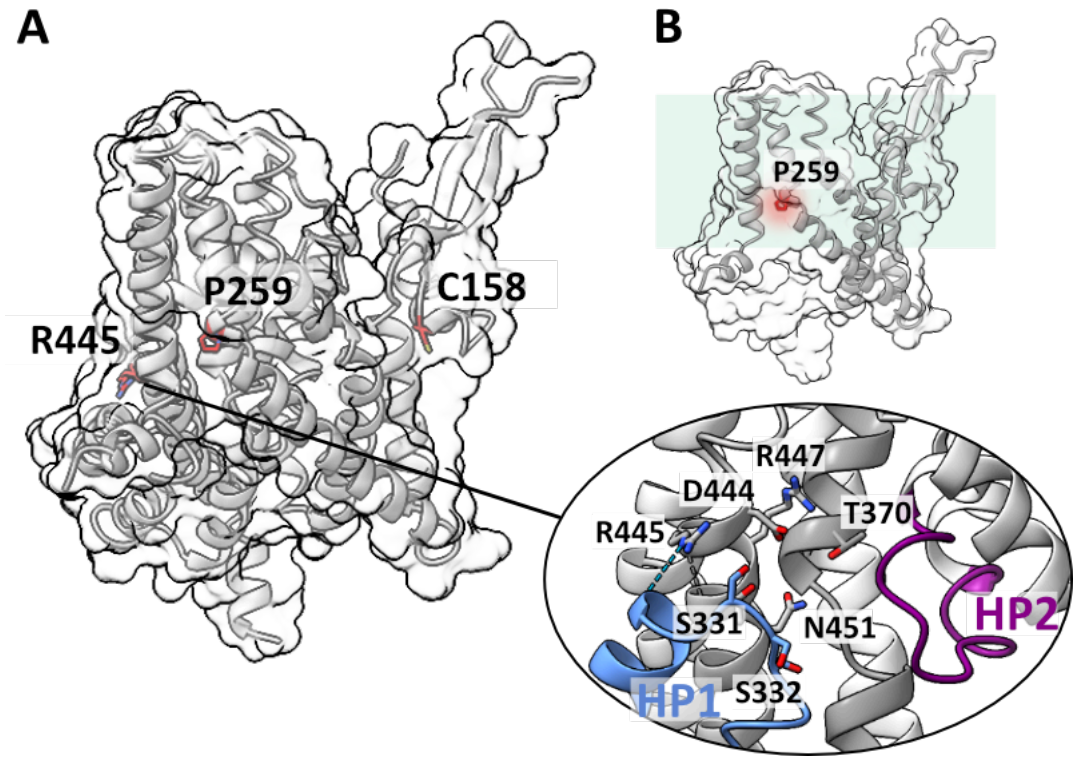


Figure 4.13: Disease-associated mutations in the SLC1 family. **A** EAAT3 monomer as seen from the membrane plane with residues C158, P259 and R455 shown as red sticks. The zoomed in section shows R445 environment in more detail with residues involved in substrate binding shown as sticks. **B** Location of P259 with respect to the membrane plane (shown in pale cyan). For clarity, only the helices forming scaffold domain are shown.

The R445W mutation in EAAT3 causes dicarboxylic aminoaciduria (DA), manifested by high levels of glutamate and aspartate in the urine due to ineffective absorption of these amino acids in the kidneys as a result of a loss of EAAT3 function. The mutant showed greatly reduced surface expression in MDCK cells. EAAT3 with the R445W mutation exhibited reduced transport currents in the presence of glutamate and increased glutamate affinity compared to the WT protein (Bailey, Ryan et al. 2011). From the structures, R445 forms a hydrogen bond with the backbone carbonyl group in HP1 loop (L328) and is positioned to form electrostatic interactions with HP1 helix dipole that would be disrupted with an R445W mutation (Figure 4.13 A). Since the highly conserved serine-stretch (S331-S333) in HP1 forms contacts with the substrate, the displacement of the HP1 loop relative to TMH8 would affect substrate coordination. The same mutation is observed in ASCT1 (R457W in ASCT1) and is causative of spastic tetraplegia, thin corpus callosum, and progressive microcephaly (SPATCCM)(Damseh, Simonin et al. 2015). The ASCT1 mutation R457W abolished L-serine and L-alanine transport without affecting expression of the protein at the plasma membrane. The differences

in the transport mechanisms (obligate exchange for ASCT1 and concentrative uptake for EAAT3) and substrate coordination within the binding site might explain the substrate transport seen in EAAT3, albeit at low rates.

An I395del in EAAT3 is also thought to cause DA (Bailey, Ryan et al. 2011). With this mutation, no transport activity was observed at the plasma membrane and there was very little plasma membrane expression (Bailey, Ryan et al. 2011). The deletion is within HP2 and would most likely impair formation of the substrate binding site, resulting in a non-functional protein.

The missense mutations P290R and C186S in EAAT1 are linked to Episodic Ataxia subtype 6 (EA6) (Jen, Wan et al. 2005). P290R (P259 in EAAT3, conserved within the EAAT family) mutant shows complete loss of glutamate transport and increased anion currents even in the absence of the glutamate. The corresponding mutation in EAAT3 slowed down the conformational changes induced by sodium binding and exhibited the same increased anion conductance as EAAT1 (Hotzy, Schneider et al. 2013). P259 is located in the TM5 within the scaffold domain near the membrane-cytoplasm interface. As show in Figure 4.13 B, it creates a kink in the TM5 helix within the membrane. P259R mutant would cause a structural rearrangement of TM5 and potentially affect the interactions with the elevator domain during transport cycle which would explain the increased anion currents associated with the mutant.

C186S (C158 in EAAT3, conserved in EAAT1-4) exhibited slightly reduced glutamate uptake (de Vries, Mamsa et al. 2009). Its location within the TM4 of the scaffold domain suggest the impaired transport is due to affected translocation process of the elevator domain. C158 is located within the central part of the trimer and appears to be interacting with the density observed within the central cavity (Figure 4.10 D).

In EAAT2, N206S (M179 in EAAT3) is linked to amyotrophic lateral sclerosis (ALS) and this mutation causes reduced transporter plasma membrane expression. This manifests as reduced glutamate clearance capacity in brain. The mutation is disrupting a predicted N-linked glycosylation site, however, the affinity for the glutamate is unaffected (Trotti, Aoki et al. 2001). Although glycosylation sites are predicted to occur within the loop between TM4b-c helices for all SLC1 family members, they are not conserved, suggesting that the post-translational processing is subtype specific.

In summary, three out of the five identified unique mutations, affect residues within the scaffold domain and have effects on the substrate transport cycle or the targeting of the transporter to the plasma membrane. The remaining two disease-associated mutations that lie within the elevator domain (R445W and I395del) show the most severe phenotypes, most likely due to the tight regulation of substrate and ion binding.

4.3.4 POST-TRANSLATIONAL MODIFICATIONS IN EAAT3

Multiple post-translational modifications have been attributed to SLC1 family members. N-linked glycosylation sites are predicted for all EAATs. While in some cases glycosylation affects protein function, it was shown that glycosylation does not affect Glutamate transport via EAAT2 (Trotti, Aoki et al. 2001). EAAT3 has been proposed to have three N-glycosylation sites – N43 on the loop between TM1 and 2, as well as N178 and N195 on the loop between the TM4 segments b and c. From the solved EAAT3 structures, N43 lies between TM1 and TM2 and there was no density attached to the sidechain, suggesting it was not glycosylated. The loop between TM4b and TM4c is disordered and could not been built in the current maps. Low resolution maps show features of glycans, but alternative methods would have to be used to identify the glycosylation sites (such as native mass spectrometry).

4.3.5 ION COORDINATION IN EAAT3

From electrophysiology studies, it is known that EAATs transport substrate amino acids with a proton and three Na^+ ions, while a single K^+ ions is counter transported (Danbolt 2001). The three Na^+ binding sites were identified in GltPh from multiple X-ray crystallography structures (Boudker, Ryan et al. 2007, Bastug, Heinzelmann et al. 2012). No clear density for Na^+ is evident in either of EAAT3 structures presented here. This could be due to the low resolution of maps in the expected Na^+ ion binding region (~3.5 Å), the degree of B-factor sharpening applied or because of radiation damage. Due to the nature of cryo-EM imaging, radiation damage first affects the charged amino acid side chains and consequently, the ions coordinated by them are lost. Nevertheless, based on the sequence alignment, the sites can be modelled in the EAAT3 and the potential ion binding sites evaluated, based on the Na^+ ion coordination distances observed in the GltPh crystal structures.

The three Na^+ binding sites identified in GltPh and the corresponding residues in EAAT3 are summarised in Table 4.4.

Na^+ binding site	GltPh residues	EAAT3 numbering	The distance between the residue and the Na^+, Å
Na1	S278 **N310** N401 D405 G306	S333 **N366** N451 D455 G362	2.5 – 2.7 Å
Na2	T352 S349 I350 T308	A408 S405 I406 T364	2.5 – 2.7 Å
Na3	T92 S93 **N310** **D312** backbone of Y89	T101 T102 **N366** **D368** Y98	2.2 – 2.4 Å

Table 4.4: Na^+ ion coordination sites as identified in GltPh. The residues in bold are part of the highly conserved NMDGT motif.

The order of affinities for the three sites are Na3 > Na1 > Na2 (Bastug, Heinzelmann et al. 2012), suggesting that the Na3 site is the first one to be occupied. Two of the coordinating residues for the Na3 site are from the highly conserved NMDGT motif (N366-T370, EAAT3 numbering), which undergoes structural rearrangements upon Na^+ binding to the Na3 site to allow Na^+ binding to the Na1 site (Guskov, Jensen et al. 2016).

In the EAAT3-TFB-TBOA complex structure, the Na3 binding site can be modelled in agreement with the Na^+ coordination distances as shown in Table 4.4 (Figure 4.14 A), which agrees with previous mutagenesis studies identifying N368 as crucial for Na^+ coordination (Tao, Zhang et al. 2006). The same site in the EAAT3-±HIP-B complex map is maintained (Figure 4.14 B), whereas the Na1 binding site is not fully formed in either model (Figure 4.14), as S333 is positioned too far from the putative Na^+ ion site (4.44 Å in TFB-TBOA model and 4.36 Å in ±HIP-B model).

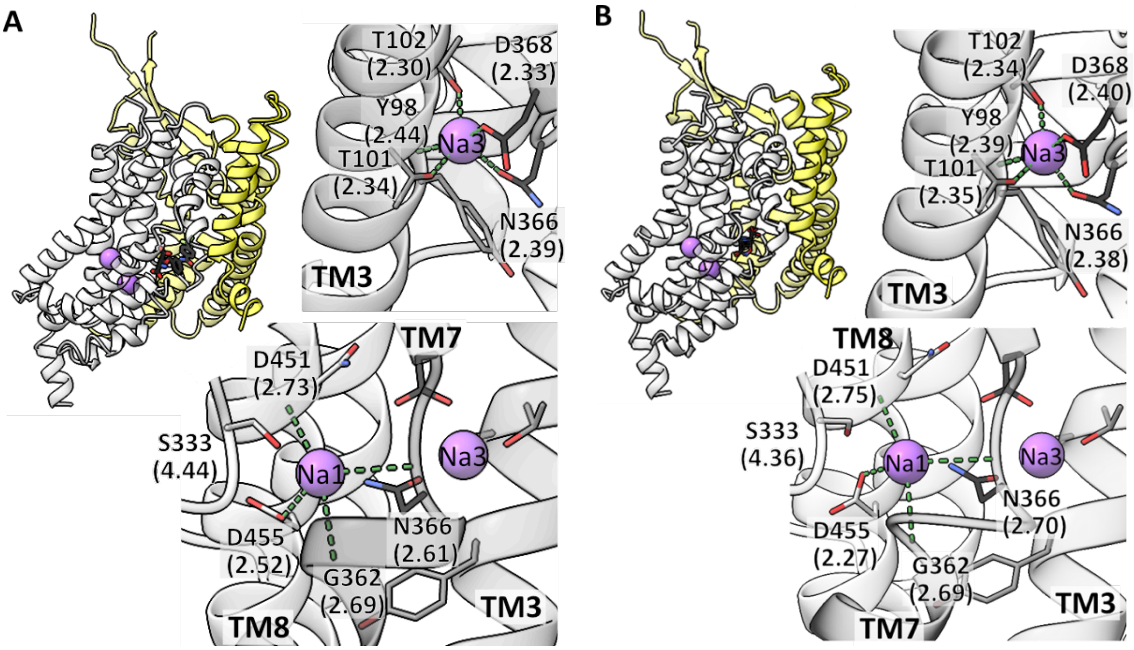


Figure 4.14: Modelling of the Na^+ binding sites in EAAT3 structures **A** TFB-TBOA model with the scaffold domain shown in yellow **B** ±HIP-B model with scaffold domain shown in yellow. The putative Na^+ ion binding sites are shown with the side chains involved in Na^+ coordination shown as sticks. The coordination distances are shown in brackets (Å).

The Na2 binding site, coordinated between the HP2 loop and TMH7 in GltPh, is disrupted in both models with inhibitors bound, since the ligands prevent the HP2 loop from closing over the binding site due to steric clashes. The binding of just one Na^+ ion was proposed to be sufficient for binding of the TFB-TBOA analogue, L-TBOA to GltPh. However two bound Na^+ ions are required for substrate binding to take place in GltPh (Boudker, Ryan et al. 2007). This is in agreement with the model presented here. The occupation of the Na3 site is proposed to prepare the Na1 site for subsequent Na^+ ion binding, before the substrate binds. This does not seem to be the case with the inhibitor binding as in both models the Na1 binding site is not fully formed while the HP1 loop is interacting with the bound substrate analogues.

4.3.6 EAAT3 LIPID INTERACTIONS

Lipids are known to bind and regulate the activity of membrane proteins and are frequently seen bound in cryo-EM and crystal structures of membrane proteins. Although no lipid was added during purification, elongated densities presumably corresponding to ordered co-purified lipids are visible in both structures (Figure 4.15 A). They lie between the elevator domains of the monomers, with a characteristic lipid tail extending into a hydrophobic pocket formed by the scaffold domain TMH2,5

and neighbouring monomer TMH4 helices (Figure 4.15 A, top right inset). Similar pocket can be seen in the ASCT2 structure, but no lipid density was seen. The density was not good enough to identify the head groups of the lipids. Phosphatidylcholine (PC) lipids were modelled as this is the most abundant lipid species in the plasma membrane of eukaryotes. Lipid-like densities lining the scaffold domains were also observed in both EAAT1 and ASCT2 structures (Canul-Tec, Assal et al. 2017, Garaeva, Oostergetel et al. 2018, Garaeva, Guskov et al. 2019).

In both EAAT3 structures, density for CHS can be seen in a groove formed by TMH3 and TMH6, and the C-terminal part of TMH8 (Figure 4.15 A,B). CHS was added during all purification steps and could potentially displace cholesterol that would bind naturally. There are reports that cholesterol affects the activity of the EAAT transporters, but it is unclear if this is via direct interaction or due to localisation within membrane domains (Butchbach, Tian et al. 2004, Canolle, Masmejean et al. 2004). EAAT3 TMH3 contains a **C**holesterol **R**ecognition/interaction **A**mino acid **C**onsensus sequence - CRAC motif. These domains can have an inverted sequence, depending on the interaction with a lipid leaflet can be in reverse, as is the case for EAAT3. The consensus pattern is broad, (–R/K-x(1-5)-Y/F-x(1-5)-L/V-, in EAAT3 (93)**R**AVV**YYF**CTT**L**) suggesting it is not indicative of specific interactions but rather an indication of membrane protein tendency to be incorporated in cholesterol-rich lipid domains (Baier, Fantini et al. 2011). CHS in the EAAT3 models pack against this motif and forms a hydrogen bond with R93 guanidino group and hydrophobic interactions with leucine and valine residues forming the groove (Figure 4.15 B) EAAT3 is the only member in the human SLC1 family to have this motif. An alternative CHS binding site has been identified in ASCT2 structure, occupying a hydrophobic pocket between the scaffold and elevator domains of a monomer located at the inner membrane leaflet (Figure 4.15 C)(Yu, Plotnikova et al. 2019). These pockets are not formed in the EAAT3 structures described here due to elevator domain packing closer to the scaffold domain.

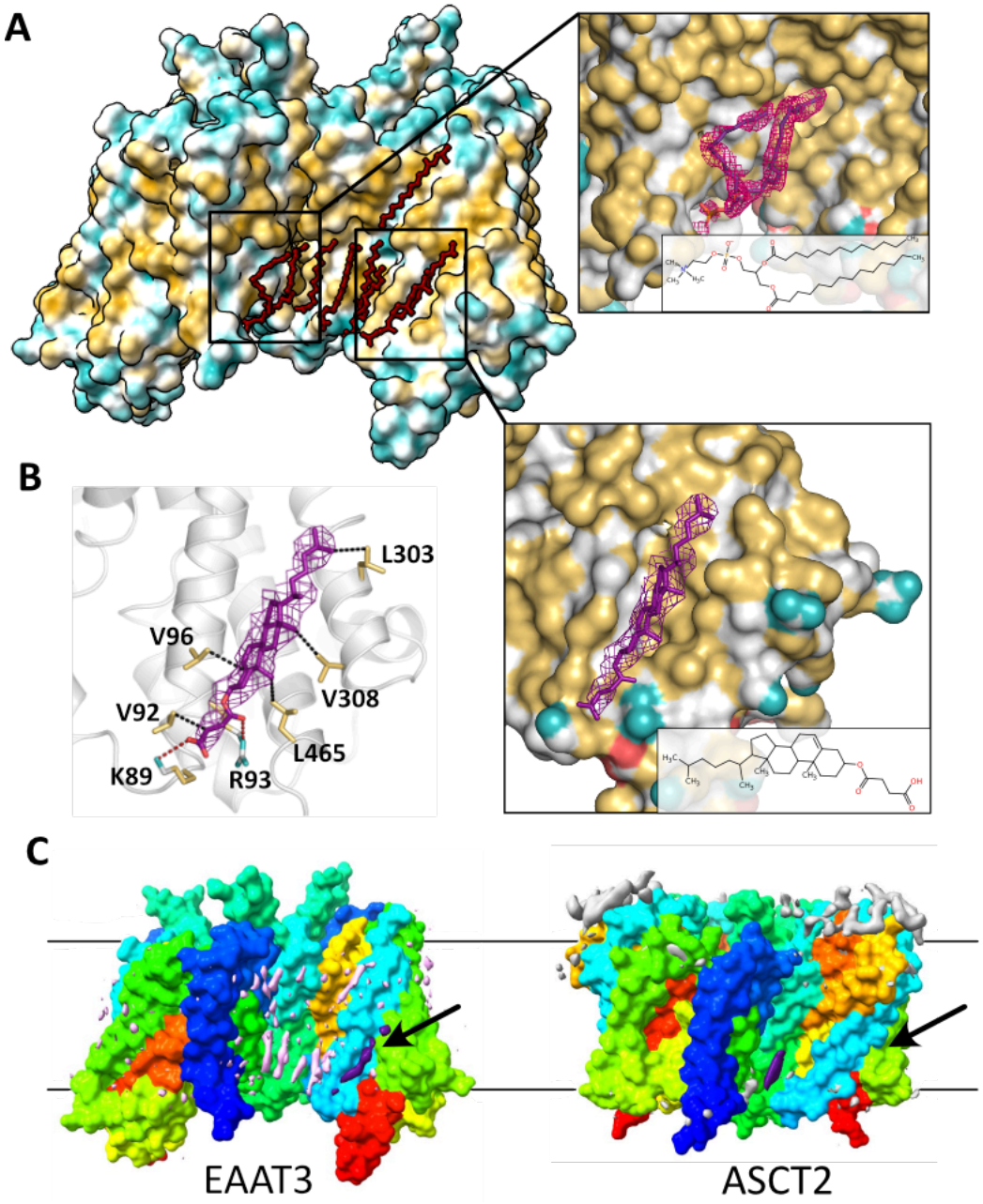


Figure 4.15: EAAT3-lipid interactions. **A** Modelled lipids for EAAT3 in the TFB-TBOA complex structure. The characteristic lipid tail poking into the cavity formed between scaffold-forming helices TM2,5 and neighbouring monomer TM4 helices is show in the top right corner. The chemical structure of modelled lipid is shown in inset. Density shown at 3σ. The density for CHS (at 3σ), assigned based on the density, is seen on the side of elevator domain in a groove formed by TMH3 and TMH6, and the C-terminal part of TMH8, shown in the bottom right corner. The chemical structure of CHS is shown in inset. **B** CHS forms hydrophobic interactions (black dashes) and hydrogen bonds (red dashes) with residues in TMH3,6 and 8. **C** The position of the density that was modelled as CHS in the ASCT2 structure (PDB: 6MP6) compared to the CHS binding site in EAAT3. Both models represent the protein surface, coloured in rainbow with N-terminus in blue and C in red. The extra densities seen in cryo-EM maps are shown in pink (EAAT3) or grey (ASCT2). The CHS density is shown in dark purple. The CHS position in EAAT3 and the corresponding location in ASCT2 is marked by an arrow.

In ASCT2, the CHS in bound in a hydrophobic pocket formed by scaffold TMH4 and TMH5 (from neighbouring monomer) and elevator TMH3 and TMH7.

4.3.7 THE BINDING SITES FOR THE INHIBITORS TFB-TBOA AND ±HIP-B IN EAAT3

The substrate binding site is highly conserved within all EAATs, with the two ASCTs having minor sequence substitutions. Multiple X-ray crystallography structures of GltPh/ GltTk have been solved with a variety of bound substrates that revealed the main interactions, including L-Aspartate (Boudker, Ryan et al. 2007), D-Aspartate (Arkhipova, Trinco et al. 2019), L-Cysteine and L-Serine (Scopelliti, Font et al. 2018). While the first structure solved was obtained in the presence of L-glutamate, the observed density in the binding site was not good enough for the substrate to be modelled (Yernool, Boudker et al. 2004). Subsequently, GltPh was characterised as an aspartate transporter as it has low affinity for glutamate and high affinity for aspartate (Boudker, Ryan et al. 2007).

Following on from the structures of bacterial homologues of EAATs, structures of the human SLC1 family members EAAT1 and ASCT2 showed that substrate binding and coordination is highly conserved across prokaryotes and eukaryotes. This is to be expected from the high sequence conservation (~60% between GltPh and human EAATs) in the C-terminal part of the transporters.

4.3.7.1 THE TFB-TBOA INHIBITOR BINDING SITE

Lauryl maltose neopentyl glycol (LMNG)-solubilised EAAT3 with TFB-TBOA bound adopted an inward-facing conformation. The strong density for the trifluoromethylbenzoyl (TFB)-group of TFB-TBOA positioned through the middle of the HP2 loop allowed unambiguous orientation of this group. The density for the L-aspartate moiety was less well defined and initially all rotational possibilities were evaluated. Once the side chains in the binding site were positioned, one conformation was more consistent with the density.

The L-aspartate moiety forms extensive contacts with residues in the binding pocket. The key interactions between the β-carboxyl-group of the aspartate involve T370 (TMH7), R447 and D444 (TMH8), while the α-amino and carboxylate groups form H-bonds with T448 (TMH8), and N451 (TMH8) and S333 (HP1), respectively. The rest of the molecule is inserted in a novel binding pocket formed by the HP2 loop, TMH2 and TMH5 (Figure 4.16 A). The pocket is lined primarily by hydrophobic residues and all the interactions with the ligand are hydrophobic (Figure 4.16 C).

TFB-TBOA locks the HP2 loop in an "open" state (where it cannot form interactions with HP1 loop), thus preventing it from closing over the binding site (Figure 4.16 A). As it is a non-transported inhibitor (Shimamoto 2008), the binding must have occurred when the transporter was in an inward-facing conformation, a feature observed with close analogue, L-TBOA in previous studies (Watzke and Grewer 2001).

To date, there are two other structures of EAAT3 homologues with TFB-TBOA bound: EAAT1 (PDB: 5MJU) and GltPh (PDB: 6X14). The EAAT1-TFB-TBOA-UCPH101 was solved in an outward-facing conformation. The L-aspartate moiety binds to the binding site and is coordinated by the same residues as seen in L-aspartate bound structure (PDB: 5LLU). The TFB tail part packs in a hydrophobic crevice formed by TMH2,4c and 7 and HP1 loop, preventing the HP2 loop from closing (Figure 4.16 B, inset)(Canul-Tec, Assal et al. 2017). The GltPh-TFB-TBOA complex was solved using cryo-EM and the transporter was in an inward-facing open conformation. The binding for the L-aspartate moiety of TFB-TBOA is similar to that seen in the EAAT3 structure, while the hydrophobic tail adopts a different rotamer with the TFB group packing against the HP2 loop and TMH1,2,5 and 8 (Wang and Boudker 2020). The binding of TFB-TBOA forces the HP2 loop away from the binding site and the binding pocket observed here is not formed (Figure 4.16 D).

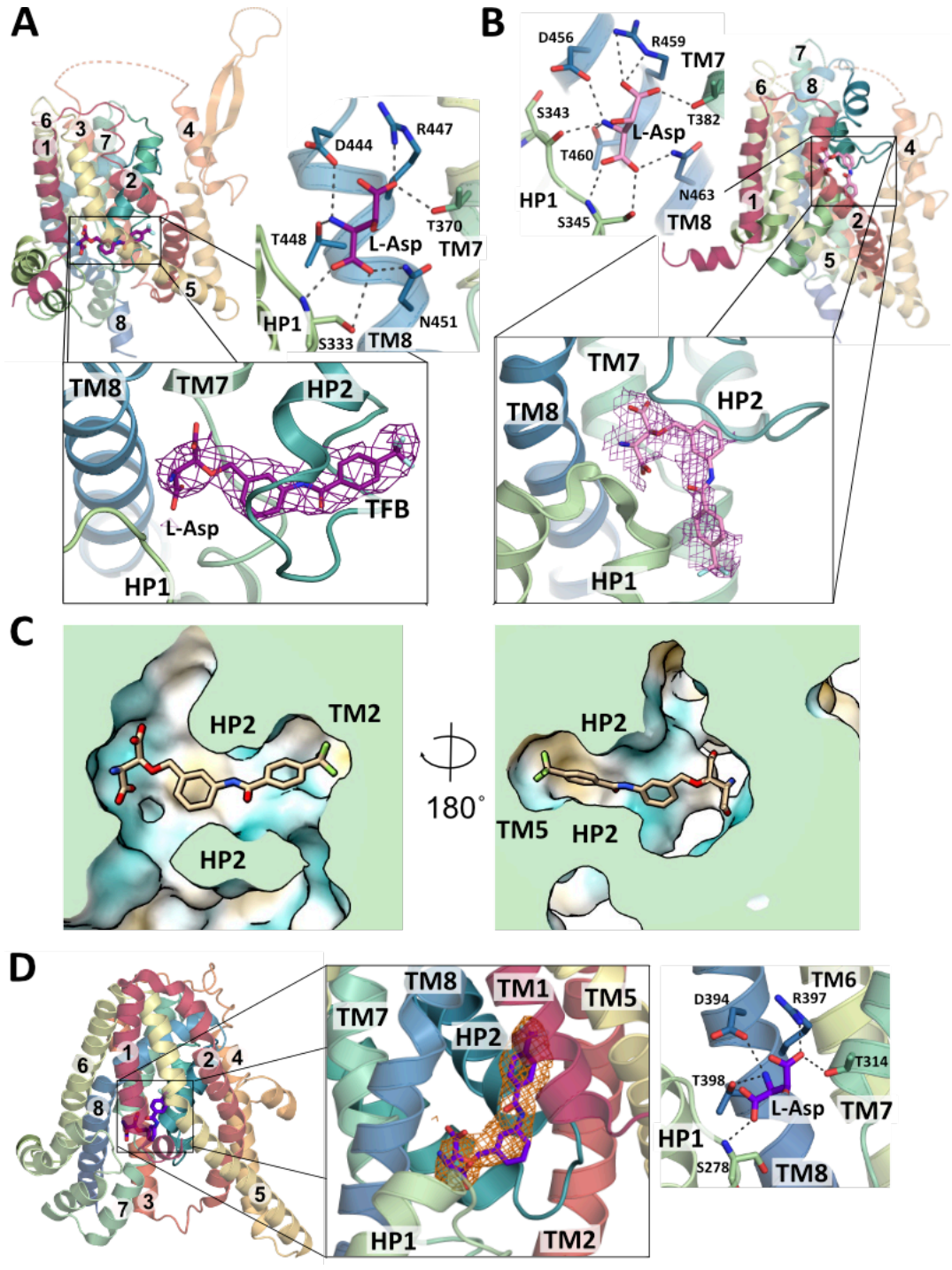


Figure 4.16: TFB-TBOA binding in EAAT3 **A** EAAT3 monomer with TFB-TBOA bound. The zoomed in section shows residues coordinating the L-Aspartate moiety, shown as sticks. The density for TFB-TBOA (at 3σ) is shown in inset. **B** EAAT1 monomer with TFB-TBOA bound (PDB: 5MJU). The residues coordinating inhibitor binding (EAAT1 numbering) are shown as sticks in the zoomed in section. The observed 2Fo-Fc density for TFB-TBOA (at 1σ) is shown in inset. **C** Binding of the TFB-TBOA in EAAT3 creates a hydrophobic pocket between TMH2,5 and HP2 loop. The surface is coloured by molecular lipophilicity potential, with dark cyan being the most hydrophilic and goldenrod being the most lipophilic surface (with white being in between) calculated in ChimeraX (Pettersen, Goddard et al. 2020). **D** GltPh monomer with TFB-TBOA bound (PDB: 6X14). The residues

coordinating inhibitor binding (GltPh numbering) are shown as sticks in the zoomed in section. The density for TFB-TBOA (at 3σ) is shown in inset.

4.3.7.2 THE ±HIP-B INHIBITOR BINDING SITE

HIP-B is commercially available as a mixture of enantiomers (±HIP-B). Studies using murine brain synaptosomes, which contain a mixture of EAATs, showed that in the presence of 10 μM L-glutamate, ±HIP-B inhibited glutamate uptake in a non-competitive manner (Funicello, Conti et al. 2004). The murine EAAT3 interaction with ±HIP-B has been characterised using SSM-based electrophysiology, suggesting the inhibition was not purely competitive (K_i of 4.6 μM and 2.6 μM in the presence of 15 μM and 100 μM L-glutamate, respectively)(Krause, Watzke et al. 2009). Chemically pure enantiomers have been characterised using murine brain synaptosomes and HEK293 cells expressing human EAAT1-3, with neither showing a clear preference for any of the EAAT subtypes and supporting mixed inhibition mechanism (Colleoni, Jensen et al. 2008, Callender, Gameiro et al. 2012).

Chemically HIP-B is a glutamate analogue with a constrained bicyclic conformation (Conti, Dallanoce et al. 1999). Site directed mutagenesis studies, combined with inhibition assays have been used to characterise the substrate binding and ±HIP-B inhibition mechanism for EAAT3. The binding of anionic substrates is proposed to be driven by coordination by the highly conserved R447, which could recognise the γ-carboxyl group of the amino acid (Bendahan, Armon et al. 2000). Similarly, it has been proposed that D444 could be crucial for orientating the substrate for the transport step and that it could prevent the transporter interacting with dicarboxylic acids (e.g., succinate) (Teichman and Kanner 2007). Therefore, the binding of ±HIP-B should be coordinated by both R447 and D444. However, studies of +HIP-B with an R446Q mutation in murine EAAT3 (R447 in hEAAT3 numbering, with this mutation EAAT3 binds neutral amino acids instead of acidic) showed that application of increasing +HIP-B concentrations inhibited the mutant transporter in the presence of transported glutamine (Callender, Gameiro et al. 2012), suggesting that R447 is not crucial for binding of this enantiomer. Together, this suggests that +HIP-B either binds allosterically to the mutant transporter or the binding mode is different from that of a glutamate. Since EAAT3 is also able to transport cysteine, it is not clear which interactions in the binding site contribute the most to substrate recognition and affinity.

The structure of EAAT3 was solved with ±HIP-B in the absence of substrate. The overall conformation is the same as is seen with the bound TFB-TBOA, with all three subunits in the inward facing

conformation. This agrees with the previous data showing that ±HIP-B has a slightly higher affinity for the intracellular binding site (Callender, Gameiro et al. 2012). In the substrate binding site, a tear-shaped density blob adjacent to residues D444 and T448 is seen. The density was quite symmetric and therefore it was not immediately clear how the inhibitor was bound or which rotamer was represented. The resolution of the density map was too low to unambiguously position the molecule, without careful analysis of the possible alternative binding modes. The alternative positions were modelled, refined and assessed visually based on the expected interactions within the binding site. The final positioning of ±HIP-B was aided by Dr. Ashley Pike. Amino acids can adopt multiple conformations in solutions, therefore the possibilities of ±HIP-B binding were assessed based on the positions of functional groups in L-aspartate involved in binding to hEAAT1 (PDB:5LLU). ±HIP-B could be binding in two ways based on the density, as the carboxylate group, which would aid in the positioning of the molecule, was not clearly visible and most likely lost due to radiation damage. The carboxyl group of ±HIP-B could bind analogous to the α-carboxyl group in aspartate, or it could be mimicking the β-carboxyl-group in aspartate. For both orientations, the amide group in ±HIP-B was aligned with the position of amino group in aspartate, since the density was most pronounced around the residues coordinating this group in other EAAT structures with bound substrate or substrate analogues (Figure 4.17).

Based on these considerations, both +HIP-B and -HIP-B binding with the carboxyl group aligned with the β-carboxyl-group in L-aspartate is more favourable (Figure 4.17). In this orientation, most of the possible enantiomers and conformations leave the ring structures facing away from the binding site in contrast to other orientation, in which the carbonyl group would be clashing with the TMH8 residues.

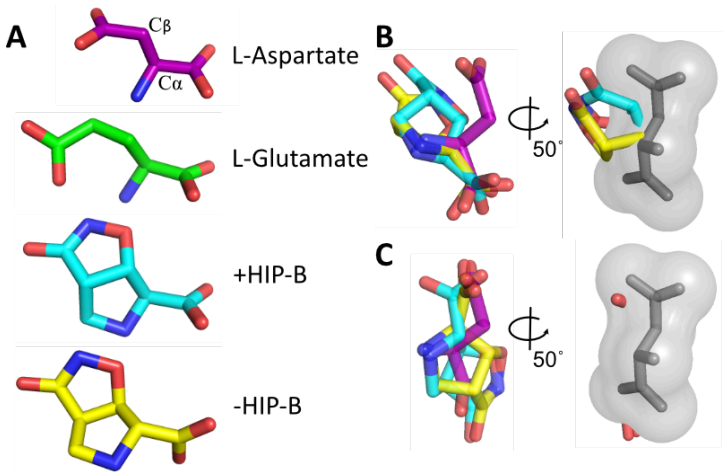


Figure 4.17: Exploration of ±HIP-B possible binding modes. **A** 3D-structures of substrates and ±HIP-B. **B** Alignment of carboxyl group in ±HIP-B with carboxyl group in L-aspartate as seen in hEAAT1

(PDB:5LLU). Shown in grey is the surface of L-Aspartate in the EAAT1-bound conformation. **C** Same as B but with ±HIP-B carboxyl group aligned with β-carboxyl-group of L-Asp.

Since a mixture of enantiomers were used in the EAAT3 complex formation, the possibility that both +HIP-B and -HIP-B are bound cannot be ruled out given the somewhat ambiguous shape of the density within the substrate binding site. Nevertheless, the 'C'-shape of the density allowed orientation of the ring structures so that the density curvature matched the selected poses. Both enantiomers were modelled in the density and the best fits are shown in Figure 4.18. The selected fits were based on the expected interactions with the highly conserved residues in the binding site (according to previous biochemical studies of EAAT3), assuming interactions with D444 were crucial and interactions with R447 were less critical. Based on the previous studies, +HIP-B should be bound with higher affinity (Callender, Gameiro et al. 2012). It cannot be ruled out that in the absence of substrate ±HIP-B can bind to the binding site in multiple conformations. However, ±HIP-B binding mode presented here is in agreement with an earlier molecular dynamics simulations using GltPh structure and glutamate (Shrivastava, Jiang et al. 2008). The glutamate appeared to bind to the binding site similarly, with its α-carboxyl group rather than γ -carboxyl group interacting with the highly conserved R447 (R397 in GltPh). Constrained glutamate analogue would be expected to bind in a similar way.

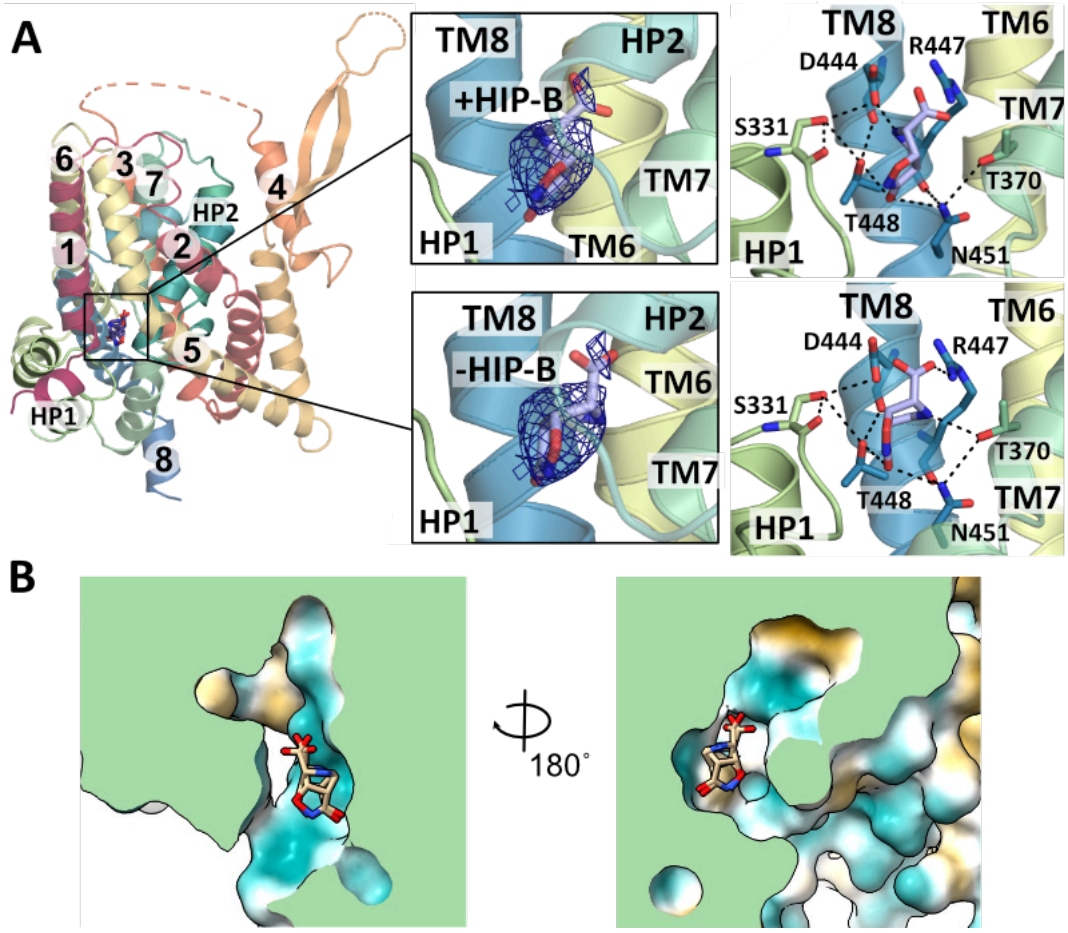


Figure 4.18: ±HIP-B binding in EAAT3. **A** EAAT3 monomer with ±HIP-B bound. Final refined masked map density (at 3σ) with the best fit for each rotamer are shown in the insets (+HIP-B shown in top, -HIP-B shown in bottom). The zoomed in sections show residues coordinating the respective ±HIP-B binding, shown as sticks. **B** The binding pocket ±HIP-B. The surface is coloured by molecular lipophilicity potential, with dark cyan being the most hydrophilic and goldenrod being the most lipophilic surface (with white being in between), calculated in ChimeraX (Pettersen, Goddard et al. 2020).

4.3.8 Comparison of Inhibitor binding modes

The overall mainchain conformation is maintained for the TFB-TBOA and ±HIP-B bound EAAT3 structures (0.3 Å Cα RMSD) with the most pronounced differences in the position of the HP2 loop. In both solved EAAT3 structures, the HP2 loop is in an open conformation, with the tip of the HP2 adopting more relaxed conformation in TFB-TBOA model (Figure 4.19 A). In the TFB-TBOA bound state, the loop shows great flexibility and is more unwound to accommodate the hydrophobic portion of the inhibitor. With ±HIP-B in the substrate binding site, the helical hairpin loop is shorter. In contrast, the HP1 loop maintains the same conformational state (Figure 4.19 A). This is in agreement

with the proposed one-gate mechanism where only HP2 loop movements are required for substrate binding and release (Garaeva, Guskov et al. 2019).

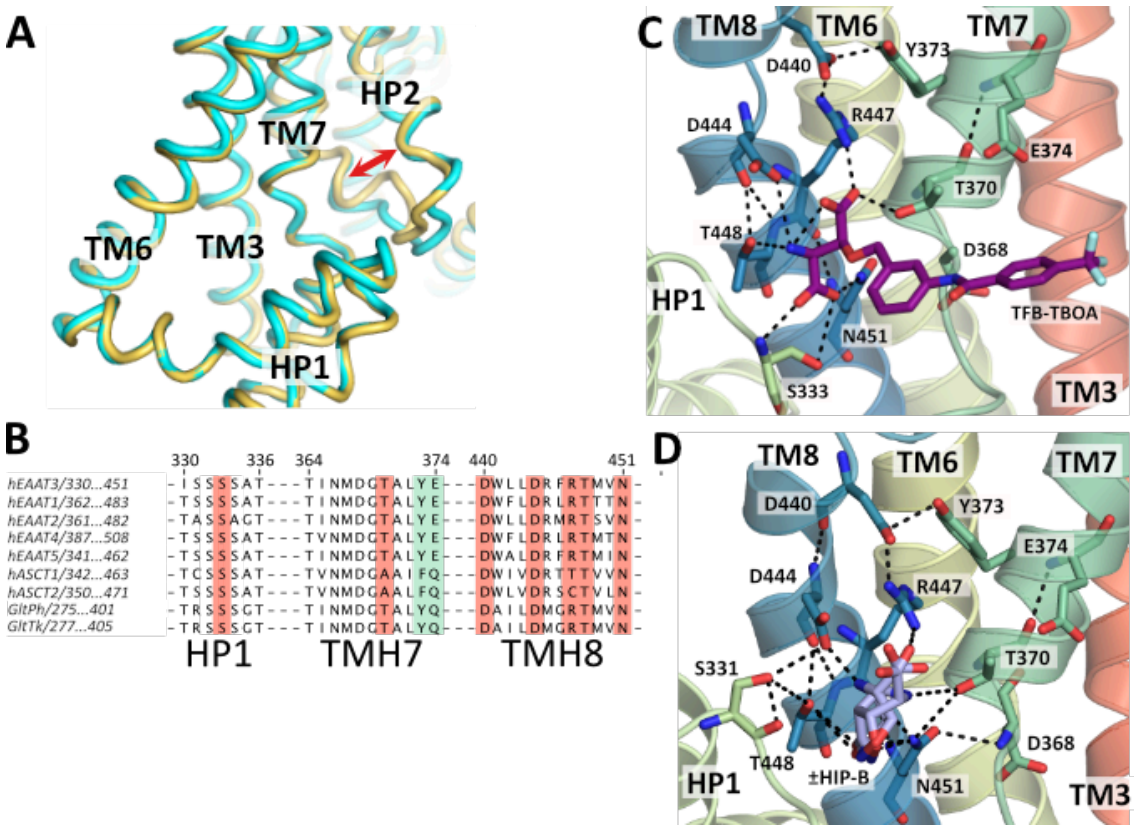


Figure 4.19: Analysis of the transport substrate binding sites of SLC1 family members. **A** HP2 loop unwinding seen in the TFB-TBOA-EAAT3 complex structure (shown in cyan). The ribbon representation of backbone carbon positions showing relaxation of HP2 loop compared to ±HIP-B model (shown in yellow). The red arrow indicates the start of separation between the two helices. **B** Sequence alignment for highly conserved residues in the substrate binding site area. EAAT3 numbering is shown for the alignment and the corresponding range of residues in the homologues are shown in brackets. The residues in red shading are involved in the substrate binding site formation while residues in green are proposed to be involved in K^+ binding. **C** Substrate binding site and inhibitor coordination in TFB-TBOA model. The HP2 loop is not shown for clarity. The conserved residues highlighted in panel B are shown as sticks. **D** Substrate binding site and inhibitor coordination in ±HIP-B model. The conserved residues highlighted in panel B (apart from S333) are shown as sticks. The HP2 loop is not shown for clarity.

In EAAT transporters, three acidic residues in the binding site region have been identified as crucial for transporter function (D368, E374, D440 and D444 in EAAT3 numbering), since mutations at D444 inactivate the transporter while no substrate transport was observed after mutation of either D374 or D440 to uncharged amino acids (Tao and Grewer 2007). As discussed previously, D368 is crucial for coordinating the binding of the first Na^+. D440 forms interactions with R447, potentially stabilising or

positioning it in a ligand-binding conformation (Figure 4.19 C,D). Neutralisation of D440 might disrupt this interaction, leading to a changed environment in the ligand binding site. D444, was shown to be important for selectivity towards dicarboxylic amino acids as the EAATs do not transport dicarboxylic acids (Teichman and Kanner 2007). In both EAAT3 structures D444 is interacting with not only the amino group of the substrate but also with other residues that coordinate the substrate (Figure 4.19 C,D). Any changes to the charge at this position would have wider implications than just lost coordination with the amino group.

Replacing E374 with a neutral amino acid gave protein with residual activity that was attributed to electroneutral substrate homo-exchange due to loss of K^+ coordination for the counter transport (Grewer, Watzke et al. 2003). The two highly conserved residues – Y373 and E374 – have been proposed to be involved in the H^+/ K^+ binding since the 373 position is a conserved Tyrosine in all the transporters that co-transport a single proton and the negative charge at position 374 is conserved in all the transporters that couple the substrate transport with a counter transport of a single K^+ ion (Figure 4.19 B). From the structure, Y373 and E374 form no interactions with the residues involved in substrate coordination, however, Y373 forms a hydrogen bond with D440 (Figure 4.19 C,D). This explains while substrate transport is abolished when either of Y373 and D440 is neutralised, as this would affect the R447 interaction with the substrate.

4.4 SUMMARY OF THE STRUCTURAL STUDIES OF EAAT3

I have solved the structures of EAAT3 in the presence of two inhibitors at 3.3 Å. Overall, these EAAT3 structures have the characteristic fold and trimeric assembly seen with other members of the family (EAAT1 and ASCT2). A novel CHS binding site and crevices occupied by lipids may offer insights in EAAT3 allosteric modulation, based on the observation that the EAAT1-selective allosteric inhibitor (UCPH 101) binds in a remote hydrophobic pocket (Canul-Tec, Assal et al. 2017). These inward-facing structures reveal novel binding modes for both TFB-TBOA and ±HIP-B. TFB-TBOA positions through the HP2 loop within a hydrophobic pocket not observed previously, while the substrate (L-aspartate) like moiety binds to the transport substrate binding site. The coordination of the residues in the binding site agrees with the previous structure of EAAT1 in the presence of TFB-TBOA, revealing the high conservation of substrate binding interactions. ±HIP-B is a glutamate analogue, and in the

absence of glutamate bound SLC1 family member structures, it is difficult to say if it binds in the same manner as glutamate. Unexpectedly, the two conserved residues – D444 and R447 – are seen to be coordinating the amino and carboxyl groups, respectively, not γ-carboxyl group as previously proposed for glutamate binding. The density is not good enough to unambiguously position ±HIP-B within the binding site but based on the ligand chemistry and the residues within the ligand binding site maintaining the same conformations as in TFB-TBOA bound structure (L-aspartate-like bound state) it is the best fit. Unfortunately, ±HIP-B is supplied as a racemate mixture, so both enantiomers were modelled, even though +HIP-B is reported to have 10 times better affinity. The structures provide essential information on ligand binding modes that could be used for design of ligands with improved selectivity and affinity.

CHAPTER 5

5 STRUCTURAL CHARACTERISATION OF FUNCTIONAL TREK-2 NANOBODIES

5.1 INTRODUCTION

TREK-2 is a potassium channel expressed in excitable cells which is required for maintenance of the resting membrane potential. It allows passive K^+ ion flow down the electrochemical gradient across the cell membrane. Initially described as a passive leak channel, TREK-2 is now known to be modulated by a diverse range of stimuli. The mechanisms underlying this regulation are still not well understood. To gain better insights into TREK-2 channel regulation, nanobodies were generated against a truncated construct of TREK-2 for which three-dimensional (3D) structures have been solved previously using X-ray crystallography. All generated nanobodies were screened to identify ones that bind to folded TREK-2. Electrophysiology studies, carried out by Alexander Cloake (Dept. of Physics, Oxford) characterised the functional effects of the different nanobodies, classified as either activatory, inhibitory or having no effect on TREK-2 function. Here I present the biophysical characterisation of three TREK-2 nanobodies – an activator, inhibitor and a non-functional nanobody – using SPR. The structures of the two functional nanobodies were determined using X-ray crystallography to further characterise the binding and to provide greater understanding of the mechanisms behind their functional effects.

5.1.1 STRUCTURAL STUDIES OF TREK-2

5.1.1.1 CHANNEL GATING IN THE TREK SUBFAMILY

While the TREK subfamily members have a large C-terminal domain that could potentially obstruct the pore from the cytoplasm, the TREK-1 channel was shown to be gated only at the SF gate (Piechotta, Rapedius et al. 2011). This was based on the observation that the inner pore was accessible to inhibitors and had similar binding affinities in both active and inactive channels. Both external and intracellular acidification regulate the channel activity. While extracellular pH inhibition is reduced at high external K^+ concentrations, it does not affect channel activation arising from intracellular acidification (Piechotta, Rapedius et al. 2011). Similarly, mutation of the TREK-1 residue identified as an

intracellular proton sensor to an alanine switches the channel to a constitutively active state that can be inhibited by extracellular acidification. Thus, intracellular signals can be overridden by extracellular stimuli suggesting both regulatory mechanisms function independently. This suggests that different regulatory mechanisms converge at the SF but likely act at different regions within it (Sandoz, Douguet et al. 2009). In fact, multiple cytoplasmic sensory signals, involving residues within the C-terminal domain, use the same gating mechanism, as mutations affecting the intracellular pH sensor affected activation by mechano-gating and inhibition by phosphorylation (Honore, Maingret et al. 2002). The three-dimensional TREK-2 structures revealed that the inner pore vestibule remains accessible in both "up" and "down" conformations, also suggesting that regulation of gating most likely occurs at the SF (Dong, Pike et al. 2015).

The structural basis of C-type inactivation was first shown for the bacterial KscA channel. The structures of this K^+ channel in high and low K^+ concentrations revealed a deformed SF in low K^+ concentrations due to the carbonyl oxygens at positions 2 and 3 flipping to face outside the pore where they form interactions with water molecules (Zhou, Morais-Cabral et al. 2001). Recently, similar observations were reported for the TREK-1 channel crystallised in the presence of high K^+ concentrations and then soaked in low K^+ concentration solutions, showing that absence or low concentration of K^+ (up to 50 mM) disrupted the carbonyl alignment in the SF filter positions 1 and 2. Importantly, both pinching and dilation of the SF pore were observed, attributed to the heterodimeric filter structure. The SF2-M4 loop dynamics was identified as crucial for the channel gating with E234 (E264 in TREK-2) supporting the loop conformation required for the conductive state. Disruption of this hydrogen bond network reduced the channel sensitivity to intracellular (pressure, temperature, small molecule) regulatory cues (Lolicato, Natale et al. 2020). In the *Shaker* K^+ channel, C-type gating was shown to depend on inter-K^+ interactions in the SF, which were affected if the interactions between the side chains of SF-forming residues and surrounding residues were altered (Ogielska and Aldrich 1999). C-type inactivation is thought to be slow process, and it is further slowed down at high extracellular K^+ concentrations (Baukrowitz and Yellen 1995). This poses a potential problem for structural studies using X-ray crystallography as high (non-physiological) salt concentrations are usually required to stabilise the protein, and improve crystal packing due to reduced protein solubility to obtain crystals that diffract to high resolution.

5.1.1.2 TREK-2 STRUCTURES REVEAL TWO CONFORMATIONS OF THE CHANNEL

TREK-2 structures in two conformational states were determined in our group (Dong, Pike et al. 2015). TREK-2 forms a homodimer with a central channel pore. The potassium permeation pathway is made up of a larger pore vestibule exposed to the cytoplasm followed by a narrow selectivity filter facing the extracellular side of the membrane. The SF forming loops are surrounded by four pseudotetrameric pore-forming helices (PH1-2 from both monomers), which are arranged as an inverted tepee. Finally, four transmembrane helices (M1-M4) from both monomers enclose the pore-forming region and form the vestibule. Specific to K2Ps is a characteristic extracellular "cap" domain, formed by two helices (EC1 and EC2) connecting the M1 and M2 helices of each monomer (Figure 5.1).

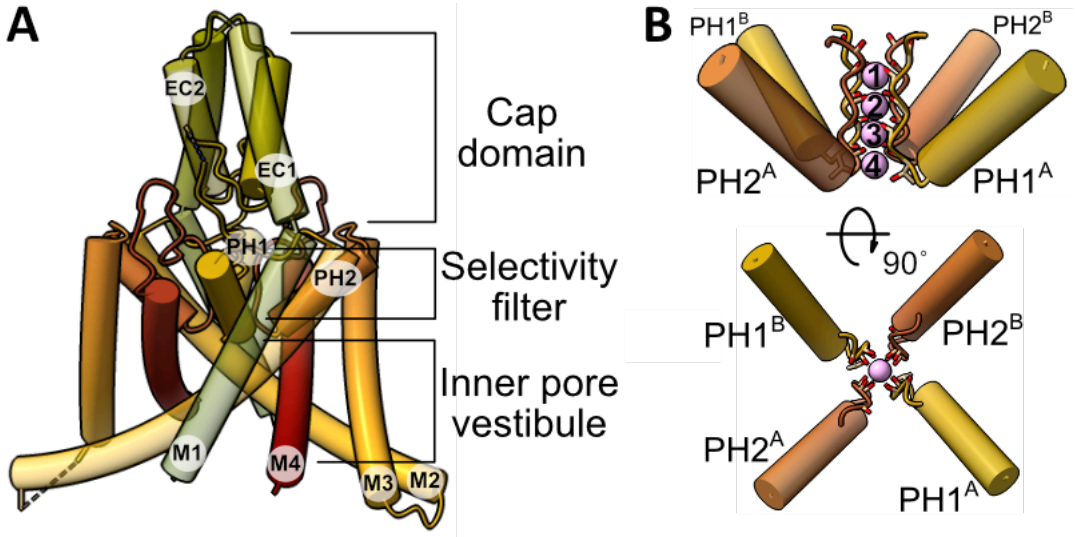


Figure 5.1: Schematic representation of the TREK-2 structure. **A** TREK-2 monomers assemble as domain-swapped homodimers with pseudotetrameric fold. For clarity, secondary structure elements (M1-4, EC1-2, PH1-2) are labelled for only one monomer. **B** The selectivity filter is positioned by four pore helices. PH1-2 are labelled A and B to indicate the two TREK-2 monomers. Four K^+ ion sites are formed by the backbone carbonyls of the SF residues (top).

Two main conformational states were observed, named the "up" and "down" states, and are identified based on the position of M4 helix. In the "up" conformation, M4's C-terminus is closer to the membrane and bent at a conserved glycine residue (G312) known as a hinge. In the "down" conformation, the M4 helix remains straightened, forming a lateral fenestration together with M2 helix. This fenestration exposes the pore vestibule to the cytoplasmic leaflet of the lipid bilayer and is closed when the M4 helix adopts the "up" conformation.

5.1.1.3 CRYSTALLISATION CHAPERONES FOR MEMBRANE PROTEINS

Structure determination of membrane proteins using X-ray crystallography remains a challenging task. The lack of solvent exposed domains, the transmembrane portion of the protein being covered by a detergent micelle and the conformational heterogeneity of membrane proteins all contribute to poor crystal contact formation, which often leads to poorly diffracting crystals. To improve crystal contact formation and diffraction quality, small soluble proteins can be used as crystallisation chaperones. These small binders are usually protein-specific and act through increasing the solvent-exposed surface area of the target protein. Monoclonal antibody fragments (known as Fabs) were used originally. However, camelid antibodies, known as nanobodies, are becoming increasingly popular. Due to their relatively small size (~14 kDa), nanobodies can reach and recognise epitopes that conventional Fabs (~50 kDa) cannot reach. This is due to the longer paratope regions of nanobodies. Nanobodies have three antigen-binding loops (complementarity determining regions—CDR1/2/3), where CDR3 determines the specificity while CDR1-2, and, occasionally, residues from the framework region, contribute to the binding strength (Figure 5.2). The flexible CDR3 loop that can adopt a finger-like shape and can recognise small pockets and narrow surfaces as epitopes. This is in contrast to classical antibodies that form a relatively flat paratope that recognises larger epitopes (Jovcevska and Muyldermans 2020). Nanobodies can also bind to a specific conformation of the antigen, resulting in modulated activity of the target. In the case of ion channels, such functional modulators would either activate or inhibit the target protein by locking it in an open or closed conformation. Structural studies of such functional nanobodies should hopefully provide insights into the molecular mechanisms of channel opening or closing.

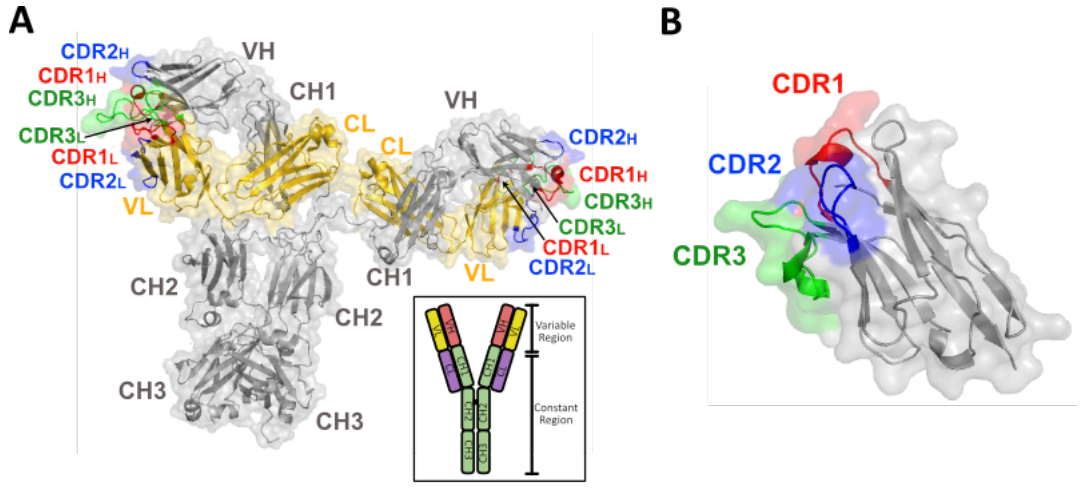


Figure 5.2: The architecture of antibodies and nanobodies. **A** Structure of a human IgG antibody (PDB:1HZH) with a cartoon schematic shown in inset. The IgG contains two heavy chains (V_H, C_H1-3, shown in grey) and two light chains (V_L, C_L, shown in gold). Both chains have a variable region with three CDRs. The CDR loops are coloured and labelled for the variable domains in the heavy (CDR1-3_H) and light chains (CDR1-3_L). **B** Structure of a nanobody raised against TREK-2. A nanobody is the heavy chain variable domain from the single chain antibodies of camelids. The three CDR loops are coloured as in **A**, with the framework region shown in grey.

Here I used the previously generated nanobodies against TREK-2 to characterise the binding kinetics of nanobodies exhibiting different modes of action and to study the mechanism behind TREK-2 activation and inhibition by these nanobodies at a structural level.

5.2 BIOPHYSICAL CHARACTERISATION OF TREK-2 BINDERS

TREK-2 nanobodies were expressed and purified as described in Section 2.1.1. Native mass spectrometry (Q-TOF) was used to verify the sequence of all nanobodies purified. Initial screening to identify nanobodies that bind to folded TREK-2 was performed by Dr. Karin Rödström using SEC on a high-performance liquid chromatography (HPLC) system (Dionex, Thermo Fisher). Nanobodies were classified as binders based on a shift to a shorter retention time compared to the apo TREK-2 retention time. Binders were further characterised using SPR. As shown in Figure 5.3, different binding kinetics were observed for each Nb. Nanobody 61 (Nb61) displayed fast on and off kinetics, Nb67 had slow on and fast off kinetics while Nb71 had slow on and slow off kinetics (Figure 5.3 A-C). As shown in Figure 5.3 D, Nb61 had an order of magnitude lower dissociation constant, K_D, than the other two nanobodies at ~ 1 μM. Nb67 and Nb71 both had high nanomolar affinity for TREK-2 (~0.4 and 0.1 μM, respectively).

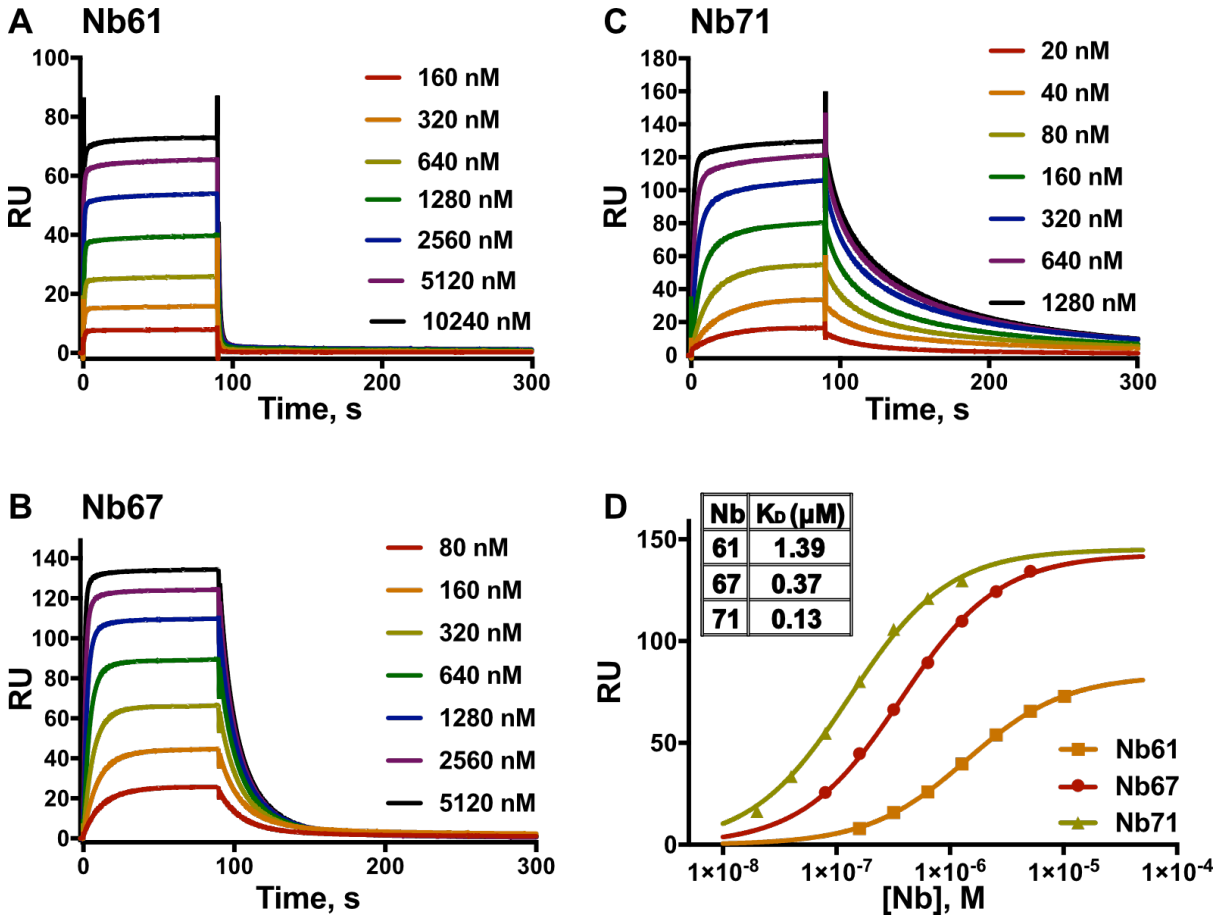


Figure 5.3: TREK-2 nanobody titrations to determine K_D by SPR. SPR measurements for 3 nanobodies previously identified as TREK-2 binders using SEC. **A**-**C** raw traces for the nanobody concentration titrations. **D** Binding curves for the nanobodies reveal a range of binding affinities. Processed results for the three nanobodies, n=1.

Next, I screened constructs with and without glycosylation mutations in two expression systems, to investigate role of TREK-2 glycosylation in nanobody binding. The initial affinity measurements were done with the TREK-2 construct that was used for nanobody generation (expressed in insect *Sf9* cells). Subsequently, I screened a construct used for the crystallographic studies (produced in the insect cell expression system but with putative glycosylation sites mutated to glutamines: N149Q, N152Q, N153Q) and mammalian-expressed TREK-2 to see if glycosylation patterns affect the nanobody binding. As shown in Figure 5.4, Nb67 bound to all TREK-2 forms with similar affinity, while the affinity of Nb71 for TREK-2 purified from *Sf9* cells was about 2-fold lower than for TREK-2 from mammalian cells or *Sf9* cells with no glycans present. Surprisingly, Nb61 showed no binding in this experiment, even though the same sample of TREK-2 was immobilised and one of the Nb61 biological replicates was from the initial experiment. This could be due to the nature of TREK-2 immobilisation

on CM5 chip. The immobilisation is random and any exposed lysines and arginines could be crosslinked to the matrix. It was very unexpected that no binding was observed for all three TREK-2 constructs with several batches of Nb61. As both Nb67 and Nb71 interactions were measured after the Nb61 binding experiment, unfolding or degradation of the immobilised TREK-2 can be eliminated as a possible cause. These results suggest Nb61 binds to a different site from the site recognised by Nb67 or Nb71 which is less accessible when TREK-2 is randomly immobilised on a surface. This phenomenon was also observed during the initial experiment when Nb61 binding resulted in only half the response observed with the other two nanobodies. Compared to the initial experiments, the K_D values measured in the subsequent experiments were all slightly higher. For measurements of ligand affinity using SPR, it is essential that the concentration of the injected ligand is accurately measured. The slight discrepancy between the results indicates the sensitivity of the system and is most likely due to slight inaccuracies in the measured protein concentrations.

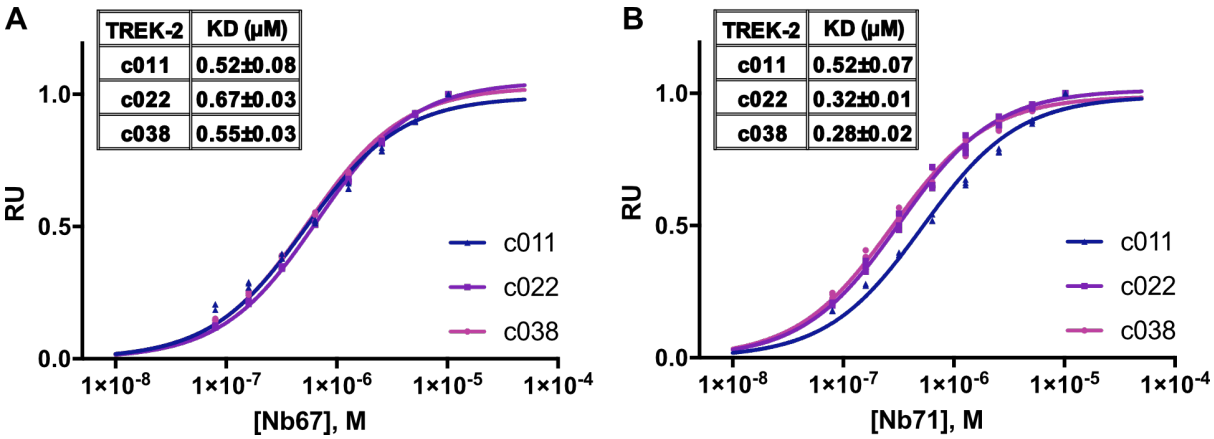


Figure 5.4: Nanobody titrations for TREK-2 protein derived from different expression systems. Binding shown for **A** Nb67 and **B** Nb71. Three biological replicates of nanobodies were used for these binding studies. TREK-2 constructs used: c011 – *Sf9* cell expression, intact glycosylation; c022 – HEK293 cell expression, intact glycosylation; c038 – crystallisation construct, *Sf9* cell expression, N-linked glycosylation sites mutated to glutamines (N149Q, N152Q, N153Q). All measurements are shown as single data points, RU – response units. Data normalised to the value for the highest nanobody concentration and the rest expressed as a ratio. Data was fitted using nonlinear regression analysis using a saturation binding equation ($Y = B_{max}*X/(K_D + X)$) in the Prism 8 GraphPad software.

In summary, I have used an SPR assay to characterise the kinetics of nanobody binding to TREK-2. TREK-2 was covalently immobilised on a CM5 chip using primary amine groups ($-NH_2$) and the affinity (K_D) of nanobodies determined, ranging from high nanomolar to low micromolar. Different kinetics of nanobody binding to TREK-2 were observed, with some of the nanobodies exhibiting fast

off-rates. This is unfavourable for co-crystallisation experiments as the complexes formed are unlikely to remain intact. To counteract this, excess nanobody could be used but this could interfere with the crystallisation due to higher sample heterogeneity or lead to crystallisation of the nanobody. Differences in the observed nanobody binding levels suggest at least one of the nanobodies recognise an epitope that is sensitive to the TREK-2 coupling to the matrix. Comparison of different expression systems reveals that nanobody binding is not affected by the presence of glycans, suggesting they do not recognise the flexible loop between the cap and TM domains with the putative glycosylation sites.

5.3 STRUCTURE DETERMINATION FOR COMPLEXES OF TREK-2 WITH FUNCTIONAL NANOBODIES

5.3.1 CRYSTALLISATION, DATA COLLECTION AND STRUCTURE SOLUTION

The functional binders were selected for the crystallisation trials. Nanobodies were incubated with TREK-2 (monomer) in 1:1 (mol:mol) ratio on ice for 30 min before setting up crystallisation plates. Both VD and LCP methods were tested to find the best conditions. Optimisation of the TREK-2 construct used was necessary to obtain well diffracting (<4Å) crystals. All initial crystallisation experiments were set up using a construct that was used for the structure determination of TREK-2 in its apo form (c011, covering residues 67-340). While initial crystals were obtained, they diffracted to only ~10 Å. As part of my crystal optimisation strategy, I tested various TREK-2 constructs with putative N- glycosylation sites removed (N to Q mutations) generated by previous group members (Dr Yin Dong and Dr Andrew Quigley). This improved crystal quality for the Nb67 complex and a relatively high resolution (2.4 Å) dataset was collected. The Nb61 complex crystallised in multiple crystal forms when grown in different VD conditions but even after extensive crystallisation condition optimisation they did not diffract to better than 6Å. In parallel, I performed LCP crystallisation trials, since the complex gave micro-crystals using monoolein (9.9 MAG) as the host lipid in initial crystallisation screening. To obtain bigger crystals with improved diffraction quality, I screened various host lipids before identifying 1-(7Z-hexadecenoyl)-rac-glycerol (7.9 MAG) as the preferred lipid for three-dimensional crystal growth. Compared to monoolein, 7.9 MAG is expected to form a thinner bilayer (the thicknesses of the bilayers at room temperature for the 9.7 and 9.9 MAGs are reported to be 33.2 and 35.6 Å, respectively (Liu and Caffrey 2005). 9.7 MAG and 7.9 MAG have the

same fatty acyl chain length (16 carbons) but 9.7 MAG has a *cis*-double bond between carbon atoms 9 and 10 while MAG7.9 has a *cis*-double bond between carbon atoms 7 and 8 (Li, Lee et al. 2011)). The crystals grown in LCP diffracted anisotropically up to 3.5Å in the best direction. Both complexes crystallised in orthorhombic space groups, with TREK-2:Nb61 complex ($C222_1$, Figure 5.5) diffracting to 3.5Å and TREK-2:Nb67 complex ($P22_12_1$, Figure 5.6) and diffracting to 2.4Å.

Membrane proteins can form 3D crystals in two ways: type I or type II. Within type I crystals, sheets of 2D crystals are organised through hydrophobic protein-detergent-lipid interactions that mimic the membrane. These layers are stacked on top of each other and held together by polar interactions. Type II crystals are formed through mainly polar interactions between the proteins, with the detergent micelle shielding the transmembrane regions (Michel 1983). TREK-2:Nb61 crystal packing represents type I, with parallel layers of TREK-2 glued together in a cap to cap orientation. Crystals grown in LCP are usually found to be type I (Caffrey, Li et al. 2012). TREK-2:Nb67 crystal packing is a mixture of types I and II. TREK-2 is assembled in parallel layers in head-to-toes arrangement (type I), while Nb67 forms polar interactions between the layers of TREK-2 (type II).

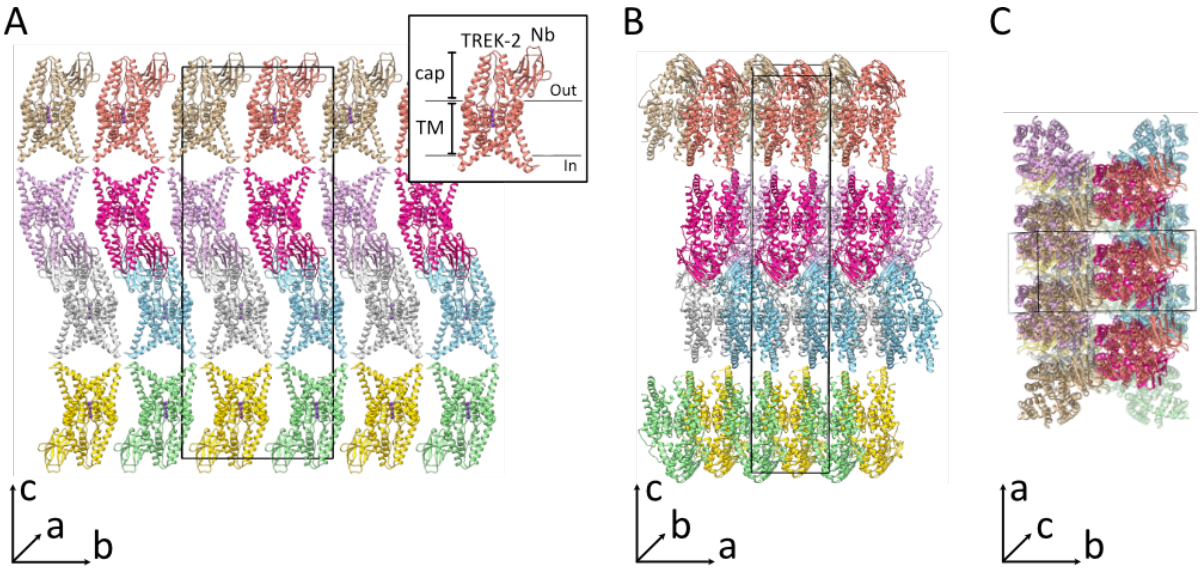


Figure 5.5: Packing arrangement of the TREK-2:Nb61 complex in the $C222_1$ crystal form. The unit cell (black rectangle) consisting of eight complexes of TREK-2 homodimers with a bound Nb61 (complex coloured gold, salmon, purple, magenta, grey, blue, yellow and green), are shown with a face-on view of the b/c plane in **A**, a/c in **B** and a/b in **C**. The structural elements of one monomer are shown in inlet in **A**. The predicted solvent content is ~60% (calculated using Matthew's coefficient (Matthews 1968)).

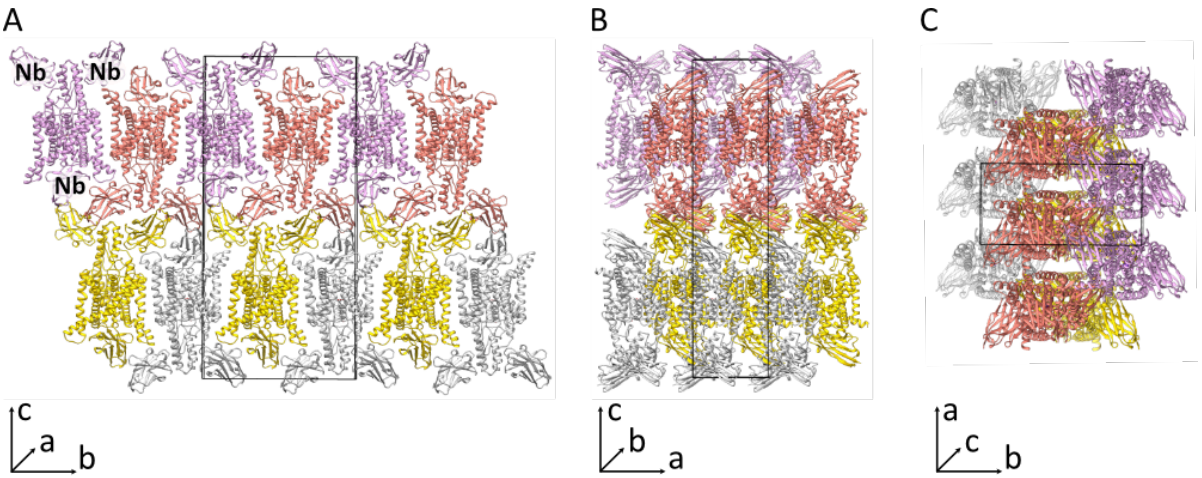


Figure 5.6: Packing arrangement of TREK-2 and Nb67 in the $P22_12_1$ crystal form. The unit cell (black rectangle) consisting of four complexes of TREK-2 homodimers with three bound Nb67 (as labelled in **A**) in gold, grey, salmon and magenta are shown with face-on view of the b/c plane in **A**, a/c in **B** and a/b in **C**. The predicted solvent content is ~54% (calculated using Matthew's coefficient (Matthews 1968)).

Data was processed as described in Section 2.4.6.3. For phasing, TREK-2 structures in the "up" (PDB:4BW5) and "down" (PDB:4XDJ) conformations were used for TREK-2:Nb67 and TREK-2:Nb61 datasets, respectively. Nanobody structures used for phasing (PDB:5IMK - for Nb61 and PDB:5UKB - for Nb67) were selected based on available structures with high sequence homology, determined using protein BLAST algorithm (Altschul, Gish et al. 1990).

It was to be expected that one nanobody would bind per TREK-2 monomer, since the recognised epitope should be highly specific, with two binding to a homodimer in the symmetry related positions. Both functional nanobodies described here crystallised in unexpected ratios. Molecular replacement solutions revealed one AU contained one Nb61 per TREK-2 dimer (1:2 Nb61:TREK-2 monomer ratio) and three Nb67s per TREK-2 dimer (3:2 Nb67:TREK-2 monomer ratio). For both complexes, Nbs that formed interactions with TREK-2 via CDR loops were chosen as binders. It is possible that Nb binding might induce conformational changes in the TREK-2 dimer, disrupting the second binding site, which could explain the TREK-2:Nb61 assembly. However, the TREK-2:Nb67 assembly is more peculiar, suggesting the Nb67 binding to the unique location was either caused by the crystal packing or the Nb recognises more than one epitope, perhaps with a much lower affinity for the second site.

The model building and refinement strategy is described in Section 2.4.6.4. For the TREK-2:Nb67 complex, the final model included residues 75-333 for chain A and residues 74-339 for chain B (where

chain A and B refers to the two monomers), 5 K^+ ions and 205 waters. For the TREK-2:Nb61 complex, the final model included residues 74-323 for chain A and residues 75-324 for chain B, and 4 K^+ ions. In both complexes, the entire nanobody could be modelled in both datasets, with only a few flexible side chains not assigned. For TREK-2, a model of the entire protein could be built in Nb67 complex structure, while in Nb61 complex structure, residues 226-236 of the loop between the M2 and M3 helices had no electron density and were not modelled. The data quality for both data sets and the final models are summarised in Table 5.1.

Data Collection	**TREK-2:Nb61**	**TREK-2:Nb67**
Space group	$C222_1$	$P22_12_1$
Cell dimensions a/b/c (Å)	56.54/111.70/ 289.21	51.26/102.10/215.82
α/β/γ (°)	90/90/90	90/90/90
Resolution (Å) (along the a*/b*/c* axes)[1]	3.5 (3.4/ 3.5/ 3.4)	2.4 (3.2/ 2.4/ 2.3)
Resolution range (Å) Overall/ Inner/ Outer shells	57.8-3.5/ 57.8-10.0/ 3.6-3.5	58.8-2.4/ 58.8-7.4/ 2.5-2.4
R_{merge} (Overall/ Inner/ Outer shells)	0.490/ 0.070/ 1.826	0.201/ 0.095/ 1.250
R_{meas} (Overall/ Inner/ Outer shells)	0.540/ 0.080 / 1.997	0.219/ 0.106/ 1.363
I/σ I	3.7	6.3
Correlation coefficient ($CC_{1/2}$)	0.997	0.989
Completeness (%) (spherical/ ellipsoidal)	95.0/ 95.0	75.6/ 94.3
Unique reflections	11445	34388
Wilson B factor (along the a*/b*/c* axes)[2]	69.33/ 58.26/ 54.71	85.33/ 41.69/ 35.56
Multiplicity	5.6	6.4
Refinement		
Resolution (Å)	3.50 (52.1–3.5)	2.4 (32.5-2.4)
R_{work}/R_{free} (%)	0.24/0.27	0.24/0.26
No. of chains in AU	3	5
No. of protein atoms	4508	6864
No. of K^+ atoms	4	5
No. of water atoms	0	205
Mean B-factor (Å)	65.61	48.78
RMSD bond lengths (Å)	0.006	0.006
RMSD angles (°)	0.78	0.78
Ramachandran favoured/outliers (%)	96.14/0.34	98.33/0.22

Table 5.1. Crystallographic data collection, phasing and refinement statistics.

[1] Reciprocal unit-cell vectors and principal axes of the ellipsoid fitted to the diffraction cut-off surface as direction cosines in the orthogonal basis (standard PDB convention):
a* (1.0000, 0.0000, 0.0000)

b* (0.0000, 1.0000, 0.0000)
c* (0.0000, 0.0000, 1.0000)
[2] Reciprocal unit-cell vectors and eigenvectors of the overall anisotropy tensor as direction cosines in the orthogonal basis (standard PDB convention):
a* (1.0000, 0.0000, 0.0000)
b* (0.0000, 1.0000, 0.0000)
c* (0.0000, 0.0000, 1.0000)

5.3.2 STRUCTURE OF A COMPLEX OF TREK-2 WITH THE ACTIVATING NANOBODY NB67

5.3.2.1 CRYSTAL PACKING IN THE TREK-2:NB67 COMPLEX

Packing of the TREK-2:Nb67 complex in the crystal lattice is facilitated by nanobody interactions. Nb67 forms extensive self-self contacts with symmetry-related nanobodies, with the conserved framework regions packing against each other (Figure 5.7).

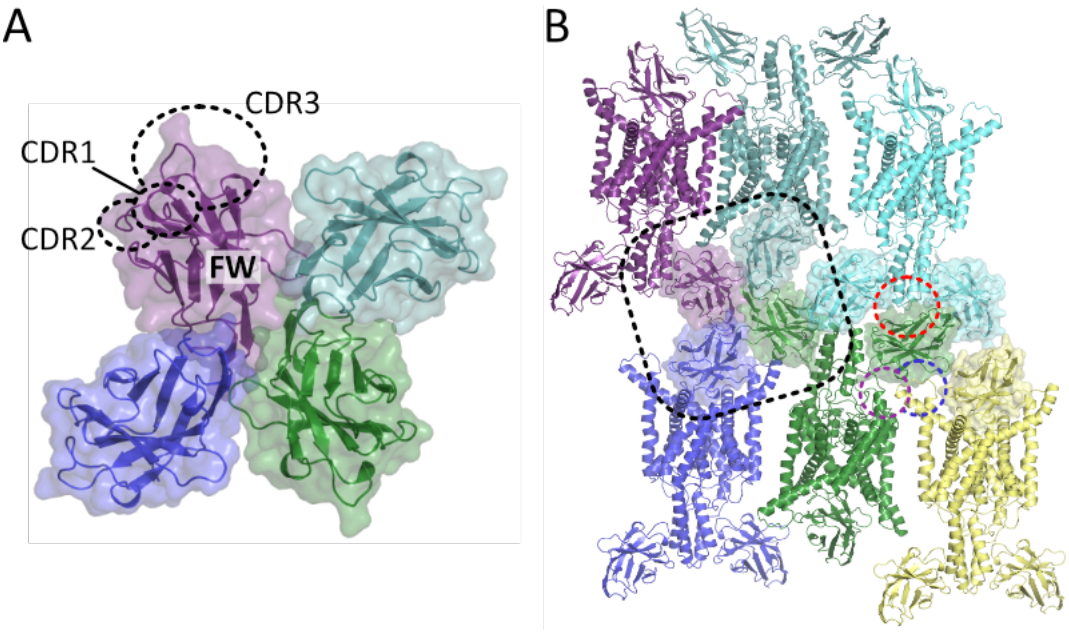
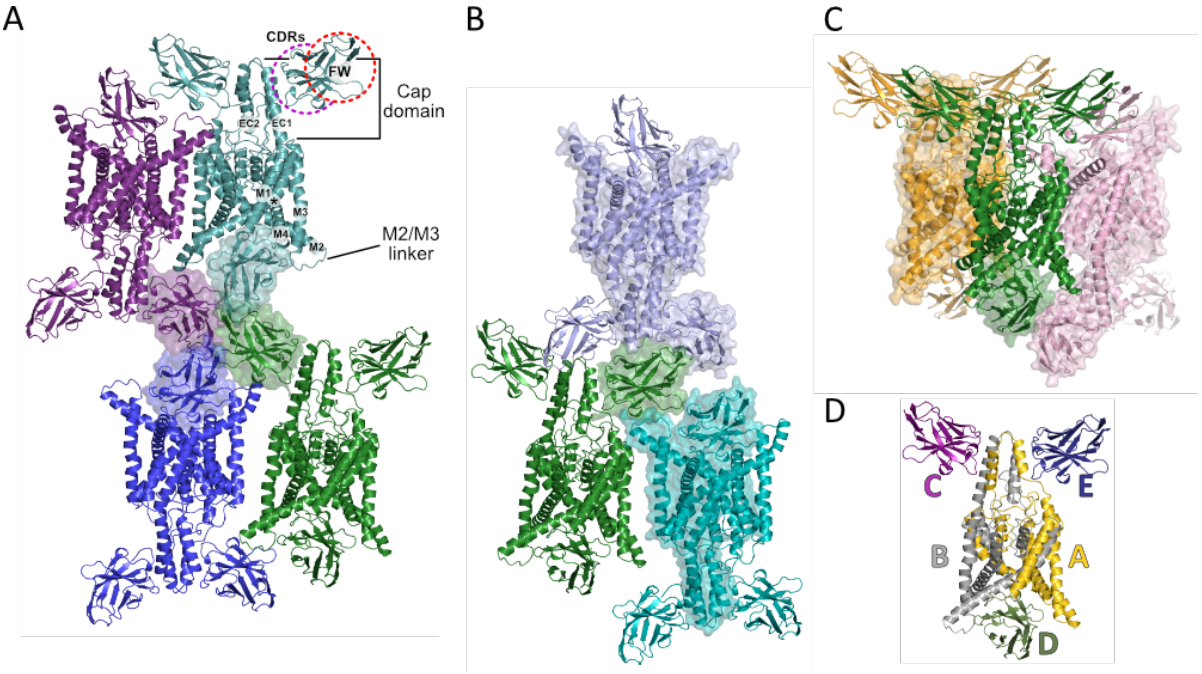


Figure 5.7: Nanobody-67 crystal contacts in the TREK-2:Nb67 complex. **A** Adjacent Nb67 monomers pack against each other forming contacts within the framework (FW) regions. The hypervariable loop regions (CDR1-3) face outwards, forming contacts with TREK-2 as shown in B (dashed rectangle). **B** Nb67 drives the crystal packing of the TREK-2:Nb67 complex. Most of the interactions within the crystal come from Nb67-Nb67 interactions since Nb67 binding to TREK-2 covers most of the solvent exposed TREK-2 surface areas. Interactions between Nb67 and the tip of the cap domain of a neighbouring TREK-2 dimer is indicated with a red, dashed circle; interactions between Nb67 and the loop connecting the M2 and M3 helices is indicated with a dark blue, dashed circle. The interaction between two TREK-2 monomers is indicated with a purple, dashed circle.

Since Nb67 binding covers most of the TREK-2 cap solvent exposed surface, the only interactions between Nb67 and the neighbouring TREK-2 dimers include the tip of the cap domain and the loop

connecting the M2 and M3 helices (Figure 5.7 B). The channels themselves form crystal contacts, with the most prominent formed between the loop connecting the M2-M3 helices in one monomer and the EC1 helix in the other (Figure 5.7 B). Interestingly, EC1 is partially unwound with both the M2/M3 linker and Nb67 binding to EC1, forming interactions within the unwound region. The rest of the interactions are ≤ 100 Å^2 and are between the M1, M2 or M4 helices (Figure 5.8).



Chains involved in crystal contacts (Panel)	Regions involved in contact formation		Surface area, Å^2	H-bonds	Salt bridges
	Symmetry mate	TREK-2:Nb67 (AU)			
C / C (A)	Nb framework	Nb framework	468	7	0
C / D (A)	Nb framework	Nb framework	436	5	0
A / E (B)	A tip of cap domain	Nb framework	292	6	0
B / E (B)	B M2/M3 linker loop	Nb framework and CDR3	289	3	6
C / D (C) *	Nb framework	Nb framework	270	1	0
B / A (B)	B M2/M3 linker loop	A EC1 helix before unwound region	179	3	0
C / A (C)	Nb CDR3 loop	A M2/M3 linker loop	122	1	2
C / E (B)	Nb framework	Nb framework	114	0	0
A / B (C)	A M1 N-terminal part	B M1 N-terminal and M4 C-terminal part	114	0	0
B / E (B)	B tip of cap domain	Nb framework	88	0	0

B / B (C)	B M2 C-terminal and M4 N-terminal part	**B** M4 end and M1 C-terminal part	74	0	0
E / D (B)	**Nb** framework	**Nb** framework	62	0	0
A / A (C)	A M2-N-terminal part	**A** M2 C-terminal part	24	0	1
A / A (C)	A M1 C-terminal part	**A** M4 N-terminal part	12	0	0
B / B (B)	**B** M2 N-terminal part	**B** M2 C-terminal part	10	0	0

Figure 5.8: Protein-protein crystal contacts between TREK-2- Nb67 complexes in the crystal. Schematic representations of unique crystal packing contacts formed by AU consisting of a TREK-2 homodimer with three Nb67 bound is shown in dark green. For clarity, unique crystal contacts formed by each AU, determined by PDBePISA analysis (Krissinel and Henrick 2007), are shown in three panels **A-C** with the chains forming crystal contacts shown in surface representation. **A** Interactions formed by Nb67 (chain C). Secondary structure elements are labelled for clarity, and the glycine hinge in M4 indicated by an asterisk. **B** Interactions formed by Nb67 (chain E). **C** Interactions formed by Nb67 (chain D). **D** The naming system used for chains in the AU. The details of the interactions, buried surface area, number of hydrogen bonds and salt bridges formed are listed in the table. The colour coding is maintained between the schematic representations and the table. *Also **C / D** (A) to illustrate the tight nanobody packing.

5.3.2.2 OVERALL STRUCTURAL FEATURES IN THE TREK-2:NB67 COMPLEX

TREK-2 co-crystallises with three Nb67 molecules bound per TREK-2 dimer. Two Nbs recognise an overlapping epitope on either side of the cap domain, while the third one binds from the intracellular side. Electrophysiology studies of the effects of Nb67 on TREK-2 revealed that Nb67 is a functional binder; it was shown to be an activator. It increases the observed TREK-2 channel currents in a dose-dependent manner with an EC_{50} value of around 100 nM (electrophysiology measurements of WT TREK-2 in *Xenopus laevis* oocytes were performed by A. Cloake, Dept. of Physics). Since the functional studies were performed with the nanobodies applied from the extracellular side, only the nanobodies bound to the cap domain are thought to modulate the channel activity. Whether Nb67 binding from the intracellular side could also modulate TREK-2 activity remains to be determined.

Overall, TREK-2 in complex with Nb67 adopts an “up” conformation since the M4 helix is rotated around the conserved glycine hinge. This is consistent with previous studies suggesting that the “up” state is a more conductive conformation (Dong, Pike et al. 2015, Brennecke and de Groot 2018). There

are some notable differences between the apo and Nb67 bound structures. The two TREK-2 monomers, here referred to as chain A and chain B, have a symmetrical cap architecture in the apo form (Figure 1.12). However, binding of Nb67 induces asymmetry in the cap, which could be due to a genuine change in the structure or could be induced by the formation of crystal contacts. The EC1 helix in chain A is unwound after Q106 and regains its helical structure after I110, causing the top of the cap to be shifted by 8.5 Å compared to chain B (Figure 5.9).

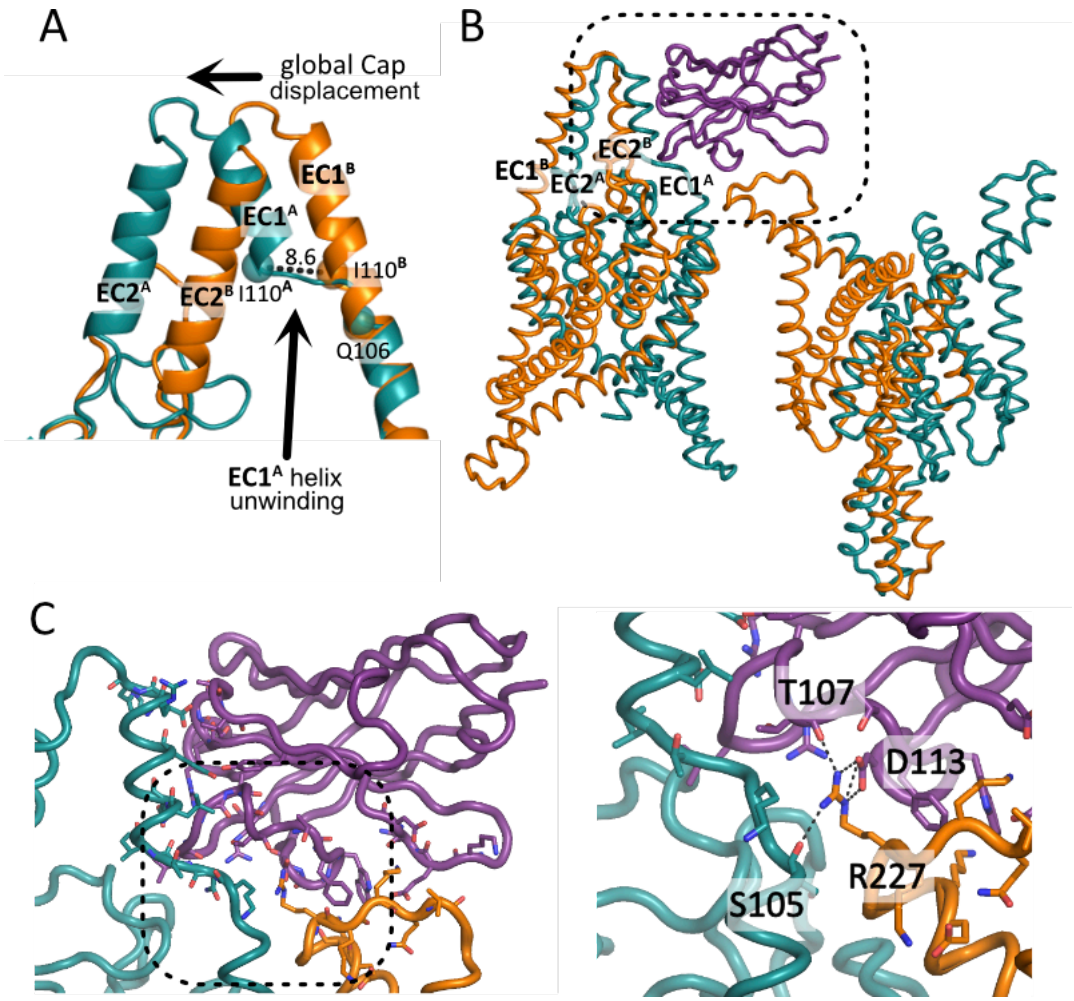


Figure 5.9: Nb67 binding causes local rearrangements in the cap domain of the TREK-2 monomer. **A** Alignment of TREK-2 monomers in the TREK-2:Nb67 complex. Arrows indicate the EC1 helix unwinding and the global cap displacement. TREK-2 chain A is shown in teal, chain B is shown in orange. Positions of residues Q106 and I110 are shown as spheres, and the RMSD distance between I110 in chain A ($I110^{A}$) and chain B ($I110^{B}$) is shown in Å. The RMSD distance between Q106 in chain A and chain B is 1.6 Å. **B** Nb67 forms interactions with two TREK-2 dimers. **C** $Nb67^{A}$ binding interface. Residues forming the binding interface are shown as sticks (left). The zoomed in view (right) on the unwound region of the EC1 helix with hydrogen bonds formed between residues from TREK-2 (teal), Nb67 (purple) and symmetry-related TREK-2 monomer (orange).

The helix unwinding causes a rigid body shift of the intact EC1-EC2 helical unit, since the Cα RMSD for the M1 helix up until Q106 is 0.104 Å, and 0.322 Å for the EC1-EC2 helices after residue I110 when comparing chains A and B. Nb67 binding to TREK-2 chain B ($Nb67^{B}$) forms hydrogen bonds with residues E113, E116 and D120 in EC1, that are maintained in the Nb67 interactions with TREK-2 chain A ($Nb67^{A}$). $Nb67^{A}$ forms additional interactions within the unwound EC1 helix region (Figure 5.10).

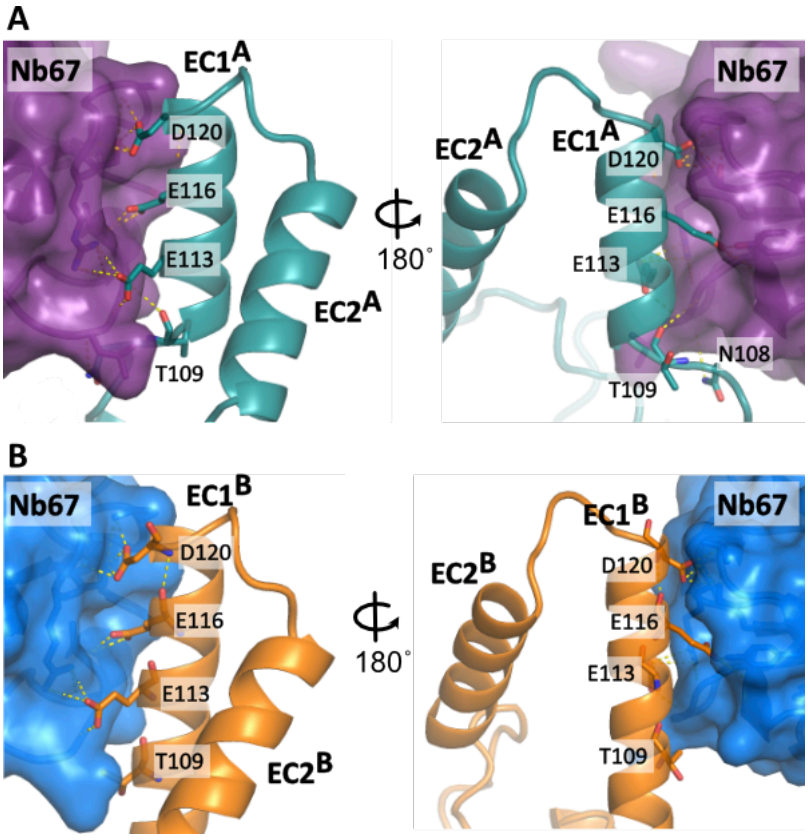


Figure 5.10: Nb67 interactions with the EC1 helix. **A** $Nb67^{A}$ forms hydrogen bonds with residues in EC1 and with N108 and T109 in the unwound EC1 section **B** $Nb67^{B}$ forms same interactions with residues in intact EC1 while the interactions with N108 and T109 are lost.

The unwound part also forms interactions with residues from the M2/M3 linker region from a symmetry-related TREK-2 molecule, suggesting the $EC1^{A}$ helix is somewhat flexible and can be unwound to accommodate the formation seen in these crystal structures (Figure 5.9 C). The whole cap domain is slightly tilted compared to the apo structure, but slight differences in cap domain position have been observed in previous TRAAK structures with bound Fabs (Brohawn, Campbell et al. 2013). The loop connecting the $EC2^{A}$ helix with $PH1^{A}$ adopts a different conformation compared to the EC2-$PH1^{B}$ loop, which adopts a conformation similar to the one in the apo form (Figure 5.11 A). The EC2-

PH1^{A} loop is looped around the extracellular exit of the SF, forming hydrogen bonds with G176 and S181 in SF1^{A} and SF1-M2^{A} connecting loop, respectively, and D286 in SF2-M4^{A} connecting loop (Figure 5.11).

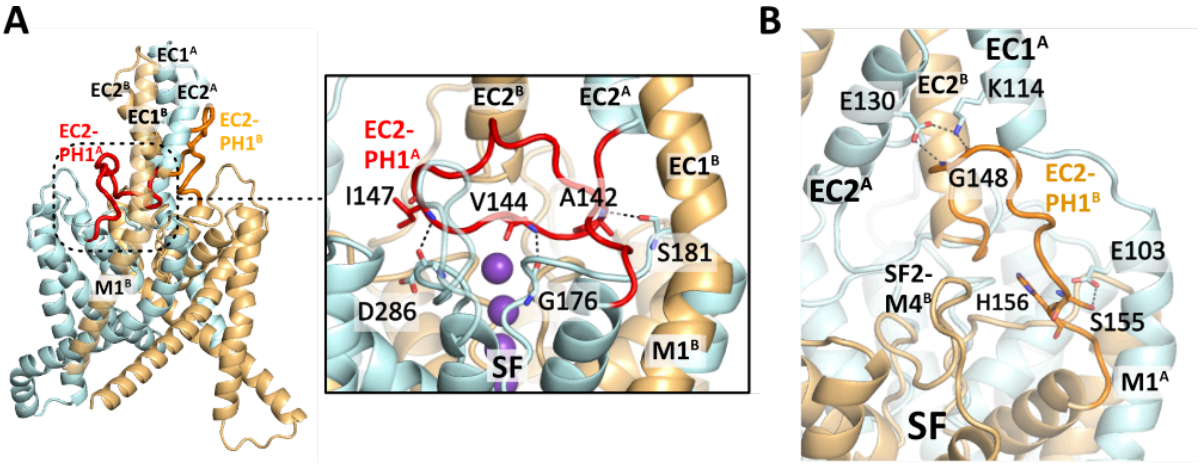


Figure 5.11: The EC2-PH1 loops two adopt different conformations in the asymmetrical TREK-2:Nb67 complex. **A** In chain A, the EC2-PH1 loop interacts with residues surrounding the SF. EC2-PH1^{A} loop is shown in red, EC2-PH1^{B} loop is shown in orange. **B** In chain B, the EC2-PH1 loop adopts the same conformation as is seen in the TREK-2 apo structures. The loop is stabilised by residues from the EC1-EC2 helices. Chain A is shown in pale cyan and chain B is shown in light orange.

The EC2-PH1 loop in chain B adopts a conformation very similar to apo structures, even though some of the interactions with the EC1 helix are lost due to it being unwound. The top of the loop is coordinated via its backbone to the side chains of K114^{A} and E130^{A}, and the C-terminal end by E103^{A} in the M1 helix (Figure 5.11 B). The position of the loop must depend on the residues not affected by EC1 helix displacement. This loop contains the putative glycosylation sites that were mutated to glutamines in this TREK-2 crystallisation construct (N149Q, N152Q, N153Q), but were intact in the apo form. While the apo form construct was treated enzymatically with PNGaseF to remove the glycosylations prior to crystallisation, residual glycans might have remained that might have affected the positioning of the loop. However, the similarities in the loop positioning in chain B and the apo form suggests that the presence of glycans is not required for this conformation. The reason behind the loop adopting different conformations could arise from the global EC2^{A} helix displacement.

Differences between the apo and Nb67-bound structures are also seen around the cytoplasmic regions of the M2 and M3 helices. Compared to the apo structure, the M2^{A} helix bends at a different position, A220 in the complex, compared to G212 in apo TREK-2 (PDB:4BW5). However, M2^{B} remains in a

straighter conformation. Since the $M2^B$ helix forms crystal contacts, the conformation it adopts could be caused by crystal packing. The M3 helices in both chains are straighter compared to the apo structure and do not bend in the hinge region (Figure 5.12 A). The M2/M3 linker region is known to be quite flexible and able to adopt different conformations as seen in multiple TREK-family structures solved to date (Lolicato, Riegelhaupt et al. 2014, Dong, Pike et al. 2015). This flexibility has been attributed to the coordinated movement of the M2, M3, and M4 helices associated with channel regulation. The M2/M3 linker region and the end of M4 helix are the most flexible parts of TREK-2 in this crystal form. The crystal packing could reduce the flexibility of chains through crystal contact formation, while in this case the whole M2/M3 region retains some flexibility (Figure 5.12 B).

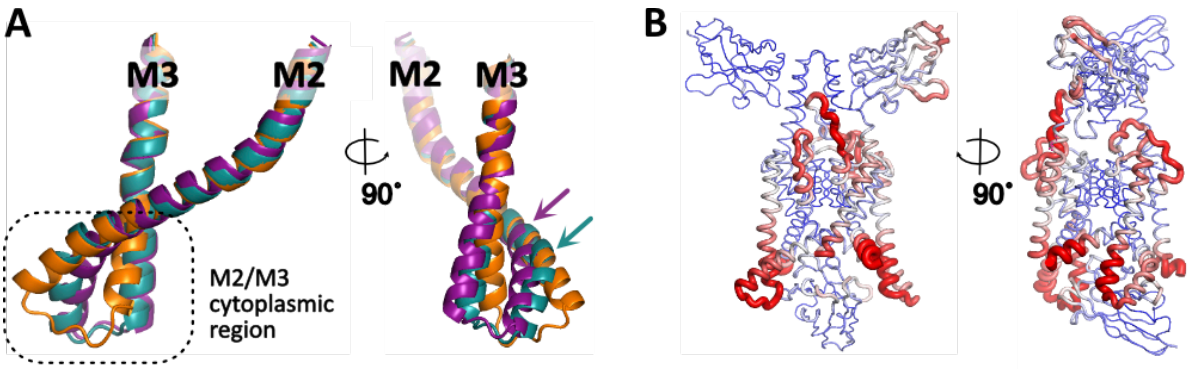


Figure 5.12: Flexibility in the TREK-2:Nb67 complex. **A** Movement of the M2-M3 helices in the TREK-2 Nb complex structures. Overlaid cartoon representations of chain A (teal) and chain B (orange) from the TREK-2:Nb67 complex and chain A (purple) from TREK-2 apo structure (PDB:4BW5). **B** Cartoon representation of the TREK-2:Nb67 complex with colouring and worm thickness weighted by temperature-factor (blue=30 $Å^2$; red = 80 $Å^2$ B-factor). The regions with highest flexibility form contacts with other flexible regions or are not involved in crystal contact formation.

It is generally thought that TREK-2 is gated at the SF, yet the SF is in the same conformation in most of the K2P crystal structures solved to date (Miller and Long 2012, Brohawn, Campbell et al. 2013, Dong, Pike et al. 2015, Lolicato, Arrigoni et al. 2017, Li, Rietmeijer et al. 2020, Rodstrom, Kiper et al. 2020). This has been attributed to the high K^+ concentrations (150-200 mM) common in the crystallographic studies, which is non-physiological for the K2P channels (Lolicato, Natale et al. 2020). The typical K^+ concentrations *in vivo* are ~140 mM intracellularly and ~5 mM extracellularly. It has also been shown that high extracellular K^+ concentrations slow down the K2P channel gating, since the extracellular K^+ binding site must be unoccupied for the channel to inactivate (Baukrowitz

and Yellen 1995). High external K^+ concentration was shown to alter the pH activation of TREK-2 (Sandoz, Douguet et al. 2009). In a recent study, structures of a crystallographic construct of TREK-1 was solved in the presence of a range of K^+ concentrations and the authors noted that inactivated channel, marked by distortions of the SF, was only observed when the K^+ concentration was <50 mM (Lolicato, Natale et al. 2020). However, this observation is not agreement with a crystal structure of TREK-1 with pinched SF (PDB: 4TWK), which was crystallised in the presence of high K^+ concentrations (~100 mM). In the TREK-2:Nb67 structure presented here the four K^+ atoms seen in the selectivity filter have strong density and a fifth K^+ ion could be modelled within the extracellular binding site (Figure 5.13).

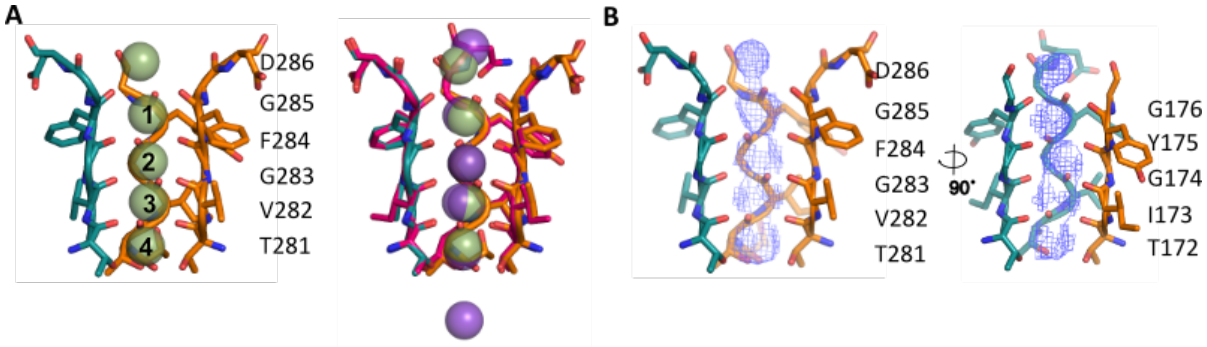


Figure 5.13: K^+ ions modelled in the TREK-2:Nb67 structure. **A** On the left, the selectivity filter of the TREK-2:Nb67 complex is shown with the positions of K^+ ions in the SF. $SF1^A$ is not shown for clarity. Chain A is shown in teal, chain B is shown in orange. On the right the TREK-2:Nb67 model is overlaid with the TREK-1 apo structure (PDB: 5VKN) shown in pink. In both models, $SF1^A$ is not shown for clarity. The K^+ ion positions in TREK-1 are shown as purple spheres. **B** The 2Fo-Fc map for the K^+ ions in the TREK-2:Nb67 structure is shown at a 1σ map contour level with $SF1^A$ (left) or $SF2^B$ not shown for clarity (right).

The position of the fifth K^+ ion could not be verified in anomalous difference maps since the dataset was collected at wavelength (0.9116 Å) where K^+ has very low anomalous signal. I chose to model a K^+ ion instead of water based on a K^+ modelled in a similar position in TREK-1 structure with bound activator (PDB:5VKN). This K^+ ion position has not been modelled before in TREK-2 structures. The structural architecture of the selectivity filter area is very conserved with a Cα RMSD of 0.407 $Å^2$ (over 311 atoms) between the apo and Nb67 bound TREK-2 structures. The A and B chains in the TREK-2:Nb67 complex adopt very similar conformations apart from the distorted cap region. The RMSD for the Cα between the chains is 0.782 $Å^2$ (over 1449 atoms).

5.3.2.3 How Nb67 activates the TREK-2 channel

Since Nb67 stabilises TREK-2 in an open conformation, it was not surprising the complex crystallised in an "up" conformation. However, the position of M4 helix has been shown not to be the sole determinant of the channel activity state (Lolicato, Natale et al. 2020). Nb67 binds both from the extracellular side to the EC1 and EC2 helices in the top part of the cap and also from the intracellular side, where it forms interactions with both chains (Figure 5.14). While the two nanobodies that bind to the cap are in practically identical conformations, the CDR3 loop in the intracellular Nb67 adopts a different conformation (Figure 5.14 E). Since the functional studies identified Nb67 as activator from extracellular application, I assume that the functional modulation of TREK-2 is achieved through binding of Nb67 to the cap. Nb67 that binds intracellularly will not be discussed further.

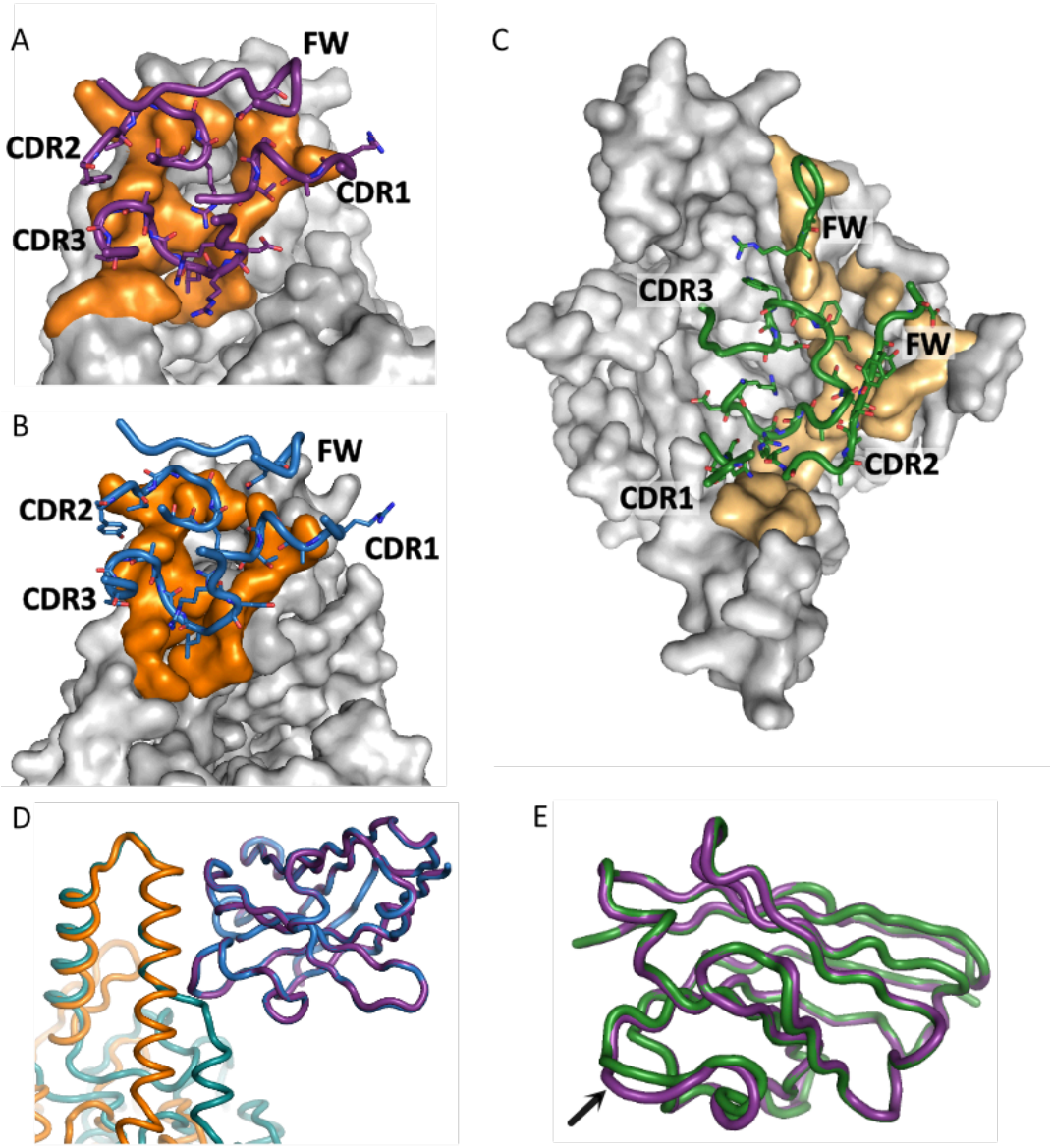


Figure 5.14: Nb67 interactions with TREK-2. **A** $Nb67^{A}$ interacts with the cap domain. The surface of TREK-2 that interacts with Nb67 is coloured in orange with Nb67 loops shown as purple cartoon. Residues forming interactions with TREK-2 are shown as sticks. **B** $Nb67^{B}$ interactions with the cap domain. The surface of TREK-2 that forms interactions with the TREK-2 cap is coloured in orange with Nb67 loops shown as blue cartoon. Residues forming interactions with TREK-2 are shown as sticks. **C** Nb67 interactions with TREK-2 from the intracellular side. Surface of TREK-2 that forms the interactions is coloured in light orange with Nb67 loops shown as a green cartoon. Residues forming interactions with TREK-2 are shown as sticks. **D** Comparison of two Nb67 molecules bound to the cap domain. Alignment of $Nb67^{A}$ with TREK-2 monomer and $Nb67^{B}$ together with TREK-2 monomer show that nanobodies adopt the same conformation and the recognised epitopes overlap on TREK-2. **E** Comparison of $Nb67^{A}$ (purple) and Nb67 (green) bound from the intracellular side. The rearrangement of the CDR3 loop is indicated by an arrow. CDR1-3 – complementarity determining region in the nanobodies (variable loops 1-3), FW – framework region in the nanobodies.

The multiple hydrogen bonds and salt bridges formed between Nb67 and TREK-2 explain the observed high nanomolar affinities (Figure 5.8). How the binding of the Nb67 to the cap is relayed to the pore is not immediately clear. The cap domain is connected to TM domains via EC2-PH1 loops as well as through the TM1-EC1 helices (Figure 5.11 A). The other extracellular signals sensed by TREK-2 involves the EC2-PH1 and SF2-M4 loops (Figure 5.11 B), as well as the tunnel structure through the cap domain, which encompasses the pore exit. A conserved His156 in EC2-PH1 loop has been identified as the extracellular pH sensor (Figure 5.11 B). External acidification activates the channel and was shown to involve the residues in SF2-M4 loop (Sandoz, Douguet et al. 2009). Small molecules modulate TREK-2 activity extracellularly, with an inhibitor binding within the tunnel structure (Braun, Lengyel et al. 2015, Pope, Lolicato et al. 2020) and an activator interacting with the SF2-M4 loop (Dadi, Vierra et al. 2017).

The structure of the TREK-2:Nb67 complex shows that the EC2-PH1 loop forms a hub of interactions with PH1, SF1-M2 loop, M2 and M1/EC1 helices centred around a conserved glutamate (E99), while the SF2-M4 loop forms no direct contacts with this hub. Instead, the SF2-M4 loop is part of a pseudo-symmetric hub formed by M3, PH2 and M4 helices, similarly centred around a conserved glutamate (E264) (Figure 5.15). Intracellular stimuli are thought to be transmitted to the pore via the M4 helix, so it is not surprising residues in SF2-M4 loop are involved in the gating process.

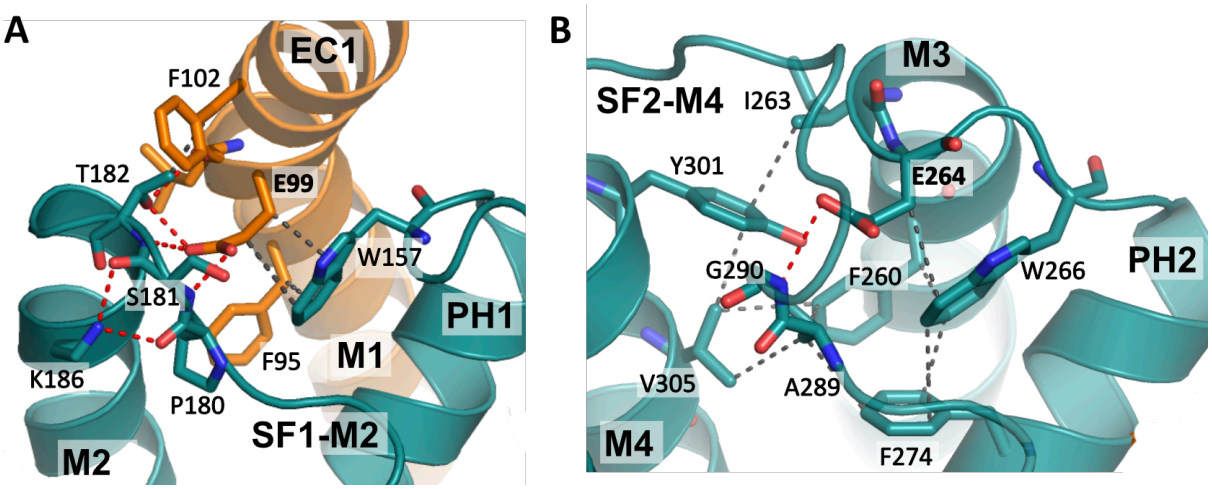


Figure 5.15: Two conserved glutamates coordinate interactions between highly connected structural elements in TREK-2. **A** E99 in the M1 helix coordinates interactions between M1/EC1, M2, PH1 and the SF1-M2 loop. **B** E264 in the M3 helix coordinates interactions between M3, M4, PH2 and SF2-M4 loop. Hydrogen bonds are shown in red, hydrophobic interactions in grey.

The two hubs form mostly hydrophobic interactions within the transmembrane region in apo TREK-2 structures. In the Nb67 bound structure, hydrophobic pockets are formed behind the SF, separating M4 and PH1 (Figure 5.16). These pockets are accessible from the extracellular side of the membrane with the entrances formed between the EC2-PH1 and PH2-M4 loops. While the pore exit pathways are lined with negatively charged side chains that would potentially attract K^+ ions, the pockets have only weakly negative charge (Figure 5.16 B). The pockets are lined with hydrophobic residues on the membrane side but have hydrophillic residues on the SF side where the backbone of PH1 is exposed to the vestibule (G167). Formation of these pockets results in reduced hydrophobic interactions formed between the PH1, PH2 and M4 helices.

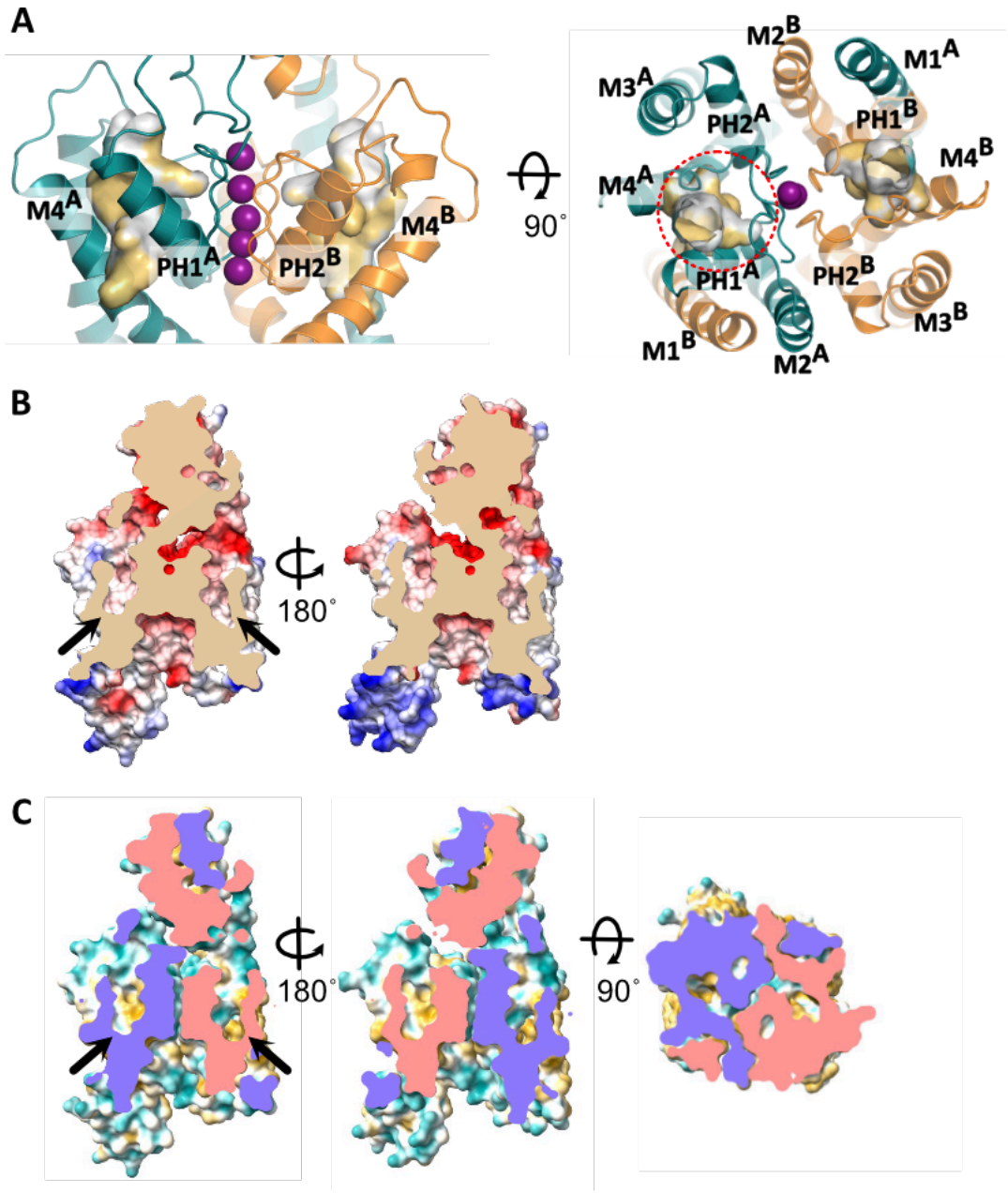


Figure 5.16: Hydrophobic pockets are formed behind the SF in the TREK-2:Nb67 complex. **A** Hydrophobic pockets are formed between the PH1 and M4 helices shown from the membrane plane view (left) and from the extracellular side (right). The pocket is indicated by a red dashed circle in the left panel. Pockets are coloured to highlight hydrophobicity and charge using YRB code, where only side chain atoms are coloured (Hagemans, van Belzen et al. 2015). Carbon atoms that can form hydrophobic contacts are coloured in yellow, nitrogen atoms in blue and oxygen atoms in red. **B** Sliced molecular surface coloured by the coulombic surface potential showing the pockets behind the SF in TREK-2:Nb-67 complex viewed from the membrane plane. Only the TREK-2 homodimer is shown for clarity. The pockets formed behind the SF are indicated by black arrows. Blue to red colouring representing -10 to +10kcal/mol*e, calculated in Chimera (Pettersen, Goddard et al. 2004). **C** A sliced molecular surface coloured by molecular lipophilicity potential (coloring based on the hydrophobicity of the molecular surface ranging from dark cyan (most hydrophilic) to white to dark goldenrod (most lipophilic), calculated using ChimeraX (Pettersen, Goddard et al. 2020)) showing the pockets behind

the SF in TREK-2 indicated by arrows (left). Viewed from the membrane plane (left and middle) and from the extracellular side (right).

The pockets are only partially formed in both TREK-1 and TREK-2 apo structures (in the "up" conformation). Only the top part of the pockets is formed, as the lower region is sealed off by the sidechain of F164 (F134 in TREK-1) (Figure 5.17 A,B). In the TREK-2:Nb67 structure, the outward movement of the sidechains of F164 and W306 towards the lipid bilayer opens up and creates the slightly negatively charged pocket behind the SF. Similar pockets have been reported for TREK-1 structures (Figure 5.17), with activator molecules slotting into the pockets and stabilising the channel in an open conformation (Lolicato, Arrigoni et al. 2017). In TREK-2:Nb67 complex, the pockets appear empty with no coordinated water molecules. This is not surprising, given the hydrophobic environment, however, water molecules are expected to fill these cavities, since they have extracellular exits.

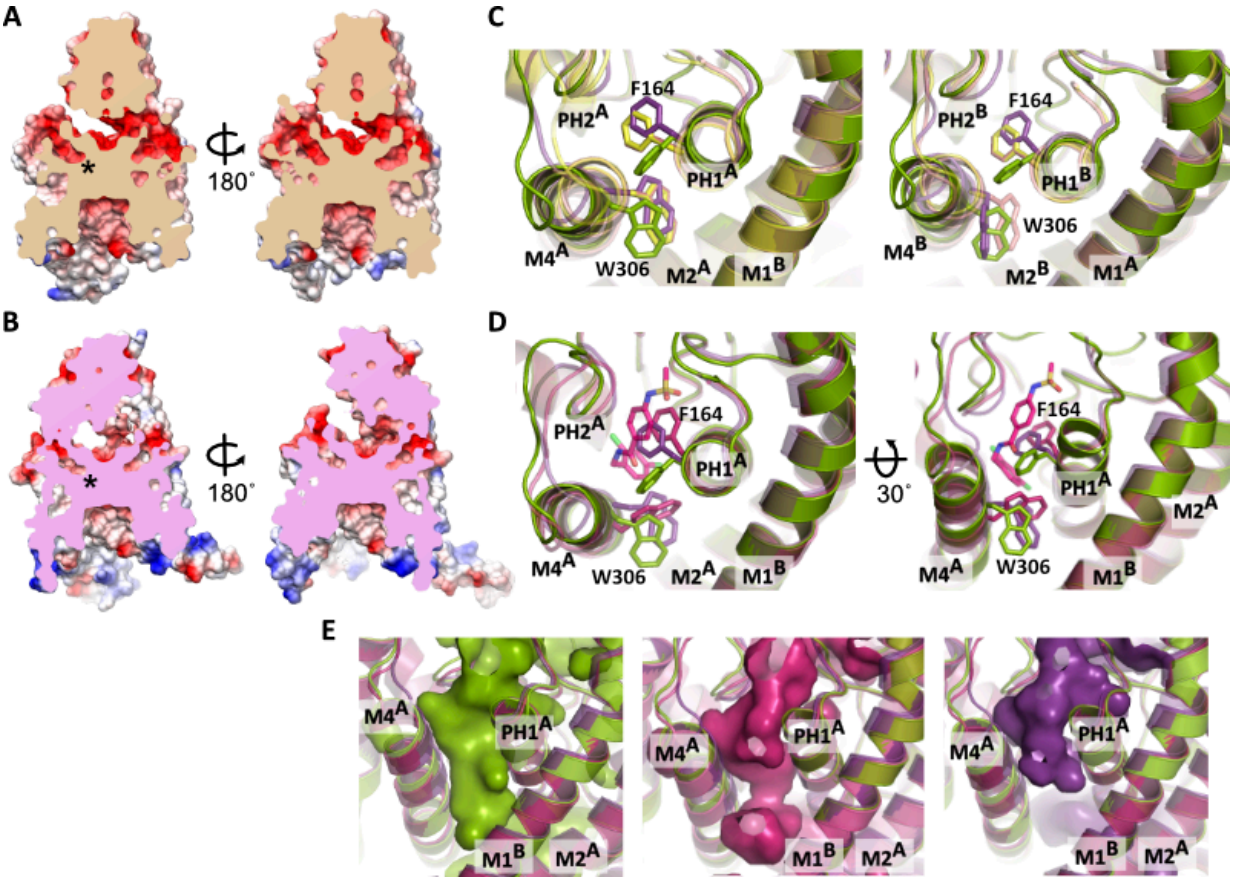


Figure 5.17: Comparison of the pockets behind the SF formed in the TREK-2 and TREK-1 structures. **A** Sliced molecular surface coloured by the coulombic surface potential showing the pockets behind the SF in TREK-2 (PDB:4BW5) viewed from the membrane plane. The position of one of the pockets formed behind the SF is indicated by an asterix. **B** Sliced molecular surface coloured by the coulombic

surface potential showing the pockets behind the SF in TREK-1 (PDB:5VK5) viewed from the membrane plane. The position of one of the pockets formed behind the SF is indicated by an asterix. **C** Comparison of the TREK-2:Nb67 (green), TREK-2 apo (PDB:4BW5 – yellow, PDB:4XDJ- pink) and TREK-1 apo (PDB:5VK5 - purple) structures. Residues F164 (F134 in TREK-1) and W306 (W275 in TREK-1) are shown as sticks. Both chain A (left) and chain B (right) are shown as W275 adopts different conformations in each. **D** Comparison of the TREK-2:Nb67 (green), TREK-1 apo (PDB:5VK5 - purple) and TREK-1:ML335 complex (PDB:5VKN - magenta) structures. Residues F164 (F134 in TREK-1) and W306 (W275 in TREK-1) and inhibitor ML335 (magenta) are shown as sticks. **E** Surface representation of the pockets formed between PH1 and M4 helices in TREK-2:Nb67 (left), TREK-1:ML335 (middle) and TREK-1 apo (right) structures. Colouring is the same as in panel D. Coulombic surface potentials (blue to red colouring representing -10 to +10kcal/mol*e) were calculated in Chimera (Pettersen, Goddard et al. 2004).

The mechanism of action of these TREK-1 activators was proposed to be via stabilisation of the SF residues through direct interaction. Support for this stabilisation mechanism was derived from lower B-factors for the SF residues in the ligand-bound structures compared to apo form (Lolicato, Arrigoni et al. 2017). As shown in Table 5.2 there appears to be no significant difference in the relative B-factors between Nb67-bound TREK-2 and TREK-2 “up” apo structure for the SF residues. However, the B-factors in “up” and Nb67-bound TREK-2 structures are lower than in “down” state, suggesting that the “down” state has more flexible SF region.

	Residue #	**Normalised B-factor**		
		TREK-2:Nb67	TREK-2 “up”	TREK-2 “down”
SF1	T172	0.56	0.63	0.77
	I173	0.59	0.63	0.80
	G174	0.64	0.62	0.82
	Y175	0.68	0.67	0.88
	G176	0.66	0.68	0.93
	N177	0.72	0.78	1.03
SF2	T281	0.60	0.66	0.71
	V282	0.61	0.66	0.75
	G283	0.63	0.65	0.79
	F284	0.62	0.71	0.87
	G285	0.71	0.75	0.90
	D286	0.81	0.85	0.97

Table 5.2: Normalised B-factors for residues in TREK-2 structures. The normalised B factor is the ratio of the average all-atom B-factors for each residue to the average all-atom B-factor for whole

TREK-2 dimer of the respective structure. TREK-2 “up” (PDB:4BW5), TREK-2 “down” (PDB:4XDJ).

In the Nb67 bound state, the SF adopts the same conformation as seen in the previous TREK-2 structures. For the SF residues the Cα RMSD is 0.204 Å (over 154 atoms) between the TREK-2:Nb67 and TREK-2 “up”, and 0.209 (over 146 atoms) between the TREK-2:Nb67 and TREK-2 “down” structures.

While the EC2-PH1 loop adopts different conformations in chain A and B for residues 139-155, there are no differences between the chains in the transmembrane region. Together with the formation of the pockets behind the SF due to movement of F164 in PH1, it seems likely that the Nb67 binding to the cap is transmitted to the SF via some of the elements coordinated by E99 (M1/EC1 and M2 helices, PH1, EC2-PH1 loop and SF1-M2 loop). This involves the highly conserved H156 which senses extracellular acidification, known to activate the channel. It is possible that both of these stimuli – pH sensing and channel activation via binding of nanobodies to the cap domain – use the same mechanism. How the formed pockets stabilise the channel in the active conformation is not clear. The reduced interactions between the PH1/M4 helices were proposed to rigidify the SF due to loss of mobility of the side chains forming the SF (fewer dynamic interactions with the surrounding residues) (Lolicato, Arrigoni et al. 2017). This was supported by TREK-1 structures in inactivated states due to pinching or dilation of SF – both motions require flexibility of the side chains forming the SF (Lolicato, Natale et al. 2020). The limitation of mobility of the two side chains involved in the pocket formation, F164 and W306, was proposed to be the main mechanism of action for the activator molecules in TREK-1 (Lolicato, Natale et al. 2020). From TREK-2 structures, it appears that the conformations adopted by the residues depend on the distance between M4 helix and PH1 (Figure 5.18). Since M4 helix is known to be involved in sensing various signals that are relayed to the pore, it is possible that reducing its interaction with PH1 stabilises the channel. Yet, the precise mechanism by which this nanobody activates the channel remains elusive.

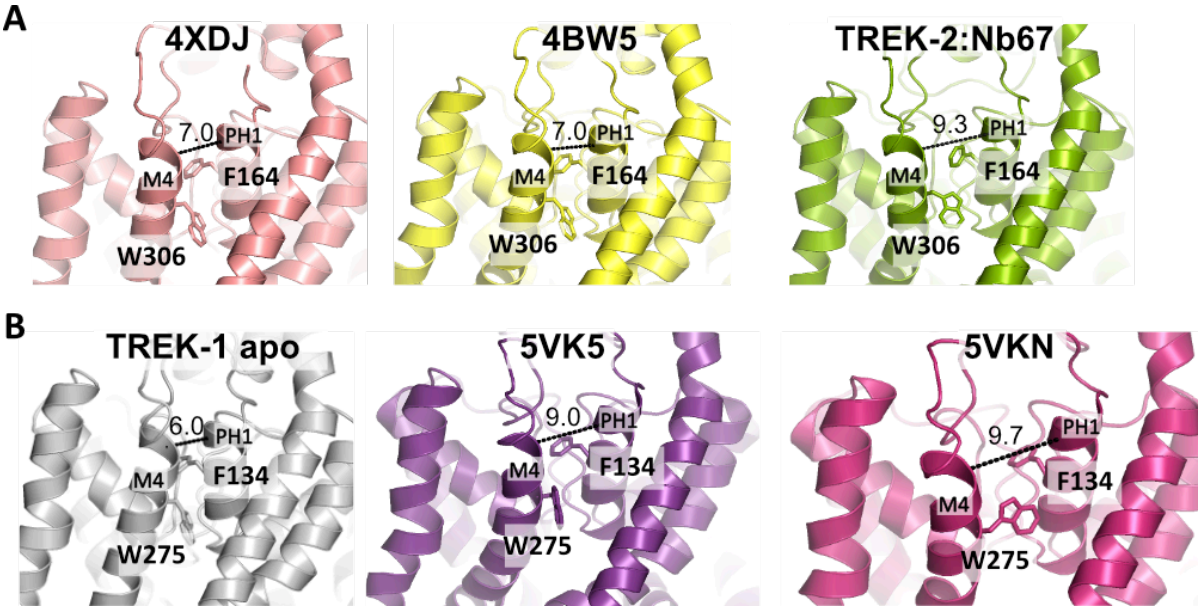


Figure 5.18: Movement of M4 opens up a hydrophobic pocket, which limits further interactions between M4 and PH1in **A** TREK-2 and **B** TREK-1. Distances between M4 and PH1 are shown (in Å), measured between Cαs of K302 and G160 (in TREK-2 numbering) and the corresponding residues in TREK-1 (K271 and G130). The apo TREK-1 structure shown here is an unpublished structure solved in our group. TREK-2 apo (PDB:4BW5 – yellow, PDB:4XDJ- pink) (Dong, Pike et al. 2015), TREK-1 apo (PDB:5VK5 - purple) and TREK-1:ML335 complex (PDB:5VKN - magenta) (Lolicato, Arrigoni et al. 2017).

5.3.3 The structure of TREK-2 in complex with the inactivating nanobody Nb61

5.3.3.1 Crystal packing in the TREK-2:Nb61 complex

TREK-2:Nb61 complexes are arranged in the crystal lattice forming interactions involving both nanobody and TREK-2 surfaces. Nb61 facilitates a compact TREK-2 dimer packing by mediating cap-to-cap domain interaction. Much weaker interactions are formed between the M2-M3 linker regions that could not be modelled due to poor electron density. This explains why the crystals diffracted poorly in one direction compared to the other two (Figure 5.19).

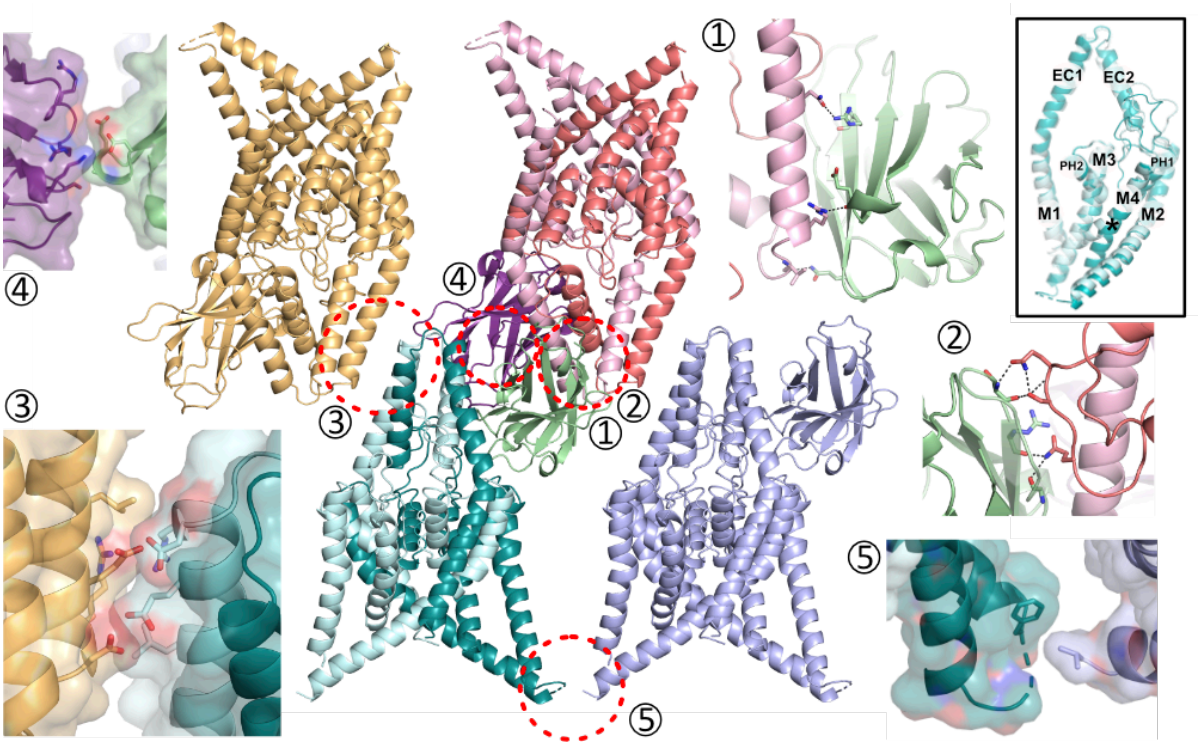


Figure 5.19: Protein-protein contacts between TREK-2:Nb61 complexes in the crystal. Schematic representations of unique crystal packing contacts formed by AU, consisting of a TREK-2 homodimer with one Nb61 bound is shown in dark teal. For clarity, unique crystal contacts formed by each AU, determined by PDBePISA analysis (Krissinel and Henrick 2007), are shown numbered based on the interface area. Weak hydrophilic and/or hydrophobic interactions are shown in surface representation. The inset shows the mixed conformation adopted by the two TREK-2 monomers. Chain B (teal) with bound Nb61 (not shown) adopts "down" conformation, while chain A (pale cyan) adopts "up" conformation, with the characteristic kink in the middle of M4 helix (indicated by an asterisk).

5.3.3.2 OVERALL STRUCTURAL FEATURES THE TREK-2:NB61 COMPLEX

TREK-2 in complex with Nb61 crystallised with just one nanobody bound per dimer. In electrophysiology studies, Nb61 inhibited TREK-2 channel currents in a dose-dependent manner with an IC_{50} around 1 µM (electrophysiology measurements of WT TREK-2 in *Xenopus laevis* oocytes were performed by A. Cloake). TREK-2 with bound Nb61 adopts a mixed conformation based on the M4 helix position (Figure 5.19 inset). Nb61 is bound to chain B, in which M4 helix adopts a "down" state. Chain A has no nanobody bound and is in "up" state and, unlike the TREK-2:Nb67 structure, the C-terminal part of the M4 helix is not involved in any crystal packing interactions. The M2/M4 helices adopting different conformations in the same dimer was described previously in the related TRAAK structures (Brohawn, Campbell et al. 2013). The asymmetric conformation suggests the

monomers are able to independently sample the different states of the M4 helix, supporting the idea that the conformation of M4 helix position is not the sole determinant of the channel conductivity state.

Nb61 interactions with TREK-2 cover a larger surface area than Nb67 (843 Å^2 vs 581 Å^2, respectively) and it forms interactions with many structural elements known to be involved in TREK-2 gating. Nb61 uses its CDR3 loop to bind to the M3-PH2 connecting loop region and forms hydrogen bonds to N292 in SF2-M4 loop and E183 in M2 helix. CDR2 loop forms interactions with residues from the EC2^A helix. It uses the framework region to pack against EC1^B helix, some of which are the same residues that Nb67 binds to: E113 and T109 (Figure 5.20).

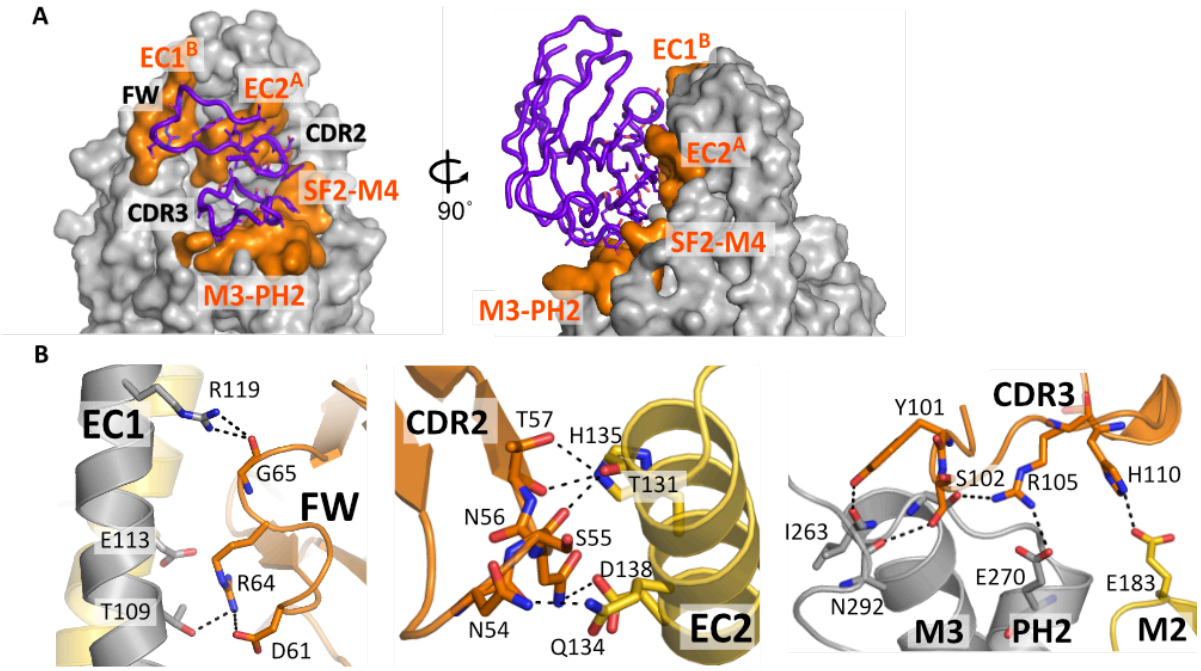


Figure 5.20: TREK-2:Nb61 interactions. **A** The interface between Nb61 and TREK-2. The surface of TREK-2 that forms the interactions is coloured in orange (strucutral elements labelled in orange) with Nb61 loops shown as purple cartoon. Residues forming interactions with TREK-2 are shown as sticks. **B** The interactions formed by the structural parts of the Nb61: framework region (FW) – left, complementarity determining region 2 (CDR2) – middle, and CDR3 – right. TREK-2 chain A is shown in gold, chain B – grey.

While the TREK-2 monomers adopt different conformations, each monomer adopts one of the states seen previously. Alignment of chain A with chain B of TREK-2 in "up" conformation has a RMSD of 0.674 Å (over 1334 atoms). The deviation is larger when compared with chain A (RMSD of 1.045 Å (over 1312 atoms)) due to differences in the M2/M3 connecting region. Similarly, alignment of chain B with TREK-2 in the "down" conformation shows little deviation in Cα positions (both chains

are similar: chain A has an RMSD equal to 0.813 Å (over 1379 atoms) and chain B has an RMSD equal to 0.879 Å (over 1369 atoms)). The pore region shows little difference compared to other TREK-2 structures (alignment of Cαs around the pore region has an RMSD of 0.225 Å between Nb61 and Nb67 bound structures, an RMSD of 0.259 Å between Nb61 bound and apo in the "up" conformation and RMSD of 0.229 Å between Nb61 bound and apo in the "down" conformation), suggesting the conductivity state of TREK-2 is the same in all models.

In the Nb61 complex structure, chain A adopts the "up" conformation, but the pocket behind the SF, observed in Nb67-bound structure, is not formed. The sidechain of W306 adopts a novel conformation by rotating 90˚ up towards the SF and restricting the opening of the lower part of the pocket. In the TREK-2 apo structures, F164 is sealing the lower part of the pocket, but in TREK-2:Nb61 complex, F164 adopts a similar conformation as in activator-bound structures and rotates out towards the membrane. As the M4 helix moves away from PH1, the movement of W306 inwards would force F164 to move outwards due to steric clashes (Figure 5.21). In chain B (where M4 is in the "down" conformation) both residues are in the same conformation as the TREK-2 apo form, with K302 additionally sealing the pocket from the outside by forming hydrogen bond with S161 in PH1 (Figure 5.21 A). The sidechain of K302 is flexible and is not resolved in the TREK-2 apo structures but the interaction is likely lost with the M4 helix moving away from PH1. With Nb67 bound, K302 adopts a conformation that opens the pocket from outside (Figure 5.21 C). Together, this supports the proposed mechanism that the pocket formation is due to M4 helix separating from PH1.

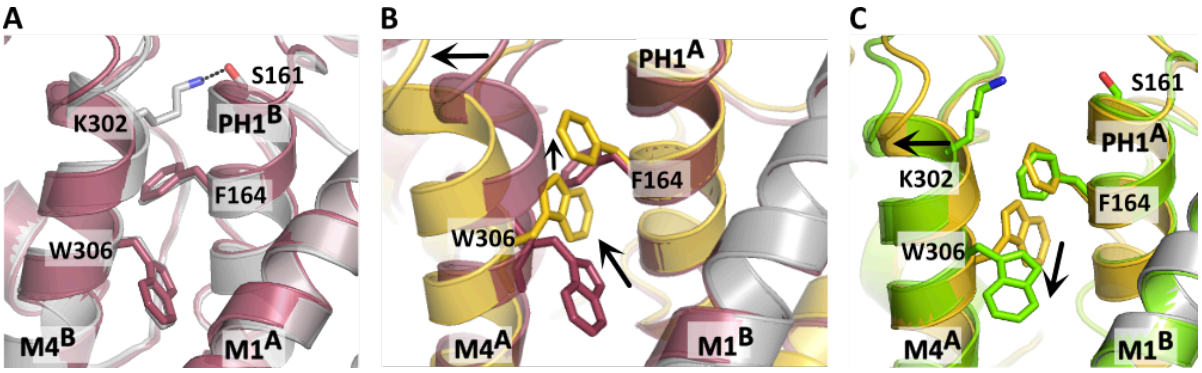


Figure 5.21: Movement of M4-PH1 interface residues in TREK-2 structures. **A** F164 and W306 adopt the same conformations in the TREK-2:Nb61^{B} (grey) and TREK-2 apo "down" states (brown). K302 is forming a hydrogen bond with S161 in TREK-2:Nb61. **B** As the M4 helix moves up in TREK-2:Nb61^{A} (gold), it separates from PH1, causing local rearrangements between the residues (indicated

by arrows) compared to TREK-2 “down” state (brown). **C** Comparison of TREK-2 monomers in the “up” state in the Nb61-bound complex (gold) and Nb67-bound complex (green). Movement of the M4 helix and W306 is indicated by arrows. This separates K302 from S161 in TREK-2:Nb67.

5.3.3.3 HOW NANOBODY INACTIVATES THE TREK-2 CHANNEL

The most notable result from Nb61 binding to TREK-2 is the rearrangements within the highly conserved network of hydrogen bonds centred around a conserved glutamate (E264) located at the C-terminus of M3 helix (Figure 5.22).

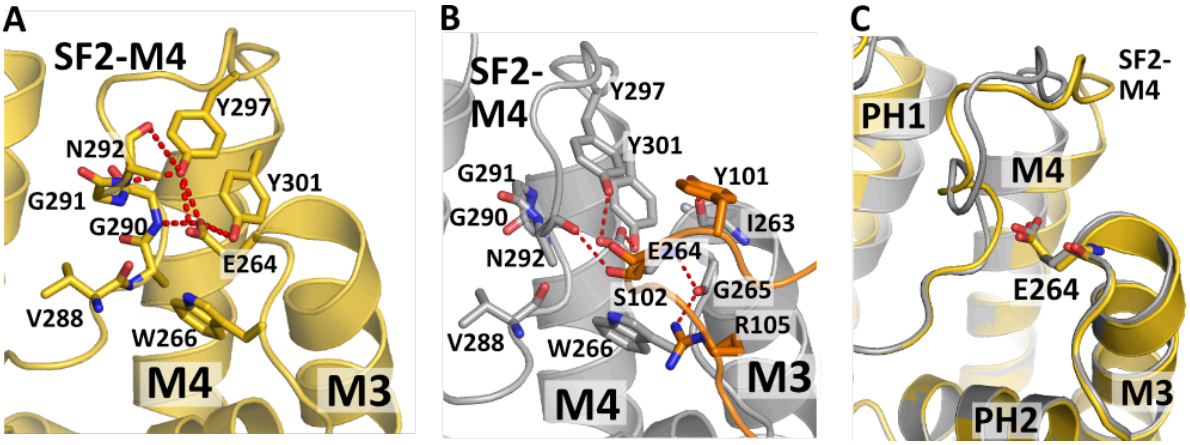


Figure 5.22: Nb61 binding to TREK-2 disrupts a hydrogen bond network around a highly conserved glutamate. **A** In nanobody-free chain A, E264 forms interactions with residues in the SF2-M4 loop (G290, Y297) and the M4 helix (Y301). **B** In Nb61-bound chain B, the interaction formed between E264 and the flexible SF2-M4 loop region is lost. Nb61 (orange) forms interactions with the SF2-M4 loop. **C** Overlay of chain A (gold) and chain B (grey) showing the differences in loop position when Nb61 is bound to chain B. E264 from both chains is shown as sticks.

The SF2-M4 loop has been shown to play a role in TREK-2 extracellular pH sensing (Sandoz, Douguet et al. 2009). While it was proposed to be involved in channel gating through interactions with H156, it forms no contacts with the EC2-PH1 loop in any of the structures solved so far. The SF2-M4 loop in all the solved structures of TREK-2 does not form many interactions with its surrounding residues (the SF2-M4 loop in TREK-2 apo form structures mainly makes hydrophobic interactions with PH1 and PH2, M3 and M4 helices). The only interactions seen when these loops are modelled are a hydrogen bond formed between E264 and G290, and Y297 and the backbone of G291 and N292 residues in TREK-2 “down” state (Figure 5.22 A). A TREK-1 study showed the crucial role of SF2-M4 loop in the C-type channel gating that relies on its flexibility and the mutagenesis studies identified E234 and

Y270 (E264 and Y301 in TREK-2 numbering) playing important roles in the stabilisation of SF2-M4 loop (Lolicato, Natale et al. 2020). The E264 and Y301 interaction is maintained with the Nb61 bound while E264 only forms a weak hydrogen bond with the SF2-M4 loop (Figure 5.22 B). The position of E264 is unchanged in Nb-bound or apo forms (Figure 5.22 C), suggesting the loop rearrangements are due to Nb61 binding. Together, this suggests that the nanobody binding weakens the stabilisation of SF2-M4 loop, increasing its flexibility, an effect that has been linked to channel inactivation. Whilst the SF in the Nb61 complex adopts the same conformation as seen in the majority of solved K2P structures, it is possible that under physiological conditions it can adopt the inactivated state.

5.3.3.4 COMPLEMENTARITY OF STRUCTURAL AND BIOPHYSICAL STUDIES

The TREK-2:Nb structures described here could explain the observed behaviour of nanobodies in the SPR studies. The only side chains with amine groups that can be coupled to the dextran matrix on the SPR chip are lysines and arginines (as explained in Section 2.2.1). As shown in Figure 5.23, the Nb61 epitope is surrounded by residues that could be used to immobilise TREK-2 on an SPR chip. There are two lysine residues flanking the M3-PH2 loop that is recognised by Nb61, which, if coupled to the dextran, would obstruct nanobody binding. This could explain the poor binding observed for Nb61 in the assay. Since the two arginines close to the Nb67 epitope are flexible and solvent exposed, they are unlikely to affect the nanobody binding, even if they are crosslinked onto the chip (Figure 5.23).

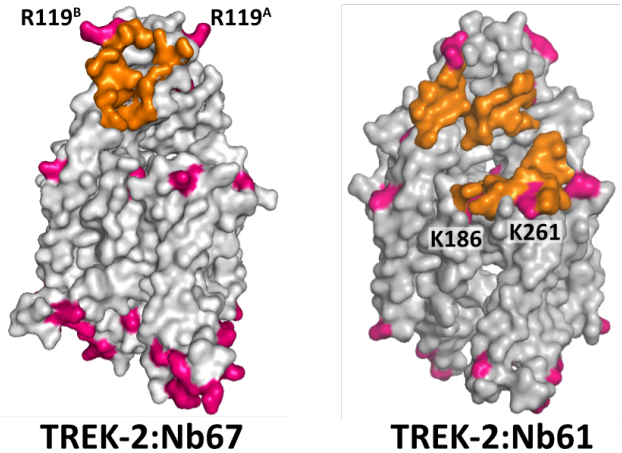


Figure 5.23: Nanobody epitope locations with respect to the potential immobilisation sites on TREK-2 for SPR studies. Arginines and lysines in TREK-2 are coloured in pink to show the potential immobilisation sites for amine-coupled crosslinking. The nanobody epitopes on TREK-2 are shown in orange.

5.4 SUMMARY OF THE STRUCTURAL CHARACTERISATION OF FUNCTIONAL TREK-2 BINDERS

Here I report the biophysical and structural characterisation of two functional nanobodies that elicit the opposite effects on TREK-2 channel gating. Using an SPR assay, I characterise the interactions between functional and non-functional nanobodies with TREK-2 and show that the binding is not affected by differences arising from the expression systems used to produce TREK-2. I present structures of TREK-2 in complex with activating or inactivating nanobodies solved by X-ray crystallography and propose a mechanism of action for both. These structures are consistent with a mechanism in which the activating nanobody binds to the extracellular cap domain and stabilises TREK-2 in the conductive state, by promoting the formation of pockets behind the SF. These pockets are thought to stabilise the SF by reducing the interactions between PH1 and the M4 helix, known to be involved in signal transduction to the SF. The signal could be relayed through the same pathway that is used by H156 and could involve the EC2-PH1 loop coordinating the movement of PH1. Two residues on the interface between PH1 and M4, F164 and W306, could be mediating the observed separation between PH1 and M4. The inactivating nanobody binds to the M3-PH2 loop and affects the hydrogen bond network centred around a highly conserved glutamate residue. This is thought to destabilise the PH2-M4 loop, and flexibility of this loop is thought to be required for channel inactivation. However, the TREK-2 selectivity filter adopts the same conformation in both structures, assumed to be a conductive state, most likely due to high K^+ concentration used in the crystallisation experiments. This has been shown to slow down the channel inactivation. These results provide insight into the TREK-2 channel gating by extracellular binders. The two nanobodies interact with different parts of the channel and evoke opposite actions while using mechanisms that converge at a single gate in the channel.

CHAPTER 6

6 DISCUSSION

In the brain, there is a finely tuned interplay between multiple membrane proteins, which is required for cells to sense and respond to the extracellular stimuli and shape the cellular response. The movement of solutes across the cell membrane in a regulated manner is of particular importance in the CNS where cells communicate with each other using neurotransmitters (such as glutamate, GABA and dopamine). The concerted uptake and release of these signalling molecules are crucial for sustainable homeostasis and are carried out by the action of transporters and receptors. These signalling events happen in specialised parts of cells and signals must be relayed between them. This is achieved through localised changes in membrane potential that propagate through the axons, cell body and dendrites of neuronal cells. These currents are the result of tightly regulated ion fluxes across the membrane through ion channels. The importance of ion channels and transporters in the CNS is underlined by the multitude of diseases and disorders arising from the malfunction of theses membrane proteins. For us to understand the basis of membrane protein function and how it can be modulated, it is crucial to have the three-dimensional (3D) information on the structures of these proteins. Ideally, the models span a range of conformations, allowing us to understand the mechanism of transport or ions and signalling molecules in detail. This knowledge can then be used to design modulators that would induce the desired response.

Here I present work on two types of membrane proteins found in the CNS involved in ion and solute transport. EAAT3, a transporter from SLC1A family, which uses an elevator mechanism to transport solutes across the membrane, and the TREK-2 potassium channel from the K2P family, which regulates ion flow through a tightly regulated channel pore. Both are associated with neurological disorders making them potential therapeutic drug targets. The knowledge of the 3D structure and mechanism of function would facilitate rational drug design.

For the first of these two projects, the aim of my work was to structurally and functionally characterise EAAT3 – a member of SLC1A family, involved in glutamate reuptake in the CNS. Malfunction of

EAAT3 is associated with a number of neurological disorders and causative of dicarboxylic aminoaciduria (OMIM: 222730) making it a potential drug target.

While SLC family is the second biggest family of membrane proteins, much less structural information is available compared to other families (GPCRs, ABC transporters, ion channels and others). When the work described in this thesis was started, only 5 structures of human SLC transporters from 4 families were solved (GLUT1 and GLUT3 [*SLC2A1* and *SLC2A3*] (Deng, Xu et al. 2014, Deng, Sun et al. 2015), Band 3 [*SLC4A1*] (Arakawa, Kobayashi-Yurugi et al. 2015), SERT [*SLC6A4*] (Coleman, Green et al. 2016), and RhCG [*SLC42A3*]) (Gruswitz, Chaudhary et al. 2010). The advances in the cryo-EM field resulted in multiple structures of human SLC transporters being solved during my DPhil (for example, *SLC7A5* (Yan, Zhao et al. 2019), *SLC12A2* (Yang, Wang et al. 2020), *SLC16A7* (Zhang, Jin et al. 2020)). This included solved human structures of closely related EAAT1 and ASCT2, greatly expanding our knowledge of the function in SLC1 family (Canul-Tec, Assal et al. 2017, Garaeva, Oostergetel et al. 2018, Yu, Plotnikova et al. 2019). Yet important questions relating to substrate selectivity within the family remained elusive.

I solved the structure of EAAT3 using cryo-EM and, in line with the SGC's practice of releasing coordinates ahead of publication, I deposited my structure in the PDB and released the coordinates in July 2020, providing the first published structure of EAAT3. During the writing of this thesis, a publication on EAAT3 structure in the presence of substrate (L-aspartate) was deposited in BioRxiv (Qiu 2020), which provides some valuable insights, but the PDB coordinates were not released in time to compare with the structures described here. Based on the publication, the group solved both inward- and outward-facing conformations of the transporter, with the main focus on EAAT3 substrate binding and transport. In this thesis, I focused on the binding of two pharmacologically relevant EAAT3 inhibitors, TFB-TBOA and ±HIP-B, to EAAT3 and these results complement the work in the Qiu et al., paper, advancing our understanding of the mechanisms underlying EAAT3 substrate selectivity, transport and pharmacology. Recently, the structure of the EAAT bacterial homologue, GltPh, with bound TFB-TBOA was solved in the inwards facing conformation (Wang and Boudker 2020). The PDB coordinates were released just recently and interestingly, they show a different inhibitor binding mode to that seen with human EAAT3, as discussed here. This highlights the necessity for human SLC structures for subtype selective ligand design. While homology modelling successfully worked for

ligand discovery for ASCT2 (Colas, Grewer et al. 2015), the information obtained from homologue structures does not reveal the intricate details between human subtypes required for selective ligand design.

To pharmacologically characterise EAAT3, I screened a selection of commercially available inhibitors to identify those that bound to purified EAAT3. I chose two inhibitors that represented analogues of two of the substrates for structural studies with EAAT3 and I used cryo-EM to determine the structures of the compound/EAAT3 complexes. To obtain high-resolution structures, the inhibitors that increased the stability of EAAT3 the most in the thermal unfolding assay were selected.

As described in Chapter 3, the pharmacological characterisation of the selected inhibitors was done with proteoliposome-reconstituted EAAT3. To facilitate the drug screening process, a high-throughput screening assay is needed. In collaboration with Antje Pommereau in Sanofi, we established a proteoliposome reconstitution protocol compatible with high-throughput ligand screening using the SURFE^{2}R system. The substrate transport results discussed in Chapter 3 suggest that EAAT3 inserts bidirectionally in the proteoliposomes, contributing to a mixed readout for substrate transport kinetics. Never-the-less, this assay did effectively identify inhibitors of EAAT3 glutamate transport. As a proof of concept, the binding characteristics of the two inhibitors used in structural studies were determined. ±HIP-B is an unusual ligand due to the conflicting reports on its mode of action. Chemically, it is a constrained glutamate analogue, so it would be expected to bind to EAAT3 in a competitive manner. However, reports so far have suggested that it is a non-competitive inhibitor, as the inhibition mechanism cannot be explained as purely competitive (Colleoni, Jensen et al. 2008, Pinto, Conti et al. 2008). This was observed with both ±HIP-B and optically pure +HIP-B (Callender, Gameiro et al. 2012). From the inhibition assay presented in Section 3.2.1.5, ±HIP-B appears to behave as a competitive inhibitor. Moreover, in the EAAT3 co-structure, ±HIP-B is binding within the substrate binding site. The previously proposed allosteric modulation by ±HIP-B was determined in the presence of L-glutamate, but the structure presented here was solved in the absence of any of the substrates, so it cannot be ruled out that multiple different binding modes exist for ±HIP-B. TFB-TBOA is the most potent inhibitor of EAAT3 to date, and this was verified in our assay with measured IC_{50} values in high nanomolar range (~300 nM).

The structures of EAAT3 in complex with the inhibitors discussed in Chapter 4 help to explain some of the observations from previous studies. TFB-TBOA exhibits unexpectedly tight binding to the transporter as discussed in Section 3.2.1.5 and in multiple functional studies reported previously (Shimamoto, Sakai et al. 2004, Bozzo and Chatton 2010). From the EAAT3-TFB-TBOA model presented here, the tight binging could arise from the way the inhibitor binds to the transporter. The TFB-TBO moiety is inserted through the HP2 loop which, together with the extensive contacts in the substrate binding site, must contribute to the tight binding (as it cannot dissociate easily). The EAAT3 structure represents TFB-TBOA binding from the intracellular side and while this explains the SURFE^{2}R results presented here (transporter can insert bidirectionally in the proteoliposome, so both inward- and outward- facing conformations are likely to be exposed to the external solution), the similar observations from *in vivo* experiments are more peculiar. Since TFB-TBOA is not transported by EAAT3, since it does not elicit transport currents, it should be tightly bound when applied from the extracellular side (Shimamoto, Sakai et al. 2004). While there is no EAAT3 structure in the outward facing conformation with TFB-TBOA bound, an EAAT1 crystal structure (with 75% identity of the human EAAT3 sequence) revealed that the hydrophobic tail of the inhibitor packs against a hydrophobic crevice (Canul-Tec, Assal et al. 2017). The additional interactions might add to the interactions arising from aspartate moiety binding to the binding site and result in the tight binding observed in the functional studies.

The EAAT3 structure with ±HIP-B presented here is the first of a kind, since no structures with the glutamate-like moiety in the binding site have been reported to date. It provides us with insights into glutamate-analogue binding to EAATs. The available ±HIP-B sample was a mixture of enantiomers, and the resulting density for the ligand was not optimal for unambiguous fitting of the ligand, as described in Chapter 4. However, careful analysis of the density and the alternative potential binding modes of the two enantiomers suggested that the ligand binds to the transporter in an unanticipated way. Based on well characterised L-aspartate binding, it was proposed that L-glutamate would be coordinated in a similar manner, with the highly conserved R447 residue coordinating its γ-carboxyl group. However, based on the modelled positions of the side chains surrounding the binding site, I propose the binding mode of ±HIP-B, where the carboxyl group is coordinated by R447. Compared to unrestrained L-glutamate, this would correspond to the α-carboxyl group. Such positioning is in

agreement with previous molecular dynamics simulations where glutamate was seen binding to the GltPh in the same manner as described here (Shrivastava, Jiang et al. 2008). When modelled in this orientation, ±HIP-B makes fewer interactions with the residues in the binding site than does L-Asp. If glutamate binding occurs in a similar manner, it would explain the lower glutamate affinity for EAAT3 (K_M for glutamate is ~30 μM, while K_M for aspartate is ~ 10 μM). The constrained nature of the inhibitor, which mimics the substrate, suggests that this conformation of glutamate might bind EAAT3 with higher affinity than the other physiological conformers. However, the work presented here was done with a mixture of HIP-B isoforms that could adopt novel binding modes unrelated to the physiological glutamate binding mode.

Overall, EAAT3 structures with bound inhibitors explain the higher affinity of TFB-TBOA compared to ±HIP-B. It forms more hydrogen bonds within the binding site (stronger binding) while the hydrophobic region creates and inserts in a deep pocket that it cannot dissociate from freely. ±HIP-B forms fewer interactions within the binding site and is not transported due to the inability of the HP2 loop to close over the binding site due to steric clashes. This agrees with the observation that ±HIP-B preferentially inhibits glutamate-induced D-aspartate release (IC_{50} = 1.2 μM) rather than L-glutamate uptake (IC_{50} = 16.9 μM) (Funicello, Conti et al. 2004). Since the binding of ±HIP-B prevents the elevator domain from traversing the membrane, it cannot be exchanged for D-aspartate. In contrast, L-glutamate competes with the ±HIP-B for the same binding site.

The structures of EAAT3 provide us with information for subtype-specific drug design. Due to different expression patterns, with EAAT3 selectively expressed in neurons, specific inhibitors are of particular interest. This is needed for conditions such as ischemia when EAAT3 is more likely to run in reverse transport mode, releasing glutamate from the cells and contributing to neuronal damage. Selective inhibitors for EAAT3 would reduce the damage since glial EAAT1 and EAAT2 were both shown to take up some glutamate even when the ion gradient across the plasma membrane is (Mitani and Tanaka 2003, Fujimoto, Katsuki et al. 2004). Although the substrate binding site is highly conserved, there are subtype-specific differences, highlighted by the EAAT2-specific inhibitor WAY-213613, which is substrate (L-aspartate) analogue (Dunlop, McIlvain et al. 2005). Allosteric modulators are an attractive alternative that would limit the cross-reactivity. This was successfully demonstrated by the EAAT1-specific inhibitor UCPH101 which binds in a conformation-dependent

hydrophobic pocket, locking the transporter in outward-facing state. With the available 3D models of EAAT3, these conformation-dependent pockets can be explored for their druggability. Since EAAT3 plasma membrane expression is highly regulated, with the majority of the protein within intracellular vesicles, modulators that prevent its internalisation by shielding the internalisation motif could be used to increase its apparent activity.

While the structures of EAAT3 explain the binding modes of two inhibitors and reveal the binding pocket environment for subtype specific ligand design, there are still many unanswered questions. EAAT3 is the only subtype known to transport cysteine at physiologically relevant concentrations. From the available structures, aspartate is coordinated in the same manner in both EAAT structures, suggesting a conserved mechanism. Since the binding pocket is not fully formed in either of the structures presented here due to HP2 loop remaining in open state it is not possible to compare the binding site environments between EAAT1 and EAAT3. Similarly, K^+ countertransport by EAATs is still not well understood. While residues proposed to be involved in K+ coordination have been investigated biochemically, the coordination mechanism remains elusive.

Determination of initial 3D structures is not always sufficient to explain all the important aspects of membrane protein function. This was demonstrated for the K2P family of potassium channels. While a multitude of structures of various members of the family have been solved, the mechanism underlying the C-type channel gating is still under debate. To learn more about the K2P gating mechanism, protein binders (nanobodies) were generated against TREK-2, a K2P whose structure was solved previously in our group (Dong, Pike et al. 2015). The nanobodies were functionally characterised by Alexander Cloake and Stephen Tucker (Dept of Physics, Oxford) using electrophysiology methods, and nanobodies that affected the function of TREK-2 were identified. As described in Chapter 5, I assessed the kinetics of binding of these nanobodies to TREK-2 using the SPR method. This revealed that the nanobodies exhibit different binding modes with different apparent affinities, ranging from nanomolar to low micromolar. As TREK-2 is known to be glycosylated, different expression systems were tested to see if nanobody binding is affected by different glycosylations. Nanobodies showed similar binding to protein expressed in mammalian or insect cells either with glycans present or not, suggesting the binding site is not located close to the extracellular loop with glycan modifications.

To learn more about K2P channel activation and inactivation mechanisms, the 3D structures of TREK-2 with bound functional nanobodies were solved using X-ray crystallography. The activating nanobody Nb67 was found to bind to the cap domain with a single nanobody molecule interacting with both TREK-2 monomers. To date, the cap domain has not been identified as a modulatory site in TREK-2. How the nanobody binding to the cap is then relayed to the channel pore to activate is less obvious. The channel adopts "up" conformation associated with more conducting state, and has hydrophobic pockets formed behind the selectivity filter not seen before in TREK-2 apo structures. Similar pockets were observed in the TREK-1 structure with activating ligands occupying them (PDB:5VKN). The reduced interface between the PH1 and M4 helices was proposed to reduce the flexibility of the residues forming the SF, leading to a more rigid channel, stabilised in a conducting state. The cap is positioned over the exit of the channel pore and the most likely interactions to relay the signal to the SF is between the EC2-PH1 loop or via direct interactions between EC2 and loops connecting the SF to the TM helices. The only other signal regulating TREK-2 from the extracellular side is activation by extracellular acidification (Sandoz, Douguet et al. 2009). This has been attributed to a conserved histidine, located in the EC2-PH1 loop. It could be that both activatory signals are transmitted by the same mechanism. In the crystal structure, there is an additional Nb67 bound to the intracellular side of the channel. Since the activating effect was seen with Nb67 applied from the extracellular side (Alex Cloake and Stephen Tucker, unpublished results), it is assumed the intracellular binding is a crystallisation artefact. To see if the nanobody has any functional effect from the intracellular side, electrophysiology experiments on inside-out TREK-2 channels could be performed. To investigate the mechanism of channel activation, mutagenesis studies of residues involved in Nb67 binding to the cap could be performed. This would potentially identify the residues within the cap domain involved in signal sensing that the Nb67 is utilising.

The inactivating nanobody Nb61 bound to a M3-PH2 forming loop and EC2 helix. Interestingly, it interacts with some of the residues in EC1 helix that are involved in Nb67 binding. While the SF region is identical to the Nb67-bound TREK-2 structure as well as TREK-2 apo structures (PDB: 4BW5 and 4XDJ), suggesting the pore is in a conductive state. However, Nb61 binding to TREK2 disrupts the hydrogen bond network coordinated by the highly conserved glutamate (E264). This residue has been shown to play a crucial role in related K2Ps and, most importantly, to stabilise the SF2-M4 loop

(Lolicato, Natale et al. 2020). It was shown in TREK-1 that flexibility of SF2-M4 loop was required for the channel inactivation (Lolicato, Natale et al. 2020). Nb61 binding destabilises the SF2-M4 loop by reducing the number of interactions formed between the loop and M3, M4 helices. This is expected to increase the loop flexibility, leading to channel inactivation. To test this theory, mutagenesis studies stabilising the SF2-M4 helix relative to M3/ M4 helices could be performed to see if it affects channel inactivation.

In summary, this thesis presents the structural studies of two human membrane proteins (a transporter and a channel) involved in the regulation of neuronal function. The work presented here illustrates that the combination of a protein in multiple conformational states and with bound modulators is essential to understand the function and how this can be modulated. It shows that studies with human proteins, rather than bacterial homologues, is required to elucidate the minute differences that confer the specificity to isoforms, allowing more selective modulators to be designed.

CHAPTER 7

7 APPENDIX

7.1 THEORETICAL BASIS OF BIOPHYSICAL AND STRUCTURAL METHODS

7.1.1 SURFACE PLASMON RESONANCE (SPR)

SPR is an optical, label-free detection method that follows biomolecular interactions in real-time. SPR principle is used in Biacore systems (Cytiva) for high-throughput screening of a target protein and its various binders. Biacore system consists of the SPR detection system, microfluidics system and sensor chip.

SPR detection system is graphically shown in Figure 7.1. As the light from the light source passes through the prism, it is reflected by the sensor chip on the detector. At certain angle, the light is absorbed by the sensor chip gold layer causing the electrons in the gold to resonate – these electrons are known as surface plasmons, that are sensitive to their environment. In biochemistry, SPR is used to analyse the interactions between a probe molecule immobilised on a surface and the analyte sample in solution. Once the analyte sample is introduced and there are binding events, the surface plasmons interact differently with the environment which can be observed as a shift in the reflected light (from red to green). As more analytes bind, the resonance signal increases until the system is in equilibrium. Microfluidics system allows for small sample requirements and automated handling.

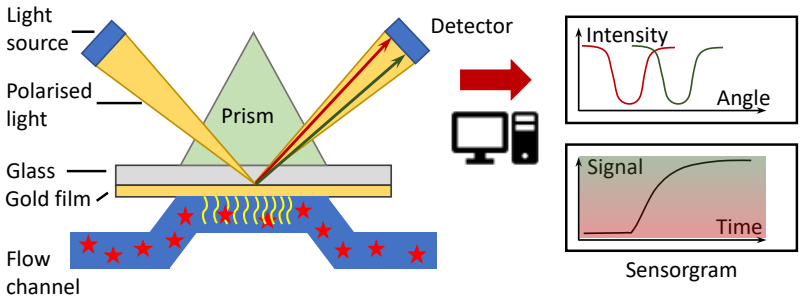


Figure 7.1: SPR detection principle in Biacore system. The real time analyte binding events are observed as changes in the angle of the reflected polarised light. Single angle from the reflected light (shown as red arrow) is observed when only buffer solution is flown past immobilised ligand. When an analyte is added, it binds to the ligand and increases the total mass bound to the surface dextran,

resulting in a shift in the angle of the reflected light (green arrow). The shift in the angle is correlated to the analyte binding to the ligand and is commonly referred to as response signal that is followed in real time. Adapted from (Locatelli-Hoops, Yeliseev et al. 2013).

SPR sensor chips schematic is shown in Figure 7.2. The glass support is covered by a thin layer of gold to which a linker layer with the flexible dextran matrix is attached. The ligands can be immobilised directly (covalently) or using capture approach (using target-specific antibodies or tags). The most popular chip, CM5 captures the ligand protein in a covalent way. This can be done using either amine coupling (uses N-terminus of the target protein and lysines; may result in the ligand attaching to the surface in different ways), ligand or surface-thiol coupling (ligand or sensor surface has free thiol groups that can interact with active disulphide groups, respectively), maleimide coupling (thiol groups on the ligand interact with maleimide reagents on the dextran matrix) or aldehyde coupling (for ligands containing aldehyde groups). In this work, I used CM5 chip and amine coupling to immobilise the target protein.

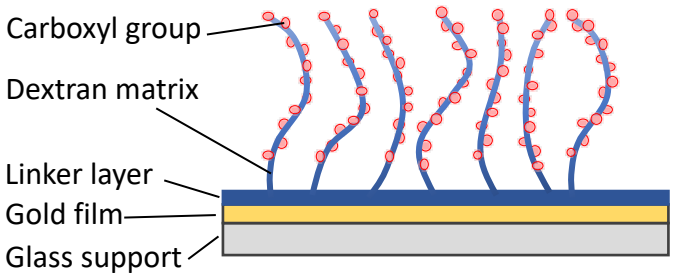


Figure 7.2. Composition of an SPR chip. Glass support is covered with a thin layer of gold which is then coated with a layer of carboxylated methyl dextran (CMD). It forms long strings with many carboxyl groups exposed that increases the total surface area available for ligand immobilisation. Adapted from (Locatelli-Hoops, Yeliseev et al. 2013)

A typical SPR assay consists of 3 steps – surface preparation (ligand immobilisation), application of sample (analyte injection) and regeneration of surface (removal of the analyte without damaging the ligand). For the ligand immobilisation, the appropriate pH must be identified at which the protein carries a net positive charge. Theoretically, this can be determined from the pI (isoelectric point) of the target protein – the pH at which the molecule carries no net charge. However, this tends to be more complicated with membrane proteins as they are embedded in detergent micelle that also carries a charge. Thus, an experimental method called pH scouting is usually performed. This involves injecting ligand diluted in buffers with various pHs. Since the dextran matrix carries negative charge at pH >

3.5, the ideal conditions are when 3.5 < pH < pI, since this will result in electrostatic attraction between the ligand and the matrix, allowing the protein to be concentrated at the sensor surface.

The recommended protein concentration for immobilisation is between 10-50 µg/ml. Depending on the type of experiment carried out, different levels of immobilised ligand are optimal. For affinity measurements, it is important that the analyte can saturate the bound ligand within appropriate time frame so usually low to medium binding capacity chips are used. The amount of protein bound to the matrix required to see binding events can be calculated based on the analyte binding capacity (R_{max}, for 1:1 binding stoichiometry):

$$R_{max}(RU) = \frac{analyte\ M_w}{ligand\ M_w} * immobilised\ ligand\ level\ (RU)$$

Binding can be achieved by either setting target immobilisation level in Response Units (RU) or by specifying time. The amine coupling is a chemical reaction that results in covalent bond between the ligand and the support matrix (Figure 7.3).

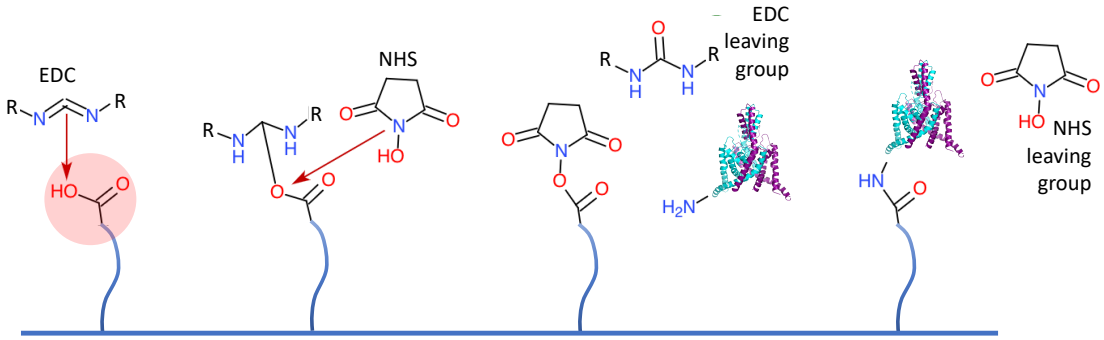


Figure 7.3: Amine coupling scheme for ligand immobilisation in SPR. The carboxyl groups (red circle) on the dextran are activated with a 1:1 mixture of 1-Ethyl-3-(3-dimethylaminopropyl)carbodiimide (EDC) and n-hydroxysuccinimide (NHS). EDC group reacts with the carboxyl group to form unstable ester and NHS reacts with the unstable ester to form a stable one. The ligand of choice is then applied and the primary amines on the ligand can react with NHS-ester to form a covalent amide bond. Adapted from (Fischer 2010).

For the analyte injection step, it is important to have a reference surface as the system is very sensitive to differences in buffer compositions. There are three ways how to prepare a reference surface – it can be left unmodified; it can be treated as the sample surfaces without applying the ligand or unrelated ligand can be immobilised to mimic the active surface as closely as possible. Finally, in the regeneration of the surface step, the bound analyte must be completely removed from the ligand and

the ligand should retain its initial activity. Here, the analyte was removed using a long wash with ligand buffer until the signal returned to the baseline level.

7.1.2 CRYO-EM

7.1.2.1 THEORY AND BASIC PRINCIPLES OF CRYO-EM

Cryo-EM is an electron microscopy (EM) technique used to study biomolecules in a thin layer of vitrified ice. The sample of a target biomolecule in a solution is prepared by applying it on a mesh support, blotting away the excess liquid and plunging it in liquid ethane. Single particle analysis (SPA) is then used to process the images to obtain a 3D reconstruction of the target. "Single" refers to the fact that the target molecule is not in contact with other molecules. Similar to X-ray crystallography, the cryo-EM technique allows us to study biomolecular structures at atomic resolution. In contrast to crystallography, where the molecules must adopt a single conformation to form ordered arrays (crystals), in cryo-EM the biomolecules are snap frozen while in solution and native conformations in biologically meaningful states can be captured. This allows us to follow the dynamic motion of proteins and protein complexes as multiple conformations can be visualised within a single sample.

With the recent advances in the hardware (more sensitive detectors, more powerful computers) and in the analysis software (processing programs and algorithms), sub-4Å structures can be routinely determined for proteins and protein complexes up to about 100 kDa in size. The technique is particularly suited for studies of complexes and large particles (viruses) as these provide the best signal to noise ratio.

7.1.2.1.1 SAMPLE PREPARATION

Electron microscopy is now commonly used along with X-ray crystallography to reconstruct 3D models of macromolecules for structural studies. The imaging conditions in EM (under vacuum) dictate the need for the specimen to be in a solid state. Special preparation methods have been developed to allow imaging of biological samples under vacuum (Orlova and Saibil 2011).

There are multiple sample preparation methods. Depending on the information one wants to obtain, negative staining or vitrification methods can be used. For SPA, negative staining is a popular initial method to quickly assess the sample quality (Figure 7.4).

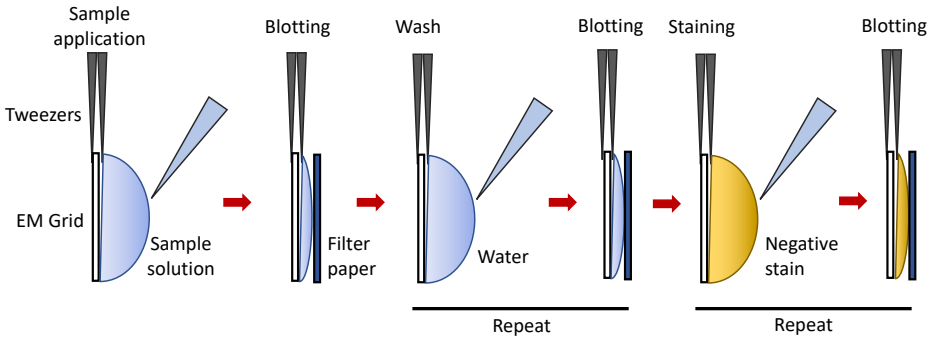


Figure 7.4: Negative stain EM grid preparation. The sample is applied to EM grid with continuous carbon layer and left for the macromolecules to settle on the support (by gravity). The excess solution is blotted away with a filter paper and the adherent macromolecules are washed with water to remove excess ions left over from the buffer and blotted again. The washing step can be repeated a few times before negative stain is applied and blotted away. This is repeated a few times and the grids are left to air dry before imaging in the TEM.

The solution of macromolecules is applied onto an EM grid overlaid with a continuous carbon support film. The excess liquid is blotted away before covering the macromolecules with a heavy metal stain. The resolution is limited to ~20Å due to the grain size of the stain (commonly used uranyl acetate and uranyl formate has the grain size of 4 - 5 Å) and only the outline of the particle is captured. A high relative contrast between the less electron dense particle and the surrounding stain allows for visualisation of even small particles (Ohi, Li et al. 2004). For high-resolution SPA, the samples are prepared using plunge-freezing method (Figure 7.5 B). Plunge freezing gained popularity after it was demonstrated that water can be frozen in vitreous state if applied in a thin layer on EM grid and plunge frozen in liquid ethane (Dubochet and Mcdowall 1981). Manual and semi-automatic plunge-freezer models are commonly used, while the process remains challenging, with extensive optimisation of the freezing conditions often required (Dobro, Melanson et al. 2010). One important consideration for cryo-EM sample preparation is the support type. Most commonly, perforated carbon films over the grid support are used where the macromolecules are suspended in a thin ice layer across the holes (Figure 7.5 A) (Dobro, Melanson et al. 2010). Commercially available grids (e.g., Quantifoil grids, Quantifoil Micro Tools GmbH; C-flat grids, Protochips, Inc.) have regularly spaced holes convenient for automated data collection (Orlova and Saibil 2011). For successful cryo-EM imaging, the sample thickness is crucial. The thickness of the sample is limited to ~100 nm and the samples must maintain their integrity under vacuum and the electron beam. The goal is to have the thinnest sample possible

for high contrast without affecting the macromolecule distribution within the ice (Orlova and Saibil 2011).

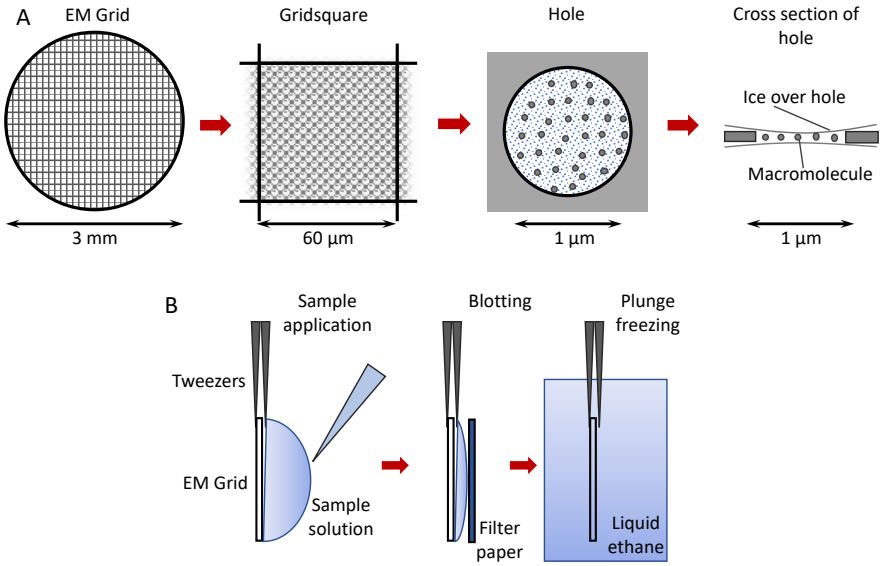


Figure 7.5: Vitrified cryo-EM grid preparation. **A** The composition of a cryo-EM grid. An EM grid consists of a grid support (mesh), most commonly made of copper or gold. The support is overlaid with a perforated carbon film with each gridsquare having many ordered holes. The hole with the macromolecule suspended in a solution is only around 1 µm in diameter and this is where the sample is imaged with the TEM. **B** Plunge freezing method. A hydrophilic cryo-EM grid is held by tweezers. The sample is applied to the grid and blotted away with a filter paper to leave a thin layer of ice suspended over the holes in the grid. The grid is plunged in liquid ethane and transferred to storage at liquid nitrogen temperature (77 K).

The carbon film must be made hydrophilic for the sample to spread evenly. This is achieved by plasma cleaning the grids ("glow discharging") shortly before applying the sample. After sample application, the excess solution is blotted away and the grid is plunged in liquid ethane.

Afterwards the grid is always kept at liquid nitrogen temperature for storage and cryo-EM imaging.

7.1.2.1.2 ACHIEVABLE RESOLUTION WITH ELECTRON MICROSCOPES

Electron microscopes are similar to the light (optical) microscopes but use electrons instead of light to image the sample. In microscopy, the term resolution is used to describe the ability to distinguish two separate points on the specimen – it is the shortest distance that can be observed between two points (Figure 7.6).

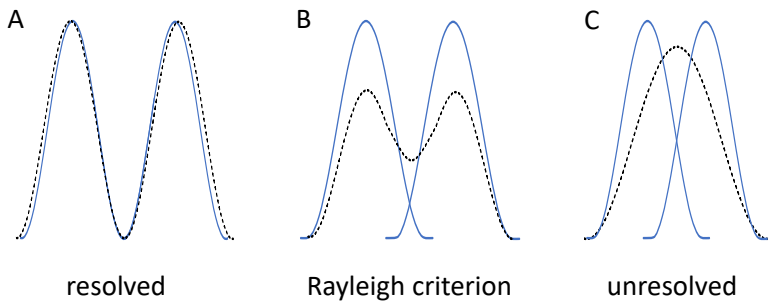


Figure 7.6: Optical resolution is defined as the smallest distance between two points on a specimen that can be distinguished as two separate entities. Assuming the blur introduced by the microscope to be Gaussian (shown as blue line) with a known standard deviation, the resolution is defined as a distance between points that equals at least one standard deviation (**A** – resolved, **B –** the minimum resolvable distance). For distances smaller or than one standard deviation, the observed pattern, that is a sum of two Gaussian functions (dashed line), has an appearance of a pseudo-Gaussian with one maximum (**C**). Adapted from (Orlova and Saibil 2011).

According to the Abbe criterion, the theoretical resolution d achievable by a microscope is:

$$d = 0.61\frac{\lambda}{n\sin\alpha}$$

where λ is the wavelength, n is the refractive index of the imaging medium, and $n\sin\alpha$ is the numerical aperture (~1 for light microscope and ~0.01 for electron microscope) (Penczek 2010). Since visible light has a wavelength of 380-740 nm, it can only be used to resolve samples up to 200 nm which is not sufficient to study proteins (<10 nm) at atomic resolution.

Since the wavelength is proportional to the resolution, a shorter wavelength will give better resolution, therefore X-rays (wavelength of 0.01 to 10 nm) are commonly used in X-ray crystallography. For electron microscopes, the electron wavelength decreases with increasing acceleration voltage. While the electron wavelength (and thus theoretically achievable resolution) for a microscope operating at 300 keV is 1.97 pm, the practical resolution is limited by the quality of electron optics (Penczek 2010). Electrons, unlike X-rays, can be focused using an electromagnetic field yet their use in imaging is a balancing act: higher energy electrons damage the sample more, while low energy electrons are worse at penetrating the sample. Additionally, electrons interact strongly with the matter and can travel only short distances in the atmosphere. This distance is greatly increased under vacuum conditions. In summary, electron microscopes are well suited for the structural studies of biomolecules. While the sample gets irreversibly damaged during the imaging process, the operation of EMs at cryogenic temperatures to keep the samples in vitreous ice together with low-dose imaging methods reduce the

radiation damage. The favourable physical properties of electrons (i.e., the tuneable wavelength, ability to be focussed) makes cryo-EM a valuable tool for structural studies of macromolecules.

7.1.2.1.3 IMAGING USING ELECTRON MICROSCOPES

The additional requirements for the vacuum and high accelerating voltage explain the main operational differences between the light and the electron microscopes while the overall imaging concept remains the same (Figure 7.7).

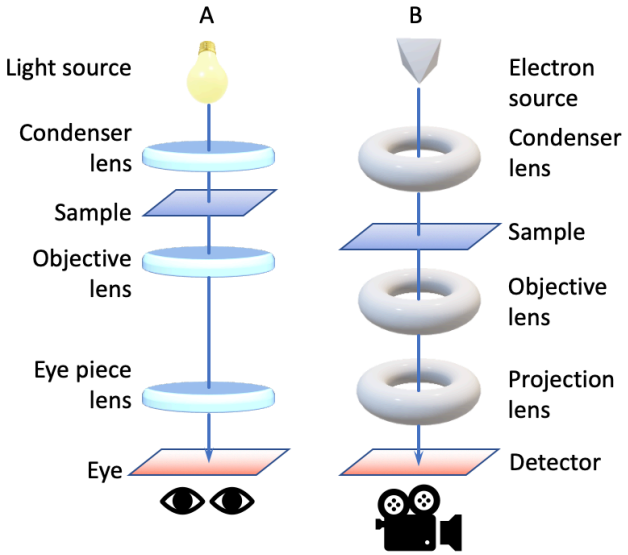


Figure 7.7: Composition of light and electron microscopes. The radiation beam is generated at the source – light or electron. Both microscopes consist of three lens systems. A condenser lens system aligns the beam before it interacts with the sample. The specimen is positioned between the condenser and objective lens systems. The objective lens controls image formation while the last lens system – the projection lens in electron microscopes and the eyepiece lens in light microscopes – controls the magnification. The formed image is then detected by eye (light microscope) or detector (electron microscope).

Like light microscopes, electron microscopes use lens systems to condense the (electron) beam onto the specimen. The electrons are generated in the electron gun. It both extracts and accelerates the electrons from the source. Depending on the type of the gun, the incident beam will have varying degree of temporal and spatial coherence that has to be corrected. The microscope lens system is what corrects the incident beam (Figure 7.7 B*)*. The EM lenses are solenoids that use electromagnetic field to condense and parallelise the beam before it interacts with the sample. They are important for general microscope alignments – to correct for the beam shift/ shape. All TEMs have 3 lens systems – a condenser (to regulate beam intensity), an objective (to regulate the image) and a projection (to regulate

the magnification). The objective lens is the key optical element, since its aberrations affect the image formation the most (Orlova and Saibil 2011). The aperture placed after the objective lens removes electrons that are scattered at high angles in order to increase the contrast on the image plane.

The parallel, aligned electron beam then interacts with the sample – biomolecules embedded in vitreous ice that are kept at liquid N_2 temperature. In transmission electron microscopy, the signal is generated from electrons passing through the specimen (Figure 7.8).

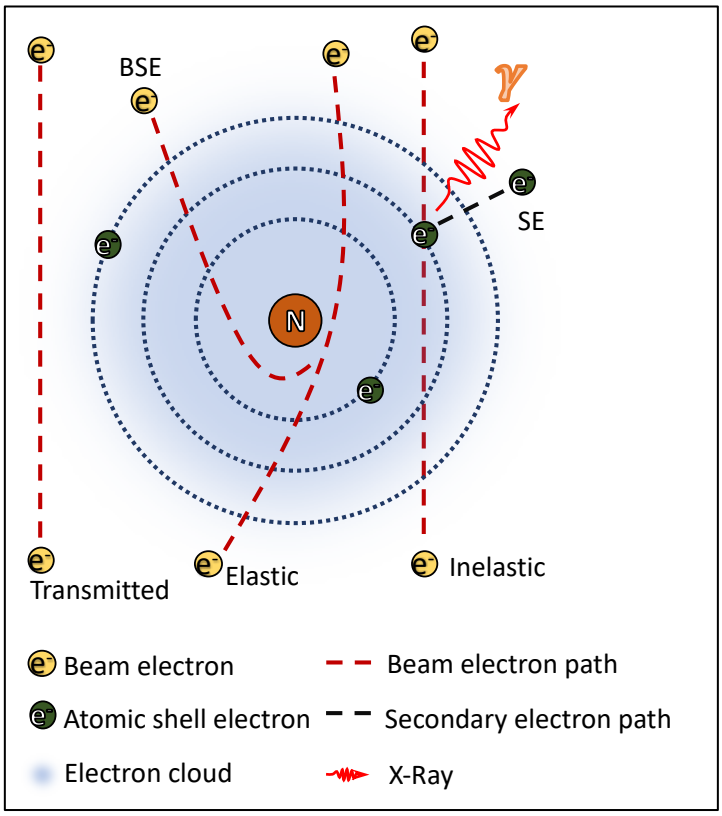


Figure 7.8: Interaction types between the electron beam and a sample. Electron interactions with the sample depend on the sample composition and the electron energy. In single particle cryo-EM, most of the electrons will pass through the sample without any interactions (Transmitted electrons). Some will be deflected by the electrostatic field of the nucleus (N; back-scattered electrons, BSE) while only a few will interact with the sample. These interactions, or electron scattering, can arise from beam electrons interacting with the atomic shell electrons and with the associated energy transfer (Inelastic scattering) or without energy loss (Elastic scattering). Adapted from (Orlova and Saibil 2011).

Most of the electrons don't interact with the sample and thus don't contribute to the image formation. The electrons can interact with the specimen in two ways – they can be scattered without energy loss (elastic scattering) or transfer energy to the specimen (inelastic scattering). In the image formation, elastically scattered electrons contribute to the signal while inelastically scattered contribute to the noise. In the meantime, biomolecules are very sensitive to radiation damage. Upon exposure, the

protein molecules are exposed to ionising radiation, which results in formation of free radicals that can move around and damage the molecule. At liquid N_2 temperature, this movement is reduced but not eliminated. Radiation damage affects high resolution features first, so in order to get higher resolution, one must reduce the total exposure (Orlova and Saibil 2011).

7.1.2.1.4 IMAGE FORMATION

Images in cryo-EM represent variations in the **intensity** of electron beam after it has interacted with the specimen. This interaction causes changes in both, the amplitude and the phase, of the electron beam. The image contrast arising from the deflection of part of the beam is known as amplitude contrast. Biological macromolecules are composed mainly of light atoms (C, H, N, O) and mostly just deflect the electrons, resulting in nearly no loss of electrons after sample interaction. Since only a small fraction of electrons are deflected (from inelastic interactions), the intensity modulations are insufficient to produce features in the images (Orlova and Saibil 2011). For cryo-EM data, the amplitude contrast is often assumed to be constant (in the range of 6–12%) (Penczek 2010). Thus, other methods are needed to increase the contrast.

Since all electrons contribute to image formation, the interference of the elastically scattered electrons with the transmitted beam is known as a phase contrast. Sample thickness plays an important role – thinner samples minimise the inelastic scattering events while thicker samples scatter more and, as the sample thickness increases, absorb all the electrons. In thick samples, initially elastically scattered electrons can be inelastically scattered as they continue travelling through the sample.

Macromolecules embedded in a thin layer of ice can be considered as weak phase objects since they scatter electrons through small angles. The minimal phase contrast can be transferred in amplitude contrast by applying a phase shift to the elastically scattered electrons. In practice such a phase shift between the scattered and unscattered electrons can be introduced by applying spherical aberration (Figure 7.9 A) and image defocus (Figure 7.9 B), essentially shifting the image plane away from the instrument focus. At this shifted image plane the scattered beam arrives ahead of the unscattered beam. The common practice is to underfocus the image to generate phase contrast, with greater phase shifts (larger underfocus values) generating more contrast, while altering the image data. This alteration is

described as the contrast transfer function (CTF). Underfocusing the image causes destructive interference at the underfocus plane. The larger the scattering angle, the larger the path difference of the scattered wave – thus contrast varies with the scattering angle.

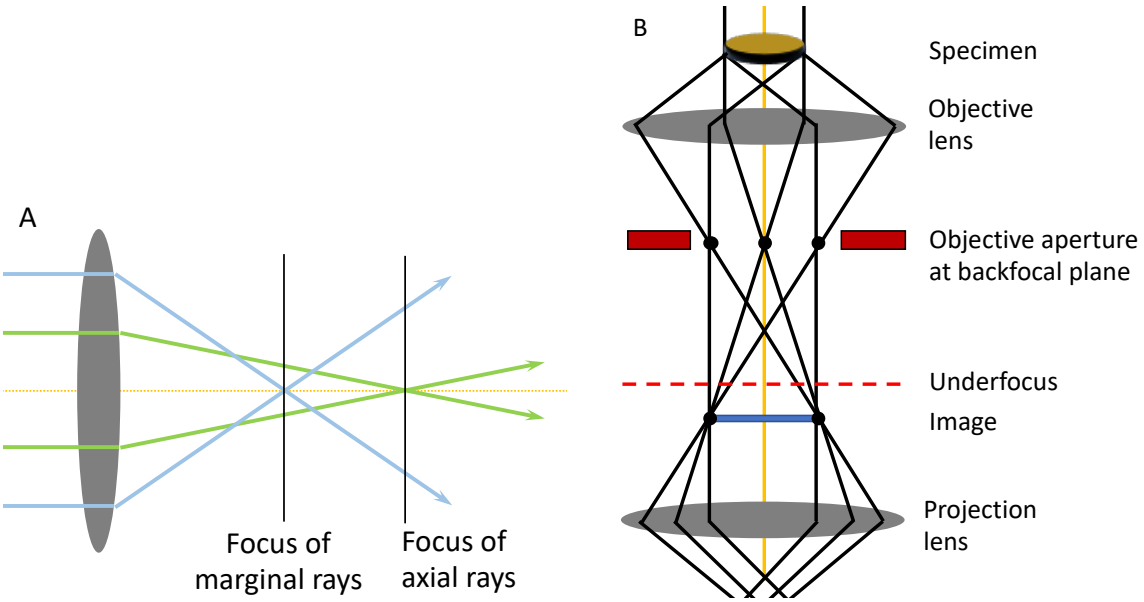


Figure 7.9: A Spherical aberration in microscopes. Beams further away from optical axis are focused at a point closer to the lens (Focus of marginal rays) than the beams closer to the optical axis (Focus of axial rays). **B** Defocus and contrast formation. When a specimen scatters the electron beam (black lines), the scattered beam is redirected by the lens (Objective lens) to recombine with the unscattered beam (yellow line) at the image plane (Image). Both scattered and unscattered beams arrive at the image plane at the same time (the original wave front is regenerated). The specimen only affects the wave front shape, not the amplitude, so an image has no contrast in-focus. To generate phase contrast, underfocus is applied, shifting the image plane to a position before image plane (Underfocus). At this plane, the scattered beam arrives before the unscattered beam (to arrive in-phase at the focal plane). This generates destructive interference between the scattered and unscattered waves, causing particles to appear dark.

Electron microscopes are not perfect instruments, and all components have inherent defects that can impact on data quality. Electron sources have defects (beam coherence - spatial and temporal), lenses have aberrations (both spherical and chromatic) and imperfections in beam alignment introduces coma (the direction of incident beam is not aligned with the optical axis) and astigmatism (caused by an oblique angle of the incident beam). During imaging, as the electron beam hits the specimen, it introduces defects such as beam induced sample movement. Any defect reduces image quality, in particular, the high-resolution details, and the sum effect is that each point in the object is imaged as a two-dimensional (2D) function or Point Spread Function (PSF). In a perfect instrument, the PSF would

be a single, sharp peak, while in reality it resembles a spread Gaussian peak, with the area around peak increasing with increasing defocus (Orlova and Saibil 2011).

It is more convenient to explain the effects of the PSF in Fourier (diffraction) space, where it is called phase contrast transfer function (CTF). CTF models the PSF effects on the image and once all the parameters are determined, the image can be corrected. CTF is given as

$$CTF = E(f)\sin[\pi(C_s\lambda^3 q^4/2 - \Delta z\lambda q^2)]$$

where Cs is the spherical aberration coefficient, Δz is the defocus, q is the spatial frequency, λ is the electron wavelength and E(f) is an envelope function (Wade 1992). Since Cs is a microscope-specific constant and the wavelength is known, the only variables are the defocus and the spherical aberrations, which affect the spatial frequency (for example, astigmatism). Since the microscope is not ideal, the degree of coherence of the scattered waves (expressed in the envelope function) due to energy differences (from changes in the voltage) and the angular spread (from non-parallel illumination, defocus-dependent) should be taken into consideration when correcting CTF as it describes the high-resolution information loss. Therefore, to correct the image obtained from the microscope, one must determine the defocus from the data and calculate the actual CTF.

The formed 2D projections of the specimen are recorded on a camera. The most commonly used cameras nowadays are direct detection devices (DDD) which can tolerate exposure to high energy electrons (higher energy electrons deposit a lower amount of energy at the point of incident but subsequent backscattering leads to lower signal-to-noise ratio) and record the position of each incident electron using an array of small pixels. Direct detection can be used in one of three modes: integration (or “linear”), where all electrons striking the detector are recorded over a fixed time period, integrated and then summed for the full exposure; counting, were individual positions of electrons striking the detector are recorded and counted for full exposure; and super-resolution, where counting mode in combination with pixel size smaller than the individual electron events allows to calculate the position of the deposited signal with sub-pixel precision (Cheng 2015, Chiu, Li et al. 2015). In general, imaging in counting mode records less noise leading to better signal to noise ratio compared to integration mode. The digital cameras can record dose-fractionated image stacks (“movies”) and typical exposure times are based on the total dose one chooses to apply to the specimen sample.

7.1.2.2 SINGLE PARTICLE ANALYSIS

SPA is a technique that uses a set of image processing tools in a workflow with an aim to reconstruct the original target molecule. After imaging the desired 3D structure of the macromolecule, the 2D EM projections are recorded. In theory, a collection of a set of 2D projection views would allow us to reconstruct the structure of the 3D object. In practice, there are many problems that limit the achievable resolution, as discussed before.

7.1.2.2.1 PRE-PROCESSING OF IMAGES

In a typical SPA workflow, first, the movie frames must be aligned to generate a single image. Movie alignment is usually done as a combination of a whole frame alignment and a correction of local motion since during exposure not all regions of a frame moves at the same rate (e.g. more drift is observed in thin ice close to the hole centre, while less is seen closer to the carbon support film). Ideally, per-particle alignment should be used as this corrects the movement experienced by an individual particle. By applying defocus during image acquisition, we corrupt information, but if we can properly fit the CTF, this information can be recovered. CTF only modulates the signal from elastically scattered electrons – thus only signal from protein or water is modulated by CTF.

To correct the distortions, the image must be corrected for the effects of the CTF, which in turn is modulated by an envelope decay. The procedure for restoring the real image by eliminating the effects of CTF is called CTF "correction" (Orlova and Saibil 2011). Since the information is missing at frequencies where CTF is 0, one cannot fully correct the image.

7.1.2.2.2 CTF ESTIMATION

To accurately model and correct for the CTF, the exact value of defocus and astigmatism must be determined. First, the power spectrum is calculated, as the magnitude squared of the FT of the images (as Thon rings). The positive and negative halves of the CTF are not discerned due to the squaring operation. The spectrum's background is estimated and subtracted. Then rotational averaging is applied to compare model and experimental data using cross-correlation. The fitting is performed in 2D where the amplitude profile is compared to a range of theoretical 2D CTF functions until similarity is maximised. The CTF oscillations are dependent on the defocus, with larger defocus values having

higher frequency oscillations, which affect the accuracy of the fit. Once the best-fitting defocus value is determined, the CTF can be corrected (Rohou and Grigorieff 2015).

Astigmatism, manifested by elliptical Thon rings, if present, must be accounted for in the CTF model. Most of the programs commonly used today determine the astigmatism in the images – CTFFIND4 (Rohou and Grigorieff 2015) assumes it can be approximated as an ellipse (true for small astigmatism). Up until now, the majority of CTF fitting software (e.g., CTFFIND4) determine the fit assuming CTF is in 2D. However, as shown in a recent study the particles in most cases are not in a flat environment (Noble, Dandey et al. 2018). The particles at different positions within the ~100 Å ice layer will have different defocus values. Ideally, defocus should be measured for each particle but in most cases, there is not enough signal. For more accurate CTF calculations, software that uses patch-based CTF estimation (Warp (Tegunov and Cramer 2019), cryoSPARC (Punjani, Rubinstein et al. 2017) have been developed. In this case, the local CTF landscape is estimated).

7.1.2.2.3 CTF CORRECTION

There are a number of different methods to apply corrections in order to undistort the images affected by the applied defocus during imaging:

- Correct the phases only: Phase flipping. Since the worst part of the CTF is the alternating polarity, the Fourier transform (FT) of an image can be multiplied by the sign of the CTF and transformed back. This results in CTF having 0 values at certain frequencies, and to handle this, information of data collected at various defocus values is used. This allows the CTF values of 0 to be filled by the data from other images.
- Correct the phases and amplitudes: Performing “inverse filtering”, e.g., with a Wiener filter. This is normally done in two steps: the phases are flipped first followed by amplitude correction. Each image FT is multiplied by its own CTF, all equivalent views are summed and divided by the sum of all CTFs squared. To avoid division by 0, a constant – Wiener factor – related to signal-to-noise ratio (SNR) is added (Penczek 2010).

7.1.2.2.4 PARTICLE PICKING

Nowadays particle picking from micrographs is an automated process and three different approaches can be used:

1. Template based picking (RELION, others). Template images (from data, model, or a related structure) are used to locate individual particles in the micrographs by a cross-correlation search.
2. Gaussian blob picking (RELION (Zivanov, Nakane et al. 2018), Gautomatch (http://www.mrc-lmb.cam.ac.uk/kzhang/). Uses circular and/or elliptical blobs of a specified diameter to identify particle positions.
3. Deep learning algorithms (Warp (Tegunov and Cramer 2019), crYOLO (Wagner, Merino et al. 2019), Topaz (Bepler, Morin et al. 2019)). Based on convolutional neural networks, these algorithms are trained by user to recognise positively labelled classifier to be used for prediction-based picking.

Once the particle positions have been identified in the micrographs, they are extracted in separate square images, called boxes. The dimensions of the extraction box is typically estimated based on the particle diameter with an additional surrounding area, since high-resolution information is delocalised with defocus. By making box size too small, the CTF signal will be cut out, essentially restricting the achievable resolution. As a rule of thumb, the box size is 1.5-2 times the size of the particle diameter (Scheres 2016).

7.1.2.2.5 IMAGE NORMALISATION AND PARTICLE SORTING

During image acquisition, variations in the sample environment lead to differences in background grey level and image contrast and have to be normalised before the 3D reconstruction. In RELION, the mean density of particles is set to a zero, and a standard deviation of one for all the pixels in the background (Scheres 2016). It is important for image alignment that all the images are scaled to the same value.

With the first two picking methods, it is inevitable to pick lots of noise, so it is essential to "clean" the particles and get rid of the junk. Deep learning algorithms can be trained to pick considerably less noise, but not to avoid it completely. There are many ways of removing noise and bad particles, and depending on the sample, some are more efficient. These include:

- sorting based on image statistics (not considered effective anymore)
- 2D classification rounds (most commonly used, but not useful if particles do not align well or do not have high numbers)
- multi-reference *ab-initio* model (usually used for trickier datasets)
- 3D classification (hetero-refinement using initial model)

7.1.2.2.6 2D CLASSIFICATION

In most cases, the extracted particles are initially sorted using reference-free 2D class averaging to improve the low SNR. The relative rotation and translation of the images must be known before averaging, so iterative 2D-alignment of the projections is followed by classification of the alignments in classes, known as multi-reference refinement (Scheres, Valle et al. 2005). In RELION, reference-free 2D classes are obtained in an unsupervised manner from random subsets of the initial data, with the user supplying initial number of references (Scheres 2010).

The two main approaches for both averaging 2D projections and reconstruction of a 3D map are the maximum-likelihood (ML) and the least-squares methods. The main difference between the two is how the unknown parameters of the 2D projections (relative orientations are not known) are handled (Sigworth, Doerschuk et al. 2010). In both approaches, the particles are superimposed and averaged to increase the SNR and enhance the features, while eliminating noise. This is not a trivial task and the initial assumptions include:

- All particles are the same molecule and have approximately identical structure.
- All are linked by a 3D rigid body transformation (rotation/ translation)
- Particles have both a signal and a noise part

The alignment is an iterative process which involves successive steps of centring the particles within the box, grouping and averaging them. To reduce noise in the images, a mask is applied around the particle to exclude background in real space. In reciprocal space, selected band-pass filters can be applied to remove low- or high-frequency components of the image that contributes to the noise. The experimental projection images are compared to a set of references (or templates) before averaging them to a new set of references for the next iteration. As this is a computationally expensive step, particles can be binned to reduce the image size and speed up the calculations.

In the least-squares approach, each particle is assigned to a single reference image based on the highest cross-correlation (CC) coefficient (Sigworth, Doerschuk et al. 2010). The alignment of the projections is performed by the cross-correlation function (CCF) using both translational and rotational searches, since the particles adopt random orientations in the ice. The calculations are much faster in Fourier space and padding (applying larger frame around the original image) is required. Without padding, the image would get superimposed on a copy of itself. CC alignment is not very reliable at low SNR, so the alignments are iterated with the output serving as an input for the next cycle, resulting in better resolved averages and thus improved reference images.

In the ML approach, each particle is assigned a CC value (a probability-weighted average) for all of the reference images to define the possible orientations (Scheres, Valle et al. 2005). The statistical noise model used in the ML approach allows us to deal with the low SNR in the CCF (Sigworth, Doerschuk et al. 2010). The Bayesian approach, implemented in RELION (Scheres 2012), introduced a regularization term to the likelihood function, which imposes prior distributions on model parameters, affecting ML optimisation. Optimisation of the resulting posterior distribution is called ***regularized likelihood*** optimization (Scheres 2012).

7.1.2.2.7 FROM 2D TO 3D RECONSTRUCTION

The goal of the 2D classification is to effectively sort all the particles of interest in a limited number of classes while maintaining the adequate representation of the different projections.

For the 3D reconstruction, the relative orientations of 2D projections must be identified. The experimental approach involves collecting images of the same particles at known tilt angles, while the computational approach relies on a collection of projections arising from the majority of all the possible 3D orientations.

For 3D reconstruction from its 2D projections, many approaches have been developed, that can be split into two groups. Reconstruction in real-space includes back-projection and algebraic reconstructions (Orlova and Saibil 2011). Otherwise, reconstructions can be done in Fourier space. This is based on the projection theorem that the 2D FT of the projection of a 3D density is a central section of the 3D FT (Figure 7.10).

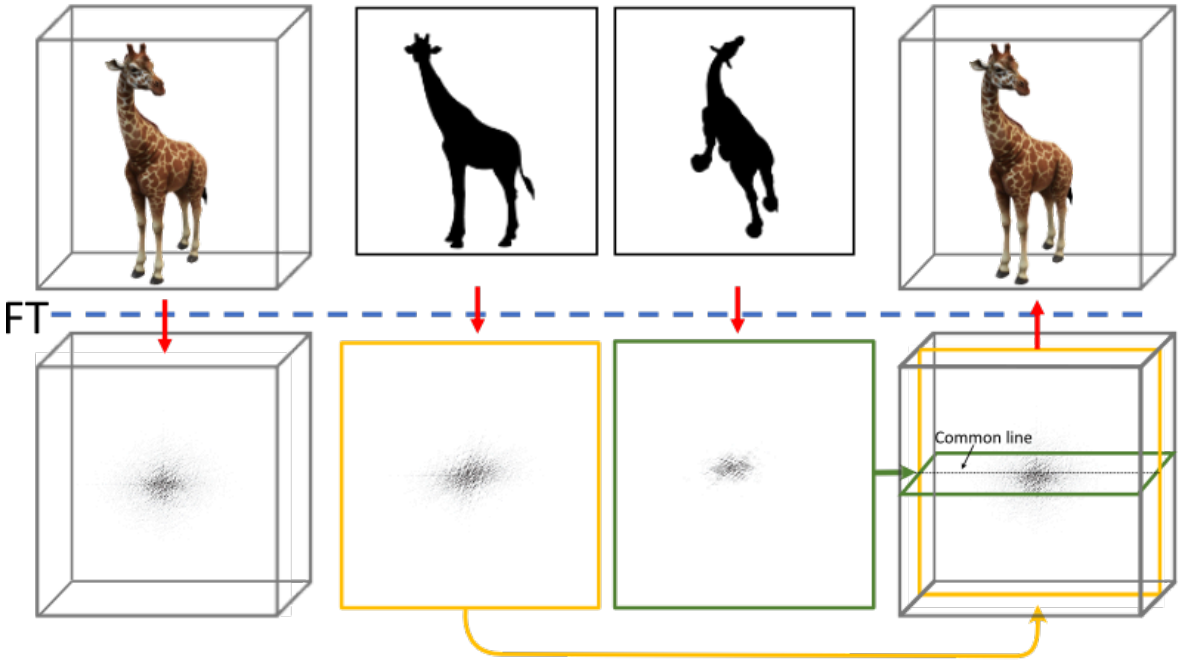


Figure 7.10: Central section theorem. For each 2D projection of a 3D volume, there is a common line that both projections share (shown as a dashed line). The Fourier transform (FT) of each 2D projection is a slice passing through the origin of the 3D FT of the original object. With enough 2D FT from the projections, the 3D FT can be recovered, and the original 3D volume calculated by applying inverse FT operation on the experimentally estimated 3D FT. The more evenly the space is sampled, the more isotropic the resolution of the final model.

7.1.2.2.8 INITIAL MODEL

All cryo-EM 3D refinement algorithms require an initial reference model. While in theory the correct solution can be reached with random initialisation, accurate starting models ensure that the refinement converges at the correct solution. Since the FT of a 2D projection is a central slice in the 3D FT of the original object, for 3D reconstruction we need angles describing the relative orientation of each projection. Euler angles are used to describe the possible 3D orientations in a fixed coordinate system using three angles (typically denoted φ, θ, ψ). For an unknown structure, there are two methods to determine the orientation of the projections relative to the model (both use unsupervised classification):

- Random-conical tilt
- Common lines/ angular reconstitution

Of these, most software programs nowadays use Common lines/ angular reconstitution method that will be discussed here. 3D structure determination is considered an optimisation problem with a goal to find the 3D structure that is best described by the observed images. In RELION, this is done by

iterative rounds of marginalised assignment of unknown pose to observed images, describing the 3D rotation and 2D translation. Such refinement methods depend on the initial model – a starting model far from the correct 3D model will converge to a locally optimal probability, resulting in an incorrect structure (Scheres 2012). The stochastic gradient descent (SGD) algorithm, initially implemented in cryoSPARC, uses random subsets of particle images to start from randomly generated initial models to sample the possible 3D structures and eventually converge near the correct structure (Punjani, Rubinstein et al. 2017). This has been proven to be successful in identification of multiple initial models, representing different conformational states of the macromolecule. Compared to other methods developed for initial model generation, SGD algorithm is less likely to converge to the wrong solution as it samples much broader range of the 3D space.

7.1.2.2.9 3D REFINEMENT

In RELION, during 3D refinement, the structure is improved though iterative steps. First, 2D projections of the user provided initial model are generated and compared with all the experimental images, called projection matching (expectation) step. This is done by calculating a maximum CC to determine reference-based relative orientations of the experimental projections (in the same manner as in 2D classification described earlier). The ML approach means that orientations are assigned as a probability distribution for all the possible alignments.

In the next step, the experimental images with the information obtained in the previous step are combined and the new structure is then used as the initial model for the following iteration. Iterations are stopped after the model does not improve anymore (Scheres 2012).

All the methods used in 3D model reconstruction suffer from blurring of the signal owing to heterogeneity and the resulting loss of contrast at high resolution. To compensate for high resolution amplitude decay, described by temperature (B-) factor, it is a standard procedure to scale the refined experimental maps by applying an inverse B-factor to increase the high resolution amplitudes (Orlova and Saibil 2011). During 3D refinement, the particles in the dataset used are split into two half-data sets of equal size that are kept separate for the rest of the data processing to prevent overfitting. The resulting ‘half maps’ are combined at the end of the refinement procedure to generate a reconstruction with contribution from all aligned particles

7.1.2.2.10 VALIDATION

Once the 3D model is obtained, the resolution of the reconstruction is calculated using Fourier shell correlation (FSC) of two independent reconstructions, each containing half of the particles used in the 3D refinement. Therefore, FSC is a cross-correlation **coefficient** calculated for the two half maps as a function of **resolution** (split in resolution **shells**) in **Fourier** space. The standard in the field ("gold standard FSC") is to split the data in half before initial reconstruction and process it separately throughout the refinement. The FSC between the two independent datasets is a correlation of structure factors. The standard resolution criterion to use when reporting in literature was proposed to be the value of FSC at 0.143. This represents the resolution at which the correlation between an experimentally calculated density and a perfect reference is 0.5 (Rosenthal and Henderson 2003).

7.1.3 X-RAY CRYSTALLOGRAPHY

7.1.3.1 THEORY OF PROTEIN X-RAY CRYSTALLOGRAPHY

In crystallography, lattices, defined by vectors **a**, **b** and **c**, are made of regular, translationally periodic units. These units, when occupied by macromolecules, are called unit cells. Protein crystals are translationally periodic arrangements of unit cells, where the contents of the units are identical (Figure 7.11).

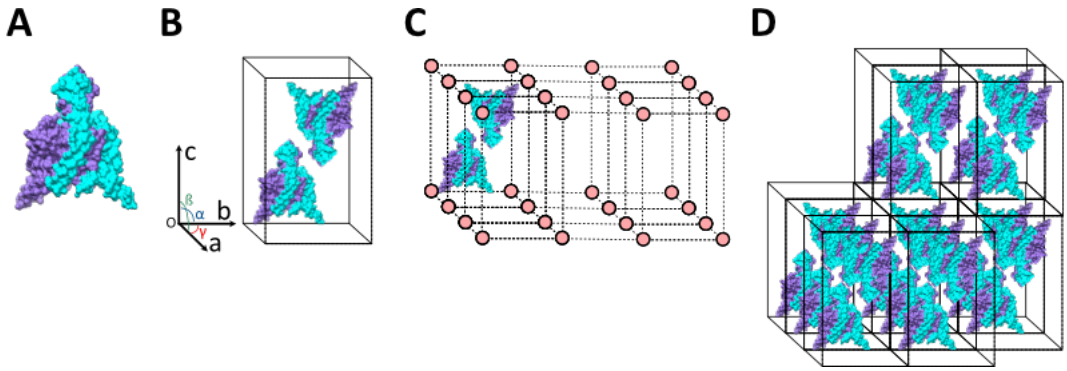


Figure 7.11: Assembly and contents of a crystalline lattice. **A** Asymmetric unit (molecule) **B** Unit cell containing two asymmetric units **C** Crystal lattice with one unit cell shown **D** Unit cells in a crystalline lattice.

The unit cells can contain multiple macromolecules, which are related by symmetry operations. Due to the chirality of protein molecules, the requirement for the object (protein) properties to remain uniform while applying symmetry operations reduces the number of allowed symmetry operations and introduces translational constraints. The asymmetric unit (AU) is defined as the smallest unit needed

to assemble the entire unit cell by applying symmetry operations (Figure 7.11). The instructions on how to generate the unit cell are described by the 230 **space groups**. The common notion for assignment of axes and angles describing a unit cell are shown in Figure 7.11 B. There are 14 lattice cell possibilities, defined by the relation between their axes, angles and internal translations, known as Bravais lattices. The symmetry operations allowed for chiral molecules (here – proteins composed of chiral amino acids) in 3D space includes only plain rotation and screw axes (N-fold rotation followed by a translation operation), since inversions, glides or mirror axes would change the isomeric form of amino acids (i.e., L- to D-). Due to these translational periodicity requirements in crystal packing, there are only 65 space groups that the asymmetric, chiral macromolecules can arrange in in 3D space. In addition to crystallographic symmetry, NCS exists when more than one copy of the same molecule is present in the AU. This is the case for macromolecular oligomers that can exhibit some local variability between monomers. Although the copies adopt the same fold, they are not related by crystallographic symmetry as this requires two identical objects (Rupp 2010).

Diffraction in macromolecular crystallography is the interaction of X-rays with periodically arranged protein molecules. Diffraction by a single molecule is too small to be detected while in protein crystals the periodically arranged molecules systematically amplify the signal. Diffraction can only be detected for waves that remain in phase (constructive interference) after the scattering event, since waves that are not in phase (destructive interference) will have resulting amplitude of zero. Bragg's Law describes the conditions that will produce constructive interference between the scattered waves. The equation describes the quantitative relationship between the lattice spacing in the crystal and the diffraction angle of unique reflections by treating X-ray diffraction as a reflection on a set of parallel planes in the crystal (Figure 7.12):

$$n\lambda = 2d \sin \Theta$$

where n is an integer, λ is the wavelength, d is the lattice spacing d_{hkl} and Θ is the diffraction angle.

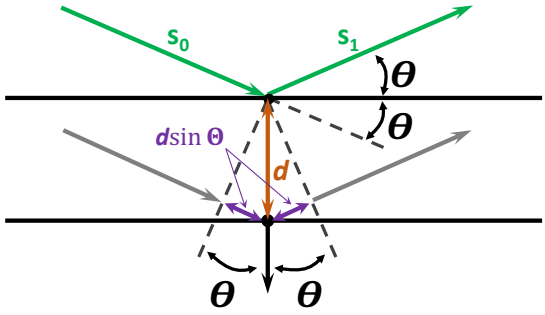


Figure 7.12: Graphical representation of Bragg's law. It shows the conditions that will produce constructive diffraction. The path difference between the two incoming (s_0 and the parallel arrow in grey) waves after the scattering incident (s_1 and the parallel arrow in grey) is 2d*sinθ, which must be equal to multiple of nλ for maximum constructive interference, where λ is the wavelength. d - the spacing of the lattice.

The diffraction geometry is best described using the reciprocal lattice representation. The geometric relationship between real space and reciprocal space is illustrated in Figure 7.13.

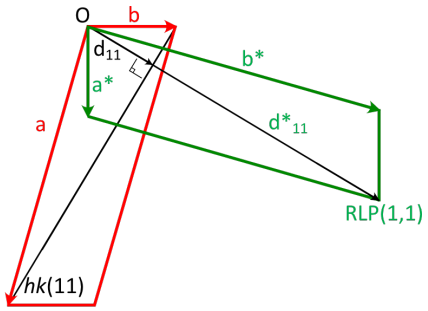


Figure 7.13: Reciprocal space generation in 2D. Real space lattice (red) and its corresponding reciprocal lattice (green) are shown. Both lattices share the same origin (O). The reciprocal axes a* and b* are generated so that they are perpendicular to real space axes b and a, respectively. The lattice vector d^*_{11} is perpendicular to the lattice planes with indices (11) and points to the reciprocal lattice point (RLP (1,1). Adapted from (Rupp 2010).

Essentially, the reciprocal lattice represents the scattering possibilities of a given crystal. The conditions required for diffraction to be observed is conveniently shown by Ewald's sphere (Figure 7.14).

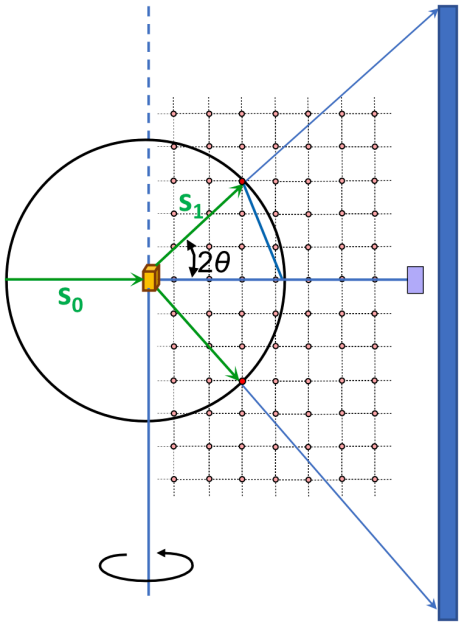


Figure 7.14: Ewald's sphere and the crystal diffraction. The Ewald's sphere (black circle of radius of 1/ λ, Å), centred at the crystal (yellow cube) show the reciprocal lattice points that fulfil Bragg's law (red spheres) when they are sampled by the scattered waves (S_1) and are recorded on the detector (blue rectangle) as reflections. To record as many reflections as possible, the crystal is rotated around its origin. S_0 – incident beam, purple square – beamstop. Adapted from (Rupp 2010).

It shows that at a single orientation of crystal, only a few reflections will fulfil the constructive diffraction conditions, but majority will not lie on the surface of the Ewald sphere. To collect full reflection information of a crystal, it must be rotated around its origin, which will result in more reciprocal space points being recorded as reflections on the detector.

The choice of a data collection strategy is mostly automated with data collection and analysis software ensuring that a sufficient amount of data will be collected based on initial screening images. It is important to select the total angular range appropriate for the crystal symmetry that would result in measuring all the possible reflections. In principle, collecting 180° of data will ensure maximum completeness. However, depending on crystal symmetry and orientation relative to the beam, a minimum complete data set can be collected with a much smaller rotation range. The most common method used for data collection is the rotation method. The crystal in the X-ray beam is rotated around a single axis by small increments (0.1° or less) as the diffraction images are recorded. This results in reflections being split over multiple images but can give more accurate integration of the peaks (Rupp 2010).

7.1.3.2 DATA PRE-PROCESSING IN X-RAY CRYSTALLOGRAPHY

The first step in data processing is indexing – the assignment of a unit cell based on the observed diffraction pattern and the determination of the orientation of the crystal. In most cases, this is done after collecting a few initial images at relatively large (e.g., 45˚) offset angles to resolve the reciprocal lattice vectors representing all 3 principal axes. The indexing programs map the spot positions in the diffraction image to the coordinates of the reciprocal lattice point that gave rise to that spot based on the geometry of Ewald's sphere. Since indexing relies only on the spot positions, only the shape of the unit cell can be determined at this stage. The lattice of the identified unit cell determines the data collection strategy with reflections that cover the whole asymmetric unit of the reciprocal space as a minimum. In practice, more data is commonly collected to achieve higher redundancy and more accurate data.

After a data set is collected, the initial indexing is refined using more diffraction images for more accurate spot detection in the whole data set. The pixel intensities of the diffraction spots from the digital diffraction images are integrated, with reflections distributed over multiple images combined. Integration is the estimation of the intensity value of each reflection and its uncertainty.

Following integration of spots on the set of diffraction images, the measurements of identical reflections (crystal symmetry equivalents) are merged and scaled. Scaling involves normalisation of the integrated intensity values over all the images, by correcting the instrument or the crystal inaccuracies. After scaling, the remaining differences between the reflections can be analysed to estimate the data quality. The measures regarding the data quality include merging R-values, redundancy and the SNR ratio, computed for the whole data set and for separate resolution bins. The traditional R_{merge} value increases with redundancy even if the data quality improves and so is not a particularly useful measure. The redundancy-independent R-value, R_{meas} give larger values than R_{merge} while R_{pim} (precision-indicating merging) accounts for increasing data accuracy with increasing redundancy. These two statistics are therefore more reliable indicators of overall data quality. Additionally, the correlation coefficient between random half-datasets, $CC_{1/2}$ (Karplus and Diederichs 2012), is statistically meaningful and can show the actual quality of weak data. As a rule of thumb, a $CC_{1/2}$ value of between 0.3-0.5 in the high-resolution shells is used to judge the reliability of weak reflections. Determination of the point group or, if possible, space group, based on the symmetry of the diffraction pattern, merging statistics and systematic absences can now be done. Finally, truncation

analyses the scaled and merged data and produces the diagnostics on the intensity distributions of the experimental data. The deviations from the expected model can be analysed to describe the degree of order in the crystal (Wilson B-factor) and the crystal pathologies (such as twinning) (Rupp 2010).

7.1.3.3 DATA POST-PROCESSING IN X-RAY CRYSTALLOGRAPHY

Each reflection in a diffraction image represents an X-ray wave that consists of amplitude and phase. The amplitude can be calculated as the square root of the intensity of the reflection, while the phase information is lost during data collection, as the detectors can only record the intensities. Without the phases, the original electron density distribution in the crystal cannot be computed. In practice, the phases are supplied from a separate phasing experiment (Rupp 2010).

7.1.3.4 PHASING – MOLECULAR REPLACEMENT

Experimental phasing is unavoidable for novel structures and can be used as a general approach to solve protein structures, yet it is a complex task. In cases where known structures of the target or close structural homologs are available, molecular replacement (MR) can be used to obtain the initial phase estimates. This method applies rotational and translational searches on the known model placed in the unit cell or asymmetric unit of the unknown structure until a solution with the best fit between the calculated diffraction data from the model and the observed diffraction from the target protein is found. Given the ever-increasing number of Protein Data Bank (PDB) depositions, MR is the method of choice for most of the newly determined X-ray crystallography structures.

During molecular replacement, a prepared search model is used to determine the proper orientation and location of it in the unit cell of the target protein. The search is a 6-dimensional problem that can be split into two parts: the 3D rotation search, which searches only the rotation matrix, followed by the 3D translation search that determines the translation vector for the determined rotation matrix. After the known model is properly orientated in the unit cell of the target protein, the initial phase estimates can be calculated for the target protein.

Depending on the sequence identity between the search model and the target protein, it is often necessary to use multiple models resulting in multiple possible solutions that should be evaluated carefully. This can be done by evaluating the solution based on the proposed crystal packing (clashes or large areas of void probably suggest the solution is wrong) or by refinement considerations (LLG score and the Z-score (>6) in Phaser (McCoy, Grosse-Kunstleve et al. 2007)). Since only model phase

information in known, the model phase bias arising from model bias should be minimised. The partial and flawed target phase information is accounted for by applying ML coefficients during map reconstruction (Rupp 2010). The initial MR phases can be further improved, for example, by density modification. For this, experimental amplitudes and an atomic model are used to calculate new phase estimates by imposing prior expectations (e.g., matching NCS-related density, density for the built model matching the expected density, etc) (Terwilliger 2002).

7.1.3.5 MEMBRANE PROTEIN CRYSTALLISATION TECHNIQUES

7.1.3.5.1 VAPOUR DIFFUSION

Vapour diffusion (VD) is the method of choice for macromolecule crystallisation. The method involves mixing a protein containing solution with a crystallisation solution, a cocktail containing salts and chemicals (precipitants) that aid in the formation of crystals. The resulting drop is equilibrated against a reservoir in a closed system, which causes diffusion process and gradual concentration of the protein and the precipitants in the drop. Different methods have been developed with sitting drop and hanging drop being the most commonly used (Figure 7.15 A, B). During the equilibration process, the protein in the drop solution will proceed through many conditions before the crystals are formed, as shown in Figure 7.15 (Chayen 1998).

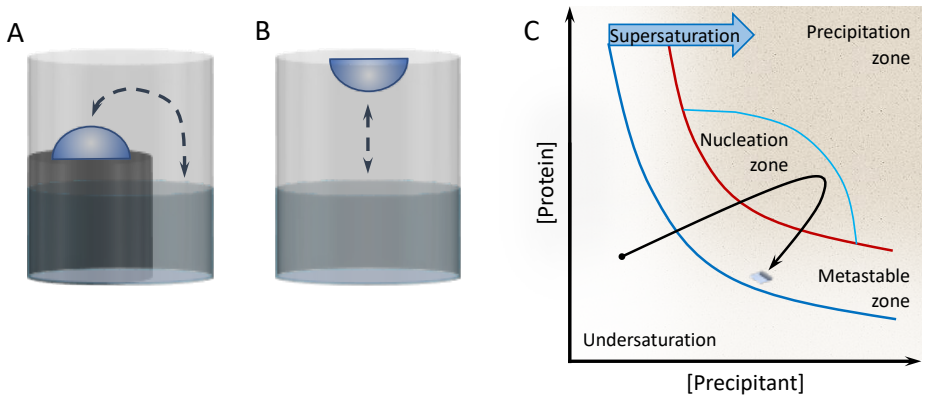


Figure 7.15. Protein crystal formation in vapour diffusion experiments. **A** Sitting drop experimental set up. A drop of a mixed protein sample and the crystallisation solution is placed in a chamber with a reservoir of crystallisation solution. Due to the mixing, the crystallisation solution concentration is lower in the drop than in the reservoir. To achieve the equilibrium, water vapour leaves the drop to achieve the equilibrium between the two solution. As the water content of the drop decreases, the increase in supersaturation takes place, driving protein crystal formation. **B** Hanging drop experimental set up. The physical chemistry is the same as described in A. The drop is placed on a cover slip that is

sealed over a chamber with reservoir solution. **C** A phase diagram showing the principle of protein crystallization in vapour diffusion system. The different protein solubility states (undersaturation and supersaturation) depend on the protein and the precipitating agent concentrations in the drop. The black arrow shows one of the pathways for crystal formation and growth. As the drop equilibrates with the reservoir solution, the protein and the precipitant concentrations increase linearly, up until nucleation zone. If the experimental conditions favour protein crystal formation, the protein molecules will form spontaneous clusters that can lead to crystal formation. This process reduces the protein molecule concentration in the solution, and the crystal growth continues in the metastable zone. Crystal growth would continue until the conditions reach the solubility boundary (dark blue line). Adapted from (Chayen 1998).

7.1.3.5.2 LIPIDIC CUBIC PHASE

Lipidic cubic phase (LCP) is an *in meso* crystallisation system developed for membrane protein crystallisation. The lipids – monoacylglycerols (MAGs) – after melting can be hydrated (with, for example, a protein solution) which give rise to a number of mesophases, whose properties depend on the water content and the temperature. The mesophase suited for protein crystallisation can be imagined as a sponge composed of lipidic bilayer with the pores representing the aqueous channels. The mesophases are dynamic systems, which is essential feature for crystal formation. The technique involves membrane protein reconstitution in a lipid bilayer of the cubic phase. Upon reconstitution, the protein is no longer constrained by the detergent micelle and can freely diffuse through the plane of lipid bilayer. The mesophase with the reconstituted protein is dispensed in small blobs that are covered with a precipitation solution. The diffusion of the precipitant solution in the mesophase causes local phase transitions, some of which will become enriched in protein leading to protein crystal formation (Caffrey 2009).

7.2 SEQUENCE ALIGNMENT OF HUMAN AND BACTERIAL SLC1 TRANSPORTERS

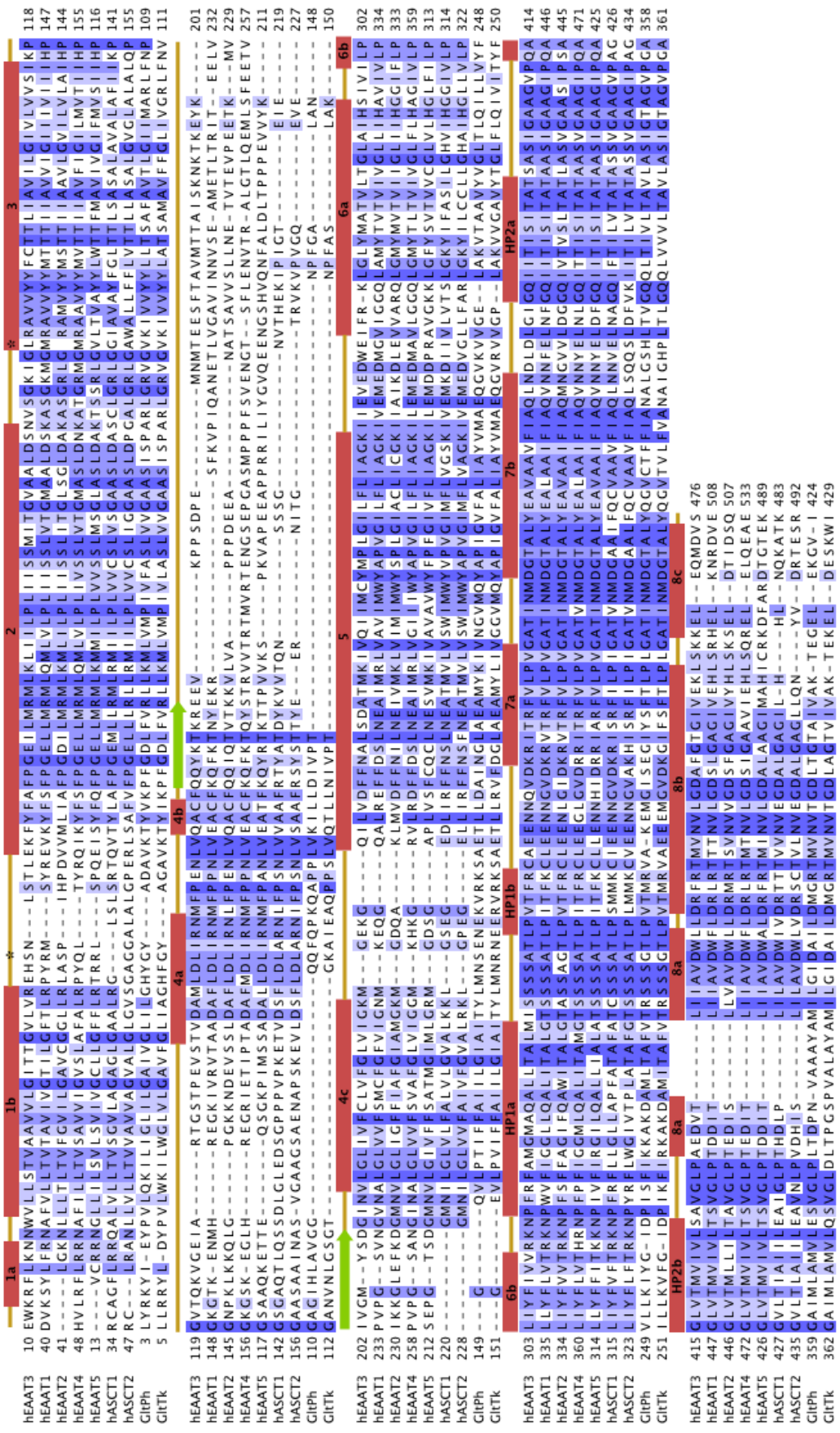


Figure 7.16. Sequence alignment of human and bacterial SLC1 transporters. Amino acid sequences of hEAAT1-5, hASCT1-2 and bacterial homologues GltPh and GltTk are compared. The α-helices are shown as red rectangles, and the ß-strands as green arrows in positions as seen in the EAAT3 structure.

The EAAT3 construct used had two point mutations introduced during cloning (marked with *), but both substitutions (S42R and L92V) are found in EAAT5. Sequences were coloured based on percentage identity in Jalview (Waterhouse, Procter et al. 2009). The colouring is based on the percentage of the residues in each column that agree with the consensus sequence, with white being <40%, light blue >40%, blue >60% and dark blue >80%.

BIBLIOGRAPHY

Acosta, C., L. Djouhri, R. Watkins, C. Berry, K. Bromage and S. N. Lawson (2014). "TREK2 Expressed Selectively in IB4-Binding C-Fiber Nociceptors Hyperpolarizes Their Membrane Potentials and Limits Spontaneous Pain." Journal of Neuroscience **34**(4): 1494-1509.

Afonine, P. V., B. P. Klaholz, N. W. Moriarty, B. K. Poon, O. V. Sobolev, T. C. Terwilliger, P. D. Adams and A. Urzhumtsev (2018). "New tools for the analysis and validation of cryo-EM maps and atomic models." Acta Crystallogr D Struct Biol **74**(Pt 9): 814-840.

Afshari, P., M. Myles-Worsley, O. S. Cohen, J. Tiobech, S. V. Faraone, W. Byerley and F. A. Middleton (2015). "Characterization of a Novel Mutation in SLC1A1 Associated with Schizophrenia." Mol Neuropsychiatry **1**(3): 125-144.

Afshari, P., W. D. Yao and F. A. Middleton (2017). "Reduced Slc1a1 expression is associated with neuroinflammation and impaired sensorimotor gating and cognitive performance in mice: Implications for schizophrenia." PLoS One **12**(9): e0183854.

Aggarwal, S. and O. V. Mortensen (2017). "In Vitro Assays for the Functional Characterization of the Dopamine Transporter (DAT)." Curr Protoc Pharmacol **79**: 12 17 11-12 17 21.

Alberts, B. (2002). Molecular biology of the cell. New York, Garland Science.

Alexander, S. P. H., E. Kelly, A. Mathie, J. A. Peters, E. L. Veale, J. F. Armstrong, E. Faccenda, S. D. Harding, A. J. Pawson, J. L. Sharman, C. Southan, J. A. Davies and C. Collaborators (2019). "THE CONCISE GUIDE TO PHARMACOLOGY 2019/20: Transporters." Br J Pharmacol **176 Suppl 1**: S397-S493.

Allen, C. L. and U. Bayraktutan (2009). "Oxidative stress and its role in the pathogenesis of ischaemic stroke." Int J Stroke **4**(6): 461-470.

Altschul, S. F., W. Gish, W. Miller, E. W. Myers and D. J. Lipman (1990). "Basic local alignment search tool." J Mol Biol **215**(3): 403-410.

Andin, J., M. Hallbeck, A. H. Mohammed and J. Marcusson (2007). "Influence of environmental enrichment on steady-state mRNA levels for EAAC1, AMPA1 and NMDA2A receptor subunits in rat hippocampus." Brain Res **1174**: 18-27.

Aoyama, K., S. W. Suh, A. M. Hamby, J. Liu, W. Y. Chan, Y. Chen and R. A. Swanson (2006). "Neuronal glutathione deficiency and age-dependent neurodegeneration in the EAAC1 deficient mouse." Nat Neurosci **9**(1): 119-126.

Arakawa, T., T. Kobayashi-Yurugi, Y. Alguel, H. Iwanari, H. Hatae, M. Iwata, Y. Abe, T. Hino, C. Ikeda-Suno, H. Kuma, D. Kang, T. Murata, T. Hamakubo, A. D. Cameron, T. Kobayashi, N. Hamasaki and S. Iwata (2015). "Crystal structure of the anion exchanger domain of human erythrocyte band 3." Science **350**(6261): 680-684.

Arkhipova, V., G. Trinco, T. W. Ettema, S. Jensen, D. J. Slotboom and A. Guskov (2019). "Binding and transport of D-aspartate by the glutamate transporter homolog GltTk." Elife **8**.

Arriza, J. L., W. A. Fairman, J. I. Wadiche, G. H. Murdoch, M. P. Kavanaugh and S. G. Amara (1994). "Functional comparisons of three glutamate transporter subtypes cloned from human motor cortex." J Neurosci **14**(9): 5559-5569.

Baier, C. J., J. Fantini and F. J. Barrantes (2011). "Disclosure of cholesterol recognition motifs in transmembrane domains of the human nicotinic acetylcholine receptor." Sci Rep **1**: 69.

Bailey, C. G., R. M. Ryan, A. D. Thoeng, C. Ng, K. King, J. M. Vanslambrouck, C. Auray-Blais, R. J. Vandenberg, S. Broer and J. E. Rasko (2011). "Loss-of-function mutations in the

glutamate transporter SLC1A1 cause human dicarboxylic aminoaciduria." J Clin Invest **121**(1): 446-453.
Bastug, T., G. Heinzelmann, S. Kuyucak, M. Salim, R. J. Vandenberg and R. M. Ryan (2012). "Position of the third Na+ site in the aspartate transporter GltPh and the human glutamate transporter, EAAT1." PLoS One **7**(3): e33058.
Baukrowitz, T. and G. Yellen (1995). "Modulation of K+ current by frequency and external [K+]: a tale of two inactivation mechanisms." Neuron **15**(4): 951-960.
Baukrowitz, T. and G. Yellen (1996). "Use-dependent blockers and exit rate of the last ion from the multi-ion pore of a K+ channel." Science **271**(5249): 653-656.
Bayburt, T. H. and S. G. Sligar (2003). "Self-assembly of single integral membrane proteins into soluble nanoscale phospholipid bilayers." Protein Science **12**(11): 2476-2481.
Bayliss D.A., C. G., Enyedi P., Goldstein S.A., Lesage F., Minor, Jr. D.L., Plant L.D., Sepúlveda F. and Winn B.T. (2019). "Two P domain potassium channels (version 2019.4) in the IUPHAR/BPS Guide to Pharmacology Database." IUPHAR/BPS Guide to Pharmacology CITE **2019(4)**.
Bazzone, A., M. Barthmes and K. Fendler (2017). "SSM-Based Electrophysiology for Transporter Research." Methods Enzymol **594**: 31-83.
Beghein, E. and J. Gettemans (2017). "Nanobody Technology: A Versatile Toolkit for Microscopic Imaging, Protein-Protein Interaction Analysis, and Protein Function Exploration." Front Immunol **8**: 771.
Bendahan, A., A. Armon, N. Madani, M. P. Kavanaugh and B. I. Kanner (2000). "Arginine 447 plays a pivotal role in substrate interactions in a neuronal glutamate transporter." J Biol Chem **275**(48): 37436-37442.
Bepler, T., A. Morin, M. Rapp, J. Brasch, L. Shapiro, A. J. Noble and B. Berger (2019). "Positive-unlabeled convolutional neural networks for particle picking in cryo-electron micrographs." Nat Methods **16**(11): 1153-1160.
Berg, J. M., J. L. Tymoczko, L. Stryer and G. J. Gatto (2012). Biochemistry. New York Basingstoke Palgrave Macmillan,, W.H. Freeman ;.
Bergles, D. E., J. S. Diamond and C. E. Jahr (1999). "Clearance of glutamate inside the synapse and beyond." Curr Opin Neurobiol **9**(3): 293-298.
Bianchi, M. G., D. Bardelli, M. Chiu and O. Bussolati (2014). "Changes in the expression of the glutamate transporter EAAT3/EAAC1 in health and disease." Cell Mol Life Sci **71**(11): 2001-2015.
Boudker, O., R. M. Ryan, D. Yernool, K. Shimamoto and E. Gouaux (2007). "Coupling substrate and ion binding to extracellular gate of a sodium-dependent aspartate transporter." Nature **445**(7126): 387-393.
Bozzo, L. and J. Y. Chatton (2010). "Inhibitory effects of (2S, 3S)-3-[3-[4-(trifluoromethyl)benzoylamino]benzyloxy]aspartate (TFB-TBOA) on the astrocytic sodium responses to glutamate." Brain Res **1316**: 27-34.
Brandstatter, J. H., P. Koulen and H. Wassle (1998). "Diversity of glutamate receptors in the mammalian retina." Vision Res **38**(10): 1385-1397.
Braun, G., M. Lengyel, P. Enyedi and G. Czirjak (2015). "Differential sensitivity of TREK-1, TREK-2 and TRAAK background potassium channels to the polycationic dye ruthenium red." Br J Pharmacol **172**(7): 1728-1738.
Brennecke, J. T. and B. L. de Groot (2018). "Mechanism of Mechanosensitive Gating of the TREK-2 Potassium Channel." Biophys J **114**(6): 1336-1343.
Bricogne G., B. E., Brandl M., Flensburg C., Keller P., Paciorek W., and S. A. Roversi P, Smart O.S., Vonrhein C., Womack T.O. (2019). "BUSTER version 2.10.3."

Bridges, R. J. and C. S. Esslinger (2005). "The excitatory amino acid transporters: pharmacological insights on substrate and inhibitor specificity of the EAAT subtypes." Pharmacol Ther **107**(3): 271-285.
Brohawn, S. G. (2015). "How ion channels sense mechanical force: insights from mechanosensitive K2P channels TRAAK, TREK1, and TREK2." Annals Reports, Vol 1352 **1352**: 20-32.
Brohawn, S. G., E. B. Campbell and R. MacKinnon (2013). "Domain-swapped chain connectivity and gated membrane access in a Fab-mediated crystal of the human TRAAK K+ channel." Proc Natl Acad Sci U S A **110**(6): 2129-2134.
Brohawn, S. G., J. del Marmol and R. MacKinnon (2012). "Crystal structure of the human K2P TRAAK, a lipid- and mechano-sensitive K+ ion channel." Science **335**(6067): 436-441.
Browne, H. A., S. L. Gair, J. M. Scharf and D. E. Grice (2014). "Genetics of obsessive-compulsive disorder and related disorders." Psychiatr Clin North Am **37**(3): 319-335.
Butchbach, M. E., G. Tian, H. Guo and C. L. Lin (2004). "Association of excitatory amino acid transporters, especially EAAT2, with cholesterol-rich lipid raft microdomains: importance for excitatory amino acid transporter localization and function." J Biol Chem **279**(33): 34388-34396.
Caffrey, M. (2009). "Crystallizing membrane proteins for structure determination: use of lipidic mesophases." Annu Rev Biophys **38**: 29-51.
Caffrey, M., D. F. Li and A. Dukkipati (2012). "Membrane Protein Structure Determination Using Crystallography and Lipidic Mesophases: Recent Advances and Successes." Biochemistry **51**(32): 6266-6288.
Callender, R., A. Gameiro, A. Pinto, C. De Micheli and C. Grewer (2012). "Mechanism of inhibition of the glutamate transporter EAAC1 by the conformationally constrained glutamate analogue (+)-HIP-B." Biochemistry **51**(27): 5486-5495.
Canolle, B., F. Masmejean, C. Melon, A. Nieoullon, P. Pisano and S. Lortet (2004). "Glial soluble factors regulate the activity and expression of the neuronal glutamate transporter EAAC1: implication of cholesterol." J Neurochem **88**(6): 1521-1532.
Canul-Tec, J. C., R. Assal, E. Cirri, P. Legrand, S. Brier, J. Chamot-Rooke and N. Reyes (2017). "Structure and allosteric inhibition of excitatory amino acid transporter 1." Nature **544**(7651): 446-451.
Carlson, M. L., J. W. Young, Z. Zhao, L. Fabre, D. Jun, J. Li, J. Li, H. S. Dhupar, I. Wason, A. T. Mills, J. T. Beatty, J. S. Klassen, I. Rouiller and F. Duong (2018). "The Peptidisc, a simple method for stabilizing membrane proteins in detergent-free solution." Elife **7**.
Chayen, N. E. (1998). "Comparative studies of protein crystallization by vapour-diffusion and microbatch techniques." Acta Crystallogr D Biol Crystallogr **54**(Pt 1): 8-15.
Chen, H., D. Zuo, J. Zhang, M. Zhou and L. Ma (2014). "Classification of 2-pore domain potassium channels based on rectification under quasi-physiological ionic conditions." Channels (Austin) **8**(6): 503-508.
Chen, W. W., M. Niepel and P. K. Sorger (2010). "Classic and contemporary approaches to modeling biochemical reactions." Genes & Development **24**(17): 1861-1875.
Cheng, Y. F. (2015). "Single-Particle Cryo-EM at Crystallographic Resolution." Cell **161**(3): 450-457.
Cheung, M., N. Kajimura, F. Makino, M. Ashihara, T. Miyata, T. Kato, K. Namba and A. J. Blocker (2013). "A method to achieve homogeneous dispersion of large transmembrane complexes within the holes of carbon films for electron cryomicroscopy." Journal of Structural Biology **182**(1): 51-56.

Chiu, P. L., X. Li, Z. Li, B. Beckett, A. F. Brilot, N. Grigorieff, D. A. Agard, Y. Cheng and T. Walz (2015). "Evaluation of super-resolution performance of the K2 electron-counting camera using 2D crystals of aquaporin-0." J Struct Biol **192**(2): 163-173.
Colas, C., C. Grewer, N. J. Otte, A. Gameiro, T. Albers, K. Singh, H. Shere, M. Bonomi, J. Holst and A. Schlessinger (2015). "Ligand Discovery for the Alanine-Serine-Cysteine Transporter (ASCT2, SLC1A5) from Homology Modeling and Virtual Screening." PLoS Comput Biol **11**(10): e1004477.
Colas, C., P. M. Ung and A. Schlessinger (2016). "SLC Transporters: Structure, Function, and Drug Discovery." Medchemcomm **7**(6): 1069-1081.
Coleman, J. A., E. M. Green and E. Gouaux (2016). "X-ray structures and mechanism of the human serotonin transporter." Nature **532**(7599): 334-339.
Colleoni, S., A. A. Jensen, E. Landucci, E. Fumagalli, P. Conti, A. Pinto, M. De Amici, D. E. Pellegrini-Giampietro, C. De Micheli, T. Mennini and M. Gobbi (2008). "Neuroprotective effects of the novel glutamate transporter inhibitor (-)-3-hydroxy-4,5,6,6a-tetrahydro-3aH-pyrrolo[3,4-d]-isoxazole-4-carboxylic acid, which preferentially inhibits reverse transport (glutamate release) compared with glutamate reuptake." J Pharmacol Exp Ther **326**(2): 646-656.
Conti, P., C. Dallanoce, M. De Amici, C. De Micheli and R. Fruttero (1999). "Synthesis of new bicyclic analogues of glutamic acid." Tetrahedron **55**(17): 5623-5634.
Cowtan, K. (2010). "Recent developments in classical density modification." Acta Crystallogr D Biol Crystallogr **66**(Pt 4): 470-478.
D'Amico, A., A. Soragna, E. Di Cairano, N. Panzeri, N. Anzai, F. Vellea Sacchi and C. Perego (2010). "The surface density of the glutamate transporter EAAC1 is controlled by interactions with PDZK1 and AP2 adaptor complexes." Traffic **11**(11): 1455-1470.
Dadi, P. K., N. C. Vierra, E. Days, M. T. Dickerson, P. N. Vinson, C. D. Weaver and D. A. Jacobson (2017). "Selective Small Molecule Activators of TREK-2 Channels Stimulate Dorsal Root Ganglion c-Fiber Nociceptor Two-Pore-Domain Potassium Channel Currents and Limit Calcium Influx." ACS Chem Neurosci **8**(3): 558-568.
Dall'Igna, O. P., L. D. Bobermin, D. O. Souza and A. Quincozes-Santos (2013). "Riluzole increases glutamate uptake by cultured C6 astroglial cells." Int J Dev Neurosci **31**(7): 482-486.
Damseh, N., A. Simonin, C. Jalas, J. A. Picoraro, A. Shaag, M. T. Cho, B. Yaacov, J. Neidich, M. Al-Ashhab, J. Juusola, S. Bale, A. Telegrafi, K. Retterer, J. G. Pappas, E. Moran, J. Cappell, K. Anyane Yeboa, B. Abu-Libdeh, M. A. Hediger, W. K. Chung, O. Elpeleg and S. Edvardson (2015). "Mutations in SLC1A4, encoding the brain serine transporter, are associated with developmental delay, microcephaly and hypomyelination." J Med Genet **52**(8): 541-547.
Danbolt, N. C. (2001). "Glutamate uptake." Progress in Neurobiology **65**(1): 1-105.
Davis, K. E., D. J. Straff, E. A. Weinstein, P. G. Bannerman, D. M. Correale, J. D. Rothstein and M. B. Robinson (1998). "Multiple signaling pathways regulate cell surface expression and activity of the excitatory amino acid carrier 1 subtype of Glu transporter in C6 glioma." J Neurosci **18**(7): 2475-2485.
de Vries, B., H. Mamsa, A. H. Stam, J. Wan, S. L. Bakker, K. R. Vanmolkot, J. Haan, G. M. Terwindt, E. M. Boon, B. D. Howard, R. R. Frants, R. W. Baloh, M. D. Ferrari, J. C. Jen and A. M. van den Maagdenberg (2009). "Episodic ataxia associated with EAAT1 mutation C186S affecting glutamate reuptake." Arch Neurol **66**(1): 97-101.
Delgado-Acevedo, C., S. F. Estay, A. K. Radke, A. Sengupta, A. P. Escobar, F. Henriquez-Belmar, C. A. Reyes, V. Haro-Acuna, E. Utreras, R. Sotomayor-Zarate, A. Cho, J. R. Wendland, A. B. Kulkarni, A. Holmes, D. L. Murphy, A. E. Chavez and P. R. Moya (2019).

"Behavioral and synaptic alterations relevant to obsessive-compulsive disorder in mice with increased EAAT3 expression." Neuropsychopharmacology **44**(6): 1163-1173.
Deng, D., P. Sun, C. Yan, M. Ke, X. Jiang, L. Xiong, W. Ren, K. Hirata, M. Yamamoto, S. Fan and N. Yan (2015). "Molecular basis of ligand recognition and transport by glucose transporters." Nature **526**(7573): 391-396.
Deng, D., C. Xu, P. Sun, J. Wu, C. Yan, M. Hu and N. Yan (2014). "Crystal structure of the human glucose transporter GLUT1." Nature **510**(7503): 121-125.
Diallinas, G. (2014). "Understanding transporter specificity and the discrete appearance of channel-like gating domains in transporters." Front Pharmacol **5**: 207.
Dobro, M. J., L. A. Melanson, G. J. Jensen and A. W. McDowall (2010). "Plunge freezing for electron cryomicroscopy." Methods Enzymol **481**: 63-82.
Dong, Y. Y., A. C. Pike, A. Mackenzie, C. McClenaghan, P. Aryal, L. Dong, A. Quigley, M. Grieben, S. Goubin, S. Mukhopadhyay, G. F. Ruda, M. V. Clausen, L. Cao, P. E. Brennan, N. A. Burgess-Brown, M. S. Sansom, S. J. Tucker and E. P. Carpenter (2015). "K2P channel gating mechanisms revealed by structures of TREK-2 and a complex with Prozac." Science **347**(6227): 1256-1259.
Dowd, L. A. and M. B. Robinson (1996). "Rapid stimulation of EAAC1-mediated Na+-dependent L-glutamate transport activity in C6 glioma cells by phorbol ester." J Neurochem **67**(2): 508-516.
Doyle, D. A., J. Morais Cabral, R. A. Pfuetzner, A. Kuo, J. M. Gulbis, S. L. Cohen, B. T. Chait and R. MacKinnon (1998). "The structure of the potassium channel: molecular basis of K+ conduction and selectivity." Science **280**(5360): 69-77.
Dubochet, J. and A. W. Mcdowall (1981). "Vitrification of Pure Water for Electron-Microscopy." Journal of Microscopy-Oxford **124**(Dec): Rp3-Rp4.
Dunlop, J., H. B. McIlvain, T. A. Carrick, B. Jow, Q. Lu, D. Kowal, S. Lin, A. Greenfield, C. Grosanu, K. Fan, R. Petroski, J. Williams, A. Foster and J. Butera (2005). "Characterization of novel aryl-ether, biaryl, and fluorene aspartic acid and diaminopropionic acid analogs as potent inhibitors of the high-affinity glutamate transporter EAAT2." Mol Pharmacol **68**(4): 974-982.
Emsley, P., B. Lohkamp, W. G. Scott and K. Cowtan (2010). "Features and development of Coot." Acta Crystallogr D Biol Crystallogr **66**(Pt 4): 486-501.
Enyedi, P. and G. Czirjak (2010). "Molecular background of leak K+ currents: two-pore domain potassium channels." Physiol Rev **90**(2): 559-605.
Escartin, C., S. J. Won, C. Malgorn, G. Auregan, A. E. Berman, P. C. Chen, N. Deglon, J. A. Johnson, S. W. Suh and R. A. Swanson (2011). "Nuclear factor erythroid 2-related factor 2 facilitates neuronal glutathione synthesis by upregulating neuronal excitatory amino acid transporter 3 expression." J Neurosci **31**(20): 7392-7401.
Feliciangeli, S., F. C. Chatelain, D. Bichet and F. Lesage (2015). "The family of K2P channels: salient structural and functional properties." J Physiol **593**(12): 2587-2603.
Fink, M., F. Duprat, F. Lesage, R. Reyes, G. Romey, C. Heurteaux and M. Lazdunski (1996). "Cloning, functional expression and brain localization of a novel unconventional outward rectifier K+ channel." EMBO J **15**(24): 6854-6862.
Fischer, M. J. E. (2010). "Amine Coupling Through EDC/NHS: A Practical Approach." Surface Plasmon Resonance: Methods and Protocols **627**: 55-73.
Fournier, K. M., M. I. Gonzalez and M. B. Robinson (2004). "Rapid trafficking of the neuronal glutamate transporter, EAAC1: evidence for distinct trafficking pathways differentially regulated by protein kinase C and platelet-derived growth factor." J Biol Chem **279**(33): 34505-34513.

Fournier, K. M. and M. B. Robinson (2006). "A dominant-negative variant of SNAP-23 decreases the cell surface expression of the neuronal glutamate transporter EAAC1 by slowing constitutive delivery." Neurochem Int **48**(6-7): 596-603.
Frauenfeld, J., R. Loving, J. P. Armache, A. F. Sonnen, F. Guettou, P. Moberg, L. Zhu, C. Jegerschold, A. Flayhan, J. A. Briggs, H. Garoff, C. Low, Y. Cheng and P. Nordlund (2016). "A saposin-lipoprotein nanoparticle system for membrane proteins." Nat Methods **13**(4): 345-351.
Fujimoto, S., H. Katsuki, T. Kume, S. Kaneko and A. Akaike (2004). "Mechanisms of oxygen glucose deprivation-induced glutamate release from cerebrocortical slice cultures." Neurosci Res **50**(2): 179-187.
Funicello, M., P. Conti, M. De Amici, C. De Micheli, T. Mennini and M. Gobbi (2004). "Dissociation of [3H]L-glutamate uptake from L-glutamate-induced [3H]D-aspartate release by 3-hydroxy-4,5,6,6a-tetrahydro-3aH-pyrrolo[3,4-d]isoxazole-4-carboxylic acid and 3-hydroxy-4,5,6,6a-tetrahydro-3aH-pyrrolo[3,4-d]isoxazole-6-carboxylic acid, two conformationally constrained aspartate and glutamate analogs." Mol Pharmacol **66**(3): 522-529.
Gadsby, D. C. (2009). "Ion channels versus ion pumps: the principal difference, in principle." Nat Rev Mol Cell Biol **10**(5): 344-352.
Gambin, T., Z. C. Akdemir, B. Yuan, S. Gu, T. Chiang, C. M. B. Carvalho, C. Shaw, S. Jhangiani, P. M. Boone, M. K. Eldomery, E. Karaca, Y. Bayram, A. Stray-Pedersen, D. Muzny, W. L. Charng, V. Bahrambeigi, J. W. Belmont, E. Boerwinkle, A. L. Beaudet, R. A. Gibbs and J. R. Lupski (2017). "Homozygous and hemizygous CNV detection from exome sequencing data in a Mendelian disease cohort." Nucleic Acids Res **45**(4): 1633-1648.
Gameiro, A., S. Braams, T. Rauen and C. Grewer (2011). "The discovery of slowness: low-capacity transport and slow anion channel gating by the glutamate transporter EAAT5." Biophys J **100**(11): 2623-2632.
Garaeva, A. A., A. Guskov, D. J. Slotboom and C. Paulino (2019). "A one-gate elevator mechanism for the human neutral amino acid transporter ASCT2." Nat Commun **10**(1): 3427.
Garaeva, A. A., G. T. Oostergetel, C. Gati, A. Guskov, C. Paulino and D. J. Slotboom (2018). "Cryo-EM structure of the human neutral amino acid transporter ASCT2." Nat Struct Mol Biol **25**(6): 515-521.
Gazzola, G. C., V. Dall'Asta, O. Bussolati, M. Makowske and H. N. Christensen (1981). "A stereoselective anomaly in dicarboxylic amino acid transport." J Biol Chem **256**(12): 6054-6059.
Geertsma, E. R., N. A. Nik Mahmood, G. K. Schuurman-Wolters and B. Poolman (2008). "Membrane reconstitution of ABC transporters and assays of translocator function." Nat Protoc **3**(2): 256-266.
Gimpl, G., U. Klein, H. Reilander and F. Fahrenholz (1995). "Expression of the human oxytocin receptor in baculovirus-infected insect cells: high-affinity binding is induced by a cholesterol-cyclodextrin complex." Biochemistry **34**(42): 13794-13801.
Goldschen-Ohm, M. P. and B. Chanda (2017). "SnapShot: Channel Gating Mechanisms." Cell **170**(3): 594-594 e591.
Goldstein, M., S. Rinne, A. K. Kiper, D. Ramirez, M. F. Netter, D. Bustos, B. Ortiz-Bonnin, W. Gonzalez and N. Decher (2016). "Functional mutagenesis screens reveal the 'cap structure' formation in disulfide-bridge free TASK channels." Scientific Reports **6**.
Gonzalez, M. I., E. Krizman-Genda and M. B. Robinson (2007). "Caveolin-1 regulates the delivery and endocytosis of the glutamate transporter, excitatory amino acid carrier 1." J Biol Chem **282**(41): 29855-29865.

Gonzalez, M. I., B. T. Susarla, K. M. Fournier, A. L. Sheldon and M. B. Robinson (2007). "Constitutive endocytosis and recycling of the neuronal glutamate transporter, excitatory amino acid carrier 1." J Neurochem **103**(5): 1917-1931.
Grewer, C., P. Balani, C. Weidenfeller, T. Bartusel, Z. Tao and T. Rauen (2005). "Individual subunits of the glutamate transporter EAAC1 homotrimer function independently of each other." Biochemistry **44**(35): 11913-11923.
Grewer, C., A. Gameiro and T. Rauen (2014). "SLC1 glutamate transporters." Pflugers Arch **466**(1): 3-24.
Grewer, C., A. Gameiro, Z. Zhang, Z. Tao, S. Braams and T. Rauen (2008). "Glutamate forward and reverse transport: from molecular mechanism to transporter-mediated release after ischemia." IUBMB Life **60**(9): 609-619.
Grewer, C. and T. Rauen (2005). "Electrogenic glutamate transporters in the CNS: molecular mechanism, pre-steady-state kinetics, and their impact on synaptic signaling." J Membr Biol **203**(1): 1-20.
Grewer, C., N. Watzke, T. Rauen and A. Bicho (2003). "Is the glutamate residue Glu-373 the proton acceptor of the excitatory amino acid carrier 1?" J Biol Chem **278**(4): 2585-2592.
Grewer, C., N. Watzke, M. Wiessner and T. Rauen (2000). "Glutamate translocation of the neuronal glutamate transporter EAAC1 occurs within milliseconds." Proc Natl Acad Sci U S A **97**(17): 9706-9711.
Griffith, O. W. (1999). "Biologic and pharmacologic regulation of mammalian glutathione synthesis." Free Radic Biol Med **27**(9-10): 922-935.
Groeneveld, M. and D. J. Slotboom (2007). "Rigidity of the subunit interfaces of the trimeric glutamate transporter GltT during translocation." J Mol Biol **372**(3): 565-570.
Gruswitz, F., S. Chaudhary, J. D. Ho, A. Schlessinger, B. Pezeshki, C. M. Ho, A. Sali, C. M. Westhoff and R. M. Stroud (2010). "Function of human Rh based on structure of RhCG at 2.1 A." Proc Natl Acad Sci U S A **107**(21): 9638-9643.
Gu, W., G. Schlichthorl, J. R. Hirsch, H. Engels, C. Karschin, A. Karschin, C. Derst, O. K. Steinlein and J. Daut (2002). "Expression pattern and functional characteristics of two novel splice variants of the two-pore-domain potassium channel TREK-2." J Physiol **539**(Pt 3): 657-668.
Guskov, A., S. Jensen, I. Faustino, S. J. Marrink and D. J. Slotboom (2016). "Coupled binding mechanism of three sodium ions and aspartate in the glutamate transporter homologue GltTk." Nat Commun **7**: 13420.
Hagemans, D., I. A. van Belzen, T. Moran Luengo and S. G. Rudiger (2015). "A script to highlight hydrophobicity and charge on protein surfaces." Front Mol Biosci **2**: 56.
Hediger, M. A., M. F. Romero, J. B. Peng, A. Rolfs, H. Takanaga and E. A. Bruford (2004). "The ABCs of solute carriers: physiological, pathological and therapeutic implications of human membrane transport proteinsIntroduction." Pflugers Arch **447**(5): 465-468.
Hodgkin, A. L. and A. F. Huxley (1952). "A quantitative description of membrane current and its application to conduction and excitation in nerve." J Physiol **117**(4): 500-544.
Holmseth, S., Y. Dehnes, Y. H. Huang, V. V. Follin-Arbelet, N. J. Grutle, M. N. Mylonakou, C. Plachez, Y. Zhou, D. N. Furness, D. E. Bergles, K. P. Lehre and N. C. Danbolt (2012). "The density of EAAC1 (EAAT3) glutamate transporters expressed by neurons in the mammalian CNS." J Neurosci **32**(17): 6000-6013.
Honore, E. (2007). "The neuronal background K2P channels: focus on TREK1." Nat Rev Neurosci **8**(4): 251-261.
Honore, E., F. Maingret, M. Lazdunski and A. J. Patel (2002). "An intracellular proton sensor commands lipid- and mechano-gating of the K(+) channel TREK-1." EMBO J **21**(12): 2968-2976.

Hotzy, J., N. Schneider, P. Kovermann and C. Fahlke (2013). "Mutating a Conserved Proline Residue within the Trimerization Domain Modifies Na+ Binding to Excitatory Amino Acid Transporters and Associated Conformational Changes." Journal of Biological Chemistry **288**(51): 36492-36501.
Hu, Q. X., S. Ottestad-Hansen, S. Holmseth, B. Hassel, N. C. Danbolt and Y. Zhou (2018). "Expression of Glutamate Transporters in Mouse Liver, Kidney, and Intestine." J Histochem Cytochem **66**(3): 189-202.
Huang, Y., X. Feng, J. J. Sando and Z. Zuo (2006). "Critical role of serine 465 in isoflurane-induced increase of cell-surface redistribution and activity of glutamate transporter type 3." J Biol Chem **281**(50): 38133-38138.
Huynh, T. H., B. Abrahamsen, K. K. Madsen, A. Gonzalez-Franquesa, A. A. Jensen and L. Bunch (2012). "Design, synthesis and pharmacological characterization of coumarin-based fluorescent analogs of excitatory amino acid transporter subtype 1 selective inhibitors, UCPH-101 and UCPH-102." Bioorg Med Chem **20**(23): 6831-6839.
Jen, J. C., J. Wan, T. P. Palos, B. D. Howard and R. W. Baloh (2005). "Mutation in the glutamate transporter EAAT1 causes episodic ataxia, hemiplegia, and seizures." Neurology **65**(4): 529-534.
Jensen, A. A. and H. Brauner-Osborne (2004). "Pharmacological characterization of human excitatory amino acid transporters EAAT1, EAAT2 and EAAT3 in a fluorescence-based membrane potential assay." Biochem Pharmacol **67**(11): 2115-2127.
Jensen, A. A., M. N. Erichsen, C. W. Nielsen, T. B. Stensbol, J. Kehler and L. Bunch (2009). "Discovery of the first selective inhibitor of excitatory amino acid transporter subtype 1." J Med Chem **52**(4): 912-915.
Jensen, S., A. Guskov, S. Rempel, I. Hanelt and D. J. Slotboom (2013). "Crystal structure of a substrate-free aspartate transporter." Nat Struct Mol Biol **20**(10): 1224-1226.
Jovcevska, I. and S. Muyldermans (2020). "The Therapeutic Potential of Nanobodies." BioDrugs **34**(1): 11-26.
Kabsch, W. (2010). "Xds." Acta Crystallogr D Biol Crystallogr **66**(Pt 2): 125-132.
Kanai, Y. and M. A. Hediger (1992). "Primary structure and functional characterization of a high-affinity glutamate transporter." Nature **360**(6403): 467-471.
Kanai, Y. and M. A. Hediger (2003). "The glutamate and neutral amino acid transporter family: physiological and pharmacological implications." Eur J Pharmacol **479**(1-3): 237-247.
Kang, D., C. Choe and D. Kim (2005). "Thermosensitivity of the two-pore domain K+ channels TREK-2 and TRAAK." J Physiol **564**(Pt 1): 103-116.
Karplus, P. A. and K. Diederichs (2012). "Linking crystallographic model and data quality." Science **336**(6084): 1030-1033.
Kavanaugh, M. P., A. Bendahan, N. Zerangue, Y. Zhang and B. I. Kanner (1997). "Mutation of an amino acid residue influencing potassium coupling in the glutamate transporter GLT-1 induces obligate exchange." J Biol Chem **272**(3): 1703-1708.
Kerr, I. D. and M. S. Sansom (1995). "Cation selectivity in ion channels." Nature **373**(6510): 112.
Kimanius, D., B. O. Forsberg, S. H. Scheres and E. Lindahl (2016). "Accelerated cryo-EM structure determination with parallelisation using GPUs in RELION-2." Elife **5**.
Knol, J. (1999). Membrane reconstitution and functional analysis of a sugar transport system. Doctor of Philosophy, University of Groningen.
Knowles, T. J., R. Finka, C. Smith, Y. P. Lin, T. Dafforn and M. Overduin (2009). "Membrane proteins solubilized intact in lipid containing nanoparticles bounded by styrene maleic acid copolymer." J Am Chem Soc **131**(22): 7484-7485.

Koch, H. P., M. P. Kavanaugh, C. S. Esslinger, N. Zerangue, J. M. Humphrey, S. G. Amara, A. R. Chamberlin and R. J. Bridges (1999). "Differentiation of substrate and nonsubstrate inhibitors of the high-affinity, sodium-dependent glutamate transporters." Mol Pharmacol **56**(6): 1095-1104.
Krause, R., N. Watzke, B. Kelety, W. Dorner and K. Fendler (2009). "An automatic electrophysiological assay for the neuronal glutamate transporter mEAAC1." J Neurosci Methods **177**(1): 131-141.
Krissinel, E. and K. Henrick (2007). "Inference of macromolecular assemblies from crystalline state." J Mol Biol **372**(3): 774-797.
Kugler, P. and A. Beyer (2003). "Expression of glutamate transporters in human and rat retina and rat optic nerve." Histochem Cell Biol **120**(3): 199-212.
Larkin, M. A., G. Blackshields, N. P. Brown, R. Chenna, P. A. McGettigan, H. McWilliam, F. Valentin, I. M. Wallace, A. Wilm, R. Lopez, J. D. Thompson, T. J. Gibson and D. G. Higgins (2007). "Clustal W and Clustal X version 2.0." Bioinformatics **23**(21): 2947-2948.
Lee, G., Y. Huang, J. M. Washington, N. W. Briggs and Z. Zuo (2005). "Carbamazepine enhances the activity of glutamate transporter type 3 via phosphatidylinositol 3-kinase." Epilepsy Res **66**(1-3): 145-153.
Lesage, F., E. Guillemare, M. Fink, F. Duprat, M. Lazdunski, G. Romey and J. Barhanin (1996). "TWIK-1, a ubiquitous human weakly inward rectifying K+ channel with a novel structure." EMBO J **15**(5): 1004-1011.
Lesage, F. and M. Lazdunski (2000). "Molecular and functional properties of two-pore-domain potassium channels." Am J Physiol Renal Physiol **279**(5): F793-801.
Lesage, F., C. Terrenoire, G. Romey and M. Lazdunski (2000). "Human TREK2, a 2P domain mechano-sensitive K+ channel with multiple regulations by polyunsaturated fatty acids, lysophospholipids, and Gs, Gi, and Gq protein-coupled receptors." J Biol Chem **275**(37): 28398-28405.
Levenson, J., E. Weeber, J. C. Selcher, L. S. Kategaya, J. D. Sweatt and A. Eskin (2002). "Long-term potentiation and contextual fear conditioning increase neuronal glutamate uptake." Nat Neurosci **5**(2): 155-161.
Li, B., R. A. Rietmeijer and S. G. Brohawn (2020). "Structural basis for pH gating of the two-pore domain K(+) channel TASK2." Nature **586**(7829): 457-462.
Li, D., J. Lee and M. Caffrey (2011). "Crystallizing Membrane Proteins in Lipidic Mesophases. A Host Lipid Screen." Cryst Growth Des **11**(2): 530-537.
Liebschner, D., P. V. Afonine, M. L. Baker, G. Bunkoczi, V. B. Chen, T. I. Croll, B. Hintze, L. W. Hung, S. Jain, A. J. McCoy, N. W. Moriarty, R. D. Oeffner, B. K. Poon, M. G. Prisant, R. J. Read, J. S. Richardson, D. C. Richardson, M. D. Sammito, O. V. Sobolev, D. H. Stockwell, T. C. Terwilliger, A. G. Urzhumtsev, L. L. Videau, C. J. Williams and P. D. Adams (2019). "Macromolecular structure determination using X-rays, neutrons and electrons: recent developments in Phenix." Acta Crystallographica Section D-Structural Biology **75**: 861-877.
Lin, C. I., I. Orlov, A. M. Ruggiero, M. Dykes-Hoberg, A. Lee, M. Jackson and J. D. Rothstein (2001). "Modulation of the neuronal glutamate transporter EAAC1 by the interacting protein GTRAP3-18." Nature **410**(6824): 84-88.
Liu, W. and M. Caffrey (2005). "Gramicidin structure and disposition in highly curved membranes." J Struct Biol **150**(1): 23-40.
Liu, Y., S. Vidensky, A. M. Ruggiero, S. Maier, H. H. Sitte and J. D. Rothstein (2008). "Reticulon RTN2B regulates trafficking and function of neuronal glutamate transporter EAAC1." J Biol Chem **283**(10): 6561-6571.

Liu, Z., T. Zhou, A. C. Ziegler, P. Dimitrion and L. Zuo (2017). "Oxidative Stress in Neurodegenerative Diseases: From Molecular Mechanisms to Clinical Applications." Oxid Med Cell Longev **2017**: 2525967.
Locatelli-Hoops, S., A. A. Yeliseev, K. Gawrisch and I. Gorshkova (2013). "Surface plasmon resonance applied to G protein-coupled receptors." Biomed Spectrosc Imaging **2**(3): 155-181.
Lolicato, M., C. Arrigoni, T. Mori, Y. Sekioka, C. Bryant, K. A. Clark and D. L. Minor, Jr. (2017). "K2P2.1 (TREK-1)-activator complexes reveal a cryptic selectivity filter binding site." Nature **547**(7663): 364-368.
Lolicato, M., A. M. Natale, F. Abderemane-Ali, D. Crottes, S. Capponi, R. Duman, A. Wagner, J. M. Rosenberg, M. Grabe and D. L. Minor, Jr. (2020). "K2P channel C-type gating involves asymmetric selectivity filter order-disorder transitions." Sci Adv **6**(44).
Lolicato, M., P. M. Riegelhaupt, C. Arrigoni, K. A. Clark and D. L. Minor, Jr. (2014). "Transmembrane helix straightening and buckling underlies activation of mechanosensitive and thermosensitive K(2P) channels." Neuron **84**(6): 1198-1212.
Lopez-Barneo, J., T. Hoshi, S. H. Heinemann and R. W. Aldrich (1993). "Effects of external cations and mutations in the pore region on C-type inactivation of Shaker potassium channels." Receptors Channels **1**(1): 61-71.
Lortet, S., B. Canolle, F. Masmejean and A. Nieoullon (2008). "Plasma membrane expression of the neuronal glutamate transporter EAAC1 is regulated by glial factors: evidence for different regulatory pathways associated with neuronal maturation." Neurochem Int **52**(7): 1373-1382.
Lotshaw, D. P. (2007). "Biophysical, pharmacological, and functional characteristics of cloned and native mammalian two-pore domain K+ channels." Cell Biochem Biophys **47**(2): 209-256.
Luo, Q., L. Chen, X. Cheng, Y. Ma, X. Li, B. Zhang, L. Li, S. Zhang, F. Guo, Y. Li and H. Yang (2017). "An allosteric ligand-binding site in the extracellular cap of K2P channels." Nat Commun **8**(1): 378.
Makrides, V., S. M. Camargo and F. Verrey (2014). "Transport of amino acids in the kidney." Compr Physiol **4**(1): 367-403.
Malik, A. R., K. Szydlowska, K. Nizinska, A. Asaro, E. A. van Vliet, O. Popp, G. Dittmar, R. Fritsche-Guenther, J. A. Kirwan, A. Nykjaer, K. Lukasiuk, E. Aronica and T. E. Willnow (2019). "SorCS2 Controls Functional Expression of Amino Acid Transporter EAAT3 and Protects Neurons from Oxidative Stress and Epilepsy-Induced Pathology." Cell Rep **26**(10): 2792-2804 e2796.
Malik, A. R. and T. E. Willnow (2019). "Excitatory Amino Acid Transporters in Physiology and Disorders of the Central Nervous System." Int J Mol Sci **20**(22).
Manglik, A., B. K. Kobilka and J. Steyaert (2017). "Nanobodies to Study G Protein-Coupled Receptor Structure and Function." Annu Rev Pharmacol Toxicol **57**: 19-37.
Marheineke, K., S. Grunewald, W. Christie and H. Reilander (1998). "Lipid composition of Spodoptera frugiperda (Sf9) and Trichoplusia ni (Tn) insect cells used for baculovirus infection." FEBS Lett **441**(1): 49-52.
Mastronarde, D. N. (2005). "Automated electron microscope tomography using robust prediction of specimen movements." Journal of Structural Biology **152**(1): 36-51.
Mathews, G. C. and J. S. Diamond (2003). "Neuronal glutamate uptake Contributes to GABA synthesis and inhibitory synaptic strength." J Neurosci **23**(6): 2040-2048.
Matthews, B. W. (1968). "Solvent content of protein crystals." J Mol Biol **33**(2): 491-497.

McClenaghan, C., M. Schewe, P. Aryal, E. P. Carpenter, T. Baukrowitz and S. J. Tucker (2016). "Polymodal activation of the TREK-2 K2P channel produces structurally distinct open states." J Gen Physiol **147**(6): 497-505.
McCoy, A. J., R. W. Grosse-Kunstleve, P. D. Adams, M. D. Winn, L. C. Storoni and R. J. Read (2007). "Phaser crystallographic software." J Appl Crystallogr **40**(Pt 4): 658-674.
McCullumsmith, R. E. and J. H. Meador-Woodruff (2002). "Striatal excitatory amino acid transporter transcript expression in schizophrenia, bipolar disorder, and major depressive disorder." Neuropsychopharmacology **26**(3): 368-375.
Michel, H. (1983). "Crystallization of Membrane-Proteins." Trends in Biochemical Sciences **8**(2): 56-59.
Miller, A. N. and S. B. Long (2012). "Crystal structure of the human two-pore domain potassium channel K2P1." Science **335**(6067): 432-436.
Mitani, A. and K. Tanaka (2003). "Functional changes of glial glutamate transporter GLT-1 during ischemia: an in vivo study in the hippocampal CA1 of normal mice and mutant mice lacking GLT-1." J Neurosci **23**(18): 7176-7182.
Muyldermans, S. (2013). "Nanobodies: natural single-domain antibodies." Annu Rev Biochem **82**: 775-797.
Myles-Worsley, M., J. Tiobech, S. R. Browning, J. Korn, S. Goodman, K. Gentile, N. Melhem, W. Byerley, S. V. Faraone and F. A. Middleton (2013). "Deletion at the SLC1A1 glutamate transporter gene co-segregates with schizophrenia and bipolar schizoaffective disorder in a 5-generation family." Am J Med Genet B Neuropsychiatr Genet **162B**(2): 87-95.
Nicholls, D. and D. Attwell (1990). "The release and uptake of excitatory amino acids." Trends Pharmacol Sci **11**(11): 462-468.
Noble, A. J., V. P. Dandey, H. Wei, J. Brasch, J. Chase, P. Acharya, Y. Z. Tan, Z. Zhang, L. Y. Kim, G. Scapin, M. Rapp, E. T. Eng, W. J. Rice, A. Cheng, C. J. Negro, L. Shapiro, P. D. Kwong, D. Jeruzalmi, A. des Georges, C. S. Potter and B. Carragher (2018). "Routine single particle CryoEM sample and grid characterization by tomography." Elife **7**.
O. S. Smart, T. O. W., A. Sharff, C. Flensburg, P. Keller, W. Paciorek, C. Vonrhein, and G. Bricogne. (2011). "grade, v1.104."
Ogielska, E. M. and R. W. Aldrich (1999). "Functional consequences of a decreased potassium affinity in a potassium channel pore. Ion interactions and C-type inactivation." J Gen Physiol **113**(2): 347-358.
Ohi, M., Y. Li, Y. Cheng and T. Walz (2004). "Negative Staining and Image Classification - Powerful Tools in Modern Electron Microscopy." Biol Proced Online **6**: 23-34.
Orlova, E. V. and H. R. Saibil (2011). "Structural analysis of macromolecular assemblies by electron microscopy." Chem Rev **111**(12): 7710-7748.
Palos, T. P., B. Ramachandran, R. Boado and B. D. Howard (1996). "Rat C6 and human astrocytic tumor cells express a neuronal type of glutamate transporter." Brain Res Mol Brain Res **37**(1-2): 297-303.
Papadopoulos, J. S. and R. Agarwala (2007). "COBALT: constraint-based alignment tool for multiple protein sequences." Bioinformatics **23**(9): 1073-1079.
Patel, A. J., E. Honore, F. Lesage, M. Fink, G. Romey and M. Lazdunski (1999). "Inhalational anesthetics activate two-pore-domain background K+ channels." Nat Neurosci **2**(5): 422-426.
Pau, V., Y. F. Zhou, Y. Ramu, Y. P. Xu and Z. Lu (2017). "Crystal structure of an inactivated mutant mammalian voltage-gated K+ channel." Nature Structural & Molecular Biology **24**(10): 857-+.
Pearson-Smith, J. N. and M. Patel (2017). "Metabolic Dysfunction and Oxidative Stress in Epilepsy." Int J Mol Sci **18**(11).

Peghini, P., J. Janzen and W. Stoffel (1997). "Glutamate transporter EAAC-1-deficient mice develop dicarboxylic aminoaciduria and behavioral abnormalities but no neurodegeneration." EMBO J **16**(13): 3822-3832.
Penczek, P. A. (2010). Image Restoration in Cryo-Electron Microscopy. Cryo-EM, Part B: 3-D Reconstruction**:** 35-72.
Penczek, P. A. (2010). "Resolution measures in molecular electron microscopy." Methods Enzymol **482**: 73-100.
Perego, C., E. S. Di Cairano, M. Ballabio and V. Magnaghi (2012). "Neurosteroid allopregnanolone regulates EAAC1-mediated glutamate uptake and triggers actin changes in Schwann cells." J Cell Physiol **227**(4): 1740-1751.
Pereira, V., J. Busserolles, M. Christin, M. Devilliers, L. Poupon, W. Legha, A. Alloui, Y. Aissouni, E. Bourinet, F. Lesage, A. Eschalier, M. Lazdunski and J. Noel (2014). "Role of the TREK2 potassium channel in cold and warm thermosensation and in pain perception." Pain **155**(12): 2534-2544.
Pettersen, E. F., T. D. Goddard, C. C. Huang, G. S. Couch, D. M. Greenblatt, E. C. Meng and T. E. Ferrin (2004). "UCSF Chimera--a visualization system for exploratory research and analysis." J Comput Chem **25**(13): 1605-1612.
Pettersen, E. F., T. D. Goddard, C. C. Huang, E. C. Meng, G. S. Couch, T. I. Croll, J. H. Morris and T. E. Ferrin (2020). "UCSF ChimeraX: Structure visualization for researchers, educators, and developers." Protein Sci.
Piechotta, P. L., M. Rapedius, P. J. Stansfeld, M. K. Bollepalli, G. Ehrlich, I. Andres-Enguix, H. Fritzenschaft, N. Decher, M. S. Sansom, S. J. Tucker and T. Baukrowitz (2011). "The pore structure and gating mechanism of K2P channels." EMBO J **30**(17): 3607-3619.
Pingitore, P., L. Pochini, M. Scalise, M. Galluccio, K. Hedfalk and C. Indiveri (2013). "Large scale production of the active human ASCT2 (SLC1A5) transporter in Pichia pastoris--functional and kinetic asymmetry revealed in proteoliposomes." Biochim Biophys Acta **1828**(9): 2238-2246.
Pinto, A., P. Conti, M. De Amici, L. Tamborini, G. Grazioso, S. Colleoni, T. Mennini, M. Gobbi and C. De Micheli (2008). "Synthesis of enantiomerically pure HIP-A and HIP-B and investigation of their activity as inhibitors of excitatory amino acid transporters." Tetrahedron-Asymmetry **19**(7): 867-875.
Pita-Almenar, J. D., M. S. Collado, C. M. Colbert and A. Eskin (2006). "Different mechanisms exist for the plasticity of glutamate reuptake during early long-term potentiation (LTP) and late LTP." J Neurosci **26**(41): 10461-10471.
Pope, L., M. Lolicato and D. L. Minor, Jr. (2020). "Polynuclear Ruthenium Amines Inhibit K2P Channels via a "Finger in the Dam" Mechanism." Cell Chem Biol **27**(5): 511-524 e514.
Popot, J. L., E. A. Berry, D. Charvolin, C. Creuzenet, C. Ebel, D. M. Engelman, M. Flotenmeyer, F. Giusti, Y. Gohon, Q. Hong, J. H. Lakey, K. Leonard, H. A. Shuman, P. Timmins, D. E. Warschawski, F. Zito, M. Zoonens, B. Pucci and C. Tribet (2003). "Amphipols: polymeric surfactants for membrane biology research." Cell Mol Life Sci **60**(8): 1559-1574.
Povey, S., R. Lovering, E. Bruford, M. Wright, M. Lush and H. Wain (2001). "The HUGO Gene Nomenclature Committee (HGNC)." Hum Genet **109**(6): 678-680.
Powell, H. R., T. G. G. Battye, L. Kontogiannis, O. Johnson and A. G. W. Leslie (2017). "Integrating macromolecular X-ray diffraction data with the graphical user interface iMosflm." Nat Protoc **12**(7): 1310-1325.
Punjani, A., J. L. Rubinstein, D. J. Fleet and M. A. Brubaker (2017). "cryoSPARC: algorithms for rapid unsupervised cryo-EM structure determination." Nat Methods **14**(3): 290-296.
Qiu, B., Matthies, D., Fortea, E., Yu, Z., Boudker, O. (2020). "Transport mechanism of the neuronal excitatory amino acid transporter." bioRxiv.

Read, R. J. and A. J. Schierbeek (1988). "A Phased Translation Function." Journal of Applied Crystallography **21**: 490-495.
Renigunta, V., G. Schlichthorl and J. Daut (2015). "Much more than a leak: structure and function of K(2)p-channels." Pflugers Arch **467**(5): 867-894.
Reyes, N., C. Ginter and O. Boudker (2009). "Transport mechanism of a bacterial homologue of glutamate transporters." Nature **462**(7275): 880-885.
Rodstrom, K. E. J., A. K. Kiper, W. Zhang, S. Rinne, A. C. W. Pike, M. Goldstein, L. J. Conrad, M. Delbeck, M. G. Hahn, H. Meier, M. Platzk, A. Quigley, D. Speedman, L. Shrestha, S. M. M. Mukhopadhyay, N. A. Burgess-Brown, S. J. Tucker, T. Muller, N. Decher and E. P. Carpenter (2020). "A lower X-gate in TASK channels traps inhibitors within the vestibule." Nature.
Rodstrom, K. E. J., A. K. Kiper, W. Zhang, S. Rinne, A. C. W. Pike, M. Goldstein, L. J. Conrad, M. Delbeck, M. G. Hahn, H. Meier, M. Platzk, A. Quigley, D. Speedman, L. Shrestha, S. M. M. Mukhopadhyay, N. A. Burgess-Brown, S. J. Tucker, T. Muller, N. Decher and E. P. Carpenter (2020). "A lower X-gate in TASK channels traps inhibitors within the vestibule." Nature **582**(7812): 443-447.
Rohou, A. and N. Grigorieff (2015). "CTFFIND4: Fast and accurate defocus estimation from electron micrographs." J Struct Biol **192**(2): 216-221.
Rose, C. R., D. Ziemens, V. Untiet and C. Fahlke (2018). "Molecular and cellular physiology of sodium-dependent glutamate transporters." Brain Res Bull **136**: 3-16.
Rosenthal, P. B. and R. Henderson (2003). "Optimal determination of particle orientation, absolute hand, and contrast loss in single-particle electron cryomicroscopy." J Mol Biol **333**(4): 721-745.
Rossi, D. J., T. Oshima and D. Attwell (2000). "Glutamate release in severe brain ischaemia is mainly by reversed uptake." Nature **403**(6767): 316-321.
Rothstein, J. D., M. Dykes-Hoberg, C. A. Pardo, L. A. Bristol, L. Jin, R. W. Kuncl, Y. Kanai, M. A. Hediger, Y. Wang, J. P. Schielke and D. F. Welty (1996). "Knockout of glutamate transporters reveals a major role for astroglial transport in excitotoxicity and clearance of glutamate." Neuron **16**(3): 675-686.
Rothstein, J. D., L. Martin, A. I. Levey, M. Dykes-Hoberg, L. Jin, D. Wu, N. Nash and R. W. Kuncl (1994). "Localization of neuronal and glial glutamate transporters." Neuron **13**(3): 713-725.
Rubaiy, H. N. (2017). "A Short Guide to Electrophysiology and Ion Channels." J Pharm Pharm Sci **20**: 48-67.
Rupp, B. (2010). "Biomolecular Crystallography: Principles, Practice, and Application to Structural Biology." Biomolecular Crystallography: Principles, Practice, and Application to Structural Biology: 1-809.
Saier, M. H., Jr. (2000). "A functional-phylogenetic classification system for transmembrane solute transporters." Microbiol Mol Biol Rev **64**(2): 354-411.
Sandoz, G., D. Douguet, F. Chatelain, M. Lazdunski and F. Lesage (2009). "Extracellular acidification exerts opposite actions on TREK1 and TREK2 potassium channels via a single conserved histidine residue." Proc Natl Acad Sci U S A **106**(34): 14628-14633.
Scheres, S. H. (2010). "Classification of structural heterogeneity by maximum-likelihood methods." Methods Enzymol **482**: 295-320.
Scheres, S. H. (2012). "A Bayesian view on cryo-EM structure determination." J Mol Biol **415**(2): 406-418.
Scheres, S. H. (2012). "RELION: implementation of a Bayesian approach to cryo-EM structure determination." J Struct Biol **180**(3): 519-530.
Scheres, S. H. (2016). "Processing of Structurally Heterogeneous Cryo-EM Data in RELION." Methods Enzymol **579**: 125-157.

Scheres, S. H., M. Valle, R. Nunez, C. O. Sorzano, R. Marabini, G. T. Herman and J. M. Carazo (2005). "Maximum-likelihood multi-reference refinement for electron microscopy images." J Mol Biol **348**(1): 139-149.
Schewe, M., E. Nematian-Ardestani, H. Sun, M. Musinszki, S. Cordeiro, G. Bucci, B. L. de Groot, S. J. Tucker, M. Rapedius and T. Baukrowitz (2016). "A Non-canonical Voltage-Sensing Mechanism Controls Gating in K2P K(+) Channels." Cell **164**(5): 937-949.
Schulz, J. B., J. Lindenau, J. Seyfried and J. Dichgans (2000). "Glutathione, oxidative stress and neurodegeneration." Eur J Biochem **267**(16): 4904-4911.
Scimemi, A., H. Tian and J. S. Diamond (2009). "Neuronal transporters regulate glutamate clearance, NMDA receptor activation, and synaptic plasticity in the hippocampus." J Neurosci **29**(46): 14581-14595.
Scopelliti, A. J., J. Font, R. J. Vandenberg, O. Boudker and R. M. Ryan (2018). "Structural characterisation reveals insights into substrate recognition by the glutamine transporter ASCT2/SLC1A5." Nature Communications **9**.
Sepkuty, J. P., A. S. Cohen, C. Eccles, A. Rafiq, K. Behar, R. Ganel, D. A. Coulter and J. D. Rothstein (2002). "A neuronal glutamate transporter contributes to neurotransmitter GABA synthesis and epilepsy." J Neurosci **22**(15): 6372-6379.
Shanker, G., J. W. Allen, L. A. Mutkus and M. Aschner (2001). "The uptake of cysteine in cultured primary astrocytes and neurons." Brain Res **902**(2): 156-163.
Sharom, F. J. and P. D. Eckford (2003). "Reconstitution of membrane transporters." Methods Mol Biol **227**: 129-154.
Shayakul, C., Y. Kanai, W. S. Lee, D. Brown, J. D. Rothstein and M. A. Hediger (1997). "Localization of the high-affinity glutamate transporter EAAC1 in rat kidney." Am J Physiol **273**(6): F1023-1029.
Sheldon, A. L. and M. B. Robinson (2007). "The role of glutamate transporters in neurodegenerative diseases and potential opportunities for intervention." Neurochem Int **51**(6-7): 333-355.
Shimamoto, K. (2008). "Glutamate transporter blockers for elucidation of the function of excitatory neurotransmission systems." Chem Rec **8**(3): 182-199.
Shimamoto, K., B. Lebrun, Y. Yasuda-Kamatani, M. Sakaitani, Y. Shigeri, N. Yumoto and T. Nakajima (1998). "DL-threo-beta-benzyloxyaspartate, a potent blocker of excitatory amino acid transporters." Mol Pharmacol **53**(2): 195-201.
Shimamoto, K., R. Sakai, K. Takaoka, N. Yumoto, T. Nakajima, S. G. Amara and Y. Shigeri (2004). "Characterization of novel L-threo-beta-benzyloxyaspartate derivatives, potent blockers of the glutamate transporters." Mol Pharmacol **65**(4): 1008-1015.
Shimamoto, K., Y. Shigeri, Y. Yasuda-Kamatani, B. Lebrun, N. Yumoto and T. Nakajima (2000). "Syntheses of optically pure β-hydroxyaspartate derivatives as glutamate transporter blockers." Bioorganic & Medicinal Chemistry Letters **10**(21): 2407-2410.
Shouffani, A. and B. I. Kanner (1990). "Cholesterol Is Required for the Reconstitution of the Sodium-Coupled and Chloride-Coupled, Gamma-Aminobutyric-Acid Transporter from Rat-Brain." Journal of Biological Chemistry **265**(11): 6002-6008.
Shrivastava, I. H., J. Jiang, S. G. Amara and I. Bahar (2008). "Time-resolved mechanism of extracellular gate opening and substrate binding in a glutamate transporter." J Biol Chem **283**(42): 28680-28690.
Sigworth, F. J., P. C. Doerschuk, J. M. Carazo and S. H. Scheres (2010). "An introduction to maximum-likelihood methods in cryo-EM." Methods Enzymol **482**: 263-294.
Sims, K. D., D. J. Straff and M. B. Robinson (2000). "Platelet-derived growth factor rapidly increases activity and cell surface expression of the EAAC1 subtype of glutamate

transporter through activation of phosphatidylinositol 3-kinase." J Biol Chem **275**(7): 5228-5237.
Smart, O. S., T. O. Womack, C. Flensburg, P. Keller, W. Paciorek, A. Sharff, C. Vonrhein and G. Bricogne (2012). "Exploiting structure similarity in refinement: automated NCS and target-structure restraints in BUSTER." Acta Crystallogr D Biol Crystallogr **68**(Pt 4): 368-380.
Stafstrom, C. E. (2006). "Epilepsy: a review of selected clinical syndromes and advances in basic science." J Cereb Blood Flow Metab **26**(8): 983-1004.
Stein, N. (2008). "CHAINSAW: a program for mutating pdb files used as templates in molecular replacement." Journal of Applied Crystallography **41**: 641-643.
Strelow, J., W. Dewe, P. W. Iversen, H. B. Brooks, J. A. Radding, J. McGee and J. Weidner (2004). Mechanism of Action Assays for Enzymes. Assay Guidance Manual. S. Markossian, G. S. Sittampalam, A. Grossman et al. Bethesda (MD).
Su, J. F., J. Wei, P. S. Li, H. H. Miao, Y. C. Ma, Y. X. Qu, J. Xu, J. Qin, B. L. Li, B. L. Song, Z. P. Xu and J. Luo (2016). "Numb directs the subcellular localization of EAAT3 through binding the YxNxxF motif." J Cell Sci **129**(16): 3104-3114.
Tailor, C. S., A. Nouri, Y. Zhao, Y. Takeuchi and D. Kabat (1999). "A sodium-dependent neutral-amino-acid transporter mediates infections of feline and baboon endogenous retroviruses and simian type D retroviruses." J Virol **73**(5): 4470-4474.
Tao, Z. and C. Grewer (2007). "Cooperation of the conserved aspartate 439 and bound amino acid substrate is important for high-affinity Na+ binding to the glutamate transporter EAAC1." J Gen Physiol **129**(4): 331-344.
Tao, Z., Z. Zhang and C. Grewer (2006). "Neutralization of the aspartic acid residue Asp-367, but not Asp-454, inhibits binding of Na+ to the glutamate-free form and cycling of the glutamate transporter EAAC1." Journal of Biological Chemistry **281**(15): 10263-10272.
Tegunov, D. and P. Cramer (2019). "Real-time cryo-electron microscopy data preprocessing with Warp." Nat Methods **16**(11): 1146-1152.
Teichman, S. and B. I. Kanner (2007). "Aspartate-444 is essential for productive substrate interactions in a neuronal glutamate transporter." Journal of General Physiology **129**(6): 527-539.
Terwilliger, T. C. (2002). "Statistical density modification with non-crystallographic symmetry." Acta Crystallogr D Biol Crystallogr **58**(Pt 12): 2082-2086.
Tickle, I. J., Flensburg, C., Keller, P., Paciorek, W., Sharff, A., Vonrhein, C., Bricogne, G. (2018). "STARANISO."
Trotti, D., M. Aoki, P. Pasinelli, U. V. Berger, N. C. Danbolt, R. H. Brown, Jr. and M. A. Hediger (2001). "Amyotrophic lateral sclerosis-linked glutamate transporter mutant has impaired glutamate clearance capacity." J Biol Chem **276**(1): 576-582.
Trotti, D., J. B. Peng, J. Dunlop and M. A. Hediger (2001). "Inhibition of the glutamate transporter EAAC1 expressed in Xenopus oocytes by phorbol esters." Brain Res **914**(1-2): 196-203.
Tsantoulas, C. and S. B. McMahon (2014). "Opening paths to novel analgesics: the role of potassium channels in chronic pain." Trends Neurosci **37**(3): 146-158.
Tsukada, S., M. Iino, Y. Takayasu, K. Shimamoto and S. Ozawa (2005). "Effects of a novel glutamate transporter blocker, (2S, 3S)-3-[3-[4-(trifluoromethyl)benzoylamino]benzyloxy]aspartate (TFB-TBOA), on activities of hippocampal neurons." Neuropharmacology **48**(4): 479-491.
Turko, P., K. Groberman, F. Browa, S. Cobb and I. Vida (2019). "Differential Dependence of GABAergic and Glutamatergic Neurons on Glia for the Establishment of Synaptic Transmission." Cereb Cortex **29**(3): 1230-1243.

van Meer, G. and A. I. de Kroon (2011). "Lipid map of the mammalian cell." J Cell Sci **124**(Pt 1): 5-8.
Vandenberg, R. J. and R. M. Ryan (2013). "Mechanisms of glutamate transport." Physiol Rev **93**(4): 1621-1657.
Verdon, G. and O. Boudker (2012). "Crystal structure of an asymmetric trimer of a bacterial glutamate transporter homolog." Nat Struct Mol Biol **19**(3): 355-357.
Wade, R. H. (1992). "A Brief Look at Imaging and Contrast Transfer." Ultramicroscopy **46**(1-4): 145-156.
Wadiche, J. I., S. G. Amara and M. P. Kavanaugh (1995). "Ion fluxes associated with excitatory amino acid transport." Neuron **15**(3): 721-728.
Wagner, T., F. Merino, M. Stabrin, T. Moriya, C. Antoni, A. Apelbaum, P. Hagel, O. Sitsel, T. Raisch, D. Prumbaum, D. Quentin, D. Roderer, S. Tacke, B. Siebolds, E. Schubert, T. R. Shaikh, P. Lill, C. Gatsogiannis and S. Raunser (2019). "SPHIRE-crYOLO is a fast and accurate fully automated particle picker for cryo-EM." Communications Biology **2**.
Wang, X. Y. and O. Boudker (2020). "Large domain movements through the lipid bilayer mediate substrate release and inhibition of glutamate transporters." Elife **9**.
Watabe, M., K. Aoyama and T. Nakaki (2008). "A dominant role of GTRAP3-18 in neuronal glutathione synthesis." J Neurosci **28**(38): 9404-9413.
Waterhouse, A., M. Bertoni, S. Bienert, G. Studer, G. Tauriello, R. Gumienny, F. T. Heer, T. A. P. de Beer, C. Rempfer, L. Bordoli, R. Lepore and T. Schwede (2018). "SWISS-MODEL: homology modelling of protein structures and complexes." Nucleic Acids Res **46**(W1): W296-W303.
Waterhouse, A. M., J. B. Procter, D. M. Martin, M. Clamp and G. J. Barton (2009). "Jalview Version 2--a multiple sequence alignment editor and analysis workbench." Bioinformatics **25**(9): 1189-1191.
Watzke, N. and C. Grewer (2001). "The anion conductance of the glutamate transporter EAAC1 depends on the direction of glutamate transport." FEBS Lett **503**(2-3): 121-125.
Watzke, N., T. Rauen, E. Bamberg and C. Grewer (2000). "On the mechanism of proton transport by the neuronal excitatory amino acid carrier 1." J Gen Physiol **116**(5): 609-622.
Williams, C. J., J. J. Headd, N. W. Moriarty, M. G. Prisant, L. L. Videau, L. N. Deis, V. Verma, D. A. Keedy, B. J. Hintze, V. B. Chen, S. Jain, S. M. Lewis, W. B. Arendall, J. Snoeyink, P. D. Adams, S. C. Lovell, J. S. Richardson and D. C. Richardson (2018). "MolProbity: More and better reference data for improved all-atom structure validation." Protein Science **27**(1): 293-315.
Wolfersberger, M. G. (1994). "Uniporters, symporters and antiporters." J Exp Biol **196**: 5-6.
Woo, J., Y. K. Jeon, Y. H. Zhang, J. H. Nam, D. H. Shin and S. J. Kim (2019). "Triple arginine residues in the proximal C-terminus of TREK K(+) channels are critical for biphasic regulation by phosphatidylinositol 4,5-bisphosphate." Am J Physiol Cell Physiol **316**(3): C312-C324.
Woo, J., Y. K. Jun, Y. H. Zhang, J. H. Nam, D. H. Shin and S. J. Kim (2018). "Identification of critical amino acids in the proximal C-terminal of TREK-2 K(+) channel for activation by acidic pHi and ATP-dependent inhibition." Pflugers Arch **470**(2): 327-337.
Wu, P., W. E. Bjorn-Yoshimoto, M. Staudt, A. A. Jensen and L. Bunch (2019). "Identification and Structure-Activity Relationship Study of Imidazo[1,2-a]pyridine-3-amines as First Selective Inhibitors of Excitatory Amino Acid Transporter Subtype 3 (EAAT3)." ACS Chem Neurosci **10**(10): 4414-4429.
Yan, R., X. Zhao, J. Lei and Q. Zhou (2019). "Structure of the human LAT1-4F2hc heteromeric amino acid transporter complex." Nature **568**(7750): 127-130.

Yang, X., Q. Wang and E. Cao (2020). "Structure of the human cation-chloride cotransporter NKCC1 determined by single-particle electron cryo-microscopy." Nat Commun **11**(1): 1016.
Yellen, G. (2002). "The voltage-gated potassium channels and their relatives." Nature **419**(6902): 35-42.
Yernool, D., O. Boudker, Y. Jin and E. Gouaux (2004). "Structure of a glutamate transporter homologue from Pyrococcus horikoshii." Nature **431**(7010): 811-818.
Yoon, H. J., Y. J. Lim, Z. Zuo, W. Hur and S. H. Do (2014). "Nicotine decreases the activity of glutamate transporter type 3." Toxicol Lett **225**(1): 147-152.
Yu, H., H. Yan, L. Wang, J. Li, L. Tan, W. Deng, Q. Chen, G. Yang, F. Zhang, T. Lu, J. Yang, K. Li, L. Lv, Q. Tan, H. Zhang, X. Xiao, M. Li, X. Ma, F. Yang, L. Li, C. Wang, T. Li, D. Zhang, W. Yue and C. Chinese Antipsychotics Pharmacogenomics (2018). "Five novel loci associated with antipsychotic treatment response in patients with schizophrenia: a genome-wide association study." Lancet Psychiatry **5**(4): 327-338.
Yu, X., O. Plotnikova, P. D. Bonin, T. A. Subashi, T. J. McLellan, D. Dumlao, Y. Che, Y. Y. Dong, E. P. Carpenter, G. M. West, X. Qiu, J. S. Culp and S. Han (2019). "Cryo-EM structures of the human glutamine transporter SLC1A5 (ASCT2) in the outward-facing conformation." Elife **8**.
Yu, Y. X., L. Shen, P. Xia, Y. W. Tang, L. Bao and G. Pei (2006). "Syntaxin 1A promotes the endocytic sorting of EAAC1 leading to inhibition of glutamate transport." J Cell Sci **119**(Pt 18): 3776-3787.
Zerangue, N. and M. P. Kavanaugh (1996). "Flux coupling in a neuronal glutamate transporter." Nature **383**(6601): 634-637.
Zerangue, N. and M. P. Kavanaugh (1996). "Interaction of L-cysteine with a human excitatory amino acid transporter." J Physiol **493 (Pt 2)**: 419-423.
Zhang, B., Q. H. Jin, L. Z. Xu, N. N. Li, Y. Meng, S. H. Chang, X. Zheng, J. Q. Wang, Y. Chen, D. Neculai, N. Gao, X. K. Zhang, F. Yang, J. T. Guo and S. Ye (2020). "Cooperative transport mechanism of human monocarboxylate transporter 2." Nature Communications **11**(1).
Zhang, Z., Z. Tao, A. Gameiro, S. Barcelona, S. Braams, T. Rauen and C. Grewer (2007). "Transport direction determines the kinetics of substrate transport by the glutamate transporter EAAC1." Proc Natl Acad Sci U S A **104**(46): 18025-18030.
Zheng, S. Q., E. Palovcak, J. P. Armache, K. A. Verba, Y. Cheng and D. A. Agard (2017). "MotionCor2: anisotropic correction of beam-induced motion for improved cryo-electron microscopy." Nat Methods **14**(4): 331-332.
Zhou, Y., J. H. Morais-Cabral, A. Kaufman and R. MacKinnon (2001). "Chemistry of ion coordination and hydration revealed by a K+ channel-Fab complex at 2.0 A resolution." Nature **414**(6859): 43-48.
Zilberberg, N., N. Ilan and S. A. Goldstein (2001). "KCNKO: opening and closing the 2-P-domain potassium leak channel entails "C-type" gating of the outer pore." Neuron **32**(4): 635-648.
Zivanov, J., T. Nakane, B. O. Forsberg, D. Kimanius, W. J. Hagen, E. Lindahl and S. H. Scheres (2018). "New tools for automated high-resolution cryo-EM structure determination in RELION-3." Elife **7**.